Retinal function of the voltage-gated calcium channel subunit $\alpha_2\delta$-3

Light-dependent effects in $\alpha_2\delta$-3 mutant and in wild type retina

Dissertation

zur Erlangung des Grades eines

Doktors der Naturwissenschaften

der Mathematisch-Naturwissenschaftlichen Fakultät

und

der Medizinischen Fakultät

der Eberhard-Karls-Universität Tübingen

vorgelegt

von

Hartwig Seitter

aus Stuttgart, Deutschland

Dezember 2016

Tag der mündlichen Prüfung: 30.03.2017

Dekan der Math.-Nat. Fakultät: Prof. Dr. W. Rosenstiel

Dekan der Medizinischen Fakultät: Prof. Dr. I. B. Autenrieth

1. Berichterstatter: Dr. Thomas Münch

2. Berichterstatter: Prof. Dr. Jutta Engel

Prüfungskommission:

Dr. Thomas Münch

Prof. Dr. Jutta Engel

Prof. Dr. Bernd Wissinger

Hon.-Prof. Dr. Joachim Ostwald

Erklärung / Declaration:

Ich erkläre, dass ich die zur Promotion eingereichte Arbeit mit dem Titel:

„Retinal function of the voltage-gated calcium channel subunit $\alpha_2\delta$-3

Light-dependent effects in $\alpha_2\delta$-3 mutant and in wild type retina“

selbständig verfasst, nur die angegebenen Quellen und Hilfsmittel benutzt und wörtlich oder inhaltlich übernommene Stellen als solche gekennzeichnet habe. Ich versichere an Eides statt, dass diese Angaben wahr sind und dass ich nichts verschwiegen habe. Mir ist bekannt, dass die falsche Abgabe einer Versicherung an Eides statt mit Freiheitsstrafe bis zu drei Jahren oder mit Geldstrafe bestraft wird.

I hereby declare that I have produced the work entitled “Retinal function of the voltage-gated calcium channel subunit $\alpha_2\delta$-3 - Light-dependent effects in $\alpha_2\delta$-3 mutant and in wild type retina“, submitted for the award of a doctorate, on my own (without external help), have used only the sources and aids indicated and have marked passages included from other works, whether verbatim or in content, as such. I swear upon oath that these statements are true and that I have not concealed anything. I am aware that making a false declaration under oath is punishable by a term of imprisonment of up to three years or by a fine.

Tübingen, den ....

Datum / Date Unterschrift /Signature

Table of contents

I. Abstract

The retina employs a large number of cell types that fulfill a broad spectrum of computations. It comes as no surprise that this complex network would make use of an equal diversity of molecular tools, such as voltage-gated calcium channels (VGCC). In fact, all pore-forming α_1 subunits of VGCC and modulatory β and auxiliary $\alpha_2\delta$ subunits were found in the retina. Yet, little detail is known about the functional implementation of individual VGCC subunits in the retinal circuitry.

My work described in part 1 focused on the retinal expression and function of one VGCC subunit, called $\alpha_2\delta$-3, employing an $\alpha_2\delta$-3 knockout mouse. I found transcription of all $\alpha_2\delta$ subunit genes throughout postnatal retinal development and strong expression of $\alpha_2\delta$-3 in horizontal cells. Yet, in my patch-clamp recordings from isolated horizontal cells I did not find an impact on their somatic calcium currents, leaving a possible involvement of $\alpha_2\delta$-3 in the horizontal cell axon-to-rod connection. Outer retina function, determined by electroretinogram, and optokinetic reflex behavior was normal in $\alpha_2\delta$-3 knockout animals. However, I discovered changes to the retinal output in micro-electrode array recordings of ganglion cell responses. I applied a paradigm of light stimulation at different ambient luminance levels that revealed effects of the $\alpha_2\delta$-3 knockout only in scotopic and mesopic light levels. In summary, $\alpha_2\delta$-3 is a candidate for horizontal cell axon-specific calcium signal modulation and exerts its function in non-photopic regimes.

The retina constantly adapts to features of the current visual environment, most prominently, the ambient light intensity or luminance. These adaptations are based on mechanisms throughout the retinal network. Adaption is commonly considered to keep signal processing within the dynamic range of the system as well as keep the retinal output stable across changing conditions, such as the light intensity. The results of part 1 show that different building blocks of retinal circuits - here the $\alpha_2\delta$-3 subunit - can contribute to retinal function at distinct light level regimes.

In part 2, we looked more generally at the output of the retina (responses of ganglion cells) across different levels of ambient luminance. We found that ganglion cell responses were not stable across luminance levels, neither in single ganglion cell types nor in the ganglion cell population, but that they changed their responses qualitatively.

These response changes were also reflected downstream in the activity of the lateral geniculate nucleus.

Furthermore, we observed that rod photoreceptors could drive visual responses of ganglion cells in photopic luminance levels, where they were commonly thought to be saturated. While experiencing initial incremental saturation upon stepping to photopic luminance, rods recovered responsiveness at all light levels tested, but the rate of recovery was faster with brighter ambient light intensity. Computational modeling suggested adaptive translocation of elements of the signal transduction cascade as potential explanations for rod signaling at high light intensities. The photopic rod activity dynamics have important implications for the interpretation of experimental data and for the question of rod photoreceptor contributions to daylight vision.

In summary, while some circuitry elements associated with luminance regimes are known (e.g. rod and cone pathways), details on the underlying molecular mechanisms are scarce. My data suggests $\alpha_2\delta$-3 as a promising candidate for a molecular determinant of light adaptation that could exert its function within horizontal cells in an axonal compartment-specific way. It will be interesting to pinpoint the exact role of $\alpha_2\delta$-3 in retinal light adaptation and to determine what (sub-)cellular function this protein serves in horizontal cells.

II. Synopsis

1. General introduction

I started out my thesis work with a simple question: Does the knockout of voltage-gated calcium channel subunit $\alpha_2\delta$-3 affect the function of the mouse retina? There was nothing known about whether it is expressed in the retina and, if yes, where and what its function is. During my investigation, I found a surprising expression localization for the *Cacna2d3* gene that codes for $\alpha_2\delta$-3. Yet to nail down the physiological significance of $\alpha_2\delta$-3 for the mouse retina I resorted to looking at the retinal output, encoded in retinal ganglion cell spiking activity. In the course of my work on ganglion cell recordings I partook in studies of light adaptational effects on retinal coding and contributions of rod photoreceptors to photopic vision. Some of the insights gained from these experiments fed back to my research on the $\alpha_2\delta$-3 subunit. Herein I will outline the importance of studying voltage-gated calcium channels in the retina for the understanding of both calcium channel functional properties and their influence on neuronal computation.

1a. Voltage-gated calcium channels

Voltage-gated calcium channels (VGCC) are key molecular components in muscle excitation-contraction coupling, cardiac and neuronal pace-making, synaptic vesicle release, regulation of gene transcription, long-term plasticity and more. Neuronal VGCC of the L-, P/Q-, N- and R-Type form complexes composed of pore-forming α_1 subunits (Catterall et al., 2005), modulatory β subunits and auxiliary $\alpha_2\delta$ subunits (Dolphin, 2012), whereas T-Type channels do not seem to associate with $\alpha_2\delta$ or β subunits.

α_1 subunits

The main biophysical properties and pharmacological profiles of VGCC are determined by the α_1 subunits (Catterall et al., 2005; Zamponi et al., 2015). The α_1 subunits are encoded by a family of ten genes (termed *Cacna1**, * = a to f or s), subdivided into high-voltage activated channels of classes Ca_V1 (L-Type, 4 isoforms) and Ca_V2 (P/Q-,

N-, R-Type, 3 isoforms) and low-voltage activated class Ca_V3 (T-Type, 3 isoforms). A single α_1 subunit consists of four homologous repeats (I to IV) with six transmembrane domains each (S1 to S6). The S4 segments comprise the main part of the voltage-sensor, while the S5 to S6 loops line the conduction pore and are crucial for the ion selectivity. Large intracellular loops and the C-terminal tail form the binding sites for intracellular interaction partners like β subunits and calmodulin. The interaction site for $\alpha_2\delta$ subunits seems to be in the C-terminal half of α_1, most likely within extracellular parts of S5-S6 in repeat III (Gurnett et al., 1997), although recently also S1-S2 of repeat I has been implicated (Wu et al., 2015).

Mouse retina expresses all Cav1 and Cav2 genes (Specht et al., 2009; Knoflach et al., 2013), yet there have been only isolated reports on expression of individual α_1 subunits in different cell types of the retina. The most prominent α_1 subunit in mouse retina is $Ca_V1.4$, which is mediating synaptic vesicle release in photoreceptors (Morgans, 2001; Bartoletti et al., 2011) and bipolar cells (Berntson et al., 2003; Mercer et al., 2011). $Ca_V1.4$ (α1F; gene Cacna1f) is characterized by little voltage-dependent inactivation and a complete lack of calcium-dependent inactivation (Koschak et al., 2003; Singh et al., 2006) which makes it ideally suited for sustained calcium currents in photoreceptor synaptic terminals. Mutations in human $Ca_V1.4$ (Wutz et al., 2002) lead to photoreceptor degeneration (Chen et al., 2012) and to a number of X-linked visual disorders like Åland Island Eye Disease (Jalkanen et al., 2007), Cone-Rod Dystrophy (Jalkanen et al., 2006), X-linked retinal disorder (Hope et al., 2005) and congenital stationary night blindness (reviewed in Stockner & Koschak, 2013).

In mice, $Ca_V1.4$ knockout results in absence of normal photoreceptor ribbon synapses (Zabouri and Haverkamp, 2013), leads to dendritic sprouting of bipolar and horizontal cells (Bayley and Morgans, 2007) and postsynaptic modifications (Specht et al., 2009). Even a functional dysregulation of $Ca_V1.4$ channels disrupts maturation of photoreceptor synaptic ribbons and causes severe disturbances of signal transmission (Knoflach et al., 2013, 2015; Liu et al., 2013b; Regus-Leidig et al., 2014).

β subunits

The β subunits are encoded by four genes, *Cacnb1* - *Cacnb4*, giving rise to four principle isoforms β_1 to β_4. β subunits modulate calcium channel gating characteristics by directly increasing open probability (Meir et al., 2000) as well as indirectly by

interaction with other regulatory factors like G proteins (De Waard et al., 1997). They also promote cell surface expression by promoting forward trafficking from the endoplasmic reticulum (reviewed in Buraei and Yang, 2013). Structurally, β subunits resemble membrane-associated guanylate kinases (MAGUK (Takahashi, 2005)), lacking the kinase activity, but instead binding to α-interaction domains (AID) within the I-II linker of α_1 subunits (Pragnell et al., 1994). Splice variants of β_4 also exhibit nuclear targeting and exert functions in gene transcription regulation (Hibino et al., 2003; Etemad et al., 2014).

All β subunits are expressed in mouse retina, with the expression level of β_2 being the highest (Knoflach et al., 2013), likely because β_2 is the predominant β subunit of photoreceptors. β_3 was found in cholinergic amacrine cells and Calretinin-positive cells, while β_1 and β_4 expression is less defined (Ball et al., 2011). A knockout of β_2 leads to photoreceptor synaptic ribbon disorganization and to abolished synaptic transmission especially from rods (Ball et al., 2002; Katiyar et al., 2015).

$\alpha_2\delta$ subunits

Four genes (*Cacna2d1 to Cacna2d4*) encode for the $\alpha_2\delta$ subunits $\alpha_2\delta$-1 to $\alpha_2\delta$-4 (Curtis and Catterall, 1984; Leung et al., 1987; Ellis et al., 1988; Klugbauer et al., 1999; Qin et al., 2002). The $\alpha_2\delta$ subunits are subject to strong post-translational modification. The precursor proteins of $\alpha_2\delta$ get proteolytically cleaved into α_2 and δ parts that are re-linked by disulfide bonds (Andrade et al., 2007; Calderón-Rivera et al., 2012) and the extracellular α_2 part is highly glycosylated (Sandoval et al., 2004; Tetreault et al., 2016). Membrane association of $\alpha_2\delta$ is achieved through a glycosylphosphatidylinositol (GPI)-anchor (Davies et al., 2010; Alvarez-Laviada et al., 2014) or via type I transmembrane topology of the δ part (Robinson et al., 2011). Membrane anchoring however is not absolutely necessary for calcium current enhancement by $\alpha_2\delta$ subunits (Kadurin et al., 2012). Yet, since the $\alpha_2\delta$ protein is largely extracellular it can interact also with other extracellular proteins apart from the α_1 subunits. Several protein domains are found in the α_2 part. Cache domains and Von Willebrand factor type A (VWA) domains were identified by sequence homology. VWA domains are found in extracellular matrix/cell-cell interaction proteins and contain a metal ion-dependent adhesion site (MIDAS), whose integrity was shown to be required for the effect of $\alpha_2\delta$-2 on calcium channel trafficking (Canti et al., 2005). The $\alpha_2\delta$ subunits play a role in trafficking of calcium

channel complexes by increasing the number of functional channels on the membrane (Davies et al., 2007; Dolphin, 2013), leading to an enhanced calcium current density. This increase in current can be limited to a single calcium channel isoform within a neuronal cell type (D'Arco et al., 2015). While the calcium current density increase seems to be a general effect mediated by $\alpha_2\delta$ subunits, $\alpha_2\delta$-1, $\alpha_2\delta$-3 and $\alpha_2\delta$-4 can also influence biophysical properties of the channels, such as kinetics and the voltage-dependence of activation (Felix et al., 1997; Klugbauer et al., 1999; Lee et al., 2015), which was not found for $\alpha_2\delta$-2 (Gao et al., 2000; Brodbeck et al., 2002). The $\alpha_2\delta$ subunits also play a role in localization and stabilization of channel complexes within target structures like synaptic ribbons (Thoreson et al., 2013) or lipid rafts (Robinson et al., 2011), thereby participating in establishing calcium nanodomains. It was also suggested that $\alpha_2\delta$-2 is an important component in autophagy (Tian et al.,2015). Furthermore there is evidence that $\alpha_2\delta$ subunits can influence synaptogenesis (Kurshan et al., 2009) also by acting as a neuronal thrombospondin receptor (Eroglu et al., 2009), which might play a role in epilepsy (Mendus et al., 2015). In $\alpha_2\delta$-3 knockout mice defects in $Ca_V2.1$ targeting as well as in synapse formation and synaptic morphology of auditory nerve fiber terminals have been found (Pirone et al., 2014). Some of these roles of $\alpha_2\delta$ subunits in synaptic structuring may even be independent of calcium channel complexes. $\alpha_2\delta$-1 and $\alpha_2\delta$-2 are the target of gabapentinoid drugs gabapentin and pregabalin which are used in treatment of neuropathic pain. Chronic application of gabapentinoids leads to a reduction in calcium currents, most likely due to interference with trafficking of channel complexes (Bauer et al., 2009; Tran-Van-Minh and Dolphin, 2010), but also acute effects of gabapentinoid application have been found (Farrell et al., 2010; Uchitel et al., 2014).

$\alpha_2\delta$ subunits in the retina

My own data shows mRNA expression of all $\alpha_2\delta$ isoforms in mouse retina from early postnatal development through adulthood (publication 1, Fig. 2). Ganglion cells of rat retina were shown to express $\alpha_2\delta$-1 (Huang et al., 2013) and a role in retinal synaptogenesis has been suggested (Eroglu et al., 2009). There is no published data on $\alpha_2\delta$-2 expression localization in the retina. $\alpha_2\delta$-4 is the highest expressed isoform in mouse retina (Knoflach et al., 2013) and it is expressed by photoreceptors and bipolar cells (Wycisk et al., 2006; Mercer et al., 2011; de Sevilla Muller et al., 2013;

Thoreson et al., 2013). A truncating mutation of $\alpha_2\delta$-4 causes severe changes in the electroretinogram and leads to photoreceptor degeneration (Wycisk et al., 2006), as well as mislocalization of calcium-activated chloride channels in photoreceptors (Caputo et al., 2015). Interestingly a naturally occurring splice variant that truncates the $\alpha_2\delta$-4 open reading frame in a similar way as the mutation has been found in mouse retina (Bacchi et al., 2015), leading to $\alpha_2\delta$-4 protein that lacks the membrane-anchoring δ part.

Expression of $\alpha_2\delta$-3 had previously been reported in isolated mouse ON bipolar cells (Nakajima et al., 2009). However, the in situ hybridization data from the study of Nakajima et al. could represent a horizontal cell staining pattern (see publication 1, Fig. 3). Horizontal cells were indeed found to have strongest $\alpha_2\delta$-3 expression of all retinal cell types by an extensive micro-array study (Siegert et al., 2012). A recent study, using evidence from co-immunolabeling, proposed absence of $\alpha_2\delta$-3 staining in horizontal cells, but suggested expression in photoreceptors, bipolar cells, glycinergic amacrine cells and most cells in the ganglion cell layer (Pérez de Sevilla Müller et al., 2015).

1b. Retina anatomy and connectivity

We humans, like many mammals, rely strongly on vision to navigate our environment. Indeed, much of our sensory experience is determined by the visual world. All of this sensory experience starts within our retina, a dense neuronal tissue lining the back of our eyes that constitutes the first stage of our visual system. In the following, the features of mouse retina are presented, however most of it generalizes to other mammalian retinae including human retina.

Light is detected by two classes of photoreceptors, rods and cones, within which photon absorption gets transformed into electrical signals in a biochemical cascade called phototransduction (Molday and Moritz, 2015). Photoreceptors give glutamatergic input to bipolar cells which relay the signal to the inner retina where they provide excitatory glutamatergic drive to amacrine and retinal ganglion cells (Figure 1A) (Wässle, 2004). This glutamatergic feedforward signaling gets modulated through (mostly) inhibitory feedback and lateral connections by horizontal cells in the outer retina (Thoreson and Mangel, 2012) and amacrine cells in the inner retina (Eggers and Lukasiewicz, 2011). The ganglion cells are the sole output neurons of the retina,

sending a spike-encoded representation of the visual world - pre-processed by the retina - through their axons down the optic nerve to visual centers in the brain, most notably the lateral geniculate nucleus and the superior colliculus (Erskine and Herrera, 2014). The retina also contains a unique glia cell type, the Müller cell. These glia form the inner and outer limiting membranes of the retina, help maintain homeostasis and might serve as a light guide to the photoreceptors (Reichenbach and Bringmann, 2013). Adjacent to the neural retina, the retinal pigment epithelium provides stray light reduction through photon absorption, recycling of bleached photopigments, retinal homeostasis and phagocytosis of shedded outer segment parts of photoreceptors (Lamb and Pugh, 2004).

The glutamate receptor identity on bipolar cell dendrites determines the polarity of bipolar cell activation and therefore of the postsynaptic cells, giving rise to the principal separation into parallel ON and OFF channels (Wässle, 2004). ON-responding bipolar cells express metabotropic glutamate receptors (mGluR6) and depolarize to light increments, while OFF-responding bipolar and horizontal cells express ionotropic glutamate receptors and depolarize upon light decrements (Figure 1B). The division into ON and OFF pathways is also correlated anatomically to the stratification level of bipolar cells within the inner plexiform layer (IPL). OFF bipolar cells synapse in the distal (outer) sublaminae of the IPL, while ON bipolar cells have longer axons and terminate in the proximal (inner) sublaminae. Consequently, OFF and ON ganglion and amacrine cell dendrites ramify in distal parts and proximal parts of the IPL respectively and ON/OFF responding ganglion and amacrine cells have dendritic branchings in both (although this definite morphology-function relationship has been challenged by publication 3).

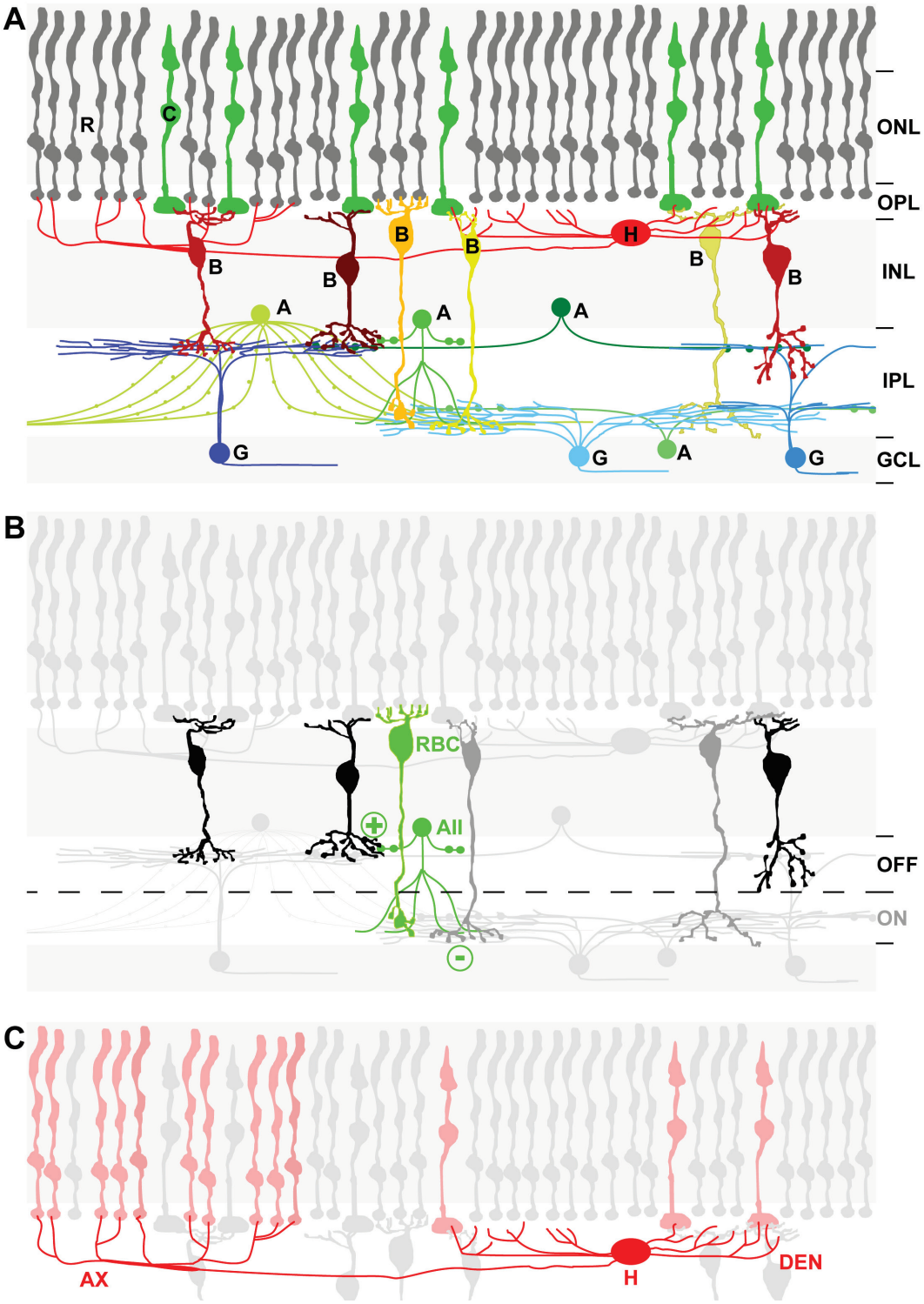

Figure 1: Neuronal cell types and connectivity of the mouse retina.

(A) *Rod (R) and cone (C) photoreceptors are connected through bipolar cells (B) to amacrine (A) and ganglion cells (G). Horizontal cells (H) in the outer retina and amacrine cells in the inner retina provide lateral (mostly inhibitory) connectivity while bipolar cells exert excitatory glutamatergic transmission from outer to inner retina. Ganglion cells are the output neurons of the retina and their axons form the optic nerve. ONL-outer nuclear layer, OPL-outer plexiform layer, INL-inner nuclear layer, IPL-inner plexiform layer, GCL-ganglion cell layer.* ***(B)*** *Cones are connected to several types of ON (grey) and OFF (black) cone bipolar cells, while rods (mainly) connect to a single type of bipolar cell, the rod bipolar cell (RBC). Cone bipolar cells synapse directly with ganglion cells, but rod bipolar cells feed their signals through the AII amacrine cell (AII) into ON (+) and OFF (-) cone bipolar cells. Bipolar cells terminate in different sublaminae of the inner plexiform layer (OFF cells distal, ON cells proximal).* ***(C)*** *Horizontal cells (H) connect to cones with soma-centered dendritic branchings (DEN) and to rods with axonal arborizations (AX), with both compartments functioning largely independently. (composed from (Masland, 2001))*

While cones send their signals through ON and OFF cone bipolar cells directly to ganglion cells and amacrine cells, the rod signals largely follow less straightforward paths (Figure 1B). The main route is called primary rod pathway and harnesses a rod-specific ON bipolar cell, consequently named rod bipolar cell (RBC). The RBC forms excitatory synapses onto AII amacrine cells (AII AC) (Famiglietti and Kolb, 1974). These in turn distribute the signal via gap junctional coupling to ON cone bipolar cells ('sign-conserving') and through glycinergic synapses to OFF cone bipolar cells and OFF ganglion cells (Demb and Singer, 2012), therefore 'sign-inverting' the signal. The RBC to AII AC transmission gets modulated by GABAergic inhibitory feedback from A17 amacrine cells that perform cellular multiplexing by use of independently operating varicosities along their processes (Grimes et al., 2010).

In the secondary rod pathway, rod signals get fed to cones via rod-cone gap junctions (Raviola and Gilula, 1973) and therefore harness the regular cone circuitry through ON and OFF cone bipolar cells. Additionally, a tertiary rod pathway has been found: Type 3a, 3b and Type 4 OFF cone bipolar cells make sparse direct synaptic connections with rods (Hack et al., 1999; Tsukamoto et al., 2001; Mataruga et al., 2007; Haverkamp et al., 2008). Type 3 OFF cone bipolar cells were reported to lack direct input through the primary rod pathway (Mazade and Eggers, 2013). Interestingly, there seems to be a partition of rod signals such that OFF ganglion cells receive rod-driven input either through rod-cone coupling (secondary rod pathway) or directly via the tertiary pathway, but not both (Volgyi, 2004). Among the three pathways, the primary rod pathway has been shown to be the most light-sensitive.

Aside from the aforementioned connections, rods and cones have another common interaction partner in the outer retina, the horizontal cell. Mouse retina has only one horizontal cell type and this is categorized as a (axon-bearing) b-type. B-Type horizontal cells of the mouse connect to both rod and cone photoreceptors using morphologically distinct structures (Peichl and Gonzalez-Soriano, 1994). While cones are contacted by horizontal cell dendritic branchings surrounding the horizontal cell soma, rods are contacted by processes originating from a long axon (Figure 1C). Horizontal cells form two intensively coupled networks with dendro-dendritic (through Connexin 57) and axo-axonal gap junctions (through Connexin 57 and Connexin 50 (Janssen-Bienhold et al., 2009; Dorgau et al., 2015)), thus maintaining the photoreceptor type-selective connection. There is some physiological evidence of an

interaction between both photoreceptor types through horizontal cells at least in the cone-horizontal cell-rod direction (Trumpler et al., 2008; Szikra et al., 2014).

1c. Visual processing in the retina

As the complex connectivity within the retina suggests, the retinal output is more than a mere pixel-wise representation of the visual world as a camera would produce it. The retina pre-processes the visual input (which is pixel-like on the level of photoreceptor activation) to extract features of the visual scene (Masland, 2012). Thus the retinal output encodes luminance, color, contrast and spatial/temporal properties but also complex features such as motion direction (Barlow and Levick, 1965), approaching motion (Munch et al., 2009), orientation of objects (Bloomfield, 1994) and local edge detection (Levick, 1967). Each ganglion cell type is considered to form a separate information channel, encoding different features of the visual world. Currently it is assumed, that more than 25 different ganglion cell types provide parallel encoding of the extracted features within the spikes they send down the optic nerve (Sanes and Masland, 2015; Baden et al., 2016). The complexity of these computations arises through the intricate retinal circuitry. A first step in parallel processing is realized in feeding photoreceptor signals to 13 or more different bipolar cell types (Euler et al., 2014). Apart from splitting the signal into ON and OFF channels, bipolar cells can be chromatically selective (by contacting different spectral cone types, e.g. type 9 “blue cone” bipolar cells) and also show different temporal characteristics, as well as spiking or non-spiking responses (Baden et al., 2013). The diversity of retinal computations gets increased by the interactions with horizontal cells in outer retina and dozens of amacrine cell types in the inner retina, allowing for feedforward and feedback inhibition and disinhibition type of modulatory effects.

1d. Light adaptation

Light intensities in our visual environment span 10 to 12 orders of magnitude, from a dim star in the night sky to snow on a bright sunny day. The visual system applies several mechanisms to adapt to these hugely different levels of irradiance. Pupil constriction or dilation controls some of the amount of light permitted to reach the retina (contributes ~1 order of magnitude of dynamic range). Thus, the bulk of the adaptation

to different light intensities takes place within the retina. Firstly, the two classes of photoreceptors, rods and cones, operate within different dynamic ranges (Schultze, 1866; Ingram et al., 2016). Rods are tuned for higher sensitivity (Fain and Dowling, 1973), even capable of detecting single photons (Baylor et al., 1979), and therefore vision under dim light relies solely on rod activity (scotopic regime). At higher irradiances, cones get activated and the retinal circuitry is driven by a mixed input from both photoreceptor systems (mesopic regime) (Naarendorp et al., 2010). It is currently often believed that upon reaching yet higher irradiance, rod photoreceptors saturate and merely cone photoreceptors can sustain dynamic signaling of visual inputs (photopic regime) (Lamb, 2016). This widely held view however does not hold true, as is highlighted in the dynamics of rod-driven activity throughout high photopic light intensities (publication 4). In addition to changes in photoreceptor type activity also the involved downstream cell types and retinal connectivity adapts to illumination conditions, affecting retinal processing (e.g. coupling strengths of horizontal and AII amacrine cells (Bloomfield et al., 1997; Xin and Bloomfield, 1999)). One example for processing changes during light adaption is the switch-like activation of the inhibitory receptive field surround upon reaching cone threshold (Farrow et al., 2013b). Alongside these large-scale switches in circuitry elements used by the retina at different illumination conditions, likely many more mechanisms exist for the adaptation of the processing within the retinal network to also smaller changes in ambient light level (publication 3 and publication 1).

2. Aim of the thesis

My doctoral project mainly revolved around the functional impact of voltage-gated calcium channel subunit $\alpha_2\delta$-3 in mouse retina (part 1). During the course of my work, I also participated in developing micro-electrode array (MEA) recording techniques and applied these recording techniques to studies of light-adaptational changes in the retina (part 2). The insights gained from the investigation of changes during light adaptation fed back into the design of the experiments for my main project on the $\alpha_2\delta$-3 subunit.

Part 1: Functional roles of $\alpha_2\delta$-3 in the mouse retina

I investigated the effects of a knockout of calcium channel subunit $\alpha_2\delta$-3 on retinal function with a focus on horizontal cells, the main cell type expressing $\alpha_2\delta$-3 in mouse retina. For this part, I investigated the properties of voltage-gated calcium currents in horizontal cells and used MEAs to study the impact of the knockout of $\alpha_2\delta$-3 on retinal processing (publication 1).

Part 2: Changes in retinal activity during light adaptation & methodology

- I applied MEA recording techniques to studies of light adaptational changes in retinal output and to the recovery of rod photoreceptors from saturation (publications 3 + 4).

- I participated in the development and optimisation of perforated MEA techniques for stable long-term recordings of individual retinal ganglion cell activity and photoreceptor responses to a diverse set of visual stimuli (publication 2).

3. Part 1: Functional roles of $\alpha_2\delta$-3 in the mouse retina

3a. Scientific question and summary of findings

This part of my PhD thesis focuses on the functional roles of voltage-gated calcium channel subunit $\alpha_2\delta$-3 in mouse retina (publication 1). In this project I set out to determine the retinal cell type(s) expressing $\alpha_2\delta$-3 and the potential involvement in retinal physiology and processing.

First, I could show that all $\alpha_2\delta$ subunit genes are expressed in mouse retina from early postnatal development until adulthood (publication 1, Fig. 2). I localized the strongest expression (determined by a β-galactosidase reporter) of $\alpha_2\delta$-3 in horizontal cells, but also at presumably lower expression levels in amacrine cells and melanopsin-positive ganglion cells (publication 1, Fig. 3 + 4). Behavioral analysis, however, did not reveal an effect on the optokinetic reflex of the $\alpha_2\delta$-3 knockout animals (publication 1, Fig. 1). Outer retina function, determined by *in vivo* electroretinography, was also found unperturbed by the knockout (publication 1, Fig. 7). As horizontal cells seemed the main cell type affected by the $\alpha_2\delta$-3 knockout, judged by the β-galactosidase reporter staining intensity, I chose to do patch-clamp recordings from this cell type. I performed recordings from horizontal cell somata using Barium as charge carrier to investigate differences in calcium channel-mediated currents (publication 1, Fig. 6). Unexpectedly, there were no differences in current densities or voltage-dependent inactivation properties between wildtype and $\alpha_2\delta$-3 knockout animals. In the following I chose micro-electrode array (MEA) recordings from ganglion cells as a means to elucidate if the knockout of $\alpha_2\delta$-3 had an effect on the processing of visual stimuli through the retinal network. My recordings were designed to probe a wide set of retinal response characteristics spanning the classical luminance regimes of scotopic (rod only), mesopic (mixed rod-cone driven) and higher photopic (then presumed cone only) levels. Indeed, I could find several changes in ganglion cell responses and spontaneous activity patterns that were tied to low light intensity regimes (publication 1, Fig. 8-10). More specifically, I found an elevated spontaneous spiking activity in OFF ganglion cells throughout all light levels tested and there was an apparent compression in response strength to a white noise flicker stimulus of both ON and OFF ganglion cells, tied to scotopic and mesopic regimes (publication 1, Fig. 8). Looking more closely at the spontaneous activity patterns of ON cells, I discovered an elevation of spike

rates in some cells in $\alpha_2\delta$-3 knockout that was related to spatial properties of grating stimuli that had been shown. This dependence was linked to higher spatial frequencies and only appeared during scotopic luminance levels (publication 1, Fig. 9). Furthermore, in responses to full-field contrast steps, I observed a difference in delay timings in ON ganglion cells during scotopic luminance (publication 1, Fig. 10).

Thus, the majority of differences between wild type and $\alpha_2\delta$-3 knockout animals became evident in scotopic and mesopic luminance during my MEA recordings. The approach to record across several levels of light adaptation proved to be fundamental to the discovery of phenotypes of the $\alpha_2\delta$-3 knockout. A similar basic approach laid the groundwork for the other studies contained within this thesis work.

The light level restriction of ganglion cell response effects brings the rod/cone-specific circuits and also their interactions into focus. For example, horizontal cells give feedback to rod and cone photoreceptors with their axonal and dendritic processes respectively (see Figure 1C). The restriction of phenotypes in the MEA recordings to non-photopic regimes could then derive from a specific involvement of $\alpha_2\delta$-3 in the axonal compartment of horizontal cells. Some implications of these findings concerning the lack of changes to calcium current properties in horizontal cell somata and the effects observed in ganglion cells predominantly at scotopic to mesopic luminance levels are discussed in section 5a.

3b. Scientific context I: Why study voltage-gated calcium channels in native systems

So far the vast majority of studies on calcium channel function were carried out in heterologous expression systems, e.g. HEK293 cells. This is a powerful approach in elucidating structure-function relationships of individual channel subunit isoforms and the effect of channel mutations. Examples of how expression systems are used to investigate channels and their potential interaction partners include:

- (co-)expression of different subunits and electrophysiological characterization of calcium currents and effects of channel complex compositions
- co-expression with potential interaction partners, pull-down assays and proteomic analysis of interactions

- immunolabelling of tagged channel subunits for (co-)localization and trafficking studies

However, only interactions that are provided in the experimental setting can be studied. This is particularly relevant since the protein interaction partners available can change functional characteristics of the channel complexes (Shaltiel et al., 2012; Park et al., 2014; Grabner et al., 2015). As of yet, certainly not all interaction partners of calcium channels are known, even in well-studied systems like synapses. Most likely there is also a large degree of heterogeneity in the molecular toolset utilized by different types of synapses.

Two main factors set native neuronal systems apart from heterologous expression systems: The uniqueness of the cell type in focus itself and its intercellular interactions. Composition and regulation of synaptic signaling complexes are tuned to a cell's physiology. It seems likely that some specialized functions can only be discovered by studying the specific cells that express the gene of interest because these cells provide the native protein network environment. As a consequence, the cell type studied matters, but likewise does the connectivity. The availability of crucial proteins on both sides of a connection can have profound effects on synaptic structuring. Specific properties of (heterogeneous) connections in particular cannot be recapitulated in expression systems. It is important to note that the mostly extracellular $\alpha_2\delta$ subunits are reported to mediate transsynaptic interactions (Fell et al., 2016).

3c. Scientific context II: Voltage-gated calcium channels in the retina

The vertebrate retina is an elegantly structured part of the central nervous system. Its cells and synaptic connections are organized in distinct layers that even exhibit functional subdivisions, e.g. the ON and OFF sublaminae of the inner plexiform layer. There is a very solid basic understanding of the function and computations of many well-described cell types and of the underlying morphology and connectivity. This provides an unrivaled foundation for the meaningful interpretation of novel findings as to the local function of a protein or gene of interest.

In my point of view, it is of particular relevance to study VGCC in the retina. Due to the vast diversity of cell types and synaptic transmission modes (excitatory, pre- and postsynaptic inhibitory, electrical coupling) within the retinal network there is an

extraordinary potential for finding specialized functional interactions of calcium channels. In fact, all $\alpha_2\delta$ subunit genes as well as all α_1 and β subunit genes are expressed in mouse retina (Knoflach et al., 2013), which is a unique feature within neuronal tissues. Some remarkable specialized calcium channel functions have been described in the retina, e.g. a lack of inactivation ($Ca_V1.4$ (Koschak et al., 2003) and my own data from horizontal cells) that allows for sustained calcium influx during graded membrane potential changes or, in contrast to that, the use of inactivation as a form of synaptic depression in contrast adaptation (Jarsky et al., 2011) . Also the studies of auxiliary subunits have revealed some novel aspects like the transiency of interaction between $Ca_V1.4$ and $\alpha_2\delta$-4 subunits (Mercer et al., 2011) or possible calcium channel independent functions as seen in a splice variant of $\alpha_2\delta$-4 (Bacchi et al., 2015). Consequently, the retina provides opportunities to both investigate basic calcium channel properties and to learn how calcium channels shape neuronal communication.

On the other hand, the complexity of the retinal network and the widespread expression of individual VGCC subunits within several cell types makes studies of VGCC function in retina also challenging, especially when the cell types expressing a certain VGCC subunit are only partially known. Likewise, the mixed expression of several calcium channel subunit isoforms in a single cell type can also complicate analysis, especially due to the lack of good antibodies for localization experiments. My results on mechanisms for the $\alpha_2\delta$-3 subunit show some of these difficulties. Such challenges are common when studying widely expressed calcium channels in the retina. This can also be seen in the most prominent retinal calcium channel subunit $Ca_V1.4$ (Knoflach et al., 2013) which affects retinal processing in both photoreceptor and bipolar cell ribbon synapses. A perspective on how to ameliorate some of these issues is given in the outlook (section 5c).

3d. Methodological aspects: Advantages and shortcomings of the methodological approaches I used in my study

The most direct approach of studying a retinal cell types' physiology is performing electrophysiological recordings. However, I was unsuccessful in doing patch-clamp recordings of horizontal cells in retinal slices. Horizontal cells comprise only a small fraction of cells in their retinal location and I could not distinguish them from the

surrounding bipolar cells. Superficially positioned horizontal cells that would be accessible for patching also most likely have damaged processes by the vertical sectioning because their dendrites and axonal arbors extend along the horizontal plane. I therefore chose to patch isolated horizontal cells, which has the further advantage that synaptic inputs do not obscure voltage-gated currents.

Since mouse horizontal cells have morphologically and functionally clearly separated compartments - a somatodendritic part that contacts cones and an axonal part that contacts rods - I was interested in investigating both. In the dissociated retina preparation I used, axonal arborizations of horizontal cells were detached from the somata. However, patch clamp recordings from these axon terminal systems had very low success rates and my recordings suffered from high leak currents and very low stability. Even if axonal parts did not detach, during recordings in a whole-cell configuration from the soma, the long thin axon would effectively prevent recording currents originating from the axonal arbor due to 'space clamp' problems (Trumpler et al., 2008). Therefore I chose an indirect way to look at effects of the knockout of $\alpha_2\delta$-3 on either of these compartments. Recordings of retinal ganglion cells offered the opportunity to record the retinal output under scotopic and photopic conditions, i.e. rod-driven and (mainly) cone-driven responses. The idea behind this was to functionally isolate horizontal cell axon-based (rod system) and dendritic-based (cone system) mechanisms and analyze the impact of each on ganglion cell activity.

Micro-electrode arrays (MEA) enable large scale recordings of many ganglion cells for a long time and therefore over many different visual stimuli and/or light levels (refer to section 4e for elaboration on this topic). This allowed me to screen for potential dysfunctions of the $\alpha_2\delta$-3 knockout retina on a global scale, involving horizontal cell contributions from the axonal (scotopic) and dendritic compartments (mesopic and photopic). MEA recordings from ganglion cells also have a drawback, as the identity of the cells recorded from is unknown. Consequently, details on the upstream circuitry involved are missing. This makes it challenging to draw conclusions on the mechanisms shaping the responses and to interpret or localize effects one might observe. The widespread expression of $\alpha_2\delta$-3 in several retinal cell types that I have observed was confirmed in a recent publication (Pérez de Sevilla Müller et al., 2015). Among other cell types, this study implicates expression in AII amacrine cells which

also could contribute to luminance level dependent effects of the $\alpha_2\delta$-3 knockout on retinal processing.

This uncertainty in localizing a phenotypic involvement of the $\alpha_2\delta$-3 knockout to a cell type has confounding effects on the potentially more powerful use of MEA recordings in this study. While the distribution of labor between the horizontal cell dendritic and axonal compartments would allow studying subcellular calcium channel regulation and function, the unclear origins of the observed ganglion cell phenotypes makes it speculative to deduct the mechanistic involvement of horizontal cells. Still, the approach to record under different luminance conditions to reveal the subtle effects I found was crucial in determining the impact of $\alpha_2\delta$-3 on retinal processing. This approach was derived from the studies on light adaptational changes to retinal processing (part 2) and constitutes the common basis contained within this thesis work. The power of longitudinal data collection which is fundamental to these findings are discussed in section 4e.

4. Part 2: Changes in retinal function during light adaptation

4a. Scientific questions and summaries of findings

The choices we make when designing our experimental conditions have major impact on our scientific findings. In retinal physiology a major experimental parameter is light intensity. Yet, the extent of how the light intensity that is used in experiments affects the results obtained seems underappreciated. In the following, I will describe the scientific rationale of two projects that dealt with the dependence of retinal function on the ambient light level and the methodological aspects of such studies. In the first project, we studied the changes of retinal ganglion cell light responses across many levels of luminance and, more specifically, how different luminance levels can affect response characteristics (section 4a$_1$). In the second project, we investigated rod photoreceptor contributions at presumed rod-saturating levels and beyond (section 4a$_2$).

4a$_1$. Changing retinal responses across light levels

Despite vastly changing illuminance in the visual environment – bright sunny to cloudy daylight to artificial lighting and low-light conditions – we perceive the world, e.g. colors, largely unchanged. How can we perceive the visual world in such a coherent and stable way? Does the retina keep its output constant, irrespective of the input? Is adaptation the key to stabilize the retinal output against changing input conditions? Together with Alexandra Tikidji-Hamburyan, Katja Reinhard and others, I studied retinal ganglion cell responses across many luminance levels using MEA recordings (publication 3).

Surprisingly, we found that widespread changes happen to the retinal output, not only when switching from pure rod-based vision through mixed rod and cone signals to presumed purely cone-driven levels, but also when switching light levels within a given luminance regime (a regime is equivalent to the classical scotopic, mesopic and photopic ranges). We focused on a basic property for this study, the response polarity of retinal ganglion cells, as a proxy for response stability across light adaptation. The polarity is a fundamental characteristic of a given ganglion cell, that describes whether the cell increases spike rate to an increment (ON) or decrement (OFF) of stimulus luminance, or to both (ON-OFF). The polarity is often used as a first line descriptor of

a cell and is thus far mostly considered a hard-wired property. Our data suggests that polarity is not as stable across light adaptation as previously thought and that changes in fact are a common phenomenon.

We observed that ganglion cells that seemed pure ON or OFF responding at one luminance level could exhibit an early or delayed anti-preferred response (an OFF-type response for ON cells and vice versa) at other light levels (publication 3, Fig. 2). This kind of behavior was not a singular finding but in fact could be observed in the majority of ganglion cells (publication 3, Fig. 3). Within a given light level, however, ganglion cell responses were stable. When switching back and forth between different background luminance intensities, the responses also switched back and forth between the characteristic responses at the respective luminance (publication 3, Fig. 5). Therefore, this does not constitute a peculiar response variability, but the changes are distinctly triggered by light level-dependent adaptational processes. Response polarity has commonly been thought to be strictly related to a ganglion cells' stratification level within the inner plexiform layer, with ON cells ramifying with their dendrites more proximally and OFF cells more distally. However, in our experiments ganglion cells changed their response polarity despite stratifying in a sublamina that is presumed pure ON or pure OFF (publication 3, Fig. 6). Reproducible changes were also present in ganglion cell responses to natural movies (publication 3, Fig. S3), which indicates that changes are relevant to real-life vision and not merely related to somewhat artificial stimuli. The phenomenon is also not a rodent retina peculiarity as ganglion cells in pig retina were found to exhibit similar response changes (publication 3, Fig. S5). The question arose, whether this instability of the retinal output is passed on to the visual system in the brain. The response variability seems indeed relevant to processing in higher visual centers, as neurons of the lateral geniculate nucleus (LGN), a major target of retinal ganglion cell projections, also showed changes in responses (publication 3, Fig. 7). We investigated some potential mechanisms that might be causal for the observed effects. Some of the changes were caused by inhibitory transmission (publication 3, Fig. S2) or center-surround interactions (publication 3, Fig. 8), but it is evident that there are more mechanisms involved. In section 5b I will discuss some changes I found in my study of $\alpha_2\delta$-3 knockout animals that resembled the light level-dependent effects on polarity described here.

4a$_2$. Re-emergence of rod photoreceptor activity at photopic light levels

It is widely accepted that there is a varying contribution of the different classes of photoreceptors – rods and cones – to retinal light responses across light adaptation. Despite accumulating evidence of rod signaling at higher light intensities, it is still often assumed that there are three fundamentally distinct light adaptational regimes that are caused by different sensitivity of rods and cones and – in particular – saturation of rods: scotopic = rods are active but cone activation threshold is not reached; mesopic = rods and cones are both active; photopic = cones are active but rods are saturated and are therefore not capable of dynamic signaling (i.e. are not participating in driving visual responses). Together with Alexandra Tikidji-Hamburyan, Katja Reinhard, Riccardo Storchi and others, I studied the effect of increasing luminance into and within the 'photopic' regime on the contributions of rod photoreceptors to retinal light responses. We found that rod photoreceptors cannot only escape initial incremental saturation and contribute to retinal light responses at photopic light levels, but in fact do even more so with increasing (photopic) luminance (publication 4). Our data highlights that rod signaling shows physiologically relevant complex light-dependent dynamics.

To isolate rod-based activity we used mouse lines in which cone photoreceptors were non-functional. We first looked at retinal output by recording ganglion cell spiking activity on MEAs. Showing several simple light stimuli while steadily increasing luminance levels we determined the presence of detectable light responses of the ganglion cells to our visual stimulation, which we termed responsiveness. After a first disappearance of light responsiveness upon reaching photopic levels, likely due to incremental saturation of rods, rod-driven activity of retinal ganglion cells returned but reached somewhat lower response amplitudes than at scotopic light levels (publication 4, Fig. 2B). The return of responsiveness was not switch-like (either there or absent), but depended on the cumulative light exposure (and the contrast of the stimulus). Put in simpler terms, the effect of illumination 'summed up' to create this re-emergence of responses. Even at the lowest luminance level where an initial loss of responsiveness occurred, the responsiveness eventually completely returned to comparable levels, given enough time (publication 4, Fig. 2C). Yet, it recovered faster at higher light intensities (publication 4, Fig. 2D). This observation did not only hold true for ganglion cell responsiveness. The returning activation of rods was also evident with similar time course in *in vitro* electroretinographic recordings designed to isolate photoreceptor

activity (publication 4, Fig. 3 + S3). Interestingly, the reliability of rod responses (publication 4, Fig. 3D) closely resembled the fraction of responding ganglion cells (publication 4, Fig. 2A). Using computational modeling we showed that this re-emergence of rod activity can be explained by adaptive translocation of elements of the signal transduction cascade (reducing phototransduction gain) and bleaching of rhodopsin, with higher light intensities leading to faster bleaching (publication 4, Fig. 6). The bleaching of rhodopsin then leads to a lower probability of incident photons activating the phototransduction cascade which in turn restores dynamic light signaling of rod photoreceptors. While the effects of bleaching were more pronounced in the *ex vivo* situation with isolated retina (lacking the retinal pigment epithelium and thus having lower rhodopsin regeneration rates), we showed that this process is also relevant *in vivo* by recording from the lateral geniculate nucleus (LGN, publication 4, Fig. 4 + 5).

4b. Scientific context: Luminance level-dependence of retinal coding and function

Our findings on the instability of response characteristics of individual retinal ganglion cells across luminance levels and the re-emergence of rod activity pose several implications both for the basic understanding of retinal output and for the interpretation of studies on retinal circuitry.

When studying the retina, usually the natural stimulus modality is used: Light. Various technical solutions are applied to achieve this visual stimulation, from simple flash lamps (e.g. in electroretinography), through LED-based devices up to computer screens or projectors and even structured illumination or holography techniques. This brings about varying spectral compositions and varying emission intensities of the stimulation devices. Often microscope light paths are used to deliver the light stimuli, either through the condenser or through the objective or even with custom-designed projection optics, each also with their own filter characteristics. An uneven distribution of the incident light can also easily lead to a log unit difference in intensity across the visually stimulated area. Thus, many factors influence the actual light intensity and spectral composition of the light that reaches the photoreceptors.

That being said, it becomes clear that response variabilities which depend on the actual light intensity may greatly change the outcome of an experiment with just little

divergence from the intended light level. Two studies that focus on a common ganglion cell type could come to different results by recording at slightly (< 1 log unit) different luminance. Studies where the ganglion cell type is not known, e.g. MEA recordings or calcium imaging, are even more problematic, as cells are often identified by their response patterns, which then might lead to an inconclusive assignment to a cell type. Particular care should thus be given to accurately report experimental light levels to facilitate comparisons across scientific data acquired in different labs.

The variability of a given ganglion cells' response to the same stimulus over changing luminance (publication 3) raises the question how the target areas in visual centers of the brain deal with this change of inputs. There have been reports that suggested luminance-dependent changes in visual processing of stimulus features (Enroth-Cugell et al., 1975; Dunn et al., 2007; Umino et al., 2008; Farrow et al., 2013b; Allen et al., 2014; Grimes et al., 2014; Pearson and Kerschensteiner, 2015). Recordings from primate LGN showed that OFF and ON pathways are not simply mirror images of one another, but do different computations under changing illumination conditions (Jiang et al., 2015). Also cells in monkey primary visual cortex change their coding strategy according to ambient luminance (Wang and Wang, 2016). Further research is needed to determine whether these response variabilities dilute the hitherto assumed clear-cut separation of information channels given by the individual ganglion cell types that is thought to be a hallmark of retinal processing and coding.

The light stimulation parameters also influence the interpretation of data when considering the contributions of the two principal photoreceptor systems, rods and cones, to visual responses. Our data emphasizes that rod photoreceptor signaling should be taken into consideration when interpreting data acquired under photopic conditions and that there is no easy way of studying cone pathways in isolation by simply increasing the luminance within the experiment. Rod contributions have to be considered in all studies of retinal physiology (also in the photopic regime) and in their interpretation. Even more so, experimental conditions aiming at silencing rods through saturating light levels fail especially when attempting to get far above presumed saturation threshold. Importantly, since the recovery is both light intensity- and time-dependent, short exposure times to a new light level might yield results that do not directly compare to data acquired later at that same light level.

Rods being active at all illumination conditions also sheds some new light on why our retinas are dominated by this photoreceptor type (in sheer numbers), when most of our day to day visual environment is largely photopic range. Recently, photopic level rod responses have been found to contribute to mammalian color vision (Oppermann et al., 2016). In summary, one should not take rods out of the equation merely based on ambient luminance conditions and future research into their photopic functions will help bringing rods out of the dark.

4c. Analytical aspects of our MEA data

The potential of recording many neurons at the same time in parallel is a powerful aspect of micro-electrode array data. This feature made MEAs increasingly popular over the past two decades (Chichilnisky and Kalmar, 2002; Segev et al., 2004; Zeck and Masland, 2007; Fiscella et al., 2012). Earlier MEA systems featured few dozens of electrodes while new CMOS-based MEAs can have thousands. All MEAs allow for large-scale recordings of many cells in parallel with high enough sampling rates to resolve high-frequency burst spiking. However, MEA recordings are oblivious to the origins of the spikes and there is consequently no further information on the cells recorded from. In patch-clamp recordings, the recorded cell can be filled with a dye and subsequently the morphology can be used to identify the cell type. Such complementary data is missing in MEA recordings from retinal ganglion cells and it is therefore unknown which of the 25+ described ganglion cell types a recorded cell belongs to.

There has recently been a lot of effort in trying to identify ganglion cell types based on their physiological responses (Sanes and Masland, 2015; Baden et al., 2016). Different approaches have been taken to physiologically categorize ganglion cells in the past, including inter-spike intervals (Zeck and Masland, 2007), responses to a white noise stimulation (Segev et al., 2004) and using a diverse stimulus set (Carcieri, 2003; Farrow et al., 2013a). The choice of stimuli and their parameters are critical for evoking meaningful responses upon which the analysis can be based (Masland and Martin, 2007). Still, to date it is not resolved how to reliably distinguish ganglion cell types purely on their physiological responses, in particular when considering the response variability across changes in luminance.

But how can the responses then be analyzed in a meaningful way without detailed knowledge on the recorded ganglion cell types? Three approaches shall be described here: (1) Clustering the cells based on the response parameter space, (2) individual classification of cells according to their response characteristics and (3) larger population averaging:

(1) When applying clustering methods for the identification of ganglion cell types, usually responses to different types of stimuli are considered and cells are grouped based on the similarity of their responses to all stimuli (Baden et al., 2016). This follows the assumption that all cells of a single type respond to different stimuli in a consistent way. Yet, clustering of ganglion cells by their responses remains challenging. This is especially evident from our data (publication 3), since cells could fall into a distinct cluster within one luminance condition and subsequently exhibit non-coherent characteristics upon switching to another luminance level.

(2) Another approach is to look at responses of cells to a single stimulus type. The cells can then be grouped according to the properties of their response. This will most likely not distinguish more than a few subpopulations of ganglion cells that each consist of several cell types because discrimination based on one stimulus is limited. Yet, the classification by response characteristics to one stimulus provides a functional comparison between genotypes or light levels tested.

(3) In the meantime, looking at ganglion cell activity on a population level provides a good alternative to the identification of individual cell types or distinction by responses to a single stimulus. All recorded cells can be regarded as one big population and the distribution of responses between genotypes can be compared side by side. Cells can also be broadly subdivided into ON and OFF cells and within each subdivision the responses can either be averaged or parameters can be extracted from the individual cells' responses and then compared.

In my work on the $\alpha_2\delta$-3 knockout I applied a combination of these approaches. During the analysis of ganglion cell responses to drifting sinusoidal gratings, I noticed that the spontaneous spike rates (baseline activity) of cells differed according to the spatial frequencies of the preceding grating stimulus. To classify the cells based upon their

baseline firing rate properties, I used a kmeans clustering approach. With that automatic clustering I could reliably isolate two groups that showed a similarly drastic increase in baseline activity, albeit at different spatial frequencies of the grating stimuli. It turned out that one group was composed solely of cells from $\alpha_2\delta$-3 knockout retinas, while the other one contained almost exclusively wild type cells. The ganglion cells of wild type and $\alpha_2\delta$-3 knockout retinas were pooled and subjected to the clustering together. In consequence, the segregation of the groups based on genotype represented an unbiased distinction of ganglion cell activity caused by the knockout (publication 1, Fig. 9).

For the analysis of full-field steps I characterized the responses of individual cells manually. A (semi-)automatic clustering would have been difficult because of the larger number of possible response types. Therefore, I divided the responses into discrete time windows (bins) and manually classified the cells according to their spike rate peaks in each time bin. With this classification scheme I was able to identify a group of cells with response properties exclusive to the $\alpha_2\delta$-3 knockout (publication 1, Fig. 10). In the end, this manual approach based on one stimulus yielded a similar outcome as the clustering described above: A segregation of cells into distinct groups based on response parameters, which was linked to the $\alpha_2\delta$-3 knockout.

Initially I discovered the potential $\alpha_2\delta$-3 knockout phenotype in the full-field step responses by averaging larger populations of cells (ON cells and OFF cells). I also used this *a priori* separation of the collection of cells into subgroups to analyse both spontaneous activity patterns over the whole experiment and spike rate distributions during flicker stimuli (publication 1, Fig. 8). In the retina it is quite straight-forward to utilize the polarity of the cells to distinguish subpopulations (in our case strictly ON or OFF, judged by the linear filter which is an unchanging and stringent criterion across luminance levels). The separation by polarity is biologically relevant as it describes a fundamental property of any retinal cell and its upstream connections. Comparing average responses of all ON or all OFF cells across genotypes thus is easy to apply and gives insights that are based on general connectivity.

For publication 3, we relied mainly on classification of the responses of individual cells to a full-field step stimulus. The responses were characterized according to the presence and time delay of spike rate peaks at each luminance level, similar to the full-field step analysis described above. Analysis then focused on response changes of

individual cells across luminance and on the distribution of response changes across all cells of a given polarity. A distribution of response delays across the population of ON and OFF cells was also presented (publication 3, Fig. 2b).

In publication 4 we mainly used population averages of response amplitudes of ganglion cell and LGN neuron firing rates and of rod photoreceptor activity. In this analysis we did not subdivide the cells into ON/OFF responding cells but considered the entire population (or the whole retina in the case of *in vitro* electroretinograms). For the distinction of responding versus non-responding cells, a classification of individual cell responses was applied. While the amplitude of responses was determined automatically based on set criteria, the responsiveness was classified manually.

The described approaches can all be readily applied when ganglion cell types are in principle unknown. With high-dimensional data (many cells, subpopulations, different stimuli, light levels, parameters extracted,…), like the data acquired on MEAs, the type of analysis that is used has to be carefully chosen to elucidate possible phenotypes of mutations or wild type function.

4d. Method paper: Implementation of perforated MEA recordings and application to retina

In our method paper (publication 2) we gave detailed instructions and trouble-shooting advice on how to set up and run perforated MEA recordings from retinal tissue. The perforated MEA enables the application of a suction pressure to keep tissue in place close to the recording electrodes. This offers several advantages over non-perforated MEAs and yields very reliable recording conditions. First of all, there is no tissue damage related to a physical weight holding down the retina. More importantly the constant solution flow through the tissue towards the perforation holes keeps the whole tissue well oxygenated and supplies cells with fresh solution (Egert et al., 2005). In the paper, we described the optimal setup for fine-tuning of the suction pressure (publication 2, Fig. 2) and provided step-by-step instructions how to prepare for the retinal recordings (publication 2, Fig. 3-5). In addition we gave examples of retinal data acquisition that included spike recordings (publication 2, Fig. 6) and *in vitro* electroretinography (*in vitro* ERG, publication 2, Fig. 7 + 8; see also publication 4, Fig. 3 + S3). The *in vitro* ERG implementation was developed by me and elaborated on how to make use of a simple custom reference electrode. We also illustrated the long-

time stability of perforated MEA recordings over many hours (publication 2, Fig. 9), which, as aforementioned, is a standalone feature of this technique. This last feature was central to our use of perforated MEA in longitudinal light level-changing experiments.

4e. Methodological aspects: MEAs are ideal tools for studying retinal function across different luminance levels

Longitudinal data is based on following an individual test subject (an animal in behavioral paradigms over several sessions or, in our case, a cell) over an extended period of time. In contrast to this, the typical cross-sectional studies rely on knowledge about the cells recorded from, to relate findings from one experimental condition to the findings from another, which come from different sets of experiments. In the case of retinal ganglion cells, one would for example record a cell of a given type at one condition and record another cell of that type at a second condition. By comparison of these two experiments, conclusions may be drawn about the changes that occurred between them. Still, cross-sectional experiments cannot provide the information on how an individual cell changes.

In patch clamp recordings it is often only possible to record a single cell per piece of retina when applying a change of conditions as each cell can only be newly exposed once. Furthermore, patch clamp recordings of retinal ganglion cells are usually stable for less than one hour which strongly limits the visual stimulation protocol per cell. Alternatively, calcium imaging has been successfully used to record large numbers of retinal ganglion cells in parallel for extended periods of time. However, even 2-photon excitation of calcium indicators and the visible light emission of these is enough to adapt the retina to a certain background light level, thus prohibiting the application of imaging of ganglion cell activity at scotopic light levels (Euler et al., 2009).

The MEA is ideally suited for the task of recording retinal activity across widely changing recording conditions like several luminance regimes or drug applications, as it allows stable long-term recordings of large numbers of cells in parallel from the same tissue. It was this longitudinal aspect - recording the same cells over time - that allowed for the findings we made. In this experimental set-up there is strong emphasis on the change that a given cell goes through with the change in recording conditions. With the large-scale data acquired it is possible to collect a catalogue of changes that

occurred, which is valuable even without knowing what type each individual cell belongs to. The possibility to record the same cells for long periods of time thus might be an even bigger advantage of MEA recordings than the sheer number of simultaneously recorded cells.

5. Concluding remarks

In my experiments I chose a diverse approach: I have not only studied the effect of the $\alpha_2\delta$-3 knockout directly on the cells involved by immunohistochemistry and patch clamp recordings, but also its impact on outer retinal function, the retinal output and on visually guided behavior. I could show that the $\alpha_2\delta$-3 knockout affects retinal processing, even though no effect on morphology and function of the affected cells themselves (horizontal cells) were apparent in my data set. My study thus provides an important basis to further elucidate the importance and specific functional role of $\alpha_2\delta$-3 in the retina. While using different approaches to investigate wild type function or the effects of mutations in the retina is common, it is evident from my findings that it adds considerable value to also include a range of luminance levels for retinal experiments in the future.

5a. Speculation on the role of calcium in horizontal cells

It is still unresolved by which mechanism(s) horizontal cells exert their primary function, feedback to photoreceptors. The proposed mechanisms for this feedback include ephaptic regulation of extracellular potential through open hemi-channels, modulation of extracellular pH and classical GABAergic inhibition (Thoreson and Mangel, 2012; Liu et al., 2013a; Kemmler et al., 2014; Vroman et al., 2014; Kramer and Davenport, 2015; Hirano et al., 2016; Warren et al., 2016). It yet remains an open question in what respect horizontal cells utilize calcium for exerting feedback.

It is noteworthy that horizontal cells possess an extraordinarily high calcium buffering capacity, which is evident from the strong immunolabeling of these cells for Calbindin. This calcium binding protein has high affinity for calcium and thus also provides a very fast buffering. In fact, horizontal cells are almost invulnerable to calcium overload and toxicity (Chun et al., 1999). The extraordinary capacity for handling intracellular calcium could indicate a high total calcium load of horizontal cells, for example through open hemi-channels as proposed in ephaptic feedback mechanisms. Pannexin 1, which was proposed as one possible component of hemichannel-based feedback (Kranz et al., 2013), has been reported to be gated/regulated by intracellular calcium (Locovei et al., 2006) although this has been questioned (Ma et al., 2009). The high buffering capacity could also indicate a necessity of limiting calcium spread, leading to a local

confinement of calcium close to the source. This source could be voltage-gated calcium channels which would be required for the proposed classical synaptic vesicle release of GABA (Hirano et al., 2016).

Since $\alpha_2\delta$-3 is highly expressed in horizontal cells it is conceivable that this cell type needs tight control over calcium channel localization, leading to compartmentalization of calcium influx in calcium nanodomains, e.g. in the tips of invaginating processes. The trafficking function of $\alpha_2\delta$-3 could also be utilized for targeting of calcium channels to either somatodendritic processes or axonal arborizations. This would be of particular interest, since dendritic processes contact cones and axonal processes contact rods and therefore constitute a functional specialization (Figure 1C). Notably, as of yet no mechanistic differences between the two compartments have been published. Horizontal cell feedback studies were in fact mostly either conducted in photopic light levels (with few exceptions (Thoreson et al., 2008; Babai and Thoreson, 2009)) or focused on mechanisms recordable from cones (Kemmler et al., 2014) or horizontal cell somata (Liu et al., 2013a) thus focusing on the horizontal cell to cone connection. The horizontal cell feedback to rods thus far did not receive similar attention.

I have to emphasize that my data does not provide proof for an axonal localization of $\alpha_2\delta$-3 (due to the unavailability of specific antibodies), though it would be consistent with the lack of somatic calcium current changes in $\alpha_2\delta$-3 knockout horizontal cells in my patch-clamp recordings. The mainly scotopic effects on ganglion cell activity seen in my MEA experiments are yet another indication of a stronger contribution of $\alpha_2\delta$-3 to rod mediated responses. Taken together, a role of $\alpha_2\delta$-3 only in the axonal compartment of horizontal cells could contribute to a hitherto unknown subcellular mechanistic specialization. Heterogeneity in the feedback mechanisms from horizontal cells to rods and to cones would be a fascinating novel aspect of horizontal cell function that should be explored in further detail.

5b. Luminance level-dependent coding in the retina and $\alpha_2\delta$-3 function

In the case of our wild type retina studies, the pivotal aspect was the response variability within a single luminance regime, i.e. within either scotopic, mesopic, or photopic light levels. It highlights, that retinal light adaptation is an ongoing process across the whole operational range of light levels encountered by the visual system,

likely depending on diverse mechanisms within the retinal circuitry. These mechanisms clearly go beyond switching between photoreceptors – rods and cones – and their dedicated downstream circuits. Our data shows that also within a single regime there are discreet thresholds at which mechanisms kick in or get turned off as seen in the reversibility of the response changes when stepping back and forth between light levels. This is comparable to surround inhibition which turns on at mesopic level for some ganglion cell types (Farrow et al., 2013b).

In the case of $\alpha_2\delta$-3 knockout retina, I studied only parts of the luminance range, with distinct steps from a purely scotopic level, through a mesopic to a low photopic level. Therefore, my findings more likely involve larger scale switches between photoreceptor systems and their dedicated circuitry. Nonetheless, also there the key to unravel a function of $\alpha_2\delta$-3 was to compare light responses at different adaptational states of the retina. The utility of such an approach was also apparent in a recent publication on the effect of optic atrophy on ganglion cell survival and retinal processing (González-Menéndez et al., 2015). In general, more insight may be gained in the search for the impact of mutations on retinal function, when including more than one light level.

A natural question that comes to mind: Does the $\alpha_2\delta$-3 knockout tell us something about luminance dependence of retinal coding, i.e. can some of the effects of changing responses we found be explained by the data from my $\alpha_2\delta$-3 study? Or can some of the described response changes also be found in the $\alpha_2\delta$-3 data? While some of the observed effects in my $\alpha_2\delta$-3 data were reminiscent of what we focused on in the luminance-dependent response change publication, most differences exhibited by $\alpha_2\delta$-3 knockout retinas were of subtle nature. The appearance of anti-preferred responses to full-field contrast steps for example (publication 3, Fig. 2) was not abolished by the $\alpha_2\delta$-3 knockout, but their timing was shifted to even longer delays (publication 1, Fig. 10). Therefore $\alpha_2\delta$-3 is likely not causal for this type of responses but could potentially shape their characteristics.

There is some limitation to a direct comparison between the studies on $\alpha_2\delta$-3 and luminance-dependent coding. As already pointed out, in the $\alpha_2\delta$-3 experiments I used only three discreet light levels – a scotopic, a mesopic and a photopic level - which did not include luminance increases within a single regime. Furthermore, the $\alpha_2\delta$-3 study used a different contrast range of visual stimuli (‘0’ – ‘255’, in other words maximum range of the projector from black to white) than the studies on retinal response changes

and rod re-emergence (‘0’ – ‘60’), with distinct mean background (‘128’ versus ‘30’; The smaller contrast range for the luminance-dependent contrast studies was selected to avoid overlap between light levels). This large difference in light intensities and contrasts used and the coarse three luminance level coverage makes detailed comparisons problematic. Therefore I did not systematically investigate the same luminance-dependent response changes in the $\alpha_2\delta$-3 knockout study.

5c. Outlook

Future studies: Function of $\alpha_2\delta$-3 in horizontal cells

Some of the bigger scientific questions on $\alpha_2\delta$ subunits were beyond the scope of my PhD work. Among them are the association of $\alpha_2\delta$-3 to specific α_1 subunit isoforms, its targeting and localization and putative calcium channel-independent functions.

Since patch-clamp recordings of horizontal cells were quite unstable in my hands, using calcium channel blockers to determine contributions from L-, N-, P/Q- or R-type channels was not feasible, as drug application and washout take a long time. Calcium imaging with membrane-permeable indicators like OGB1-AM would be a good alternative as this does not interfere with viability of the cells and longer recordings with blocker cocktails could be obtained to discern α_1 isoform contributions. Imaging intracellular calcium concentration would also be a promising approach to investigate horizontal cell axon terminals that are not easily patchable. However, in contrast to electrophysiological recordings, the temporal resolution of calcium imaging is rather poor and would limit the study of calcium current kinetics. Yet, since calcium currents in my patch-clamp recordings showed little inactivation, calcium imaging would be suitable to characterize the plateau phase of the calcium current.

Effects of $\alpha_2\delta$-3 knockout in horizontal cells on the feedback to photoreceptors could in principle also be investigated by recording from photoreceptors. While patch-clamp recordings of photoreceptors are not easy to begin with, patching on the soma might not allow for efficient recording of smaller feedback effects on synaptic currents due to space clamp issues. Photoreceptor synaptic endings in mouse are very small and not amenable for direct patch recordings. Calcium imaging photoreceptor terminals would consequently be the most promising approach there with similar limitations in temporal resolution as mentioned before.

The question of α2δ-3 localization within horizontal cells could be addressed by transfecting cells with tagged α2δ-3. A small V5, FLAG or HA tag on the N- or C-terminus for example should not interfere with the function and the tagged α2δ-3 is likely to be targeted to the same subcellular compartments as the endogenous α2δ-3 (Watschinger et al., 2008; Lobbestael et al., 2010). Transfection would have to be done in vivo using viral vectors or on cultured wholemount retina in a culture system to allow for translocation of the tagged proteins also to axonal endings.

Finally, calcium channel-independent functions for example on synaptogenesis or synaptic maintenance could be addressed by single-cell dye-filling experiments. This would allow for quantitative analysis of the processes and synaptic interactions of individual cells. Employing electron microscopy to study individual photoreceptor invaginations could then complement the detailed ultrastructure. The horizontal cell network forms a dense plexus of processes with several horizontal cells contacting single photoreceptors (Peichl et al., 1998) which prohibited detailed analysis of their connectivity in my immunohistochemical experiments.

Future studies: Role of α2δ-3 in retinal processing

Studying α2δ-3 function directly in horizontal cells within the context of a global knockout is a valid approach because the cells upstream in the circuitry (photoreceptors) do not express this subunit and consequently no indirect effects have to be expected. In the case of ganglion cells the diversity of upstream cell types affected by the knockout are a confounding factor in pinpointing mechanisms. To study the effect of α2δ-3 (knockout) in a single retinal cell type on ganglion cell activity, other steps have to be taken.

The use of conditional mutants, in which a mutation or knockout is only present in cells that express Cre recombinase, allows targeting genetic manipulations to subsets of cells or a single cell type. In mouse, a large number of Cre-driver lines is available, many of which are specific to a retinal cell type (Zhang et al., 2005; Kim et al., 2008; Sun et al., 2013) The conditional approach would prove effective for α2δ-3 function in horizontal cells, as they are involved in shaping photoreceptor output and therefore affect the responses of all ganglion cells. Any effect observed in a targeted knockout could then be traced back to horizontal cell function. Specific Cre-driver lines for horizontal cell-specific expression have been generated and might be available in the

future (Ströh et al., 2013; Szikra et al., 2014; Hirano et al., 2016) as well as a conditional knockout for $\alpha_2\delta$-3 (Cacna2d3$^{tm1a(KOMP)Wtsi}$).

Epilogue

Many retinal light adaptation processes revolve around switching between circuitry elements, starting from the distinct activation thresholds of rod and cone photoreceptors. Processing changes induced by the luminance level presumably also involve activation thresholds of other cell types or some of their connections, thus exhibiting similar switch-like behavior as the inhibitory surround (Farrow et al., 2013b) or polarity of contrast preference (Tikidji-Hamburyan et al., 2014; Pearson and Kerschensteiner, 2015). In fact, light adaptation-dependent signaling changes are largely described in the context of switches in the underlying circuitry and interpreted based on the differential involvement of distinct connections.

In addition to circuitry elements and pathways being (de-)activated at a certain luminance level, also the molecular toolset used by the underlying connections likely influences the transmission characteristics of the network. Visual processing could be shaped by the use of different receptor subtypes (GABA receptor types (Eggers and Lukasiewicz, 2006; Moore-Dotson et al., 2015), calcium permeable or impermeable AMPA receptors (Chávez et al., 2006), etc.) on a cell receiving several inputs. The composition of the release machinery on presynaptic cells would also have an impact even in otherwise analogous connectivity. As an example, the transiency of responses could depend on calcium channel inactivation, the proximity of channels to the release site, calcium buffering or the availability of readily releasable vesicles, just to name a few. Consequently, retinal responses are not only a product of the complex interconnections of cell types but also of the molecular mechanisms they employ.

Future studies should explore whether $\alpha_2\delta$-3 is one such molecular determinant of retinal (light) adaptation that adds to retinal response tuning in general and photoreceptor type-dependent horizontal cell feedback in particular.

6. Abbreviations

AC	amacrine cell
CMOS	complementary metal-oxide semiconductor (a type of circuitry/chip)
ERG	electroretinogram
GCL	ganglion cell layer
INL	inner nuclear layer
IPL	inner plexiform layer
MEA	micro-electrode array
LED	light-emitting diode
LGN	lateral geniculate nucleus
ONL	outer nuclear layer
OPL	outer plexiform layer
RBC	rod bipolar cell
VGCC	voltage-gated calcium channel

7. Literature cited

Allen AE, Storchi R, Martial FP, Petersen RS, Montemurro MA, Brown TM, Lucas RJ. 2014. Melanopsin-driven light adaptation in mouse vision. Curr Biol 24:2481–2490.

Alvarez-Laviada A, Kadurin I, Senatore A, Chiesa R, Dolphin AC. 2014. The inhibition of functional expression of calcium channels by prion protein demonstrates competition with a2d for GPI-anchoring pathways. Biochem J 458:365–374.

Andrade a, Sandoval A, Oviedo N, De Waard M, Elias D, Felix R. 2007. Proteolytic cleavage of the voltage-gated Ca2+ channel alpha2delta subunit: structural and functional features. Eur J Neurosci 25:1705–1710.

Babai N, Thoreson WB. 2009. Horizontal cell feedback regulates calcium currents and intracellular calcium levels in rod photoreceptors of salamander and mouse retina. J Physiol 587:2353–2364.

Bacchi N, Messina A, Burtscher V, Dassi E, Provenzano G, Bozzi Y, Demontis GC, Koschak A, Denti MA, Casarosa S. 2015. A new splicing isoform of Cacna2d4 mimicking the effects of c.2451insC mutation in the retina: Novel molecular and electrophysiological insights. Investig Ophthalmol Vis Sci 56:4846–4856.

Baden T, Berens P, Bethge M, Euler T. 2013. Spikes in mammalian bipolar cells support temporal layering of the inner retina. Curr Biol 23:48–52.

Baden T, Berens P, Franke K, Rosón MR, Bethge M, Euler T. 2016. The functional diversity of retinal ganglion cells in the mouse. Nature:1–21.

Ball SL, McEnery MW, Yunker AMR, Shin H-SS, Gregg RG. 2011. Distribution of voltage gated calcium channel beta subunits in the mouse retina. Brain Res 1412:1–8.

Ball SL, Powers PA, Shin HS, Morgans CW, Peachey NS, Gregg RG. 2002. Role of the beta(2) subunit of voltage-dependent calcium channels in the retinal outer plexiform layer. Invest Ophthalmol Vis Sci 43:1595–1603.

Barlow HB, Levick WR. 1965. The mechanism of directionally selective units in rabbit's retina. J Physiol 178:477–504.

Bartoletti TM, Jackman SL, Babai N, Mercer AJ, Kramer RH, Thoreson WB. 2011. Release from the cone ribbon synapse under bright light conditions can be controlled by the opening of only a few Ca2+ channels. J Neurophysiol 106:2922–2935.

Bauer CS, Nieto-Rostro M, Rahman W, Tran-Van-Minh A, Ferron L, Douglas L, Kadurin I, Sri Ranjan Y, Fernandez-Alacid L, Millar NS, Dickenson AH, Lujan R, Dolphin AC. 2009. The increased trafficking of the calcium channel subunit α2δ-1 to presynaptic terminals in neuropathic pain is inhibited by the α2δ ligand pregabalin. J Neurosci 29:4076–4088.

Bayley PR, Morgans CW. 2007. Rod bipolar cells and horizontal cells form displaced synaptic contacts with rods in the outer nuclear layer of the nob2 retina. J Comp Neurol 500:286–298.

Baylor D, Lamb T, Yau K. 1979. Responses of retinal rods to single photons. J Physiol:613–634.

Berntson A, Taylor WR, Morgans CW. 2003. Molecular identity, synaptic localization, and physiology of calcium channels in retinal bipolar cells. J Neurosci Res 71:146–

151.

Bloomfield S a. 1994. Orientation-sensitive amacrine and ganglion cells in the rabbit retina. J Neurophysiol 71:1672–91.

Bloomfield SA, Xin D, Osborne T. 1997. Light-induced modulation of coupling between AII amacrine cells in the rabbit retina. Vis Neurosci 14:565–576.

Brodbeck J, Davies A, Courtney JM, Meir A, Balaguero N, Canti C, Moss FJ, Page KM, Pratt WS, Hunt SP, Barclay J, Rees M, Dolphin AC. 2002. The ducky mutation in Cacna2d2 results in altered Purkinje cell morphology and is associated with the expression of a truncated alpha 2 delta-2 protein with abnormal function. J Biol Chem 277:7684–7693.

Buraei Z, Yang J. 2013. Structure and function of the β subunit of voltage-gated Ca2+ channels. Biochim Biophys Acta - Biomembr 1828:1530–1540.

Calderón-Rivera A, Andrade A, Hernández-Hernández O, González-Ramírez R, Sandoval A, Rivera M, Gomora JC, Felix R. 2012. Identification of a disulfide bridge essential for structure and function of the voltage-gated Ca(2+) channel α(2)δ-1 auxiliary subunit. Cell Calcium 51:22–30.

Canti C, Nieto-Rostro M, Foucault I, Heblich F, Wratten J, Richards MW, Hendrich J, Douglas L, Page KM, Davies A, Dolphin AC. 2005. The metal-ion-dependent adhesion site in the Von Willebrand factor-A domain of alpha2delta subunits is key to trafficking voltage-gated Ca2+ channels. Proc Natl Acad Sci U S A 102:11230–11235.

Caputo A, Piano I, Demontis GC, Bacchi N, Casarosa S, Santina L Della, Gargini C. 2015. TMEM16A is associated with voltage-gated calcium channels in mouse retina and its function is disrupted upon mutation of the auxiliary α2δ4 subunit. Front Cell Neurosci 9:1–11.

Carcieri SM. 2003. Classification of Retinal Ganglion Cells: A Statistical Approach. J Neurophysiol 90:1704–1713.

Catterall WA, Perez-Reyes E, Snutch TP, Striessnig J. 2005. International Union of Pharmacology. XLVIII. Nomenclature and structure-function relationships of voltage-gated calcium channels. Pharmacol Rev 57:411–425.

Chávez AE, Singer JH, Diamond JS. 2006. Fast neurotransmitter release triggered by Ca influx through AMPA-type glutamate receptors. Nature 443:705–8.

Chen RWS, Greenberg JP, Lazow M a., Ramachandran R, Lima LH, Hwang JC, Schubert C, Braunstein A, Allikmets R, Tsang SH. 2012. Autofluorescence imaging and spectral-domain optical coherence tomography in incomplete congenital stationary night blindness and comparison with retinitis pigmentosa. Am J Ophthalmol 153:143–154.e2.

Chichilnisky EJ, Kalmar RS. 2002. Functional asymmetries in ON and OFF ganglion cells of primate retina. J Neurosci 22:2737–2747.

Chun MH, Kim IB, Ju WK, Kim KY, Lee MY, Joo CK, Chung JW. 1999. Horizontal cells of the rat retina are resistant to degenerative processes induced by ischemia-reperfusion. Neurosci Lett 260:125–128.

Curtis BM, Catterall WA. 1984. Purification of the calcium antagonist receptor of the voltage-sensitive calcium channel from skeletal muscle transverse tubules. Biochemistry 23:2113–2118.

Davies A, Hendrich J, Van Minh AT, Wratten J, Douglas L, Dolphin AC. 2007. Functional biology of the alpha(2)delta subunits of voltage-gated calcium channels. Trends Pharmacol Sci 28:220–228.

Davies A, Kadurin I, Alvarez-Laviada A, Douglas L, Nieto-Rostro M, Bauer CS, Pratt WS, Dolphin AC. 2010. The alpha2delta subunits of voltage-gated calcium channels form GPI-anchored proteins, a posttranslational modification essential for function. Proc Natl Acad Sci U S A 107:1654–1659.

Demb JB, Singer JH. 2012. Intrinsic properties and functional circuitry of the AII amacrine cell. Vis Neurosci 29:51–60.

Dolphin AC. 2012. Calcium channel auxiliary alpha2delta and beta subunits: trafficking and one step beyond. Nat Rev Neurosci 13:542–555.

Dolphin AC. 2013. The α2δ subunits of voltage-gated calcium channels. Biochim Biophys Acta - Biomembr 1828:1541–1549.

Dorgau B, Herrling R, Schultz K, Greb H, Segelken J, Ströh S, Bolte P, Weiler R, Dedek K, Janssen-Bienhold U. 2015. Connexin50 couples axon terminals of mouse horizontal cells by homotypic gap junctions. J Comp Neurol 523:2062–2081.

Dunn FA, Lankheet MJ, Rieke F. 2007. Light adaptation in cone vision involves switching between receptor and post-receptor sites. Nature 449:603–606.

Egert U, Okujeni S, Nisch W, Boven K-H, Rudorf R, Gottschlich N, and Stett A. 2005. Perforated microelectrode arrays optimize oxygen availability and signal-to-noise ratio in brain slice recordings. MST Kongress 2005:431–434.

Eggers ED, Lukasiewicz PD. 2006. Receptor and Transmitter Release Properties Set the Time Course of Retinal Inhibition. J Neurosci 26:9413–9425.

Eggers ED, Lukasiewicz PD. 2011. Multiple pathways of inhibition shape bipolar cell responses in the retina. Vis Neurosci 28:95–108.

Ellis SB, Williams ME, Ways NR, Brenner R, Sharp AH, Leung AT, Campbell KP, McKenna E, Koch WJ, Hui A, et al. 1988. Sequence and expression of mRNAs encoding the alpha 1 and alpha 2 subunits of a DHP-sensitive calcium channel. Science (80-) 241:1661–1664.

Enroth-Cugell C, Lennie P, Shapley RM. 1975. Surround contribution to light adaptation in cat retinal ganglion cells. J Physiol 247:579–588.

Eroglu C, Allen NJ, Susman MW, O'Rourke NA, Park CY, Ozkan E, Chakraborty C, Mulinyawe SB, Annis DS, Huberman AD, Green EM, Lawler J, Dolmetsch R, Garcia KC, Smith SJ, Luo ZD, Rosenthal A, Mosher DF, Barres BA. 2009. Gabapentin receptor alpha2delta-1 is a neuronal thrombospondin receptor responsible for excitatory CNS synaptogenesis. Cell 139:380–392.

Erskine L, Herrera E. 2014. Connecting the retina to the brain. ASN Neuro 6:1759091414562107.

Etemad S, Obermair GJ, Bindreither D, Benedetti A, Stanika R, Di Biase V, Burtscher V, Koschak A, Kofler R, Geley S, Wille A, Lusser A, Flockerzi V, Flucher BE. 2014. Differential neuronal targeting of a new and two known calcium channel β4 subunit splice variants correlates with their regulation of gene expression. J Neurosci 34:1446–61.

Euler T, Hausselt SE, Margolis DJ, Breuninger T, Castell X, Detwiler PB, Denk W. 2009. Eyecup scope-optical recordings of light stimulus-evoked fluorescence

signals in the retina. Pflugers Arch Eur J Physiol 457:1393–1414.

Euler T, Haverkamp S, Schubert T, Baden T. 2014. Retinal bipolar cells: elementary building blocks of vision. Nat Rev Neurosci 15:507–19.

Fain G, Dowling J. 1973. Intracellular Recordings from Single Rods and Cones in the Mudpuppy Retina. Science (80-) 180:1178–1181.

Famiglietti EV, Kolb H. 1974. Rod and Cone Pathways in the Inner Plexiform Layer of Cat Retina. Science (80-) 186:47–49.

Farrell SR, Raymond ID, Foote M, Brecha NC, Barnes S. 2010. Modulation of voltage-gated ion channels in rat retinal ganglion cells mediated by somatostatin receptor subtype 4. J Neurophysiol 104:1347–1354.

Farrow K, Masland RH, Farrow K, Masland RH. 2013a. Physiological clustering of visual channels in the mouse retina Physiological clustering of visual channels in the mouse retina. :1516–1530.

Farrow K, Teixeira M, Szikra T, Viney TJ, Balint K, Yonehara K, Roska B. 2013b. Ambient illumination toggles a neuronal circuit switch in the retina and visual perception at cone threshold. Neuron 78:325–338.

Felix R, Gurnett CA, De Waard M, Campbell KP. 1997. Dissection of functional domains of the voltage-dependent Ca2+ channel alpha2delta subunit. J Neurosci 17:6884–6891.

Fell B, Eckrich S, Blum K, Eckrich T, Hecker D, Obermair GJ, Münkner S, Flockerzi V, Schick B, Engel J. 2016. α2δ2 Controls the Function and Trans-Synaptic Coupling of Cav1.3 Channels in Mouse Inner Hair Cells and Is Essential for Normal Hearing. 36:11024–11036.

Fiscella M, Farrow K, Jones IL, Jäckel D, Müller J, Frey U, Bakkum DJ, Hantz P, Roska B, Hierlemann A. 2012. Recording from defined populations of retinal ganglion cells using a high-density CMOS-integrated microelectrode array with real-time switchable electrode selection. J Neurosci Methods 211:103–113.

Gao B, Sekido Y, Maximov A, Saad M, Forgacs E, Latif F, Wei MH, Lerman M, Lee JH, Perez-Reyes E, Bezprozvanny I, Minna JD. 2000. Functional properties of a new voltage-dependent calcium channel alpha(2)delta auxiliary subunit gene (CACNA2D2). J Biol Chem 275:12237–12242.

González-Menéndez I, Reinhard K, Tolivia J, Wissinger B, Münch TA. 2015. Influence of Opa1 mutation on survival and function of retinal ganglion cells. Investig Ophthalmol Vis Sci 56:4835–4845.

Grabner CP, Gandini MA, Rehak R, Le Y, Zamponi GW, Schmitz F. 2015. RIM1/2-Mediated Facilitation of Cav1.4 Channel Opening Is Required for Ca2+-Stimulated Release in Mouse Rod Photoreceptors. J Neurosci 35:13133–13147.

Grimes WN, Schwartz GW, Rieke F. 2014. The synaptic and circuit mechanisms underlying a change in spatial encoding in the retina. Neuron 82:460–473.

Grimes WN, Zhang J, Graydon CW, Kachar B, Diamond JS. 2010. Retinal Parallel Processors: More than 100 Independent Microcircuits Operate within a Single Interneuron. Neuron 65:873–885.

Gurnett CA, Felix R, Campbell KP. 1997. Extracellular interaction of the voltage-dependent Ca2+ channel alpha2delta and alpha1 subunits. J Biol Chem 272:18508–18512.

Hack I, Peichl L, Brandstätter JH. 1999. An alternative pathway for rod signals in the rodent retina: rod photoreceptors, cone bipolar cells, and the localization of glutamate receptors. Proc Natl Acad Sci U S A 96:14130–14135.

Haverkamp S, Specht D, Majumdar S, Zaidi NF, Brandstätter JH, Wasco W, Wässle H, Tom Dieck S. 2008. Type 4 OFF cone bipolar cells of the mouse retina express calsenilin and contact cones as well as rods. J Comp Neurol 507:1087–101.

Hibino H, Pironkova R, Onwumere O, Rousset M, Charnet P, Hudspeth a J, Lesage F. 2003. Direct interaction with a nuclear protein and regulation of gene silencing by a variant of the Ca2+-channel beta 4 subunit. Proc Natl Acad Sci U S A 100:307–312.

Hirano AA, Liu X, Boulter J, Grove J, Pérez de Sevilla Müller L, Barnes S, Brecha NC. 2016. Targeted Deletion of Vesicular GABA Transporter from Retinal Horizontal Cells Eliminates Feedback Modulation of Photoreceptor Calcium Channels. eNeuro 3:ENEURO.0148-15.2016.

Hope CI, Sharp DM, Hemara-Wahanui A, Sissingh JI, Lundon P, Mitchell E a., Maw M a., Clover GM. 2005. Clinical manifestations of a unique X-linked retinal disorder in a large New Zealand family with a novel mutation in CACNAIF, the gene responsible for CSNB2. Clin Exp Ophthalmol 33:129–136.

Huang J, Zhou L, Wang H, Luo J, Zeng L, Xiong K, Chen D. 2013. Distribution of thrombospondins and their neuronal receptor alpha2delta1 in the rat retina. Exp Eye Res 111C:36–49.

Ingram NT, Sampath AP, Fain GL. 2016. Why are rods more sensitive than cones? J Physiol 0:1–12.

Jalkanen R, Bech-Hansen NT, Tobias R, Sankila E-M, Mäntyjärvi M, Forsius H, de la Chapelle A, Alitalo T. 2007. A novel CACNA1F gene mutation causes Aland Island eye disease. Invest Ophthalmol Vis Sci 48:2498–2502.

Jalkanen R, Mäntyjärvi M, Tobias R, Isosomppi J, Sankila E-M, Alitalo T, Bech-Hansen NT. 2006. X linked cone-rod dystrophy, CORDX3, is caused by a mutation in the CACNA1F gene. J Med Genet 43:699–704.

Janssen-Bienhold U, Trumpler J, Hilgen G, Schultz K, Muller LP, Sonntag S, Dedek K, Dirks P, Willecke K, Weiler R. 2009. Connexin57 is expressed in dendro-dendritic and axo-axonal gap junctions of mouse horizontal cells and its distribution is modulated by light. J Comp Neurol 513:363–374.

Jarsky T, Cembrowski M, Logan SM, Kath WL, Riecke H, Demb JB, Singer JH. 2011. A synaptic mechanism for retinal adaptation to luminance and contrast. J Neurosci 31:11003–11015.

Jiang Y, Purushothaman G, Casagrande VA. 2015. The functional asymmetry of ON and OFF channels in the perception of contrast. J Neurophysiol 114:2816–29.

Kadurin I, Alvarez-Laviada A, Ng SF, Walker-Gray R, D'Arco M, Fadel MG, Pratt WS, Dolphin AC. 2012. Calcium currents are enhanced by alpha2delta-1 lacking its membrane anchor. J Biol Chem 287:33554–33566.

Katiyar R, Weissgerber P, Roth E, Dörr J, Sothilingam V, Garcia Garrido M, Beck SC, Seeliger MW, Beck A, Schmitz F, Flockerzi V. 2015. Influence of the β2-Subunit of L-Type Voltage-Gated Cav Channels on the Structural and Functional Development of Photoreceptor Ribbon Synapses. Investig Opthalmology Vis Sci 56:2312.

Kemmler R, Schultz K, Dedek K, Euler T, Schubert T. 2014. Differential regulation of cone calcium signals by different horizontal cell feedback mechanisms in the mouse retina. J Neurosci 34:11826–43.

Kim I-J, Zhang Y, Yamagata M, Meister M, Sanes JR. 2008. Molecular identification of a retinal cell type that responds to upward motion. Nature 452:478–482.

Klugbauer N, Lacinova L, Marais E, Hobom M, Hofmann F. 1999. Molecular diversity of the calcium channel alpha2delta subunit. J Neurosci 19:684–691.

Knoflach D, Kerov V, Sartori SB, Obermair GJ, Schmuckermair C, Liu X, Sothilingam V, Garrido MG, Baker S a., Glösmann M, Schicker K, Seeliger M, Lee A, Koschak A. 2013. Cav1.4 IT mouse as model for vision impairment in human congenital stationary night blindness type 2. Channels 7:37–41.

Knoflach D, Schicker K, Glösmann M, Koschak A. 2015. Gain-of-function nature of Cav1.4 L-type calcium channels alters firing properties of mouse retinal ganglion cells. Channels 6950:00–00.

Koschak A, Reimer D, Walter D, Hoda J-C, Heinzle T, Grabner M, Striessnig J. 2003. Cav1.4alpha1 subunits can form slowly inactivating dihydropyridine-sensitive L-type Ca2+ channels lacking Ca2+-dependent inactivation. J Neurosci 23:6041–9.

Kramer RH, Davenport CM. 2015. Lateral Inhibition in the Vertebrate Retina: The Case of the Missing Neurotransmitter. PLoS Biol 13:1–8.

Kranz K, Dorgau B, Pottek M, Herrling R, Schultz K, Bolte P, Monyer H, Penuela S, Laird DW, Dedek K, Weiler R, Janssen-Bienhold U. 2013. Expression of Pannexin1 in the outer plexiform layer of the mouse retina and physiological impact of its knockout. J Comp Neurol 521:1119–1135.

Kurshan PT, Oztan A, Schwarz TL. 2009. Presynaptic alpha2delta-3 is required for synaptic morphogenesis independent of its Ca2+-channel functions. Nat Neurosci 12:1415–1423.

Lamb TD. 2016. Why rods and cones? Eye 30:179–185.

Lamb TD, Pugh EN. 2004. Dark adaptation and the retinoid cycle of vision. Prog Retin Eye Res 23:307–380.

Lee A, Wang S, Williams B, Hagen J, Scheetz TE, Haeseleer F. 2015. Characterization of Cav1.4 Complexes (α1 1.4, β2, and α2δ4) in HEK293T Cells and in the Retina. J Biol Chem 290:1505–1521.

Leung AT, Imagawa T, Campbell KP. 1987. Structural characterization of the 1,4-dihydropyridine receptor of the voltage-dependent Ca2+ channel from rabbit skeletal muscle. Evidence for two distinct high molecular weight subunits. J Biol Chem 262:7943–7946.

Levick WR. 1967. Receptive fields and trigger features of ganglion cells in the visual streak of the rabbit's retina. J Physiol 188:285–307.

Liu X, Hirano AA, Sun X, Brecha NC, Barnes S. 2013a. Calcium channels in rat horizontal cells regulate feedback inhibition of photoreceptors through an unconventional GABA- and pH-sensitive mechanism. J Physiol 591:3309–24.

Liu X, Kerov V, Haeseleer F, Majumder A, Artemyev N, Baker S a., Lee A. 2013b. Dysregulation of Cav1.4 channels disrupts the maturation of photoreceptor synaptic ribbons in congenital stationary night blindness type 2. Channels 7:37–41.

Lobbestael E, Reumers V, Ibrahimi A, Paesen K, Thiry I, Gijsbers R, Haute C Van Den, Debyser Z, Baekelandt V, Taymans J. 2010. Immunohistochemical detection of transgene expression in the brain using small epitope tags.

Locovei S, Wang J, Dahl G. 2006. Activation of pannexin 1 channels by ATP through P2Y receptors and by cytoplasmic calcium. FEBS Lett 580:239–244.

Ma W, Hui H, Hui H, Pelegrin P, Pelegrin P, Surprenant A, Surprenant A. 2009. Pharmacological Characterization of Pannexin-1 Currents. Pharmacology 5.

Masland RH. 2001. Neuronal diversity in the retina. Curr Opin Neurobiol 11:431–436.

Masland RH. 2012. The Neuronal Organization of the Retina. Neuron 76:266–280.

Masland RH, Martin PR. 2007. The unsolved mystery of vision. Curr Biol 17:577–582.

Mataruga A, Kremmer E, Müller F. 2007. Type 3a and Type 3b OFF Cone Bipolar Cells Provide for the Alternative Rod Pathway in the Mouse Retina. J Comp Neurol 502:1123–1137.

Mazade RE, Eggers ED. 2013. Light adaptation alters the source of inhibition to the mouse retinal OFF pathway. J Neurophysiol 110:2113–2128.

Meir A, Bell D, Stephens GJ, Page KM, Dolphin AC. 2000. Calcium Channel β Subunit Promotes Voltage-Dependent Modulation of α 1B by G βγ. Biophys J 79:731–746.

Mendus D, Rankin-Gee EK, Mustapha M, Porter BE. 2015. Increased sensitivity to kindling in mice lacking TSP1. Neuroscience 305:302–8.

Mercer AJ, Chen M, Thoreson WB. 2011. Lateral mobility of presynaptic L-type calcium channels at photoreceptor ribbon synapses. J Neurosci 31:4397–4406.

Molday RS, Moritz OL. 2015. Photoreceptors at a glance. J Cell Sci 128:4039–4045.

Moore-Dotson JM, Klein JS, Mazade RE, Eggers ED. 2015. Different types of retinal inhibition have distinct neurotransmitter release properties. J Neurophysiol:jn.00447.2014.

Morgans CW. 2001. Localization of the alpha(1F) calcium channel subunit in the rat retina. Invest Ophthalmol Vis Sci 42:2414–2418.

Munch TA, da Silveira RA, Siegert S, Viney TJ, Awatramani GB, Roska B. 2009. Approach sensitivity in the retina processed by a multifunctional neural circuit. Nat Neurosci 12:1308–1316.

Naarendorp F, Esdaille TM, Banden SM, Andrews-Labenski J, Gross OP, Pugh EN. 2010. Dark Light, Rod Saturation, and the Absolute and Incremental Sensitivity of Mouse Cone Vision. J Neurosci 30:12495–12507.

Nakajima Y, Moriyama M, Hattori M, Minato N, Nakanishi S. 2009. Isolation of ON bipolar cell genes via hrGFP-coupled cell enrichment using the mGluR6 promoter. J Biochem 145:811–818.

Oppermann D, Schramme J, Neumeyer C. 2016. Rod-cone based color vision in seals under photopic conditions. Vision Res 125:30–40.

Park S, Li C, Haeseleer F, Palczewski K, Ames JB. 2014. Structural insights into activation of the retinal L-type Ca^{2+} channel (Cav1.4) by Ca^{2+}-binding protein 4 (CaBP4). J Biol Chem 289:31262–73.

Pearson JT, Kerschensteiner D. 2015. Ambient illumination switches contrast preference of specific retinal processing streams. J Neurophysiol 114:540–550.

Peichl L, Gonzalez-Soriano J. 1994. Morphological types of horizontal cell in rodent

retinae: a comparison of rat, mouse, gerbil, and guinea pig. Vis Neurosci 11:501–517.

Peichl L, Sandmann D, Boycott BB. 1998. Comparative anatomy and function of mammalian horizontal cells. Dev Organ Retin.

Pérez de Sevilla Müller L, Sargoy A, Fernández-Sánchez L, Rodriguez A, Liu J, Cuenca N, Brecha N. 2015. Expression and cellular localization of the voltage-gated calcium channel α2 δ3 in the rodent retina. J Comp Neurol 0:1443–60.

Pirone A, Kurt S, Zuccotti A, Rüttiger L, Pilz P, Brown DH, Franz C, Schweizer M, Rust MB, Rübsamen R, Friauf E, Knipper M, Engel J. 2014. α2δ3 is essential for normal structure and function of auditory nerve synapses and is a novel candidate for auditory processing disorders. J Neurosci 34:434–45.

Pragnell M, De Waard M, Mori Y, Tanabe T, Snutch TP, Campbell KP. 1994. Calcium channel beta-subunit binds to a conserved motif in the I-II cytoplasmic linker of the alpha 1-subunit. Nature 368:67–70.

Qin N, Yagel S, Momplaisir ML, Codd EE, D'Andrea MR. 2002. Molecular cloning and characterization of the human voltage-gated calcium channel alpha(2)delta-4 subunit. Mol Pharmacol 62:485–496.

Raviola E, Gilula NB. 1973. Gap Junctions Between Photoreceptor Cells in the Vertebrate Retina. Proc Natl Acad Sci 70:1677–1681.

Regus-Leidig H, Atorf J, Feigenspan A, Kremers J, Maw M a, Brandstätter JH. 2014. Photoreceptor degeneration in two mouse models for congenital stationary night blindness type 2. PLoS One 9:e86769.

Reichenbach A, Bringmann A. 2013. New functions of müller cells. Glia 61:651–678.

Robinson P, Etheridge S, Song L, Shah R, Fitzgerald EM, Jones OT. 2011. Targeting of voltage-gated calcium channel alpha2delta-1 subunit to lipid rafts is independent from a GPI-anchoring motif. PLoS One 6:e19802.

Sandoval A, Oviedo N, Andrade A, Felix R. 2004. Glycosylation of asparagines 136 and 184 is necessary for the alpha2delta subunit-mediated regulation of voltage-gated Ca2+ channels. FEBS Lett 576:21–6.

Sanes JR, Masland RH. 2015. The Types of Retinal Ganglion Cells: Current Status and Implications for Neuronal Classification. Annu Rev Neurosci 38:221–245.

Schultze M. 1866. Zur Anatomie und Physiologie der Retina.

Segev R, Goodhouse J, Puchalla J, Berry MJ. 2004. Recording spikes from a large fraction of the ganglion cells in a retinal patch. Nat Neurosci 7:1154–61.

de Sevilla Muller LP, Liu J, Solomon A, Rodriguez A, Brecha N. 2013. Expression of voltage-gated calcium channel alpha(2) delta(4) subunits in the mouse and rat retina. J Comp Neurol.

Shaltiel L, Paparizos C, Fenske S, Hassan S, Gruner C, Rotzer K, Biel M, Wahl-Schott CA. 2012. Complex regulation of voltage-dependent activation and inactivation properties of retinal voltage-gated Cav1.4 L-type Ca2+ channels by Ca2+-binding protein 4 (CaBP4). J Biol Chem 287:36312–36321.

Siegert S, Cabuy E, Scherf BG, Kohler H, Panda S, Le Y-ZZ, Fehling HJ, Gaidatzis D, Stadler MB, Roska B. 2012. Transcriptional code and disease map for adult retinal cell types. Nat Neurosci 15:487–95, S1-2.

Singh A, Hamedinger D, Hoda J-C, Gebhart M, Koschak A, Romanin C, Striessnig J.

2006. C-terminal modulator controls Ca2+-dependent gating of Ca(v)1.4 L-type Ca2+ channels. Nat Neurosci 9:1108–16.

Specht D, Wu SB, Turner P, Dearden P, Koentgen F, Wolfrum U, Maw M, Brandstätter JH, Dieck ST, Brandstatter JH, tom Dieck S. 2009. Effects of presynaptic mutations on a postsynaptic Cacna1s calcium channel colocalized with mGluR6 at mouse photoreceptor ribbon synapses. Investig Ophthalmol Vis Sci 50:505–515.

Stockner T, Koschak A. 2013. What can naturally occurring mutations tell us about Cav1.x channel function? Biochim Biophys Acta - Biomembr 1828:1598–1607.

Ströh S, Sonntag S, Janssen-Bienhold U, Schultz K, Cimiotti K, Weiler R, Willecke K, Dedek K. 2013. Cell-specific cre recombinase expression allows selective ablation of glutamate receptors from mouse horizontal cells. PLoS One 8:15–17.

Sun LO, Jiang Z, Rivlin-Etzion M, Hand R, Brady CM, Matsuoka RL, Yau K-W, Feller MB, Kolodkin AL. 2013. On and off retinal circuit assembly by divergent molecular mechanisms. Science 342:1241974.

Szikra T, Trenholm S, Drinnenberg A, Jüttner J, Raics Z, Farrow K, Biel M, Awatramani G, Clark DA, Sahel J-A, da Silveira RA, Roska B. 2014. Rods in daylight act as relay cells for cone-driven horizontal cell-mediated surround inhibition. Nat Neurosci 17:1728–35.

Takahashi SX. 2005. A CaV SH3/Guanylate Kinase Domain Interaction Regulates Multiple Properties of Voltage-gated Ca2+ Channels. J Gen Physiol 126:365–377.

Tetreault M-P, Bourdin B, Briot J, Segura E, Lesage S, Fiset C, Parent L. 2016. Identification of Glycosylation Sites Essential for Surface Expression of the CaValpha2delta1 Subunit and Modulation of the Cardiac CaV1.2 Channel Activity. J Biol Chem 291:4826–4843.

Thoreson WB, Babai N, Bartoletti TM. 2008. Feedback from horizontal cells to rod photoreceptors in vertebrate retina. J Neurosci 28:5691–5695.

Thoreson WB, Mangel SC. 2012. Lateral interactions in the outer retina. Prog Retin Eye Res 31:407–441.

Thoreson WB, Mercer AJ, Cork KM, Szalewski RJ. 2013. Lateral mobility of L-type calcium channels in synaptic terminals of retinal bipolar cells. Mol Vis 19:16–24.

Tikidji-Hamburyan A, Reinhard K, Seitter H, Hovhannisyan A, Procyk CA, Allen AE, Schenk M, Lucas RJ, Münch TA. 2014. Retinal output changes qualitatively with every change in ambient illuminance. Nat Neurosci 18:66–74.

Tran-Van-Minh A, Dolphin AC. 2010. The alpha2delta ligand gabapentin inhibits the Rab11-dependent recycling of the calcium channel subunit alpha2delta-2. J Neurosci 30:12856–12867.

Trumpler J, Dedek K, Schubert T, de Sevilla Muller LP, Seeliger M, Humphries P, Biel M, Weiler R. 2008. Rod and cone contributions to horizontal cell light responses in the mouse retina. J Neurosci 28:6818–6825.

Tsukamoto Y, Morigiwa K, Ueda M, Sterling P. 2001. Microcircuits for night vision in mouse retina. J Neurosci 21:8616–23.

Uchitel OD, Di Guilmi MN, Urbano FJ, Gonzalez-Inchauspe C. 2014. Acute modulation of calcium currents and synaptic transmission by gabapentinoids. Channels 4:490–496.

Umino Y, Solessio E, Barlow RB. 2008. Speed, spatial, and temporal tuning of rod and cone vision in mouse. J Neurosci 28:189–198.

Volgyi B. 2004. Convergence and Segregation of the Multiple Rod Pathways in Mammalian Retina. J Neurosci 24:11182–11192.

Vroman R, Klaassen LJ, Howlett MHC, Cenedese V, Klooster J, Sjoerdsma T, Kamermans M. 2014. Extracellular ATP Hydrolysis Inhibits Synaptic Transmission by Increasing pH Buffering in the Synaptic Cleft. PLoS Biol 12.

De Waard M, Liu H, Walker D, Scott VE, Gurnett C a, Campbell KP. 1997. Direct binding of G-protein betagamma complex to voltage-dependent calcium channels. Nature 385:446–450.

Wang Y, Wang Y. 2016. Neurons in primary visual cortex represent distribution of luminance. Physiol Rep 4:e12966.

Warren TJ, Van Hook MJ, Tranchina D, Thoreson WB. 2016. Kinetics of Inhibitory Feedback from Horizontal Cells to Photoreceptors: Implications for an Ephaptic Mechanism. J Neurosci 36:10075–10088.

Wässle H. 2004. Parallel processing in the mammalian retina. Nat Rev Neurosci 5:747–757.

Watschinger K, Horak SB, Schulze K, Obermair GJ, Wild C, Koschak A, Tampé R, Striessnig J. 2008. Functional properties and modulation of extracellular epitope-tagged Ca V 2 . 1 voltage-gated calcium channels. 2:461–473.

Wu J, Yan Z, Li Z, Yan C, Lu S, Dong M, Yan N. 2015. Structure of the voltage-gated calcium channel Cav1.1 complex. Science (80-) 350:aad2395-aad2395.

Wutz K, Sauer C, Zrenner E, Lorenz B, Alitalo T, Broghammer M, Hergersberg M, de la Chapelle A, Weber BHF, Wissinger B, Meindl A, Pusch CM. 2002. Thirty distinct CACNA1F mutations in 33 families with incomplete type of XLCSNB and Cacna1f expression profiling in mouse retina. Eur J Hum Genet 10:449–456.

Wycisk KA, Budde B, Feil S, Skosyrski S, Buzzi F, Neidhardt J, Glaus E, Nurnberg P, Ruether K, Berger W. 2006. Structural and functional abnormalities of retinal ribbon synapses due to Cacna2d4 mutation. Invest Ophthalmol Vis Sci 47:3523–3530.

Xin D, Bloomfield S a. 1999. Dark- and light-induced changes in coupling between horizontal cells in mammalian retina. J Comp Neurol 405:75–87.

Zabouri N, Haverkamp S. 2013. Calcium Channel-Dependent Molecular Maturation of Photoreceptor Synapses. PLoS One 8.

Zamponi GW, Striessnig J, Koschak A, Dolphin AC. 2015. The Physiology , Pathology , and Pharmacology of Voltage-Gated Calcium Channels and Their Future Therapeutic Potential The Physiology , Pathology , and Pharmacology of Voltage-Gated Calcium Channels and Their Future Therapeutic Potential. 901758:821–870.

Zeck GM, Masland RH. 2007. Spike train signatures of retinal ganglion cell types. Eur J Neurosci 26:367–380.

Zhang XM, Chen BY, Ng AHL, Tanner J a., Tay D, So KF, Rachel R a., Copeland NG, Jenkins N a., Huang JD. 2005. Transgenic mice expressing Cre-recombinase specifically in retinal rod bipolar neurons. Investig Ophthalmol Vis Sci 46:3515–3520.

III. Publications

Publication list

- Publication 1 pp. 55 - 114

  Seitter H, Sothilingam V, Benkner B, Garcia Garrido M, Tikidji-Hamburyan A, Pirone A, Seeliger M, Münch TA. Voltage-gated calcium channel subunit $\alpha_2\delta$-3 shapes light responses of mouse retinal ganglion cells mainly in low and moderate light levels. J Comp Neurol (under revision)

- Publication 2 pp. 115 - 130

  Reinhard K*, Tikidji-Hamburyan A*, Seitter H*, Idrees S, Mutter M, Benkner B, Münch TA. 2014. Step-by-step instructions for retina recordings with perforated multi electrode arrays. PLoS One 9:e106148
  * equal contributions

- Publication 3 pp. 131 - 150

  Tikidji-Hamburyan A*, Reinhard K*, Seitter H, Hovhannisyan A, Procyk CA, Allen AE, Schenk M, Lucas RJ, Münch TA. 2014. Retinal output changes qualitatively with every change in ambient illuminance. Nat Neurosci 18:66–74.
  * equal contributions

- Publication 4 pp. 151 - 195

  Tikidji-Hamburyan H*, Reinhard K*, Storchi R*, Seitter H, Davis KE, Dietter J, Bedford R, Ueffing M, Ala-Laurila P, Lucas RJ, Münch TA. Rods escape saturation to drive visual responses in daylight conditions. (under revision)
  * equal contributions

Publication 1 – Retinal function of $\alpha_2\delta$-3

Hartwig Seitter, Vithiyanjali Sothilingam, Boris Benkner, Marina Garcia Garrido, Alexandra Tikidji-Hamburyan, Antonella Pirone, Mathias Seeliger, Thomas A Münch. *Voltage-gated calcium channel subunit $\alpha_2\delta$-3 shapes light responses of mouse retinal ganglion cells mainly in low and moderate light levels.* J Comp Neurol (under revision)

Framework:

This is an original research paper. It shows that despite strong expression of voltage-gated calcium channel subunit $\alpha_2\delta$-3 in horizontal cells, readouts of visual performance and horizontal cell calcium currents are normal in the absence of $\alpha_2\delta$-3. Yet on the retinal output subtle effects can be detected. The study combines findings on optokinetic reflex behavior, electroretinograms, gene expression, calcium current recordings and micro-electrode array recordings of ganglion cells under different luminance levels. This is a collaborative study together with the lab of Mathias Seeliger, University of Tübingen (electroretinography).

My contributions:

I performed all RT-PCR experiments, immunohistochemical and X-Gal stainings in sections and wholemount retinas, developed the subtractive wholemount staining analysis for horizontal cell mosaics and did all stainings, microscopy and data processing as well as analyzing the distribution. I established isolated horizontal cell patch-clamp recordings in the lab, designed the calcium channel recording protocols and performed all the recordings and analysis. All MEA recordings, data processing and analysis was done by me. The manuscript draft was outlined and written by me.

Other contributions:

VS performed in vivo electrographic recordings and did the analysis together with MGG. BB did the optokinetic reflex behavioral measurements and analysis. ATH wrote spike sorting scripts and initially discovered the spike rate compression in responses to white noise. TAM developed the horizontal cell mosaic analysis scripts in Mathematica. AP helped establish RT-PCR and X-Gal stainings and assisted on interpretation of histological data. VS and TAM helped writing the manuscript. ATH, AP, BB, MS critically reviewed the manuscript.

Journal of Comparative Neurology

Voltage-gated calcium channel subunit $\alpha_2\delta$-3 shapes light responses of mouse retinal ganglion cells mainly in low and moderate light levels

Abbreviated title: Ca^{2+} channel subunit $\alpha_2\delta$-3 in retina function

Hartwig Seitter [1,5], Vithiyanjali Sothilingam [2], Boris Benkner [1,3,5], Marina Garcia Garrido [2], Alexandra Tikidji-Hamburyan [1,3,5], Antonella Pirone [4], Mathias Seeliger [2], Thomas A. Münch [1,3,6]

[1] Werner Reichardt Centre for Integrative Neuroscience (CIN)
Otfried-Müller-Str. 25

[2] Division of Ocular Neurodegeneration, Institute for Ophthalmic Research, Centre for Ophthalmology, Schleichstr. 4/3

[3] Bernstein Center for Computational Neuroscience
Otfried-Müller-Str. 25

[4] Department of Otolaryngeology, Tübingen Hearing Research Center, Molecular Physiology of Hearing
Elfriede-Aulhorn-Str. 5

[5] IMPRS for Cognitive and Systems Neuroscience
Österbergstr. 3

Eberhard Karls Universität Tübingen
72076 Tübingen
Germany

[6] Corresponding author:
Thomas A. Münch
Otfried-Müller-Str. 25
72076 Tübingen
Phone: +49(0)7071-29-89182
Email: thomas.muench@cin.uni-tuebingen.de

Name of associate editor: Edward M. Callaway

Key words: horizontal cell, ganglion cell, light adaptation, multi-electrode array, RRIDs: IMSR_JAX:005780, AB_10000347, AB_10000340, AB_304560, AB_2079751, AB_1608076, AB_307210, SciRes_000137, SciRes_000168

Support or grant information:
The study was supported by funds from the Werner-Reichardt Centre for Integrative Neuroscience Tübingen (CIN, DFG EXC 307) and the Bernstein Center for Computational Neuroscience Tübingen (BMBF, FKZ 01GQ1002).

Journal of Comparative Neurology

Abstract

Little is known about the function of the auxiliary $\alpha_2\delta$ subunits of voltage-gated calcium channels in the retina. We investigated the role of $\alpha_2\delta$-3 (*Cacna2d3*) using a mouse in which $\alpha_2\delta$-3 was knocked out by LacZ insertion. Behavior experiments indicated a normal optokinetic reflex in $\alpha_2\delta$-3 knockout animals. Strong expression of $\alpha_2\delta$-3 could be localized to horizontal cells using the LacZ-reporter, but horizontal cell mosaic and currents carried by horizontal cell voltage-gated calcium channels were unchanged by the $\alpha_2\delta$-3 knockout. *In vivo* electroretinography revealed unaffected photoreceptor activity and signal transmission to depolarizing bipolar cells. We recorded visual responses of retinal ganglion cells with multi-electrode arrays in scotopic to photopic luminance levels and found subtle changes in $\alpha_2\delta$-3 knockout retinas. Spontaneous activity in OFF ganglion cells was elevated in all luminance levels. Differential response strength to high- and low-contrast Gaussian white noise was compressed in ON ganglion cells during mesopic ambient luminance and in OFF ganglion cells during scotopic and mesopic ambient luminances. In a subset of ON ganglion cells, we found a sharp increase in baseline spiking after the presentation of drifting gratings in scotopic luminance. This increase happened after gratings of different spatial properties in knockout compared to wild type retinas. In a subset of ON ganglion cells of the $\alpha_2\delta$-3 knockout, we found altered delays in rebound-like spiking to full-field contrast steps in scotopic luminance. In conclusion, $\alpha_2\delta$-3 seems to participate in shaping visual responses mostly within brightness regimes when rods or both rods and cones are active.

Journal of Comparative Neurology

Introduction

Voltage-gated calcium channels (VGCC) of the L-, P/Q-, R- and N-Type form multimeric complexes composed of pore-forming α_1 subunits, modulatory β subunits and auxiliary $\alpha_2\delta$ subunits (Dolphin, 2012). The α_1 subunits determine the main biophysical and pharmacological characteristics of the VGCC complex (Catterall et al., 2005), β subunits modulate channel properties, while the $\alpha_2\delta$ subunits mainly promote trafficking (Davies et al., 2007) and targeting of the VGCC complexes (Thoreson et al., 2013), e.g. to lipid rafts (Robinson et al., 2011). Thus, $\alpha_2\delta$ subunits increase calcium current densities and participate in establishing calcium nanodomains. Recent studies have shown a role of $\alpha_2\delta$ subunits in synaptogenesis, independent of their association with a calcium channel (Kurshan et al., 2009), as well as in synaptic structuring (Pirone et al., 2014). $\alpha_2\delta$ subunits get cleaved post-translationally into α_2 and δ parts and re-linked by disulfide bonds: The δ part anchors $\alpha_2\delta$ to the plasma membrane, putatively by a glycosylphosphatidylinositol (GPI) anchor (Davies et al., 2010), whereas the highly glycosylated extracellular α_2 part links $\alpha_2\delta$ to the α_1 subunits (Gurnett et al., 1997). Four isoforms of $\alpha_2\delta$ have been described, termed $\alpha_2\delta$-1 to $\alpha_2\delta$-4 (Curtis and Catterall, 1984; Leung et al., 1987; Ellis et al., 1988; Klugbauer et al., 1999; Qin et al., 2002).

In vertebrate retina, photoreceptors mainly express VGCC containing the α_1 subunit $Ca_V1.4$ (Morgans, 2001), β_2 (Ball et al., 2002) and $\alpha_2\delta$-4 (Wycisk et al., 2006). Loss of $\alpha_2\delta$-4 leads to an altered b-wave in the electroretinogram and to photoreceptor degeneration (Wycisk et al., 2006), reminiscent to what is observed in β_2 knockout mice (Ball et al., 2002). The other ribbon synapse-bearing cell types of the retina, the bipolar cells, also expresses $\alpha_2\delta$-4 in tiger salamander (Thoreson et al., 2013) and mouse (de Sevilla Muller et al., 2013). So far only few studies have investigated the expression of the other three $\alpha_2\delta$ subtypes in the retina. Rat retinal ganglion cells

were found to express $\alpha_2\delta$-1, acting as a receptor for thrombospondins (Eroglu et al., 2009). Expression of $\alpha_2\delta$-3 has been reported in ON bipolar cells isolated from mouse retina (Nakajima et al., 2009) and evidence from co-immunolabeling suggests widespread expression in photoreceptors, bipolar cells, glycinergic amacrine cells and most cells in ganglion cell layer (Pérez de Sevilla Müller et al., 2015). The physiological significance of $\alpha_2\delta$ subunit function in mouse retina is largely unclear.

In the present study, we used an $\alpha_2\delta$-3 (*Cacna2d3*) knockout mouse (Neely et al., 2010) to study the functional aspects of $\alpha_2\delta$-3 in the mammalian retina.

Journal of Comparative Neurology

Materials & Methods

All procedures were carried out at room temperature unless otherwise noted. Chemicals were obtained from Sigma Aldrich unless otherwise noted.

Animals

For RT-PCR experiments, wild type mice of the C3H strain (Sanyal and Bal, 1973) were used. All other experiments were carried out on B6.129P2-*Cacna2d3*^{tm1Dgen}/J mice (The Jackson Laboratory, RRID: IMSR_JAX:005780), where $\alpha_2\delta$-3 (gene name *Cacna2d3*) has been knocked out by targeted insertion of a LacZ reporter (*Cacna2d3*$^{+/+}$ will be referred to as wild type and *Cacna2d3*$^{-/-}$ as knockout animals, for genotyping protocols refer to The Jackson Lab). Animals of either sex were used for experiments. Mice were kept in a 12/12 hour dark/light cycle and were used for each set of experiments on approximately the same circadian time of day. Animal use was in accordance with German and European regulations and approved by the Regierungspräsidium Tübingen.

Behavioral tests: Optokinetic drum

The visual performance of wild type and knockout mice was examined on the behavioral level in a virtual arena, based on the optokinetic reflex (OKR). The head movements of the mouse were used as the behavioral read-out. The freely moving mouse was placed on an elevated platform in the middle of the arena consisting of four computer monitors. A projection of a virtual cylinder with rotating black and white stripes was presented on the screens. Using an automated camera-based system (Viewer³, Biobserve) we were able to automatically adjust the spatial frequency of the stripe patterns on each monitor individually, relative to the head position of the animal, so the stripe pattern appeared uniform from the view point of the mouse. The rotating stripe pattern elicited head movements corresponding to the angular velocity

of the stimulus, which were detected by the automated camera-based system and analyzed quantitatively by custom-written Mathematica (Wolfram) scripts to determine correct tracking behavior. To examine the complete range of visual acuity, the spatial frequency of the stimulus was varied between 0.014 and 0.5 cycles per degree (cpd), corresponding to bar widths of 36° to 1°. These stimuli were presented at Michelson contrast levels between 0% (equal stripe color) and 98% (black and white stripes) and rotated clock-wise or counter-clock-wise. For our experiments, rotation speed of the virtual drum was kept at 12°/s (Mitchiner et al., 1976; Abdeljalil et al., 2005; Lagali et al., 2008; Benkner et al., 2013).

RT-PCR (reverse transcription-polymerase chain reaction) of $\alpha_2\delta$ genes on total retinal RNA

Adult (8-9 weeks old) C3H mice were euthanized by CO_2 and decapitated. Young C3H mice of postnatal days 3, 6, 9, 12 and 15/16 were euthanized by decapitation. Retinas were dissected out in ice-cold RNase-free phosphate-buffered saline (PBS). Remnants of retinal pigment epithelium (RPE) were removed (adult retinas) and both retinas of each animal were put immediately in lysis buffer (RLT, Qiagen or Trizol, Invitrogen). Tissue samples were incubated for several minutes in lysis buffer, followed by strong vortexing. Unlysed tissue pieces were triturated and dispersed by pipetting.

RNA was isolated from the lysates with a spin column-based kit, following manufacturer's instructions (RNeasy Mini Kit, Qiagen). The RNA was eluted in nuclease-free water and RNA concentration and quality was measured on a Nanodrop ND-1000 (Thermo Scientific). All RNA samples had a 260/280 ratio above 1.9, indicating good RNA quality. Afterwards, RNA was stored short-term at -20°C or long-term at -150°C or immediately used in a retrotranscription reaction (ProtoScript® AMV First Strand cDNA Synthesis Kit, New England Biolabs or SuperScript® III First-Strand Synthesis System, Invitrogen). In each reaction, 48-55 ng (adult mouse) or

300-450 ng (developmental time line) of RNA was used as template and retrotranscribed with oligo d(T) primers according to the manufacturer's instructions. cDNA products were stored at -20°C and used as templates for polymerase chain reaction (PCR) using cDNA-specific primers for all $\alpha_2\delta$ transcripts. Primer details are summarized in Table 1. For negative controls, a reaction with $\alpha_2\delta$-3 primers was run in parallel with water as template. The PCR reactions contained 0.2 µM forward primer (for), 0.2 µM reverse primer (rev), 200 µM dATP, dTTP, dCTP and dGTP each, 1.5 mM $MgCl_2$, 0.125 µl Standard-Taq polymerase (New England Biolabs), 1 µl template cDNA, 2.5 µl 10X reaction buffer (New England Biolabs), nuclease-free water to fill up to 25 µl total volume. The reaction was set up on ice and run in a thermocycler (BioRad), using a touchdown PCR program: 94°C, 3 min; (94°C, 20 sec; annealing temperature, 30 sec; 72°C, 30 sec) x 35; 72°C, 5 min; 4°C, ∞. Annealing temperature for all primer pairs started at 66°C, decreasing by 1°C per cycle until 61°C for the remaining cycles.

The PCR products were run on a 1.5% agarose gel, containing 2% midori green (BioZym) or 4% ethidium bromide (Carl Roth) in tris-borate-EDTA buffer (TBE) and visualized using normal UV excitation and filters for ethidium bromide.

Immunohistochemistry, LacZ reporter expression and horizontal cell mosaic analysis

Adult mice were euthanized by CO_2 and decapitated. For cryosections, adult (40 days to 7 months) wild type (*Cacna2d3*$^{+/+}$), knockout (*Cacna2d3*$^{-/-}$), and heterozygous (*Cacna2d3*$^{+/-}$) mice were used. For wholemount LacZ stainings, adult (12 to 23 weeks) wild type and knockout animals were used. For horizontal cell mosaic stainings, adult (4-12 weeks old) littermate pairs of wild type and knockout animals were used. Cornea and lens were removed in PBS and eyecups were fixed in 4% paraformaldehyde in PBS for 30 min on ice, or the retina was dissected out, cut to clover-leaf shape, and mounted on a black nitrocellulose filter paper (Sartorius Stedim) before fixation. After washing 3 times in PBS for at least 30 min, retinas were

dissected out (wholemount stainings) and retinas/eyecups were cryoprotected by equilibration in a sequence of 10%, 20% and 30% sucrose in PBS.

Cryosections

The eyecups were transferred to cryo-embedding medium (Tissue-Tek OCT, Sakura Finetek) and frozen on an aluminum block cooled to -150°C. Oriented slices of 12 µm thickness were cut along the dorso-ventral axis in a cryostat (CM3050, Leica), mounted on coated glass slides (Superfrost Plus®, Carl Roth) and dried at 37°C for 30-60 minutes. Slices were stored at -20°C until use. Before proceeding with immunohistochemical staining, slices were thawed and washed 3 times for 10 min in PBS.

Cryoslices were incubated for 12-24 hours at 4°C in a humid chamber with primary antibodies diluted in 10% NGS, 1% BSA, and 0.5% Triton X-100. Antibodies and their dilutions are summarized in Table 2 and their characterization is described below. For negative controls, no primary antibodies were added. Slices were washed 3 times for 10 min in PBS and incubated for 1 hour in a humid chamber with secondary antibodies diluted in PBS, supplemented with 0.5% Triton X-100. Slices were washed 3 times for 10 min in PBS, before being submitted to an X-Gal staining procedure: X-Gal (5% in N,N-dimethylformamide, Carl Roth) was diluted 1:30 in staining solution pre-warmed to 42°C (in mM: 7.2 Na_2HPO_4, 2.8 NaH_2PO_4, 150 NaCl, 1 $MgCl_2$, 3 $K_3(Fe(CN)_6)$, 3 $K_4(Fe(CN)_6)$; all from Carl Roth, except $MgCl_2$, Sigma) and incubated for 12-24 hours at 37°C. Staining was stopped by washing 3 times for 10 min in PBS. Afterwards, slices were washed once in double-distilled water prior to mounting with Vectashield (Vector Laboratories). Images were acquired with an upright epifluorescence microscope (Zeiss Imager Z1), using same settings for stainings and controls, and histograms were adjusted with the min/max function in Zeiss Axiovision software. Images were processed in Adobe Photoshop CS4 and adjusted with the standard auto-contrast function.

Journal of Comparative Neurology

Wholemount stainings

Retinas were frozen three times at -150°C and thawed at room temperature for better antibody penetration. The retinas were washed three times for 30 minutes in PBS before proceeding with immunohistochemical staining.

Blocking was done in blocking solution (10% normal donkey serum (NDS) or normal goat serum (NGS, for cryoslices), 1% bovine serum albumine (BSA, Carl Roth), 0.5% Triton X-100 in PBS), 0.02% sodium azide for one hour.

One retina of each animal was incubated for 7 days with primary antibodies (see Table 2 and characterization below) diluted in 3% NDS, 1% BSA, 0.5% Triton X-100, 0.02% Na-azide in PBS, gently shaking. The second retina served as a negative control, without addition of primary antibodies. Retinas were washed three times for one hour in PBS after primary antibody incubation. Retinas were incubated with secondary antibodies (Table 2) diluted in 0.5% Triton X-100 in PBS for 24 hours, gently shaking. When biotinylated antibodies were used, retinas were washed three times for 30 min in PBS and incubated with streptavidin-Cy5 in secondary antibody solution for 2-4 hours, gently shaking. Retinas were washed three times for one hour in PBS, cut to clover-leaf shape and flat-mounted on glass slides in Vectashield (Vector Laboratories). Adhesive tape was used as a spacer before adding the coverslip and sealing with nail polish. The stainings and negative controls were evaluated on an upright epifluorescence microscope (Zeiss Imager Z1). The stainings were then visualized on a confocal laser scanning microscope in detail (Zeiss LSM 710). Pinhole sizes were adjusted to the same optical Z-slice thickness for multichannel images.

Antibody characterization

The mouse monoclonal anti-calbindin antibody (Swant Cat# 300 RRID:AB_10000347) was generated against calbindin D-28k purified from chicken.

In western blots, the antibody detects a single ~28-kDa band in brain extracts of mouse, rat, guinea pig, rabbit and macaque. There is no immunoreactivity of the antibody on hippocampal sections of calbindin D-28k knockout mice (manufacturer's data sheet, (Celio et al., 1990; Airaksinen et al., 1997)). This antibody is widely used as a marker for retinal horizontal cells in the mouse (Janssen-Bienhold et al., 2009; Phillips et al., 2010) and showed the same labeling pattern as previously described (Haverkamp and Wässle, 2000).

The rabbit polyclonal anti-calbindin antibody (Swant Cat# CB 38 RRID:AB_10000340) was generated against recombinant rat calbindin D-28K. In western blots, the antibody detects a single ~28 kDa band in brain lysates from mouse, rat, guinea pig, rabbit, macaque and chicken. There is no immunoreactivity of the antibody on cerebellar sections of a calbindin D-28k knockout mice (manufacturer's data sheet). There is minimal cross-reactivity with calretinin, that gives a ~30 kDa band in western blots and can also reveal calretinin expression in immunostainings. On the distal inner nuclear layer, the staining however is specific for horizontal cells (Haverkamp et al., 2008; Guo et al., 2009). This antibody is widely used as a marker for retinal horizontal cells in the mouse and showed the same labeling pattern as previously described (Haverkamp and Wässle, 2000).

The chicken polyclonal anti-neurofilament H antibody (Abcam Cat# ab4680, RRID:AB_304560) was generated against purified neurofilaments from bovine spinal cord. Its specificity is confirmed for immunohistochemistry (manufacturer's data sheet, (Mandadi et al., 2013)). The labeling pattern was the same as in another neurofilament H antibody, selectively labeling axonal arborizations of horizontal cells in the outer plexiform layer (Shelley et al., 2006). Also, in retinal dissociations we observed co-labeled putative horizontal cell axonal arborizations which stained positive for calbindin and the neurofilament antibody.

The goat polyclonal anti-choline acetyltransferase antibody (Millipore Cat# AB144P, RRID:AB_2079751) was generated against human placental enzyme. In western

blots, the antibody detects a 68-kDa band e.g. in NIH/3T3 lysate (manufacturer's data sheet). In the retina, the antibody labels cholinergic ON and OFF starburst amacrine cells and their stratifications in sublaminae 2 and 4 of the inner plexiform layer (Yip et al., 1991; Yonehara et al., 2011).

The rabbit polyclonal anti-melanopsin antibody (Advanced Targeting Systems Cat# AB-N39, RRID:AB_1608076) was generated against the 15 N-terminal extracellular amino acids of mouse melanopsin. Saporin conjugated to this antibody selectively ablates melanopsin-expressing RGC-5 cells and melanopsin-positive ganglion cells in mouse retina (Göz et al., 2008).

The chicken polyclonal anti-β-galactosidase antibody (Abcam Cat# ab9361, RRID:AB_307210) was generated against the full length native protein, purified from E.coli. There is no immunoreactivity in mouse brain samples, that do not transgenetically express β-galactosidase (Scott et al., 2009). We never observed immunoreactivity with this antibody in the retina of wild type animals (which are LacZ negative).

Horizontal cell mosaic analysis

Horizontal cells and their processes were stained with antibodies against calbindin and neurofilament H in retinal wholemounts. Confocal Z-stacks (5 to 10 Z planes) were acquired with a 10X objective (NA 0.3, 0.83 µm pixel size), covering the retinal wholemount (850 * 850 µm per image), so that all horizontal cells stained were completely visualized including their processes. Overlap between neighboring images was set to 20%. Z-stacks were maximum intensity projected in ZEN 2011 (Zeiss), contrast-adjusted in Fiji (RRID:SciRes_000137, (Schindelin et al., 2012)) and combined with the grid stitch plugin (Preibisch et al., 2009) to yield complete retinal wholemounts. From these, an image part of each of the two dorsal and ventral leaves per wholemount was selected in Photoshop CS4 (Adobe), covering the middle 50% from the optic nerve to outer rim span (see Fig. 5A). The images were analyzed in a custom-written Wolfram Mathematica script to detect cells and compute spacing and

mosaic regularity. The neurofilament channel was subtracted from the calbindin channel to produce cleaned-up horizontal cell somata (Peichl and Gonzalez-Soriano, 1994). Images were binarized after adjusting images with dilation/erosion functions. Cell bodies were automatically detected and centroid positions were extracted. Automatic detection correctly identified between 75 to over 95% of cells, which was then manually corrected for false-positives and false-negatives. With the centroid position information, nearest neighbor distance for each cell could be calculated. Data analysis and statistics were done with Mathematica. For significance testing, the means of the nearest neighbor distances from each individual evaluated image were used (two dorsal and two ventral from each retina).

Patch-clamp recordings of isolated horizontal cells

Retina dissociation procedure

Adult (5-16 weeks old) wild type and knockout mice were anaesthesized by CO_2, euthanized by cervical dislocation, and retinas were dissected out in CO_2-independent medium A (per 100 ml): 97 ml HBSS - Ca/Mg free (Biochrom, L2055), 1 ml 10 mM EDTA (final: 0.1 mM, Sigma, E-6511), 1 ml 1 M HEPES (final: 10 mM, Biochrom, L1613), 1 ml 10.000 U/ml Penicillin/Streptomycin (final: 100 U/ml, Biochrom, A2213). Retinas were incubated in a papain solution (medium A, supplemented with 1 mM L-Cysteine (Sigma, C-1276), 20 U/ml papain (Worthington, LS003126)) for 25-40 min at 37°C. Meanwhile medium B was pre-incubated in 5% CO_2. Medium B (per 100 ml): 10 ml 10X DMEM (Biochrom, F0455), 83.3 ml tissue culture water (PromoCell, C-49998), 2.7 ml 7.5% Sodium bicarbonate (final: 24.11 mM, Biochrom, L1713), 1 ml 1 M HEPES (final: 10 mM, Biochrom, L1613), 2 ml 200 mM L-Glutamine (final: 4 mM, Biochrom, K0283), 1 ml 10.000 U/ml Penicillin/Streptomycin (final: 100 U/ml, Biochrom, A2213). Papain digestion was stopped by replacing the papain solution with DNAse solution (90% Medium B, 10% fetal calf serum (PAA, A15-101), 100 U/ml DNAse I (Sigma, D-5025)) and incubating

for 5 min at 37°C. Retinas were centrifuged in a tabletop centrifuge (500 rpm, 3 min) and washed twice with medium B prior to mechanical trituration with fire-polished glass pipettes. In most experiments further gentle dissociation was achieved by shaking the tube for 5-10 min on the slowest setting of a vortexer (Vortex-Genie 2, Scientific Industries). Dissociated cells were seeded on coated coverslips (Ø 12 mm, Gerhard Menzel GmbH, CB00120RA1, coating: 1 mg/ml Concanavalin-A (Sigma, C-7275) in PBS) and kept in medium B at 37°C in 95% O_2/5% CO_2 for at least 30 minutes until use. Coverslips were transferred to a recording chamber inside an upright microscope and solution was switched to external solution (see below).

Whole-cell patch-clamp recordings

Patch pipettes were pulled from borosilicate glass (Science Products, GB150F-8P), backfilled with internal solution (see below) and had resistances of 4-8 MΩ. Cells were viewed on a digital camera through a 60X water immersion objective (Olympus, NA 1.0) under infrared illumination and horizontal cells were identified by their characteristic morphology (Schubert et al., 2006). Currents were recorded through a patch-clamp amplifier (EPC-10, HEKA) on a computer running PatchMaster (v2x69, RRID:SciRes_000168, HEKA). Internal and external solutions were designed to isolate currents carried by voltage-gated Ca channels.

Internal solution (mM): 110 Cs-methanesulfonate (C1426), 20 TEA (tetraethylammonium)-Cl (T2265), 10 Phosphocreatine-Tris (Santa Cruz, sc-212557), 10 HEPES (4-(2-hydroxyethyl)-1-piperazineethanesulfonic acid, H3375), 5 EGTA (ethylene glycol tetraacetic acid, 03780), 4 ATP (Adenosine triphosphate)-Na (A3377), 0.2 GTP (Guanosine triphosphate)-Na (G8877), 0.51 $CaCl_2$ (C5080, free concentration ~20 nM, calculated with WinMAXC32 v2.50, (Patton et al., 2004)), 4 $MgCl_2$ (M2670), pH = 7.2 with CsOH (516988), osmolality 295 mOsm/kg. Chemicals from Sigma, unless noted otherwise.

External solution (mM): 123 NaCl (VWR, 27810.295), 5 KCl (P9333), 10 TEA-Cl (T2265), 10 $BaCl_2$ (342920), 1 $MgCl_2$ (M2670), 10 HEPES (H3375), 10 D-Glucose

Journal of Comparative Neurology

(G7528), 1 µM TTX (Biotrend, BN0518), pH = 7.4 with NaOH (S2770), osmolality 305 mOsm/kg. Chemicals from Sigma, unless noted otherwise. For cobalt block experiments, BaCl2 was equimolarly substituted with CoCl2 (Sigma, C8661).

Liquid junction potential with these solutions was 14.5 mV (calculated with JPCalc, (Barry, 1994)) and was partially corrected online (set to 10 mV). Post-recording correction was not applied.

Horizontal cell resting membrane potentials were determined by current-clamp to 0 pA directly after establishing whole-cell configuration. Cell capacitances were determined by the Cslow function of the HEKA amplifier. Membrane resistance was generally > 1 GΩ during recording. Cells were held at -60 mV in between voltage protocols. Recording protocols started two minutes after break-in and were interleaved by 30-s pauses in between each protocol. Voltage protocols included (1) maximum current measurements with 50 ms steps to 0 mV, (2) current-voltage (IV) curves with 50 ms steps from -70 to +60 mV and (3) inactivation protocols with 400 ms inactivation steps from -60 to +20 mV and an additional 50 ms test step to 0 mV. Current amplitudes were calculated from the average during the second half (25 ms) of the test steps in each protocol. IV curves were fitted according to the following equation:

$I = G_{max} (V - V_{rev}) / \{ 1+\exp [- (V - V_{0.5,act}) / k_{act}] \}$, where I is the current amplitude, G_{max} is the maximum slope conductance, V is the test potential, V_{rev} is the reversal potential, $V_{0.5,act}$ is the half-maximal activation voltage and k_{act} is the slope factor (Ortner et al., 2014). Fitting and parameter calculations were done in SigmaPlot (v12.0, Systat Software).

Recordings were done using p/n leak subtraction (25% magnitude, 4 repetitions, min/max -128 mV/-50 mV). Within each voltage protocol, holding potential was -80 mV. At the beginning of each protocol a 50 ms test pulse to -90 mV was applied. The current difference (non-leak subtracted data) during and after the test pulse was used to calculate input resistance (R_{in}) offline using Ohm's law. Series

resistance (R_{ser}) was read off the amplifier's Cslow function after each voltage protocol. Membrane resistance (R_{mem}) was calculated by $R_{mem} = R_{in} - R_{ser}$. For maximum current analysis, only voltage protocols were considered that fulfilled two criteria: (1) $R_{ser} < 10\% R_{mem}$. (2) mean deviation from zero during 0 mV step > mean deviation from zero during 100 ms before step. Since maximum current amplitude slowly increased with recording time, only maximum current protocols between two and five minutes after break-in were considered for analysis. Only IV curves with clear U-shaped fits were used for analysis. Inactivation data to use for analysis was chosen manually. Data was analyzed with Matlab (Mathworks) and tested for significant differences using Wilcoxon ranksum test.

Electroretinography (ERG)

Animals used for ERG recordings were 27-28 days old littermates (n = 5 wild type, n = 4 knockout animals from 5 litters). ERGs were recorded as described previously (Tanimoto et al., 2009). Mice were anaesthetized using ketamine (66.7 mg/kg body weight) and xylazine (11.7 mg/kg body weight). The pupils were dilated and single-flash responses were obtained under scotopic (dark-adapted overnight) and photopic (light-adapted with a background illumination of 30 cd/m^2 starting 10 minutes before recording). Single white-flash stimuli ranged from - 4 to 1.5 log cd*s/m^2 under dark-adapted conditions, and from -2 to 1.5 log cd*s/m^2 under light-adapted conditions. Ten responses were averaged, with interstimulus intervals of 5 s (for -4 to -0.5 log cd*s/m^2) or 17 s (for 0 to 1.5 log cd*s/m^2).

Multi-electrode array (MEA) recordings: Experimental procedure

Adult (9-12 weeks old) wild type and knockout mice were dark-adapted for at least 4 hours, euthanized by cervical dislocation and retinas were isolated under dim red light in Ringer's solution containing (in mM): NaCl 110, KCl 2.5, $CaCl_2$ 1, $MgCl_2$, 1.6, D-glucose 10, $NaHCO_3$ 22; bubbled with 5% CO_2/95% O_2; pH 7.4. Retinas were

mounted on a nitrocellulose filter paper (Millipore) with a 2–3 mm rectangular aperture in the center, transferred to a 60-electrode perforated multi-electrode array (MEA) chamber (60pMEA200/30iR-Ti-gr, Multichannel Systems) and placed ganglion cell-side down on the recording electrodes. The inter-electrode distance was 200 µm, interspersed by holes through which gentle suction was applied. The MEA was put in an upright microscope, where light stimulation was supplied through the microscope condenser by a digital light processing (DLP) projector (PG-F212X-L, Sharp), presenting a diverse set of visual stimuli focused onto the photoreceptors. One batch of stimuli lasted 28 to 40 minutes and was shown at least twice per ambient luminance level. Specific luminance levels were achieved by inserting neutral density filters into the light path. The neutral density (ND) filters (Thorlabs NE10B-A to NE50B-A), had optical densities from 1 ("ND1", i.e. 10-fold light attenuation) to 5 ("ND5", 10^5-fold attenuation). To achieve light attenuation stronger than 5 log units, two ND filters were combined in series. Experiments started at ND8 (‘scotopic’; darkest setting, 10^8-fold attenuation) and continued over ND6 (‘mesopic’; 10^6-fold attenuation) to ND4 (‘photopic’; 10^4-fold light attenuation). A shutter was closed while changing ND filters during the experiment to prevent intermittent exposure to unattenuated light. During the whole experiment the retina was continuously superfused with Ringer’s solution pre-warmed to 38°C by an in-line heating system just before the MEA chamber (33-35°C inside the recording chamber). In this study, total recording times were up to 4.5 hours. Detailed description of the MEA recording procedures can be found in (Reinhard et al., 2014).

Stimuli

All stimuli were gray-scale images with pixel values between ‘0’ ("black") and ‘255’ ("white"). The stimulus projector produced an output spanning 3 log units of light intensities (i.e. 1000-fold difference between black (‘0’) and white (‘255’) pixels). We linearized the gamma-function of the projector, so that our background set at ‘128’ corresponded to the middle physical light intensity between ‘0’ and ‘255’. All stimuli

were balanced so their mean light intensity over time was '128'. Each stimulus was preceded by at least 1 s of uniform background gray ('128').

Here, we present data on the following stimuli:

1) Full-field Gaussian white noise ("flicker") (Chichilnisky, 2001): Each flicker stimulus consisted of five 20-s episodes of high-contrast flicker interleaved with five 20-s episodes of low-contrast flicker. Screen brightness was updated every frame (60 Hz), and drawn from a Gaussian distribution with mean '128' and sigma of 38.4 (high contrast) or 7.68 (low contrast). The flicker stimulus was presented four times per ambient luminance level.
2) Full-field steps: background gray ('128') → black ('0') → gray ('128') → white ('255') → gray ('128'), 2 s per step (±100% Weber contrast).
3) Drifting sine wave gratings: 30 different drifting sinusoidal gratings (combinations of six spatial periods: 100, 200, 500, 1000, 2000, 4000 µm and five temporal frequencies: 0.25, 1, 2, 4, 8 Hz) of full contrast (black: '0' to white: '255').

In addition, moving bars and natural movie stimuli were included in our stimulus batch, but are not discussed here.

Light Intensity Measurements

We measured the spectral intensity profile (in $\mu W \cdot cm^{-2} \cdot nm^{-1}$) of our light stimuli with a calibrated spectrophotometer (USB2000+, Ocean Optics). We then transformed the stimulus intensity into equivalents of photoisomerizations per rod per second, assuming dark-adapted rods, as described previously (Munch et al., 2009). Briefly, the spectrum was converted to photons$\cdot cm^{-2} \cdot s^{-1} \cdot nm^{-1}$, convolved with the normalized spectrum of rod sensitivity (Umino et al., 2008), and multiplied with the effective collection area of rods (0.5 µm²) (Nikonov et al., 2005). The mean light intensity (=background '128') used in this study was 4 $Rh^* \cdot s^{-1}$ per rod (ND8, 'scotopic'), $4 \cdot 10^2$ $Rh^* \cdot s^{-1}$ per rod (ND6, 'mesopic') and $4 \cdot 10^4$ $Rh^* \cdot s^{-1}$ per rod (ND4, 'photopic').

Spike sorting

Data was recorded at 25 kHz with a USB-MEA-system (USB-MEA1060, Multichannel Systems), high-pass filtered (500Hz, 10th-order butterworth filter) and spikes were extracted by thresholding. Spike sorting (assignment of spikes to "units", presumably individual ganglion cells) was performed semi-manually with an in-house written Matlab (Mathworks) routine, using 2-dimensional projections of e.g. spike amplitude, principal components, Euclidian distance to template waveforms. Quality of each unit was assessed by interspike interval and spike shape variation. Data analysis was based on the spike times of individual units.

Spike rate calculation

The instantaneous spike rate of each unit was calculated by convolving the spike train with a Gaussian with sigma = 40 ms and amplitude = .25 $\sqrt{e}$ $sigma^{-1}$ (≈ 10 Hz for sigma = 40 ms) and was used for further analysis in Matlab. Single units will be referred to as individual "cells" in the following text.

Determining cell polarity using the spike-triggered average.

We calculated spike-triggered averages (Chichilnisky, 2001) in response to the Gaussian flicker by summing the 500 ms stimulus history before each spike during high- or low-contrast episodes. The polarity of the spike-triggered average (STA) was assessed manually for each cell and ambient luminance level; if the first peak was negatively deflected, it was categorized as an OFF cell, if positively deflected it was categorized as an ON cell (Tikidji-Hamburyan et al., 2014).

Statistics.

Statistical significance was tested with Wilcoxon rank sum tests and data was plotted using Matlab.

Journal of Comparative Neurology

Results

1. Optokinetic reflex is present in $\alpha_2\delta$-3 knockout mice

The optokinetic reflex is a simple reflex behavior in which a moving stimulus is followed by the gaze ("tracking") of the animal with eye and head movements. In our behavioral setup, the mice were put in a virtual optokinetic drum and presented with stripe patterns of uniform stripe width (Benkner et al., 2013). Stimulus intensity was within the photopic regime. For the analysis in this study, we only considered if animals were able to track the stimulus at any of the tested conditions, to establish whether visually guided behavior is developed in $\alpha_2\delta$-3 knockout mice. Wild type and $\alpha_2\delta$-3 knockout animals performed equally well in this simple visually guided behavior (Fig. 1, n = 5 each), with only one knockout animal not showing clear tracking behavior.

2. All $\alpha_2\delta$ genes are expressed in mouse retina throughout development

We performed RT-PCR to establish which $\alpha_2\delta$ genes are expressed in the retina. Total RNA was isolated from adult C3H mouse retina (n = 3; results were the same with $\alpha_2\delta$-3 wild type retinas) as well as developing C3H retina (postnatal days 3, 6, 9, 12, 15/16; n = 3 animals each except n = 2 for P6 and P15/16), and RT-PCR was done using cDNA-specific primers for each gene. Negative controls were performed with water as template and never gave a visible band (not shown). All four $\alpha_2\delta$ isoforms were consistently detected at all developmental time points (Fig. 2). The double band for $\alpha_2\delta$-2 corresponds to different splice isoforms (verified by sequencing).

3. $\alpha_2\delta$-3 expression is widespread in the mouse retina, but strongest in horizontal cells

To determine the cell types expressing $\alpha_2\delta$-3 in mouse retina, we took advantage of the LacZ insert in knockout and heterozygous mice. After immunostaining against markers of retinal cell types in cryo slices, we performed X-gal staining for cells carrying the LacZ insert. Calbindin - a marker for horizontal cells in mouse retina - showed complete overlap with the X-gal stained cells in the distal inner nuclear layer (INL) (Fig. 3, n = 3 animals). All cells in the distal INL stained for calbindin were also X-gal-positive and vice versa. A very faint X-gal staining was observed in cells in the proximal INL (Fig. 3 A, arrows) and rarely in cells in the ganglion cell layer (Fig. 3 A, arrowhead). We consistently observed this large difference in X-gal staining intensity between horizontal cells and the labeling in proximal INL and ganglion cell layer (GCL). Strong expression of $\alpha_2\delta$-3 could also be localized to horizontal cells in wholemount immunohistochemical stainings for β-galactosidase and calbindin in developing mouse retina (postnatal day 11, not shown). We used immunohistochemical labeling of β-galactosidase (β-gal) in adult mouse retina for easier co-localization of β-gal expression with other cell type markers. Like in X-gal staining, cells in the distal INL were labeled by β-gal-antibody most intensively (Fig.4 A), while labeling intensity was weaker in proximal INL and GCL (Fig. 4 B+E). We did not find co-localization of the β-gal expression with choline acetyl-transferase (ChAT), a marker for starburst amacrine cells, in the INL (Fig. 4 B-D; n = 3 animals) or in the GCL (not shown). Co-localization of β-gal was found in the majority of Melanopsin-positive ganglion cells in the GCL (Fig. 4 E-G, arrowheads; n = 3 animals) as well as Melanopsin-positive cells in the INL (not shown). Many cells with clear β-gal labeling in the GCL were Melanopsin-negative.

4. The horizontal cell mosaic is unperturbed by the $\alpha_2\delta$-3 knockout

To assess possible disturbances of horizontal cell morphology and survival, we labeled horizontal cells (see methods) in wholemount retinas of adult wild type and knockout mice (n = 5 animals each). We covered dorsal and ventral areas between

Journal of Comparative Neurology

25% and 75% retinal eccentricity in our analysis (Fig. 5 A). Horizontal cell soma positions were determined semi-automatically with a custom Wolfram Mathematica script, and nearest neighbor distances were calculated (25932 cells in wild type and 30093 cells in knockout retinas from n = 5 animals each). Nearest neighbor distance was defined as the distance between the centroid position of a given cell body and the centroid position of the cell body closest to it (Fig. 5 B). Nearest neighbor distance was found to increase with retinal eccentricity in both the ventral and the dorsal half of the examined retinas. In the dorsal retina, distances were consistently smaller than in the ventral retina (Fig. 5 C). In dorsal retina, average distances were 22.11 ± 2.56 µm (wild type) and 22.03 ± 2.28 µm (knockout). In ventral retina, average distances were 24.29 ± 2.79 µm (wild type) and 24.14 ± 2.57 µm (knockout, means ± standard deviations). There was no statistically significant difference between wild type and knockout in neither dorsal nor ventral retina ($p = 0.947$, dorsal; $p = 0.900$, ventral; t-test), while within genotypes the difference between dorsal and ventral was significant ($p = 0.0095$, wild type; $p = 0.033$, knockout; paired t-test). The corresponding cell densities in dorsal retina were 1064 ± 209 cells/mm² for wild type and 1081 ± 234 cells/mm² for knockout retinas. Ventral retina densities were 906 ± 190 cells/mm² for wild type and 935 ± 185 cells/mm² for knockout retinas (means ± s.d.). We also looked at the horizontal cell densities as a function of retinal eccentricity but did not find any significant differences between genotypes (not shown). The regularity of the horizontal cell mosaic was assessed by looking at the variability of nearest neighbor distance, which is represented in the distribution of distances (Fig. 5 D). A larger variability of nearest neighbor distance would be reflected in a broader distribution, longer tails or larger skewness. We used the standard deviations from the mean distance of each analyzed image as a statistical measure for variability. We found no significant difference in nearest neighbor distance standard deviations between wild type and knockout in neither dorsal nor ventral retina ($p = 0.877$, dorsal; $p = 0.422$, ventral; t-test). In summary, we found no

effect of the knockout of the $\alpha_2\delta$-3 gene on horizontal cell number, distribution, and mosaic regularity.

5. Currents carried by voltage-gated calcium channels in isolated horizontal cell somata are unchanged

We performed patch-clamp recordings of currents carried by voltage-gated calcium channels (VGCC) from acutely isolated horizontal cell somata in the whole-cell mode to determine an influence of $\alpha_2\delta$-3 on calcium currents in these cells. Horizontal cell somata were identified by their characteristic morphology (Fig. 6A). Resting membrane potentials of the recorded horizontal cells were -13.06 ± 5.26 mV in wild type and -12.35 ± 4.14 mV in knockout, and membrane capacitances were 13.38 ± 3.45 pF in wild type and 12.67 ± 2.25 pF in knockout (means ± s.d.).

Currents were recorded using 10 mM barium as charge carrier while other conductances through voltage-gated sodium and potassium channels were blocked pharmacologically (see methods).

We confirmed that the currents were indeed carried by VGCC by blocking them with a solution where Ba^{2+} was equimolarly replaced by Co^{2+} (Fig. 6 A). Current-voltage relationships were tested with 50 ms steps from -70 mV to +60 mV (Fig. 6 B). No differences were found between genotypes in peak activation voltage (KO: -9.12 ± 7.69 mV; WT: -8.05 ± 4.99 mV; p = 0.950), half-maximal activation voltage (KO: -21.77 ± 8.19 mV; WT: -20.36 ± 5.97 mV; p = 0.948), slope factor (KO: 8.44 ± 4.03; WT: 9.29 ± 5.78; p = 0.951) or reversal potential (KO: 42.58 ± 7.68; WT: 46.63 ± 7.04; p = 0.222; all parameters derived from fits of IVs; Wilcoxon ranksum tests; n = 9 each). The small negative peak at -50 mV was consistently observed in many cells of both genotypes. Maximal currents were further investigated with a 50 ms step protocol to 0 mV (Fig. 6 C). Maximum current amplitudes were -27.29 ± 12.89 pA in wild type (n = 17) and -26.61 ± 8.99 pA in knockout

Journal of Comparative Neurology

(n = 14, Fig. 6 C), the corresponding current densities were -2.14 ± 1.18 pA/pF in wild type and -2.21 ± 0.85 pA/pF in kockout (means ± s.d., Fig. 6 D). There was no significant difference between genotypes in maximum current amplitudes (p = 0.739) nor current densities (p = 0.518, Wilcoxon ranksum tests). We looked for voltage-dependent inactivation by applying protocols with 400 ms long depolarizing steps from -80 mV to different target voltages (-60 mV to +20 mV), followed by a 50 ms test step to 0 mV (Fig. 6 E). We observed little to no voltage-dependent inactivation and no differences between genotypes (p > 0.05, Wilcoxon ranksum tests).

6. Electroretinography (ERG) shows normal outer retina function

To assess functionality of synaptic transmission in the outer retina, we performed ERG recordings *in vivo* (n = 4 knockout, n = 5 wild type animals).

Under dark-adapted (scotopic) conditions (Fig. 7 A), the initial part of the first negative deflection after a light flash (a-wave) is evoked mainly by the rod photoreceptors, whereas the following positive deflection (b-wave) reflects inner retinal activity, including depolarizing (ON) bipolar cells. Note that under scotopic conditions, from 10^{-2} cd*s/m² onward (arrow in Fig. 7 A), cones also get activated. Under light-adapted (photopic) conditions (Fig. 7 B) the b-wave relies on activity driven by the cone system, with the rod system being saturated by the background illumination. Scotopic single-flash ERG recorded from α_2δ-3 knockout mice did not show significantly different b-wave amplitudes or latencies from those in wild type animals (Fig. 7 C). There were also no differences in the b-wave amplitudes or latencies of photopic single-flash ERG responses of α_2δ-3 knockout and wild type mice (Fig. 7 D).

7. Multi-electrode array (MEA) recordings from retinal ganglion cells reveal several subtle phenotypes of the $\alpha_2\delta$-3 knockout retina

In order to investigate perturbances of retinal processing and possible effects downstream of bipolar cells, we isolated retinas from wild type and knockout mice and recorded the activity of retinal ganglion cells with micro-electrode arrays (MEAs). During the recording, light stimuli were presented that covered scotopic, mesopic, and photopic intensity levels (see methods). The same set of stimuli was presented twice at each ambient luminance level. A legend of the presented stimuli is shown at the bottom of Fig. 8 A.

Spontaneous activity

Spontaneous activity was determined as the spike rates during the first second of each stimulus, during which a uniform gray ('128') background was always presented. Note, that due to the short times between stimuli in our experiments (around 3 seconds), the spontaneous activity preceding a stimulus might still be influenced by the previous stimulus. Spontaneous spiking was highest during scotopic ambient luminance and decreased over the time course of the experiment in ON cells (Fig. 8 A, top) and less so in OFF cells (Fig. 8 A, bottom). ON cells had different spontaneous spike rates in wild type and knockout retina mostly during mesopic ambient luminance (Fig. 8 A, upper panel, statistical significance indicated on top with bars of different heights, Wilcoxon ranksum tests; KO: n = 71, WT: n = 97 cells). Interestingly, OFF ganglion cells in knockout retina had a markedly higher spontaneous spike rate than in wild type retina over most of the time course of the experiment (Fig. 8 A, lower panel; KO: n = 63, WT: n = 72 cells).

Gaussian white noise stimulus

One of our stimuli was a full-field Gaussian white noise ("flicker") stimulus. Each flicker stimulus consisted of episodes of high-contrast flicker interleaved with episodes of low-contrast flicker (Fig. 8 B). The stimulus was repeated four times at each ambient luminance level, for a total of 12 repetitions (marked 1 through 12 in

the legend at the bottom of Fig. 8 A). Spike rates of ganglion cells increased during high-contrast episodes, reflecting the stronger drive by the higher stimulus contrast. During low-contrast episodes, spike rates decreased and dropped to approximately the spontaneous rate before stimulus onset. In both ON and OFF cells, the spike rates during high-contrast seemed more similar between wild type and knockout, than spike rates during low-contrast.

For the analysis, we subtracted the spike rates during low-contrast episodes from the high-contrast spike rates (Fig. 8 C) for each stimulus repetition. We refer to this difference as the discrimination strength of a ganglion cell to the flicker stimulus. We only included cells in the analysis that had a clear spike-triggered average (STA) derived from the low-contrast episodes of at least one stimulus repetition per light level to ensure that the spikes are stimulus-driven (ON cells: KO n = 34; WT n = 38. OFF cells: KO n = 53; WT n = 49). In ON ganglion cells (Fig. 8 C left), we did not observe significant differences between wild type and knockout mice in discrimination strength during scotopic and photopic conditions ($0.413 < p < 0.992$). However, in mesopic conditions the discrimination strength was significantly lower in knockout compared to wild type ($p < 0.01$ for first, $p < 0.001$ for other three repetitions). In OFF ganglion cells (Fig. 8 C right), we observed significantly reduced discrimination strength in knockout during scotopic ($p = 0.012$, $p = 0.005$, $p = 0.037$, $p = 0.039$) and mesopic conditions ($p < 0.001$, all repetitions), but not in photopic conditions ($0.053 < p < 0.487$; Wilcoxon ranksum tests).

Drifting sinusoidal grating stimulus

Looking carefully at the spontaneous activity plots, we observed peculiar jumps in spontaneous activity in ON ganglion cells during drifting sinusoidal grating stimuli in scotopic luminance (Fig. 8 A, top, before stimulus number 100 and after stimulus 150). To investigate this further, we grouped ganglion cells based on their spontaneous activity following sinusoidal grating stimuli in scotopic luminance (Fig. 9 A). We clustered the ganglion cells by a k-means algorithm (Matlab) to avoid any

subjective selection bias. Most clusters were approximately equally populated by wild type and knockout cells. However, we found two clusters that were populated mostly by either wild type cells (cluster 4) or by knockout cells (cluster 8), and both exhibited a clear jump in spontaneous activity in scotopic luminance. These two clusters robustly emerged when running the k-means algorithm with a value of k (= number of clusters) between 7 and 12. Fig. 9 A shows the distribution for k = 8 clusters. Four clusters consisted exclusively of ON cells (1, 4, 5, 8), while the other four clusters were mixed. While both clusters 4 and 8 exhibited a jump in spontaneous activity, this jump happened after presentation of gratings of different spatial properties. This is evident in the spontaneous activities of the individual cells of clusters 4 and 8 during scotopic luminance shown in Fig. 9 B. Spike rates decreased after the presentation of gratings with low spatial periods, sometimes exhibiting a marked drop. Common to all cells in clusters 4 and 8 was a sharp increase in spontaneous spike rate: in cluster 8, this increase happened after presentation of the first 2000 µm grating, while cluster 4 shows a similar jump in spontaneous activity in between the 500 µm and 1000 µm gratings. In both clusters the increased spontaneous activity was maintained between presentations of the gratings with large spatial periods and only occurred in scotopic luminance. A natural question is, whether the change in spontaneous activity after the presentation of certain gratings simply reflects a persisting elevated activity of the cells during those gratings, i.e. if our observation can be explained by a lingering effect of responses to the stimulus itself. Fig. 9 C shows example responses after aligning (phase shifting) these responses by cross-correlation with the sinusoidal grating stimulus (phase-shifts in responses of different ganglion cells stem from different receptive field positions relative to the grating stimulus). Of cluster 4, only wild type cells were considered for further analysis. We averaged spike rates of cells within each cluster and determined the following response parameters with or without subtracting the spontaneous spike rate (baseline): minimal spike rate, maximal spike rate, mean spike rate, median spike

rate and response amplitude (max-min). We compared the parameters of gratings of the same temporal frequency, but with different spatial periods. Fig. 9 D plots significant changes in a heatmap (Wilcoxon ranksum test). For example, the top left entry indicates the level of significance when comparing the presentations of 0.25 Hz gratings with 100 versus 200 µm spatial periods. Of all parameters examined, only the baseline-subtracted mean spike rate yielded significant differences between gratings of different spatial properties in the range with a change in the spontaneous spike rate (Fig. 9 D, left; spatial period range marked with yellow rectangle). In all other parameters, only the strong changes between 200 µm and 500 µm gratings yielded systematically significant differences, shown here for the parameter "amplitude" of clusters 4 and 8 (Fig. 9 D, right). The situation was similar for all eight clusters (not shown). In summary, the change of spontaneous activity after the presentation of certain gratings is hardly reflected by changed response properties to the gratings themselves.

Full-field step stimulus

We next analyzed the responses to a full-field contrast step stimulus. The averaged responses were very similar in OFF ganglion cells from wild type and knockout at all three luminance levels (Fig. 10 A). Only subtle differences between genotypes in the positive contrast steps (going 'brighter') at scotopic and mesopic luminance could be observed. In OFF ganglion cells of the knockout, response peaks were partly shifted in time (arrows) and response amplitudes were increased (arrowheads). Note that classical ON-OFF cells would almost unequivocally fall into the OFF category in our classification by their STA polarity (Tikidji-Hamburyan et al., 2014).

ON cells of wild type and knockout also responded very similarly in mesopic and photopic luminance levels (Fig. 10 B). However, in scotopic luminance, upon return to the grey background after the white step, we observed different delays in response peaks. The averaged responses revealed that there are several subpopulations with different properties, as it appears from the peaks of the standard deviations of the

responses (inset). To investigate this further, subpopulations of cells were defined by manually classifying response peaks in five time windows after the offset of the white flash: 0.2 – 0.5 s, 0.5 – 1.0 s, 1.0 – 1.3 s, 1.3 – 1.5 s and 1.5 – 1.75 s. This yielded a differential distribution pattern in wild type and knockout (bar graph in Fig. 10 B). 75% of ON cells in knockout had such responses versus 45% of the wild type cells. Strikingly, almost all wild type cells with a response fell into subpopulation '2' (response peak between 0.5 and 1 s). Subpopulation '3' (1 to 1.3 s) was almost exclusively found in knockout retinas. Fig. 10 C and E illustrates the marked timing difference in these responses with two representative cells belonging to subpopulations '2' and '3' (spike raster on top, spike rate at the bottom). Fig. 10 D and F show the population averages of these two populations.

Discussion

We found especially strong expression of the voltage-gated calcium channel (VGCC) subunit $\alpha_2\delta$-3 in horizontal cells in the mouse retina. Yet, a knockout of $\alpha_2\delta$-3 did not lead to changes of the horizontal cell mosaic or of voltage-gated calcium channel currents within horizontal cell somata. Outer retinal function measured by electroretinograms was normal, as was the optokinetic reflex behavior in $\alpha_2\delta$-3 knockout animals. In ganglion cells however, we could see a number of changes in response properties to different kinds of visual stimuli, which were mostly restricted to scotopic or mesopic ambient luminance levels of our stimulation paradigm.

$\alpha_2\delta$ mRNA expression

Gene or protein expression of $\alpha_2\delta$-1 (Eroglu et al., 2009; Huang et al., 2013), $\alpha_2\delta$-3 (Nakajima et al., 2009; Pérez de Sevilla Müller et al., 2015) and $\alpha_2\delta$-4 (Wycisk et al., 2006; Mercer et al., 2011; de Sevilla Muller et al., 2013; Thoreson et al., 2013) have been reported in vertebrate retina. To the best of our knowledge, expression of $\alpha_2\delta$-2

in adult retina, or expression of any of the four $\alpha_2\delta$ subunits during mouse retinal development have not been demonstrated. We found expression of all $\alpha_2\delta$ genes in adult as well as in developing mouse retina, from at least postnatal day 3 onwards (Fig. 2). This raises the possibility for a function of the $\alpha_2\delta$ subunits in synaptogenesis (Kurshan et al., 2009) in mouse retina during development.

$\alpha_2\delta$-3 localization

It has previously been reported that $\alpha_2\delta$-3 is expressed in ON bipolar cells (Nakajima et al., 2009), photoreceptors, bipolar, amacrine and ganglion cells but not horizontal cells (Pérez de Sevilla Müller et al., 2015). Yet, we found very prominent LacZ staining in horizontal cells, driven by the endogenous $\alpha_2\delta$-3 promotor (Fig. 3). The extraordinary strength of the horizontal cell labeling by the LacZ reporter we observed is completely in line with the $\alpha_2\delta$-3 gene expression values found in the microarray data of Siegert et al. (2012) (the expression profile can be found online by selecting "*Cacna2d3*" at http://www.fmi.ch/roska.data/index.php). Therefore we believe that the clear antibody labeling of $\alpha_2\delta$-3 protein in the outer plexiform layer that has been reported by Pérez de Sevilla Müller et al. (2015) stems at least in large part from horizontal cells. The absence of this labeling from cone pedicles would thus suggest localization of $\alpha_2\delta$-3 only in horizontal cell processes contacting rods. The data of Siegert et al. (2012) also supports our finding of LacZ reporter labelling in melanopsin ganglion cells (Fig. 4). Interestingly, their microarray data shows expression of $\alpha_2\delta$-3 also in A-II and maybe other gylcinergic amacrine cells, which was also reported by Pérez de Sevilla Müller et al. (2015). This would be consistent with our observation of LacZ labeling in the proximal INL (Fig. 3+4).

Retina morphology and the horizontal cell mosaic

The mouse retina only contains one type of horizontal cell of the axon-bearing b-type (Peichl and Gonzalez-Soriano, 1994) which form a regular mosaic (Wassle and

Riemann, 1978). Mosaic formation is at least in part controlled by repulsive homotypic interactions between neighboring horizontal cells (Poche et al., 2008; Huckfeldt et al., 2009). It has been shown that $\alpha_2\delta$ subunits have a function in synaptogenesis and synaptic stabilization (Eroglu et al., 2009). The unperturbed regularity of the mosaic and spacing of horizontal cells (Fig. 5) can be interpreted as an indication of normal outer retinal development and suggests no impact on horizontal cell survival by the $\alpha_2\delta$-3 knockout. However, the connectivity and ultra-structure of the triad synapses should be investigated more closely to determine potential effects on synaptogenesis (Reese et al., 2005) and horizontal cell connectivity in detail.

Voltage-gated calcium channel currents in horizontal cell somata

The $\alpha_2\delta$ subunits are thought to enhance trafficking of VGCC to the membrane. Yet we could not detect a difference in maximum current amplitude or density in horizontal cell somata of $\alpha_2\delta$-3 knockout nor in the parameters of the current-voltage relationships or the voltage-dependent inactivation (Fig. 6). It is unknown whether $\alpha_2\delta$-3 interacts with all VGCC α_1 subunits of horizontal cells, namely L-, P/Q- and N-Type (Schubert et al., 2006; Liu et al., 2013). It is also not known if there is more than one $\alpha_2\delta$ isoform expressed in horizontal cells. Differential regulation of either α_1 or $\alpha_2\delta$ subunits could compensate for the knockout of $\alpha_2\delta$-3, rescuing horizontal cells from having a pronounced change in voltage-gated calcium channel properties. The other intriguing possibility is the putative localization of $\alpha_2\delta$-3 on the rod-contacting axonal processes. Any changes on calcium currents in the axonal compartment would likely not show up in our somatic recordings.

Outer retina function and visual reflex behavior

Horizontal cells form reciprocal synapses with photoreceptors and this feedback is thought to influence spatial (Thoreson and Mangel, 2012; Szikra et al., 2014) as well

Journal of Comparative Neurology

as temporal processing properties of the retina (Pandarinath et al., 2010). If the $\alpha_2\delta$-3 knockout had an impact on feedback, it could affect the strength or kinetics of synaptic transmission from photoreceptors also to bipolar cells, and be reflected in the properties of bipolar cell responses. Our electroretinographic (ERG) recordings did not show an effect of the $\alpha_2\delta$-3 knockout on latencies or amplitudes of the b-wave (indicative of depolarizing bipolar cell activation), in neither scotopic nor photopic conditions (Fig. 7). These results indicate that $\alpha_2\delta$-3 subunits are not essential for photoreceptor responses or the synaptic signal transmission to depolarizing bipolar cells.

As a measure for overall retinal functionality we tested the $\alpha_2\delta$-3 knockout animals for their optokinetic reflex behavior. Tracking behavior in our virtual optokinetic drum experiments was found in most knockout animals (Fig. 1), underlining general retinal functionality and suggesting meaningful output of $\alpha_2\delta$-3 knockout retina in this simple visual reflex paradigm.

Retinal processing

Our micro-electrode array (MEA) recordings of retinal ganglion cells revealed several subtle differences between wild type and $\alpha_2\delta$-3 knockout retina. Some of the effects appear rather general, such as the average spontaneous spike rate which was elevated throughout the experiment (covering all luminance levels) in OFF ganglion cells, but not in ON cells (Fig. 8 A). The compression of discrimination strength between high- and low-contrast flicker stimuli (Fig. 8 B+C) was restricted to scotopic (ON cells) or scotopic and mesopic luminance levels (OFF cells). This compression seemed to be caused mainly by an elevation of spike rates to the low contrast-condition, while the spike rates during high contrast were largely similar. The restriction of effects to lower luminance levels was a feature we observed consistently.

While OFF cells showed only minor differences in our other stimuli (Fig. 10 A), there were subsets of ON cells with changed response profiles which we found only in $\alpha_2\delta$-3 knockout retinas. We saw a jump in spontaneous spike rates during drifting grating stimuli in both wild type and knockout ON cells, reflecting changed activity after grating stimuli of certain spatial properties. However, these jumps occurred after gratings of different spatial properties in wild type and knockout ganglion cells. It is tempting to speculate that the two clusters of cells with an abrupt change in spontaneous spike rates (Fig. 9 B) reflect a change in spatial processing of the involved circuitry. We do not know, however, what brought about this change in spontaneous spike rates, as responses to the preceding grating stimuli themselves did not show any abrupt changes in both clusters. The only difference we found (a change in baseline-adjusted mean spike rates, Fig. 9 D) is likely due to the shift in the spontaneous spike rate itself, as this determines the baseline value and did not show in the non-baselined data (not shown). We didn't observe any systematic differences depending on the temporal properties of the grating stimuli we used.

The responses within different time windows of our full-field step stimuli (Fig. 10 B), on the other hand, can be seen as a change of temporal properties. We do not know the physiological significance of these responses, as they only appear on the return to the background mean luminance and most have a very long temporal scale (> 500 ms). We refer to this type of responses as delayed responses. In general, we found delayed responses to be much more abundant in ganglion cells of knockout retina. This could indicate an emergence of this kind of responses in ganglion cells, rather than a shift in the delay time in the same ganglion cell types. It could also indicate a different distribution of the abundance of single ganglion cell types in the knockout, as we cannot rule out sampling artifacts of the MEA technique, i.e. we likely record from different numbers of single ganglion cell types in each recording.

What could cause the differences in retinal ganglion cell responses which we described? Due to the widespread expression of $\alpha_2\delta$-3 in various cell types,

interpretation of the found phenotypes has to be undertaken with care. As a subunit of voltage-gated calcium channels, the $\alpha_2\delta$-3 knockout is most likely to cause a loss-of-function kind of phenotype, affecting synaptic release in the respective cells. The increased spontaneous spike rate in OFF ganglion cells might be caused by reduced inhibitory transmission somewhere in the circuitry. It is unlikely that the compression of discrimination strength in our Gaussian white noise stimulus was caused by the $\alpha_2\delta$-3 knockout in horizontal cells, since horizontal cells do not play a role in contrast gain control (Beaudoin et al., 2007) or contrast adaptation (Baccus and Meister, 2002). The shift in spontaneous spike rate during drifting sinusoidal gratings of certain spatial properties could be indicative of a change in receptive field size in one or several cell types. Finally, the abundance of delayed responses and their delay timings in our full-field step stimuli might be caused by a prolonged inhibitory input or by a change in the interaction between the ON and OFF pathways. It is also possible that some of the changes are caused by ganglion cell-intrinsic mechanisms, since $\alpha_2\delta$-3 expression in the ganglion cell layer seemed low but was widespread. Interestingly, the majority of changes we observed were restricted to brightness regimes with rod activity (scotopic and mesopic), raising the possibility of a role of $\alpha_2\delta$-3 in retinal circuitries carrying rod signals.

Horizontal cell function of $\alpha_2\delta$-3 and other possible mechanisms

It remains open how $\alpha_2\delta$-3 acts within VGCC complexes in horizontal cells and if it contributes to feedback from horizontal cells to photoreceptors (Thoreson and Mangel, 2012). Horizontal cells have two functionally separated cellular compartments that were thought to be electrically isolated from each other (Nelson et al., 1975): somato-dendritic processes contact cone pedicles, axonal arborizations contact rod spherules (Kolb, 1970, 1974). Signals can, however, spread from the dendritic compartment down this axon and impact the rod circuitry (Trumpler et al., 2008), creating a form of surround inhibition by sign-inverting activation of rod

synapses (Szikra et al., 2014). Localization of $\alpha_2\delta$-3 within the axonal compartment of horizontal cells could at least in part explain the restriction of the phenotypes we found in our MEA recordings to scotopic and mesopic regimes. Horizontal cells might thus also influence the balance between rod and cone activity by utilizing different molecular machinery for feedback in each compartment, involving $\alpha_2\delta$-3 (rods) or not involving $\alpha_2\delta$-3 (cones).

Considering a putative disturbance of the rod circuitry, A-II amacrine cells would also be a good candidate for some of the changes we observed in non-photopic regimes. Indeed, glycinergic amacrine cells were reported to express $\alpha_2\delta$-3 (Siegert et al., 2012; Pérez de Sevilla Müller et al., 2015).

A cell type-specific knockout of $\alpha_2\delta$-3 in horizontal cells or A-II amacrine cells would help to elucidate the specific effects of this isoform in certain aspects of retinal processing. Especially the possible role of $\alpha_2\delta$-3 in horizontal cell feedback to rods versus feedback to cones could be interesting to investigate.

Acknowledgements: The authors thank Sebastian Ströh and Karin Dedek for the introduction to isolated horizontal cell patch-clamp techniques, Nadine Ortner for support on fitting IV curves and Jutta Engel and Timm Schubert for fruitful discussions.

Conflict of Interest: None

Role of authors

Designed study: HS, AP, MS, TAM. Performed Experiments: HS, VS, BB, MGG. Analyzed data: HS, VS, BB, ATH, MGG. Wrote paper: HS, VS, BB, TAM.

Literature cited

Abdeljalil J, Hamid M, Abdel-Mouttalib O, Stephane R, Raymond R, Johan A, Jose S, Pierre C, Serge P. 2005. The optomotor response: a robust first-line visual screening method for mice. Vis Res 45:1439–1446.

Airaksinen MS, Eilers J, Garaschuk O, Thoenen H, Konnerth A, Meyer M. 1997. Ataxia and altered dendritic calcium signaling in mice carrying a targeted null mutation of the calbindin D28k gene. Proc Natl Acad Sci U S A 94:1488–93.

Baccus SA, Meister M. 2002. Fast and slow contrast adaptation in retinal circuitry. Neuron 36:909–19.

Ball SL, Powers PA, Shin HS, Morgans CW, Peachey NS, Gregg RG. 2002. Role of the beta(2) subunit of voltage-dependent calcium channels in the retinal outer plexiform layer. Invest Ophthalmol Vis Sci 43:1595–1603.

Barry PH. 1994. JPCalc, a software package for calculating liquid junction potential corrections in patch-clamp, intracellular, epithelial and bilayer measurements and for correcting junction potential measurements. J Neurosci Methods 51:107–16.

Beaudoin DL, Borghuis BG, Demb JB. 2007. Cellular basis for contrast gain control over the receptive field center of mammalian retinal ganglion cells. J Neurosci 27:2636–45.

Benkner B, Mutter M, Ecke G, Münch T a. 2013. Characterizing visual performance in mice: an objective and automated system based on the optokinetic reflex. Behav Neurosci 127:788–96.

Catterall W a, Perez-Reyes E, Snutch TP, Striessnig J. 2005. International Union of Pharmacology. XLVIII. Nomenclature and structure-function relationships of voltage-gated calcium channels. Pharmacol Rev 57:411–425.

Celio MR, Baier W, Schärer L, Gregersen HJ, de Viragh PA, Norman AW. 1990. Monoclonal antibodies directed against the calcium binding protein Calbindin D-28k. Cell Calcium 11:599–602.

Chichilnisky EJ. 2001. A simple white noise analysis of neuronal light responses. Network 12:199–213.

Curtis BM, Catterall WA. 1984. Purification of the calcium antagonist receptor of the voltage-sensitive calcium channel from skeletal muscle transverse tubules. Biochemistry 23:2113–2118.

Davies A, Hendrich J, Van Minh AT, Wratten J, Douglas L, Dolphin AC. 2007. Functional biology of the alpha(2)delta subunits of voltage-gated calcium channels. Trends Pharmacol Sci 28:220–228.

Davies A, Kadurin I, Alvarez-Laviada A, Douglas L, Nieto-Rostro M, Bauer CS, Pratt WS, Dolphin AC. 2010. The alpha2delta subunits of voltage-gated calcium channels form GPI-anchored proteins, a posttranslational modification essential for function. Proc Natl Acad Sci U S A 107:1654–1659.

Dolphin AC. 2012. Calcium channel auxiliary alpha2delta and beta subunits: trafficking and one step beyond. Nat Rev Neurosci 13:542–555.

Ellis SB, Williams ME, Ways NR, Brenner R, Sharp AH, Leung AT, Campbell KP, McKenna E, Koch WJ, Hui A, et al. 1988. Sequence and expression of mRNAs encoding the alpha 1 and alpha 2 subunits of a DHP-sensitive calcium channel. Science (80-) 241:1661–1664.

Eroglu C, Allen NJ, Susman MW, O'Rourke NA, Park CY, Ozkan E, Chakraborty C, Mulinyawe SB, Annis DS, Huberman AD, Green EM, Lawler J, Dolmetsch R, Garcia KC, Smith SJ, Luo ZD, Rosenthal A, Mosher DF, Barres BA. 2009. Gabapentin receptor alpha2delta-1 is a neuronal thrombospondin receptor responsible for excitatory CNS synaptogenesis. Cell 139:380–392.

Göz D, Studholme K, Lappi DA, Rollag MD, Provencio I, Morin LP. 2008. Targeted destruction of photosensitive retinal ganglion cells with a saporin conjugate alters the effects of light on mouse circadian rhythms. PLoS One 3:e3153.

Guo C, Stella Jr. SL, Hirano AA, Brecha NC. 2009. Plasmalemmal and vesicular gamma-aminobutyric acid transporter expression in the developing mouse retina. J Comp Neurol 512:6–26.

Gurnett CA, Felix R, Campbell KP. 1997. Extracellular interaction of the voltage-dependent Ca2+ channel alpha2delta and alpha1 subunits. J Biol Chem 272:18508–18512.

Haverkamp S, Specht D, Majumdar S, Zaidi NF, Brandstätter JH, Wasco W, Wässle H, Tom Dieck S. 2008. Type 4 OFF cone bipolar cells of the mouse retina

express calsenilin and contact cones as well as rods. J Comp Neurol 507:1087–101.

Haverkamp S, Wässle H. 2000. Immunocytochemical analysis of the mouse retina. J Comp Neurol 23:1–23.

Huang J, Zhou L, Wang H, Luo J, Zeng L, Xiong K, Chen D. 2013. Distribution of thrombospondins and their neuronal receptor alpha2delta1 in the rat retina. Exp Eye Res 111C:36–49.

Huckfeldt RM, Schubert T, Morgan JL, Godinho L, Di Cristo G, Huang ZJ, Wong RO. 2009. Transient neurites of retinal horizontal cells exhibit columnar tiling via homotypic interactions. Nat Neurosci 12:35–43.

Janssen-Bienhold U, Trumpler J, Hilgen G, Schultz K, Muller LP, Sonntag S, Dedek K, Dirks P, Willecke K, Weiler R. 2009. Connexin57 is expressed in dendro-dendritic and axo-axonal gap junctions of mouse horizontal cells and its distribution is modulated by light. J Comp Neurol 513:363–374.

Klugbauer N, Lacinova L, Marais E, Hobom M, Hofmann F. 1999. Molecular diversity of the calcium channel alpha2delta subunit. J Neurosci 19:684–691.

Kolb H. 1970. Organization of the outer plexiform layer of the primate retina: electron microscopy of Golgi-impregnated cells. Philos Trans R Soc Lond B Biol Sci 258:261–83.

Kolb H. 1974. The connections between horizontal cells and photoreceptors in the retina of the cat: electron microscopy of Golgi preparations. J Comp Neurol 155:1–14.

Kurshan PT, Oztan A, Schwarz TL. 2009. Presynaptic alpha2delta-3 is required for synaptic morphogenesis independent of its Ca2+-channel functions. Nat Neurosci 12:1415–1423.

Lagali PS, Balya D, Awatramani GB, Munch TA, Kim DS, Busskamp V, Cepko CL, Roska B. 2008. Light-activated channels targeted to ON bipolar cells restore visual function in retinal degeneration. Nat Neurosci 11:667–675.

Leung AT, Imagawa T, Campbell KP. 1987. Structural characterization of the 1,4-dihydropyridine receptor of the voltage-dependent Ca2+ channel from rabbit skeletal muscle. Evidence for two distinct high molecular weight subunits. J Biol Chem 262:7943–7946.

Liu X, Hirano AA, Sun X, Brecha NC, Barnes S. 2013. Calcium channels in rat horizontal cells regulate feedback inhibition of photoreceptors through an unconventional GABA- and pH-sensitive mechanism. J Physiol 591:3309–24.

Mandadi S, Hong P, Tran MA, Bráz JM, Colarusso P, Basbaum AI, Whelan PJ. 2013. Identification of multisegmental nociceptive afferents that modulate locomotor circuits in the neonatal mouse spinal cord. J Comp Neurol 521:2870–87.

Mercer AJ, Chen M, Thoreson WB. 2011. Lateral mobility of presynaptic L-type calcium channels at photoreceptor ribbon synapses. J Neurosci 31:4397–406.

Mitchiner JC, Pinto LH, Vanable Jr. JW. 1976. Visually evoked eye movements in the mouse (Mus musculus). Vis Res 16:1169–1171.

Morgans CW. 2001. Localization of the alpha(1F) calcium channel subunit in the rat retina. Invest Ophthalmol Vis Sci 42:2414–2418.

Munch TA, da Silveira RA, Siegert S, Viney TJ, Awatramani GB, Roska B. 2009. Approach sensitivity in the retina processed by a multifunctional neural circuit. Nat Neurosci 12:1308–1316.

Nakajima Y, Moriyama M, Hattori M, Minato N, Nakanishi S. 2009. Isolation of ON bipolar cell genes via hrGFP-coupled cell enrichment using the mGluR6 promoter. J Biochem 145:811–818.

Neely GG, Hess A, Costigan M, Keene AC, Goulas S, Langeslag M, Griffin RS, Belfer I, Dai F, Smith SB, Diatchenko L, Gupta V, Xia CP, Amann S, Kreitz S, Heindl-Erdmann C, Wolz S, Ly C V, Arora S, Sarangi R, Dan D, Novatchkova M, Rosenzweig M, Gibson DG, Truong D, Schramek D, Zoranovic T, Cronin SJ, Angjeli B, Brune K, Dietzl G, Maixner W, Meixner A, Thomas W, Pospisilik JA, Alenius M, Kress M, Subramaniam S, Garrity PA, Bellen HJ, Woolf CJ, Penninger JM. 2010. A genome-wide Drosophila screen for heat nociception identifies alpha2delta3 as an evolutionarily conserved pain gene. Cell 143:628–638.

Nelson R, von Litzow A, Kolb H, Gouras P. 1975. Horizontal cells in cat retina with independent dendritic systems. Science 189:137–9.

Nikonov SS, Daniele LL, Zhu X, Craft CM, Swaroop A, Pugh Jr. EN. 2005. Photoreceptors of Nrl -/- mice coexpress functional S- and M-cone opsins having distinct inactivation mechanisms. J Gen Physiol 125:287–304.

Ortner NJ, Bock G, Vandael DHF, Mauersberger R, Draheim HJ, Gust R, Carbone E, Tuluc P, Striessnig J. 2014. Pyrimidine-2,4,6-triones are a new class of voltage-gated L-type Ca2+ channel activators. Nat Commun 5:3897.

Pandarinath C, Bomash I, Victor JD, Prusky GT, Tschetter WW, Nirenberg S. 2010. A novel mechanism for switching a neural system from one state to another. Front Comput Neurosci 4:2.

Patton C, Thompson S, Epel D. 2004. Some precautions in using chelators to buffer metals in biological solutions. Cell Calcium 35:427–431.

Peichl L, Gonzalez-Soriano J. 1994. Morphological types of horizontal cell in rodent retinae: a comparison of rat, mouse, gerbil, and guinea pig. Vis Neurosci 11:501–517.

Pérez de Sevilla Müller L, Sargoy A, Fernández-Sánchez L, Rodriguez A, Liu J, Cuenca N, Brecha N. 2015. Expression and cellular localization of the voltage-gated calcium channel α2 δ3 in the rodent retina. J Comp Neurol 523:1443–60.

Phillips MJ, Otteson DC, Sherry DM. 2010. Progression of neuronal and synaptic remodeling in the rd10 mouse model of retinitis pigmentosa. J Comp Neurol 518:2071–89.

Pirone A, Kurt S, Zuccotti A, Rüttiger L, Pilz P, Brown DH, Franz C, Schweizer M, Rust MB, Rübsamen R, Friauf E, Knipper M, Engel J. 2014. α2δ3 is essential for normal structure and function of auditory nerve synapses and is a novel candidate for auditory processing disorders. J Neurosci 34:434–45.

Poche RA, Raven MA, Kwan KM, Furuta Y, Behringer RR, Reese BE. 2008. Somal positioning and dendritic growth of horizontal cells are regulated by interactions with homotypic neighbors. Eur J Neurosci 27:1607–1614.

Preibisch S, Saalfeld S, Tomancak P. 2009. Globally optimal stitching of tiled 3D microscopic image acquisitions. Bioinformatics 25:1463–1465.

Qin N, Yagel S, Momplaisir ML, Codd EE, D'Andrea MR. 2002. Molecular cloning and characterization of the human voltage-gated calcium channel alpha(2)delta-4 subunit. Mol Pharmacol 62:485–496.

Reese BE, Raven MA, Stagg SB. 2005. Afferents and homotypic neighbors regulate horizontal cell morphology, connectivity, and retinal coverage. J Neurosci 25:2167–2175.

Reinhard K, Tikidji-Hamburyan A, Seitter H, Idrees S, Mutter M, Benkner B, Münch TA. 2014. Step-by-step instructions for retina recordings with perforated multi electrode arrays. PLoS One 9:e106148.

Robinson P, Etheridge S, Song L, Shah R, Fitzgerald EM, Jones OT. 2011. Targeting of voltage-gated calcium channel alpha2delta-1 subunit to lipid rafts is independent from a GPI-anchoring motif. PLoS One 6:e19802.

Sanyal S, Bal AK. 1973. Comparative light and electron microscopic study of retinal histogenesis in normal and rd mutant mice. Z Anat Entwicklungsgesch 142:219–238.

Schindelin J, Arganda-Carreras I, Frise E, Kaynig V, Longair M, Pietzsch T, Preibisch S, Rueden C, Saalfeld S, Schmid B, Tinevez JY, White DJ, Hartenstein V, Eliceiri K, Tomancak P, Cardona A. 2012. Fiji: an open-source platform for biological-image analysis. Nat Methods 9:676–682.

Schubert T, Weiler R, Feigenspan A. 2006. Intracellular calcium is regulated by different pathways in horizontal cells of the mouse retina. J Neurophysiol 96:1278–1292.

Scott MM, Lachey JL, Sternson SM, Lee CE, Elias CF, Friedman JM, Elmquist JK. 2009. Leptin targets in the mouse brain. J Comp Neurol 514:518–32.

De Sevilla Muller LP, Liu J, Solomon A, Rodriguez A, Brecha N. 2013. Expression of voltage-gated calcium channel alpha(2) delta(4) subunits in the mouse and rat retina. J Comp Neurol.

Shelley J, Dedek K, Schubert T, Feigenspan A, Schultz K, Hombach S, Willecke K, Weiler R. 2006. Horizontal cell receptive fields are reduced in connexin57-deficient mice. Eur J Neurosci 23:3176–3186.

Siegert S, Cabuy E, Scherf BG, Kohler H, Panda S, Le Y-Z, Fehling HJ, Gaidatzis D, Stadler MB, Roska B. 2012. Transcriptional code and disease map for adult retinal cell types. Nat Neurosci 15:487–495.

Szikra T, Trenholm S, Drinnenberg A, Jüttner J, Raics Z, Farrow K, Biel M, Awatramani G, Clark DA, Sahel J-A, da Silveira RA, Roska B. 2014. Rods in daylight act as relay cells for cone-driven horizontal cell-mediated surround inhibition. Nat Neurosci 17:1728–35.

Tanimoto N, Muehlfriedel RL, Fischer MD, Fahl E, Humphries P, Biel M, Seeliger MW. 2009. Vision tests in the mouse: Functional phenotyping with electroretinography. Front Biosci 14:2730–2737.

Thoreson WB, Mangel SC. 2012. Lateral interactions in the outer retina. Prog Retin Eye Res 31:407–441.

Thoreson WB, Mercer AJ, Cork KM, Szalewski RJ. 2013. Lateral mobility of L-type calcium channels in synaptic terminals of retinal bipolar cells. Mol Vis 19:16–24.

Tikidji-Hamburyan A, Reinhard K, Seitter H, Hovhannisyan A, Procyk CA, Allen AE, Schenk M, Lucas RJ, Münch TA. 2014. Retinal output changes qualitatively with every change in ambient illuminance. Nat Neurosci 18:66–74.

Trumpler J, Dedek K, Schubert T, de Sevilla Muller LP, Seeliger M, Humphries P, Biel M, Weiler R. 2008. Rod and cone contributions to horizontal cell light responses in the mouse retina. J Neurosci 28:6818–6825.

Umino Y, Solessio E, Barlow RB. 2008. Speed, spatial, and temporal tuning of rod and cone vision in mouse. J Neurosci 28:189–198.

Wassle H, Riemann HJ. 1978. The mosaic of nerve cells in the mammalian retina. Proc R Soc L B Biol Sci 200:441–461.

Wycisk KA, Budde B, Feil S, Skosyrski S, Buzzi F, Neidhardt J, Glaus E, Nurnberg P, Ruether K, Berger W. 2006. Structural and functional abnormalities of retinal ribbon synapses due to Cacna2d4 mutation. Invest Ophthalmol Vis Sci 47:3523–3530.

Yip V, Carter JG, Pusateri ME, McDougal DB, Lowry OH. 1991. Distribution in brain and retina of four enzymes of acetyl CoA synthesis in relation to choline acetyl transferase and acetylcholine esterase. Neurochem Res 16:629–35.

Yonehara K, Balint K, Noda M, Nagel G, Bamberg E, Roska B. 2011. Spatially asymmetric reorganization of inhibition establishes a motion-sensitive circuit. Nature 469:407–10.

Resources cited

B6.129P2-*Cacna2d3*^{tm1Dgen}/J mice (The Jackson Laboratory, RRID: IMSR_JAX:005780)

mouse monoclonal anti-calbindin antibody (Swant Cat# 300 RRID:AB_10000347)

rabbit polyclonal anti-calbindin antibody (Swant Cat# CB 38 RRID:AB_10000340)

chicken polyclonal anti-neurofilament H antibody (Abcam Cat# ab4680, RRID:AB_304560)

goat polyclonal anti-choline acetyltransferase antibody (Millipore Cat# AB144P, RRID:AB_2079751)

rabbit polyclonal anti-melanopsin antibody (Advanced Targeting Systems Cat# AB-N39, RRID:AB_1608076)

chicken polyclonal anti-β-galactosidase antibody (Abcam Cat# ab9361, RRID:AB_307210)

Fiji (RRID:SciRes_000137)

PatchMaster (v2x69, RRID:SciRes_000168, HEKA)

Figure legends

Figure 1: Optokinetic reflex test. (**A**) The "optokinetic drum" virtual arena. Rotating stripe patterns were presented while the mouse was observed from above by a camera. The recorded position of the mouse head was used to adjust stimulus parameters in real time (**B**), circle = virtual drum, square = actual stripe pattern on the screens. (**C**) all 5 wild type and 4 out of 5 knockout animals showed clear tracking behavior, indicating an intact optokinetic reflex in $\alpha_2\delta$-3 knockout animals.

Figure 2: $\alpha_2\delta$ mRNA expression in mouse retina. RT-PCR on total RNA isolated from mouse retina at postnatal day 3 (P3) up to adult. All four $\alpha_2\delta$ transcripts were found throughout the developmental time points tested and in adult mouse retina (n = 3 each, n = 2 for P6 and P15/P16). Amplicon sizes: $\alpha_2\delta$-1 = 587 bp, $\alpha_2\delta$-2 = 425 bp, $\alpha_2\delta$-3 = 356 bp, $\alpha_2\delta$-4 = 480 bp. L = ladder.

Journal of Comparative Neurology

Figure 3: LacZ expression localization in adult mouse retina. Horizontal cells were immunohistochemically stained with antibodies against calbindin in cryoslices of knockout/heterozygous and wild type retina and LacZ reporter expression was revealed with X-gal. **(A)** The strongly LacZ-positive cells showed complete overlap with the calbindin-positive cells in the distal inner nuclear layer (INL). Weak X-gal staining was also observed in cells within the proximal INL (arrows) and some rare cells in the ganglion cell layer (arrowhead). **(B)** Higher magnification of the INL region from panel A. Labeling of cells in the outer INL is very strong. **(C)** The X-gal staining pattern was similar without prior immunohistochemical staining of horizontal cells. **(D)** In wild type controls, no X-gal stained cells could be observed. All scale bars: 20 µm. Abbreviations: RPE = retinal pigment epithelium, OS = photoreceptor outer segments, ONL = outer nuclear layer, OPL = outer plexiform layer, INL = inner nuclear layer, IPL = inner plexiform layer, GCL = ganglion cell layer.

Figure 4: Immunohistochemical localization of β-galactosidase in retinal wholemounts reveals more LacZ-positive cell types. LacZ-positive cells were labeled with an antibody against β-galactosidase and counterstained with markers for different cell types. (**A**) Strong labeling of cells in distal INL was observed, presumably horizontal cells. Staining in proximal INL (**B**) and GCL (**E**) was much weaker (images were acquired with the same settings of the confocal microscope). β-galactosidase staining did not co-localize (white in overlay images) with choline acetyltransferase (ChAT) staining in INL (**B-D**) or GCL (not shown), but with melanopsin staining (**E-G**). Scale bars: 20 µm. Abbreviations: INL = inner nuclear layer, GCL = ganglion cell layer.

Journal of Comparative Neurology

Figure 5: Horizontal cell mosaic analysis. (**A**) Horizontal cells were stained in retinal wholemounts and areas of dorsal and ventral retina from 25% to 75% retinal eccentricity (shaded rectangles; 0% = optic nerve head, 100% = retinal rim) were analyzed. Scale bar: 200 µm. (**B**) Nearest neighbor distances between cells (red arrow = nearest neighbor distance, dotted circle indicates no other cell within same distance; scale bar: 20 µm). (**C**) Nearest neighbor distance plotted as a function of retinal eccentricity shows larger distances between horizontal cells in ventral retina and an overall increase in distances towards the periphery in both wild type and knockout (mean ± SEM). (**D**) Distribution of nearest neighbor distances is very similar between genotypes in either dorsal or ventral retina, indicating a similar regularity of the horizontal cell mosaic. In both genotypes, the distribution in ventral retina is shifted to larger distances (pdf = probability density function). No significant differences of nearest neighbor distances were found between genotypes.

Figure 6: Patch-clamp recordings. (**A**) Acutely isolated horizontal cells were targeted for whole-cell patch-clamp recordings by their characteristic morphology. The currents were confirmed to be carried by voltage-gated calcium channels by blocking with Co^{2+} (thick lines represent averages of 3-4 traces). (**B**) Current-voltage (IV, mean ± s.e.m.) curves of knockout and wild type. The dip at -50 mV could be indicative of T-Type channel activation. There was no significant difference in fitted IV curves half-maximal activation, peak, slope or reversal potential. (**C, D**) The maximal current amplitude to a 0 mV step was the same in knockout and wild type cells, as seen in the averaged traces (**C**, mean ± s.d.) and in the quantification of the maximal current density (**D**, dots = individual cells, horizontal line = mean). (**E**) Both wild type and knockout do not show voltage-dependent inactivation. Inactivation steps from -60 to +20 mV lasted 400 ms followed by a 50 ms test step to 0 mV. Current difference

between beginning and end of the inactivation steps and current during the 0 mV step were compared and no significant differences between genotypes were found.

Figure 7: ERG *in vivo* functional analysis. (**A**) Representative single-flash ERG intensity series of wild type (black) and knockout mice (red) under scotopic conditions (arrow indicates intensities with cone activation) and (**B**) under photopic conditions. (**C**) Box-and-whisker plots showing single-flash b-wave amplitudes and b-wave latencies under scotopic conditions and (**D**) under photopic conditions of wild type and knockout mice. Asterisks = medians, connected by solid lines; boxes = 25% to 75% quantile range; whiskers = 5% and 95% quantiles.

Figure 8: Multi-electrode array recordings of ganglion cell spontaneous activity and responses to Gaussian white noise flicker. Ganglion cell activity was recorded with multi-electrode arrays while the retina was exposed to a sequence of visual stimuli, repeated at each ambient luminance level. Each visual stimulus was preceded by 1 second of uniform background gray ('128'). This time window was used to calculate spontaneous activity. (**A**) Spontaneous activity in ON and OFF ganglion cells (polarities defined by STA) over the whole experiment (stimulus durations were 12 seconds to 3 minutes; stimuli 1 to 60 were considered as "settling down period" and not analyzed). ON cell spontaneous activity (upper panel) differed mainly during mesopic conditions while OFF cells (lower panel) in knockout exhibited an increased spontaneous spike rate over all luminance levels (height of the vertical bars on top of the panels indicates p-values). Vertical lines indicate switches to the next ambient luminance level. Stimuli are indicated below: Yellow – sequence start, magenta – full field steps, cyan – Gaussian white noise flicker, black – drifting gratings, gray – other. (**B**) Mean spike rates during the full-field Gaussian white noise flicker stimulus with interleaved high-contrast (HC) and low-contrast (LC) episodes. For Gaussian flicker, only cells with a clear STA to LC episodes of at least one

stimulus repetition per luminance level were analysed. In general, spike rates during HC episodes were similar between genotypes, while spike rates during LC episodes were higher in knockout ON and OFF ganglion cells. (**C**) The difference in spike rate between HC and LC episodes was calculated as a measure of discrimination strength of the contrast modulation. ON cells (left panel) showed a clear difference in discrimination strength only during mesopic conditions, while OFF cells (right panel) had significantly different discrimination strength during mesopic and scotopic conditions.

Figure 9: Multi-electrode array recordings of ganglion cell responses to drifting sinusoidal gratings. Ganglion cells were k-means-clustered based on their spontaneous activity following sinusoidal grating stimuli in scotopic luminance. (**A**) Mean spontaneous activity of eight ganglion cell clusters. Four clusters were exclusively ON cells (1, 4, 5, 8), while the other four clusters were mixed (n numbers: total (ON cells/OFF cells)). Most clusters contained wild type and knockout ganglion cells, only clusters 4 and 8 were more specific. Columns mark spatial periods, each containing all temporal frequencies (see labels above clusters 1 and 2). Vertical dotted lines indicate the next luminance level. (**B**) Spontaneous activity of individual cells of clusters 4 (top) and 8 (bottom) during scotopic luminance. Spike rates decreased during the low spatial periods, with a sharp increase during 500 µm gratings (cluster 4) or after the presentation of the 2000 µm gratings (cluster 8). (**C**) Averaged response of cluster 4 (WT only) and cluster 8 to a subset of grating stimuli. There is a marked increase in spike rate modulation (amplitude) in the responses to the 500 µm gratings compared to the 200 µm gratings. (**D**) Only the baselined mean spike rate (left panels) differed significantly at the junctions of grating spatial periods where we saw spontaneous activity jumps (yellow rectangles). Amplitudes (right panels) showed significant differences mainly at the junction between 200 µm and 500 µm gratings.

Journal of Comparative Neurology

Figure 10: Multi-electrode array recordings of ganglion cell responses to full-field contrast steps. Ganglion cells were stimulated with full-field steps: gray → black → gray → white → gray (see bottom of each panel). (**A**) Averaged responses (mean ± s.d.) of OFF cells from wild type and knockout at all three luminance levels. Response peaks to anti-preferred contrast steps were partly delayed (arrows) and response amplitudes were increased (arrowheads) in scotopic and mesopic luminance. (**B**) Responses of ON cells of wild type and knockout were very similar in mesopic and photopic luminance levels. In scotopic luminance, responses to the last step were delayed. We observed several subpopulations characterized by the delay timings (see standard deviations in inset). Subpopulations were similar in wild type and knockout, except for cells with a delayed response in time window 3, which was almost exclusively found in knockout (bar graph). (**C**) Example scotopic response of a WT ON cell with delay 2 (top: raster plot of all 30 repetitions; bottom: averaged spike rate; thick line = mean, thin lines = s.d.). (**D**) Averaged scotopic response of all cells with a delayed response in time window 2 (mean ± s.d.). (**E**) Example scotopic response of a KO ON cell with delay 3 (top: raster plot of all 30 repetitions; bottom: averaged spike rate; thick line = mean, thin lines = s.d.). (**F**) Averaged scotopic response of all cells with a delayed response in time window 3 (mean ± s.d.).

Journal of Comparative Neurology

Table 1: RT-PCR primer details

target / gene name	*primer*	*sequence (5' --> 3')*	*Tm (°C)**	*primer length*	*amplicon size*	*reference*
$\alpha_2\delta$-1 /	Cacna2d1_for	GCACCAAGGGAATACTGCAATGA	63.86	23		**
Cacna2d1	Cacna2d1_rev	CCACCATCATCTAGAATGACACAGT	62.69	25	587	**
$\alpha_2\delta$-2 /	Cacna2d2_for	GCATGATTGACGGCGACAAAG	63.25	21		
Cacna2d2	Cacna2d2_rev	AATGCCCGTGTCCAGAATCAAG	63.68	22	425	
$\alpha_2\delta$-3 /	Cacna2d3_for	TACATTGACAGCACCCTCCC	62.06	20		
Cacna2d3	Cacna2d3_rev	GCATTTCGTAACACATCATCCC	60.46	22	356	
$\alpha_2\delta$-4 /	Cacna2d4_for	TCCTCTAGCCACAACCAAGACC	64.20	22		
Cacna2d4	Cacna2d4_rev	AAGAAACTCAGCTCCCAGCTCC	64.78	22	480	

*calculated by Perl Primer ** (Cole et al., 2005), 3' end shortened

Journal of Comparative Neurology

Table 2: Antibodies and streptavidins used in immunohistochemical stainings on cryosections (c)

Antibody name	*Immunogen*	*Supplier, catalog #, RRID*	*Host species, clonality*	*Dilutions used*
Calbindin D-28K	calbindin D-28k purified from chicken gut	Swant, 300, AB_10000347	Mouse, monoclonal IgG1	1:500 (c)
Calbindin D-28K	recombinant rat calbindin D-28k	Swant, CB-38, AB_10000340	Rabbit, polyclonal	1:1000 (w)
Neurofilament H	Full length native protein (cow spinal cord)	Abcam, ab4680, AB_304560	Chicken, polyclonal IgY	1:1000 (w)
Choline Acetyltransferase (ChAT)	Human placental enzyme	Millipore, AB144P, AB_2079751	Goat, polyclonal	1:280 (w)
Melanopsin	15 N-terminal extracellular amino acids of mouse melanopsin	Advanced Targeting Systems, AB-N39, AB_1608076	Rabbit, polyclonal	1:2800 (w)
β-galactosidase	Full length native protein (purified, E. coli)	Abcam, ab9361, AB_307210	Chicken, polyclonal IgY	1:500 (w)
Anti-mouse/Alexa 488	IgG (H+L)	Life Technologies, A-21202, AB_10049285	Donkey, polyclonal IgG	1:750 (c)
Anti-rabbit/Alexa 555	IgG (H+L)	Life Technologies, A-31572, AB_10562716	Donkey, polyclonal IgG	1:400 (w)
Anti-chicken/FITC	IgG (H+L)	Jackson ImmunoResearch, 703-095-155, AB_2340356	Donkey, polyclonal IgG	1:400 (w)
Anti-goat/biotin	IgG (H+L)	Life Technologies, D-20698, AB_10375584	Donkey, polyclonal IgG	1:400 (w)
Streptavidin/Cy5	nA	Rockland Immunochemicals, S000-06, AB_2341143	nA	1:200 (w)

Journal of Comparative Neurology

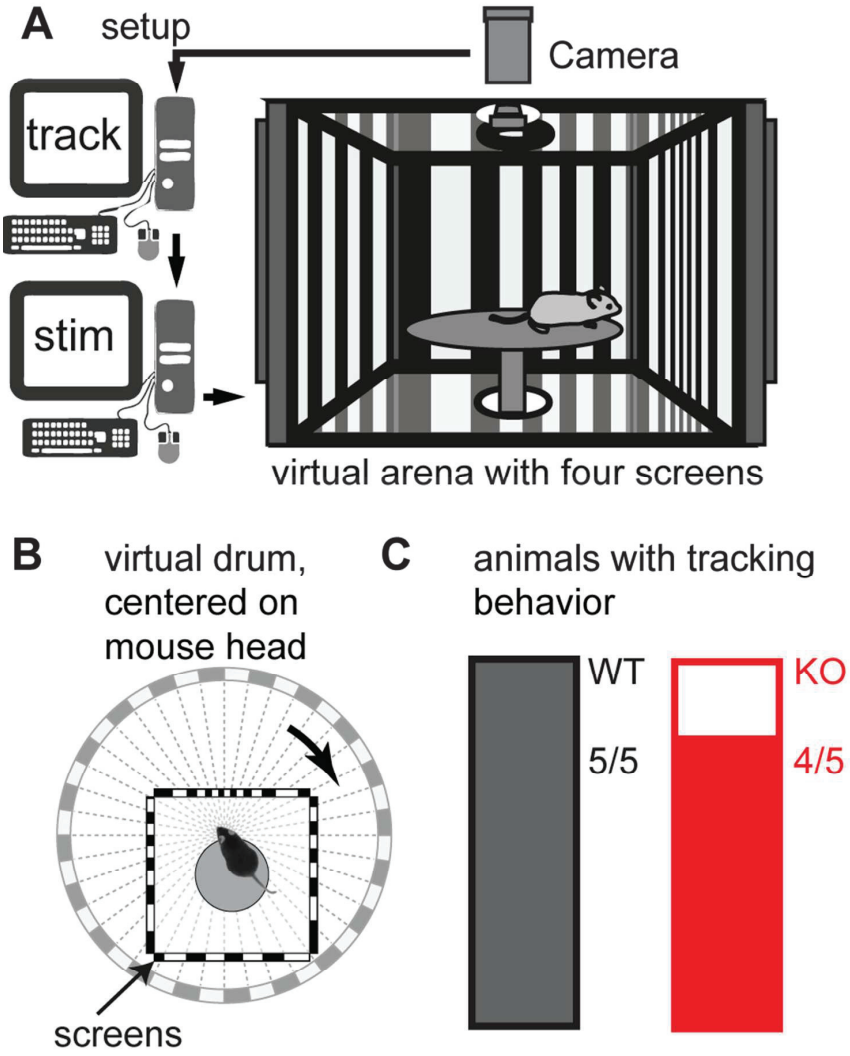

Figure 1: Optokinetic reflex test. (A) The "optokinetic drum" virtual arena. Rotating stripe patterns were presented while the mouse was observed from above by a camera. The recorded position of the mouse head was used to adjust stimulus parameters in real time (B), circle = virtual drum, square = actual stripe pattern on the screens. (C) all 5 wild type and 4 out of 5 knockout animals showed clear tracking behavior, indicating an intact optokinetic reflex in $\alpha_2\delta$-3 knockout animals.
81x103mm (300 x 300 DPI)

Journal of Comparative Neurology

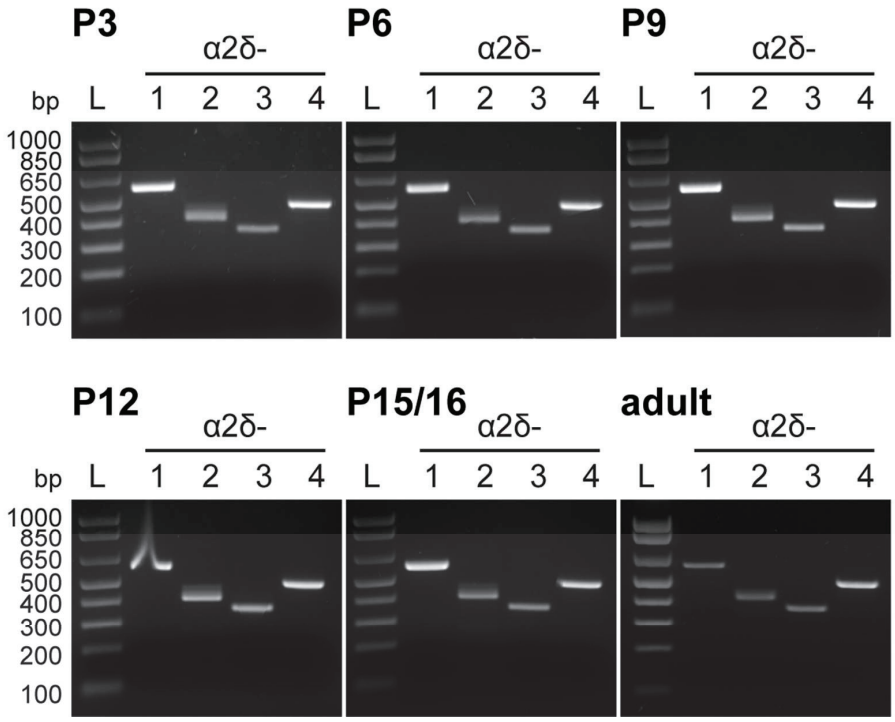

Figure 2: $\alpha_2\delta$ mRNA expression in mouse retina. RT-PCR on total RNA isolated from mouse retina at postnatal day 3 (P3) up to adult. All four $\alpha_2\delta$ transcripts were found throughout the developmental time points tested and in adult mouse retina (n = 3 each, n = 2 for P6 and P15/P16). Amplicon sizes: $\alpha_2\delta$-1 = 587 bp, $\alpha_2\delta$-2 = 425 bp, $\alpha_2\delta$-3 = 356 bp, $\alpha_2\delta$-4 = 480 bp. L = ladder.
99x80mm (300 x 300 DPI)

Journal of Comparative Neurology

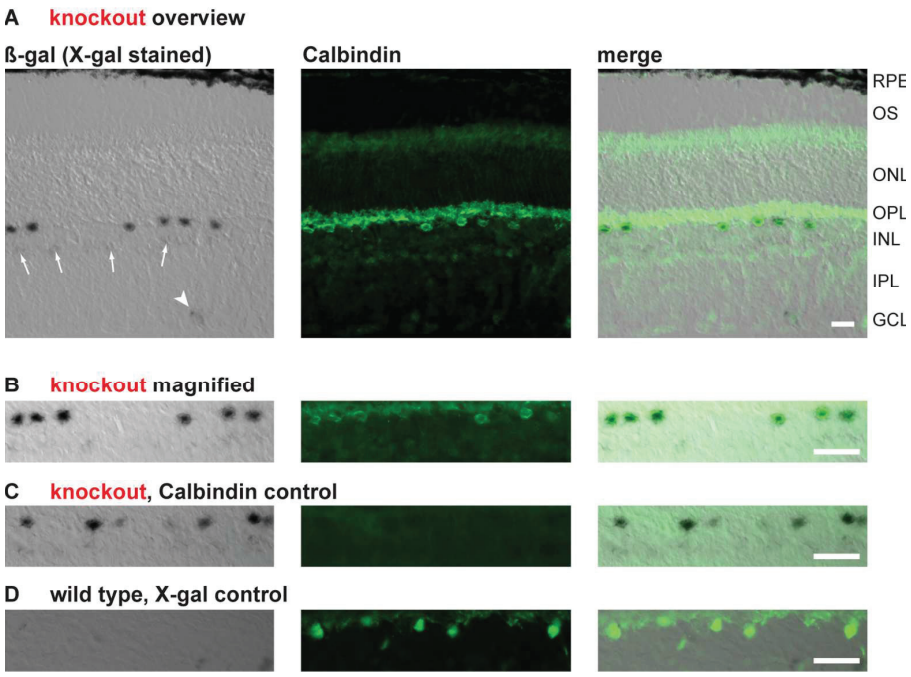

Figure 3: LacZ expression localization in adult mouse retina.
Horizontal cells were immunohistochemically stained with antibodies against calbindin in cryoslices of knockout/heterozygous and wild type retina and LacZ reporter expression was revealed with X-gal. (A) The strongly LacZ-positive cells showed complete overlap with the calbindin-positive cells in the distal inner nuclear layer (INL). Weak X-gal staining was also observed in cells within the proximal INL (arrows) and some rare cells in the ganglion cell layer (arrowhead). (B) Higher magnification of the INL region from panel A. Labeling of cells in the outer INL is very strong. (C) The X-gal staining pattern was similar without prior immunohistochemical staining of horizontal cells. (D) In wild type controls, no X-gal stained cells could be observed. All scale bars: 20 µm. Abbreviations: RPE = retinal pigment epithelium, OS = photoreceptor outer segments, ONL = outer nuclear layer, OPL = outer plexiform layer, INL = inner nuclear layer, IPL = inner plexiform layer, GCL = ganglion cell layer.

129x97mm (300 x 300 DPI)

Journal of Comparative Neurology

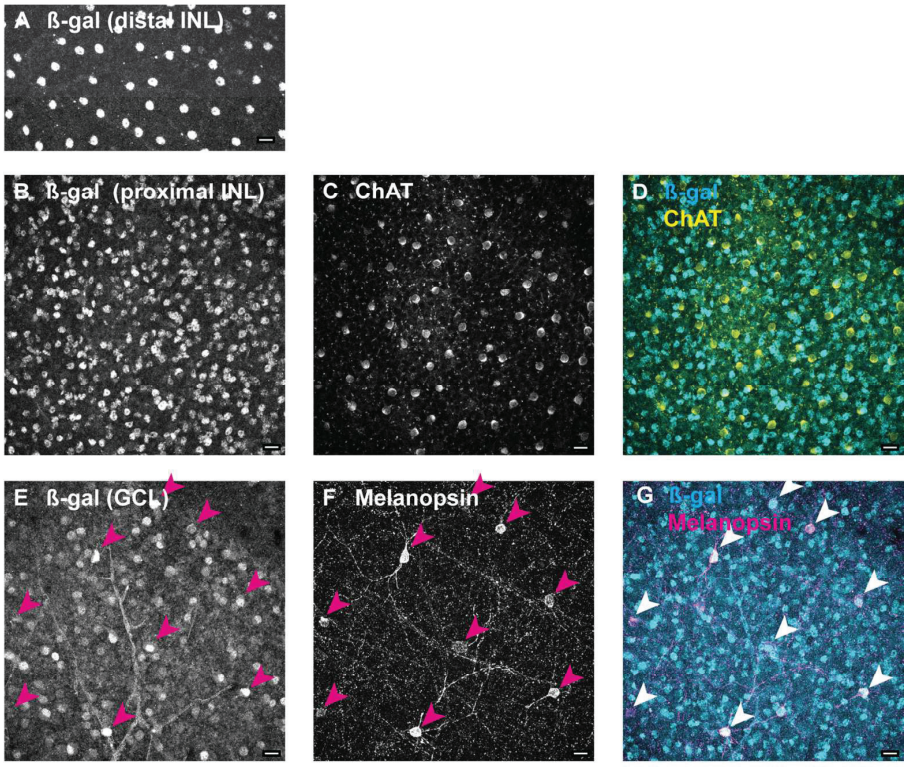

Figure 4: Immunohistochemical localization of β-galactosidase in retinal wholemounts reveals more LacZ-positive cell types. LacZ-positive cells were labeled with an antibody against β-galactosidase and counterstained with markers for different cell types. (A) Strong labeling of cells in distal INL was observed, presumably horizontal cells. Staining in proximal INL (B) and GCL (E) was much weaker (images were acquired with the same settings of the confocal microscope). β-galactosidase staining did not co-localize (white in overlay images) with choline acetyltransferase (ChAT) staining in INL (B-D) or GCL (not shown), but with melanopsin staining (E-G). Scale bars: 20 µm. Abbreviations: INL = inner nuclear layer, GCL = ganglion cell layer.
129x110mm (300 x 300 DPI)

Journal of Comparative Neurology

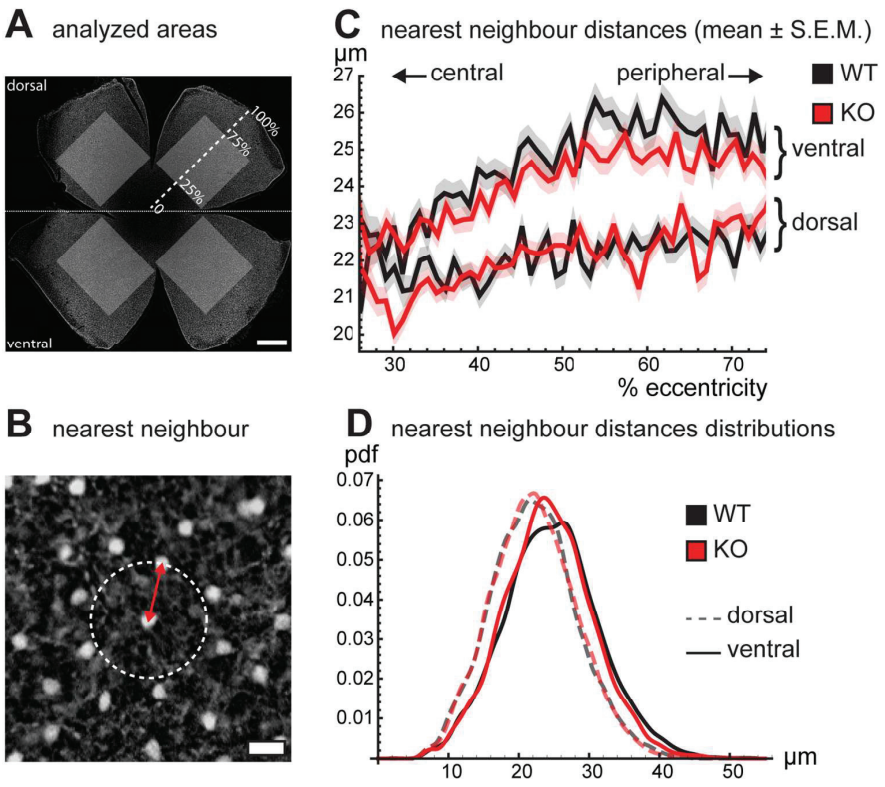

Figure 5: Horizontal cell mosaic analysis. (A) Horizontal cells were stained in retinal wholemounts and areas of dorsal and ventral retina from 25% to 75% retinal eccentricity (shaded rectangles; 0% = optic nerve head, 100% = retinal rim) were analyzed. Scale bar: 200 µm. (B) Nearest neighbor distances between cells (red arrow = nearest neighbor distance, dotted circle indicates no other cell within same distance; scale bar: 20 µm). (C) Nearest neighbor distance plotted as a function of retinal eccentricity shows larger distances between horizontal cells in ventral retina and an overall increase in distances towards the periphery in both wild type and knockout (mean ± SEM). (D) Distribution of nearest neighbor distances is very similar between genotypes in either dorsal or ventral retina, indicating a similar regularity of the horizontal cell mosaic. In both genotypes, the distribution in ventral retina is shifted to larger distances (pdf = probability density function). No significant differences of nearest neighbor distances were found between genotypes.
129x115mm (300 x 300 DPI)

Journal of Comparative Neurology

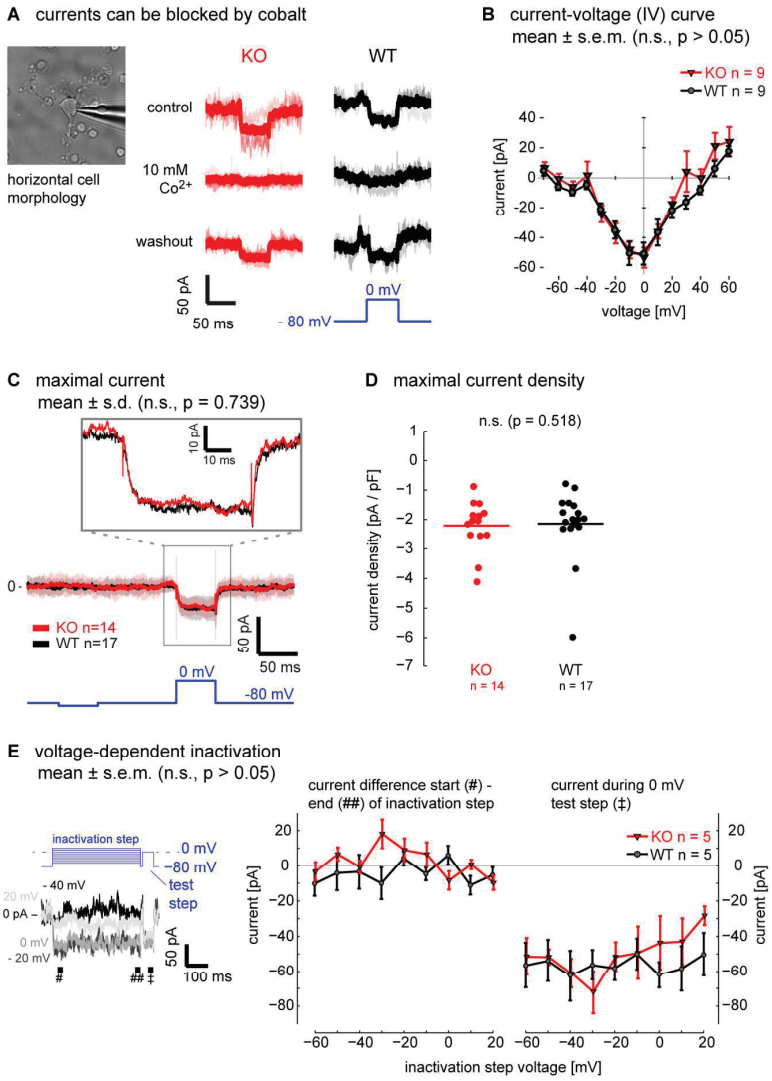

Figure 6: Patch-clamp recordings. (A) Acutely isolated horizontal cells were targeted for whole-cell patch-clamp recordings by their characteristic morphology. The currents were confirmed to be carried by voltage-gated calcium channels by blocking with Co2+ (thick lines represent averages of 3-4 traces). (B) Current-voltage (IV, mean ± s.e.m.) curves of knockout and wild type. The dip at -50 mV could be indicative of T-Type channel activation. There was no significant difference in fitted IV curves half-maximal activation, peak, slope or reversal potential. (C, D) The maximal current amplitude to a 0 mV step was the same in knockout and wild type cells, as seen in the averaged traces (C, mean ± s.d.) and in the quantification of the maximal current density (D, dots = individual cells, horizontal line = mean). (E) Both wild type and knockout do not show voltage-dependent inactivation. Inactivation steps from -60 to +20 mV lasted 400 ms followed by a 50 ms test step to 0 mV. Current difference between beginning and end of the inactivation steps and current during the 0 mV step were compared and no significant differences between genotypes were found.
129x181mm (300 x 300 DPI)

Journal of Comparative Neurology

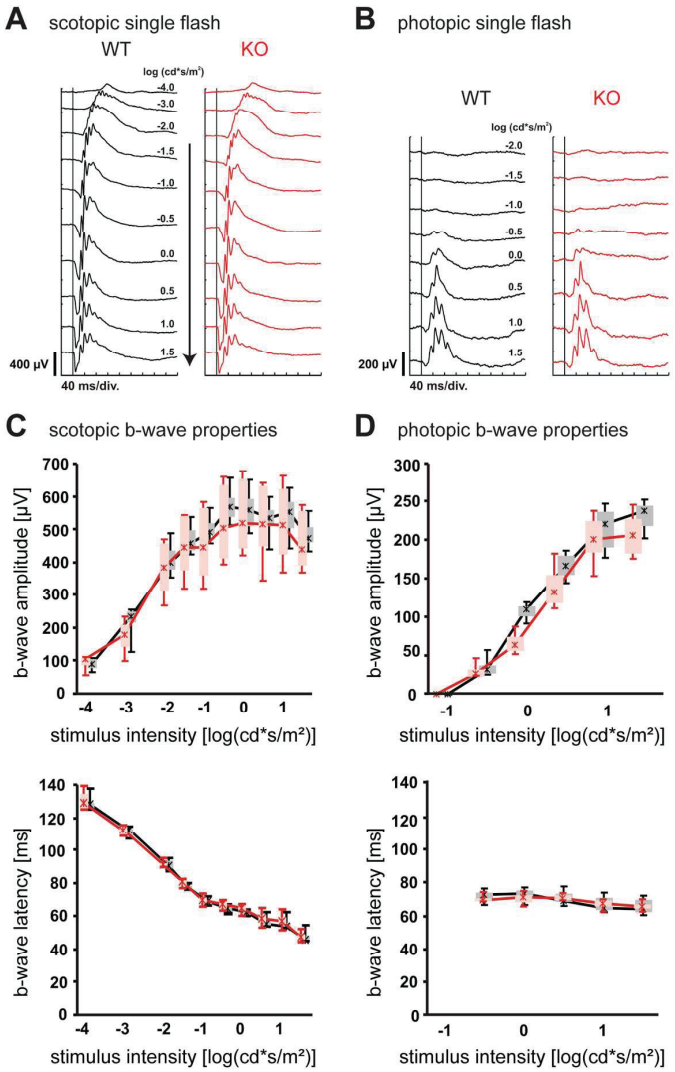

Figure 7: ERG in vivo functional analysis. (A) Representative single-flash ERG intensity series of wild type (black) and knockout mice (red) under scotopic conditions (arrow indicates intensities with cone activation) and (B) under photopic conditions. (C) Box-and-whisker plots showing single-flash b-wave amplitudes and b-wave latencies under scotopic conditions and (D) under photopic conditions of wild type and knockout mice. Asterisks = medians, connected by solid lines; boxes = 25% to 75% quantile range; whiskers = 5% and 95% quantiles.
129x198mm (300 x 300 DPI)

Journal of Comparative Neurology

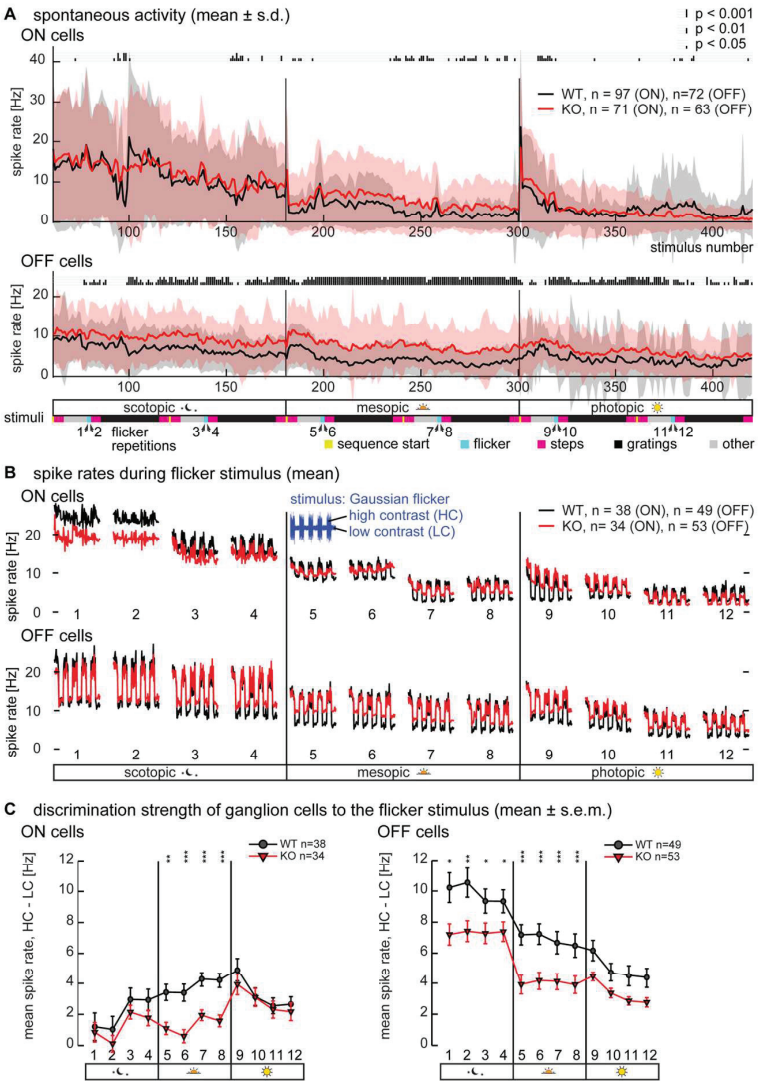

Figure 8: Multi-electrode array recordings of ganglion cell spontaneous activity and responses to Gaussian white noise flicker. Ganglion cell activity was recorded with multi-electrode arrays while the retina was exposed to a sequence of visual stimuli, repeated at each ambient luminance level. Each visual stimulus was preceded by 1 second of uniform background gray ('128'). This time window was used to calculate spontaneous activity. (A) Spontaneous activity in ON and OFF ganglion cells (polarities defined by STA) over the whole experiment (stimulus durations were 12 seconds to 3 minutes; stimuli 1 to 60 were considered as "settling down period" and not analyzed). ON cell spontaneous activity (upper panel) differed mainly during mesopic conditions while OFF cells (lower panel) in knockout exhibited an increased spontaneous spike rate over all luminance levels (height of the vertical bars on top of the panels indicates p-values). Vertical lines indicate switches to the next ambient luminance level. Stimuli are indicated below: Yellow – sequence start, magenta – full field steps, cyan – Gaussian white noise flicker, black – drifting gratings, gray – other. (B) Mean spike rates during the full-field Gaussian white noise flicker stimulus with interleaved high-contrast (HC) and low-contrast (LC) episodes. For Gaussian flicker, only cells with a clear STA to LC episodes of at least one stimulus repetition per luminance level were analysed. In general, spike rates during HC episodes were similar between genotypes, while spike rates during LC episodes were higher in knockout ON and OFF ganglion cells. (C) The difference in spike rate between HC and LC episodes was calculated as a measure of discrimination strength of the contrast modulation. ON cells (left panel) showed a clear difference in discrimination strength only during mesopic conditions, while OFF cells (right panel) had significantly different discrimination strength during mesopic and scotopic conditions.
129x176mm (300 x 300 DPI)

John Wiley & Sons

Journal of Comparative Neurology

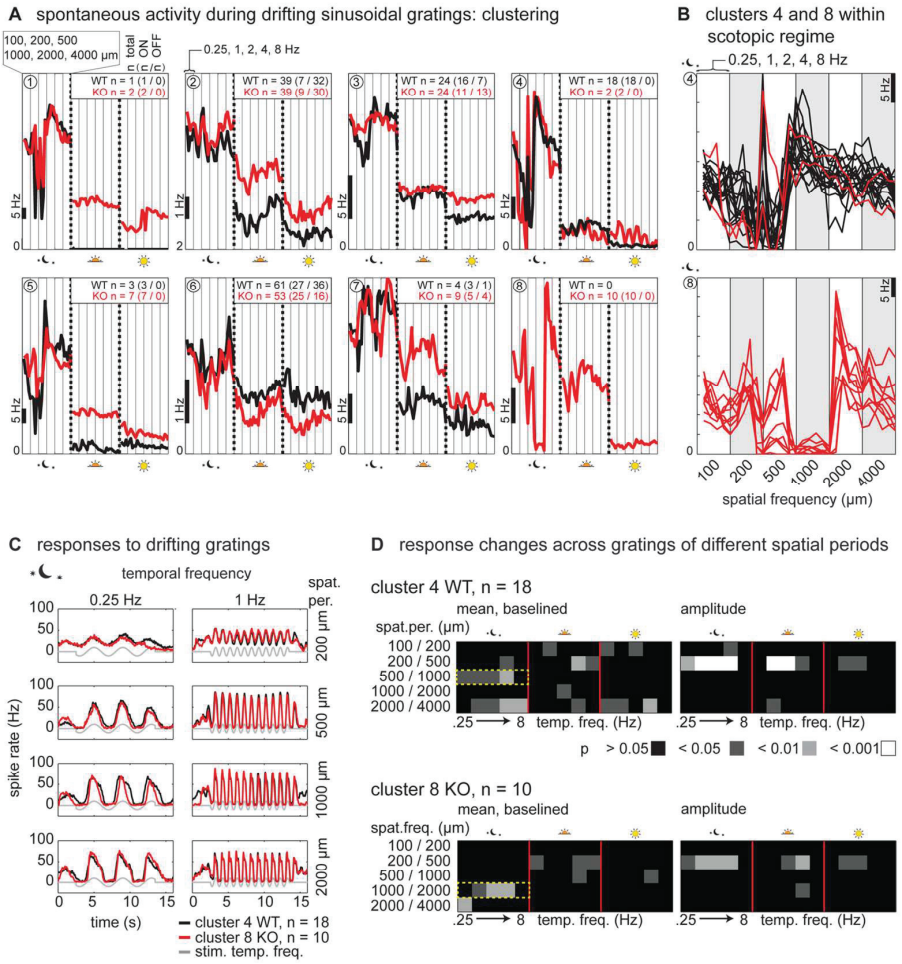

Figure 9: Multi-electrode array recordings of ganglion cell responses to drifting sinusoidal gratings. Ganglion cells were k-means-clustered based on their spontaneous activity following sinusoidal grating stimuli in scotopic luminance. (A) Mean spontaneous activity of eight ganglion cell clusters. Four clusters were exclusively ON cells (1, 4, 5, 8), while the other four clusters were mixed (n numbers: total (ON cells/OFF cells)). Most clusters contained wild type and knockout ganglion cells, only clusters 4 and 8 were more specific. Columns mark spatial periods, each containing all temporal frequencies (see labels above clusters 1 and 2). Vertical dotted lines indicate the next luminance level. (B) Spontaneous activity of individual cells of clusters 4 (top) and 8 (bottom) during scotopic luminance. Spike rates decreased during the low spatial periods, with a sharp increase during 500 µm gratings (cluster 4) or after the presentation of the 2000 µm gratings (cluster 8). (C) Averaged response of cluster 4 (WT only) and cluster 8 to a subset of grating stimuli. There is a marked increase in spike rate modulation (amplitude) in the responses to the 500 µm gratings compared to the 200 µm gratings. (D) Only the baselined mean spike rate (left panels) differed significantly at the junctions of grating spatial periods where we saw spontaneous activity jumps (yellow rectangles). Amplitudes (right panels) showed significant differences mainly at the junction between 200 µm and 500 µm gratings.
129x139mm (300 x 300 DPI)

Journal of Comparative Neurology

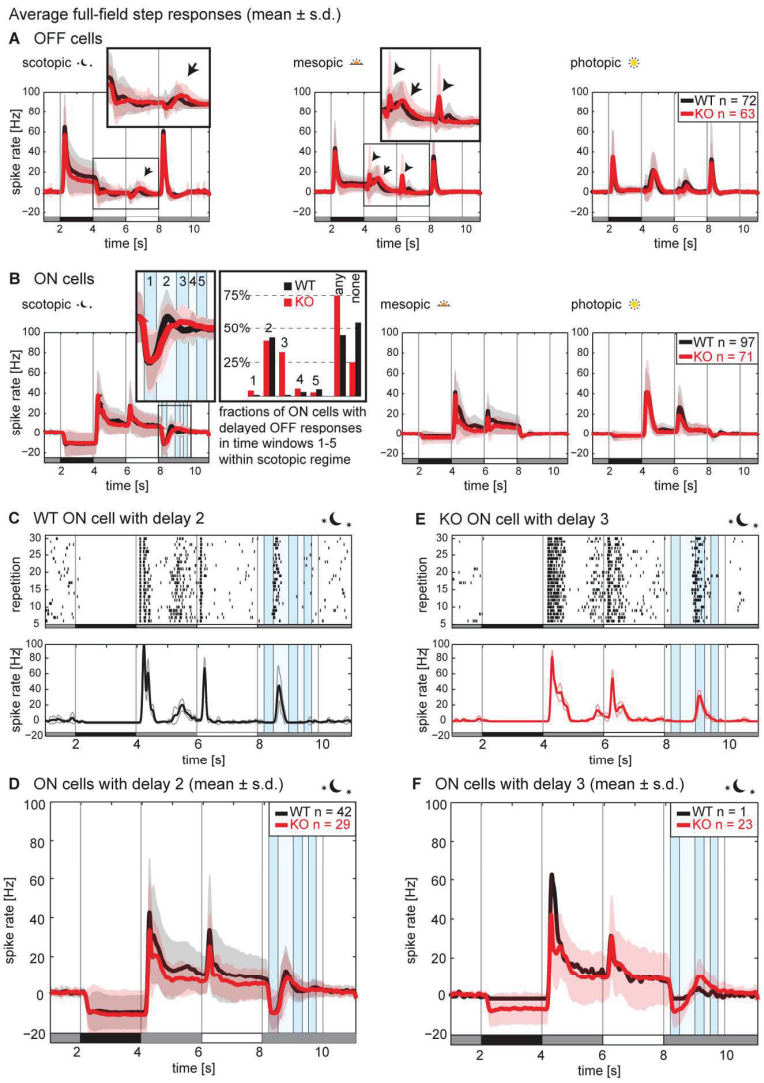

Figure 10: Multi-electrode array recordings of ganglion cell responses to full-field contrast steps. Ganglion cells were stimulated with full-field steps: gray → black → gray → white → gray (see bottom of each panel). (A) Averaged responses (mean ± s.d.) of OFF cells from wild type and knockout at all three luminance levels. Response peaks to anti-preferred contrast steps were partly delayed (arrows) and response amplitudes were increased (arrowheads) in scotopic and mesopic luminance. (B) Responses of ON cells of wild type and knockout were very similar in mesopic and photopic luminance levels. In scotopic luminance, responses to the last step were delayed. We observed several subpopulations characterized by the delay timings (see standard deviations in inset). Subpopulations were similar in wild type and knockout, except for cells with a delayed response in time window 3, which was almost exclusively found in knockout (bar graph). (C) Example scotopic response of a WT ON cell with delay 2 (top: raster plot of all 30 repetitions; bottom: averaged spike rate; thick line = mean, thin lines = s.d.). (D) Averaged scotopic response of all cells with a delayed response in time window 2 (mean ± s.d.). (E) Example scotopic response of a KO ON cell with delay 3 (top: raster plot of all 30 repetitions; bottom: averaged spike rate; thick line = mean, thin lines = s.d.). (F) Averaged scotopic response of all cells with a delayed response in time window 3 (mean ± s.d.). 129x184mm (300 x 300 DPI)

John Wiley & Sons

Publication 2 – Retina recordings with perforated MEA

Katja Reinhard*, Alexandra Tikidji-Hamburyan*, Hartwig Seitter*, Saad Idrees, Marion Mutter, Boris Benkner, Thomas A Münch. *Step-By-Step Instructions for Retina Recordings with Perforated Multi Electrode Arrays.* PLoS ONE 2014 Aug 28; 9(8): e106148. *equal contributions

Framework:

This publication is a method paper. It gives step-by-step instructions how to perform perforated micro-electrode array recordings from retina, including the necessary modifications for in vitro electroretinogram recordings and also troubleshooting for these methods. It constitutes a compilation of the methodology that we jointly developed to record retinal activity.

My contributions:

On initial implementation of the system, I aided in improving vacuum settings for the perfusion/suction. The in vitro electroretinographic recording technique was developed, implemented and tested by me. All parts concerning in vitro electroretinograms, including data recording and presentation in figures (Fig 7+8) and descriptions, have been done by me. Parts of the mouse spiking data used in evaluating the method have been acquired by me. I wrote parts of the manuscript, added upon the step-by-step instructions and troubleshooting section as well as reviewed the figures.

Other contributions:

Perforated micro-electrode array recordings were originally established by ATH. KR further developed recording techniques and collected potential issues and troubleshooting solutions. The outline and initial formulation of the instructions given in this paper was done by KR. SI and TAM helped with writing the manuscript. MM and BB helped with figures and proof-reading of the manuscript. Much of the data shown and statistics on the number of extracted neurons per experiment were based on data collected by KR, MM, and ATH.

OPEN ACCESS Freely available online

PLOS ONE

Step-By-Step Instructions for Retina Recordings with Perforated Multi Electrode Arrays

Katja Reinhard[ϑ], Alexandra Tikidji-Hamburyan[ϑ¤], Hartwig Seitter[ϑ], Saad Idrees, Marion Mutter, Boris Benkner, Thomas A. Münch*

Werner Reichardt Centre for Integrative Neuroscience and Bernstein Center for Computational Neuroscience, University of Tübingen, Tübingen, Germany

Abstract

Multi-electrode arrays are a state-of-the-art tool in electrophysiology, also in retina research. The output cells of the retina, the retinal ganglion cells, form a monolayer in many species and are well accessible due to their proximity to the inner retinal surface. This structure has allowed the use of multi-electrode arrays for high-throughput, parallel recordings of retinal responses to presented visual stimuli, and has led to significant new insights into retinal organization and function. However, using conventional arrays where electrodes are embedded into a glass or ceramic plate can be associated with three main problems: (1) low signal-to-noise ratio due to poor contact between electrodes and tissue, especially in the case of strongly curved retinas from small animals, e.g. rodents; (2) insufficient oxygen and nutrient supply to cells located on the bottom of the recording chamber; and (3) displacement of the tissue during recordings. Perforated multi-electrode arrays (pMEAs) have been found to alleviate all three issues in brain slice recordings. Over the last years, we have been using such perforated arrays to study light evoked activity in the retinas of various species including mouse, pig, and human. In this article, we provide detailed step-by-step instructions for the use of perforated MEAs to record visual responses from the retina, including spike recordings from retinal ganglion cells and *in vitro* electroretinograms (ERG). In addition, we provide in-depth technical and methodological troubleshooting information, and show example recordings of good quality as well as examples for the various problems which might be encountered. While our description is based on the specific equipment we use in our own lab, it may also prove useful when establishing retinal MEA recordings with other equipment.

Citation: Reinhard K, Tikidji-Hamburyan A, Seitter H, Idrees S, Mutter M, et al. (2014) Step-By-Step Instructions for Retina Recordings with Perforated Multi Electrode Arrays. PLoS ONE 9(8): e106148. doi:10.1371/journal.pone.0106148

Editor: Steven Barnes, Dalhousie University, Canada

Received May 23, 2014; **Accepted** June 13, 2014; **Published** August 28, 2014

Data Availability: The authors confirm that all data underlying the findings are fully available without restriction. The methods are described in the paper.

Funding: This study was supported by funds from the Deutsche Forschungsgemeinschaft to the Werner Reichardt Centre for Integrative Neuroscience Tübingen (DFG EXC 307), and the German Ministry of Education, Science, Research and Technology to the Bernstein Center for Computational Neuroscience Tübingen (BMBF FKZ 01GQ1002), and a PhD stipend of the Pro-Retina Foundation, Germany, to KR. The authors acknowledge support by Deutsche Forschungsgemeinschaft and Open Access Publishing Fund of Tuebingen University. The funders had no role in study design, data collection and analysis, decision to publish, or preparation of the manuscript.

Competing Interests: The authors of this manuscript have read the journal's policy and have the following competing interests: One of the two pMEA setups in the lab of the authors was provided free of charge by MultiChannel Systems (Reutlingen, Germany). It is an older model demonstration system formerly used by their sales department. This does not alter the authors' adherence to all the PLOS ONE policies on sharing data and materials.

* Email: thomas.muench@cin.uni-tuebingen.de

ϑ These authors contributed equally to this work.

¤ Current address: Dept. of Neurosurgery and Hansen Experimental Physics Laboratory, Stanford University, Stanford, California, United States of America

Introduction

Multi-electrode arrays (MEAs) are a state-of-the-art tool in electrophysiological studies. Such arrays consist of dozens up to thousands of electrodes and allow measurements of many neurons in parallel. Especially in retina research, MEA recordings have proven to be a powerful technique [1–5]. The retina consists of many parallel yet interacting neural circuits which extract specific information about the visual input [6]. These circuits culminate at the output neurons of the retina, the retinal ganglion cells. The retina's layered structure with ganglion cells lying close to the proximal surface makes the retina particularly amenable for MEA recordings. Further, in many common laboratory species, including mouse, the ganglion cells form a monolayer with little or no three dimensional piling of cell bodies. This monolayer is covered only by the relatively thin inner limiting membrane, such that these neurons and the flat recording array can be brought into close proximity.

When performing in-vitro MEA recordings with retina, the retina is extracted from the eye and placed ganglion cell-side down on the electrodes of the MEA. Light stimulation is then applied either from the top or, if the MEA is transparent, through the MEA from the bottom. The photoreceptors capture the light and the visual information is processed by the retinal circuits, eventually leading to spike generation in the ganglion cells. These spikes can be measured as voltage changes by the electrodes of the MEA.

Retinal recordings with standard MEAs suffer from three main problems: (1) poor signal-to-noise ratio due to insufficient contact (physical proximity) between the tissue and the MEA (this problem is particularly pronounced when recording from small retinas, e.g. mouse, due to the strong curvature of the retina, and when recording from retinas with a thick inner limiting membrane, e.g.

human), (2) insufficient oxygenation and nutrient supply to the ganglion cells lying on the bottom of the recording chamber, and (3) movement of the retina due to insufficient fixation of the tissue on the array. Poor electrode contact and fixation of the tissue are usually dealt with by using some sort of "stamp", pushing the tissue against the MEA. This has obvious disadvantages, as one needs to find a fine balance between sufficiently holding the tissue in place on one hand, and not damaging the tissue by applying too much pressure on the other hand.

In our laboratory, we have implemented retinal recordings with perforated MEAs (pMEAs, from Multi Channel Systems MCS GmbH, Reutlingen, Germany). We found that pMEAs can alleviate all three issues encountered with standard MEAs. In pMEAs, the electrodes are not embedded into a ceramic or glass carrier, but instead in a fine membrane which also contains small holes of different sizes in-between the electrodes (Fig. 1). A slight vacuum can be applied through this perforation; this vacuum gently pulls the tissue towards the electrodes. This procedure enhances the contact between the tissue and the electrodes, and therefore increases the signal-to-noise ratio and decreases tissue movement during the experiment [7]. Additionally, it has been shown with brain slices that with pMEAs, more fresh solution reaches the bottom cell layers either through the tissue or through the small space between tissue and electrodes. Oxygenation of the bottom cell layer (i.e. ganglion cells in the case of retina) is thereby greatly enhanced when using pMEAs [8].

Several adjustments are necessary compared to the procedures applicable to brain slices [9–13]. The main reason is that the retina is relatively thin and fragile compared to brain slices, so that the vacuum needs to be very carefully controlled to prevent tearing of the retinal tissue. In this article we give a detailed description of our recording setup for perforated MEAs and step-by-step instructions for two different applications (spike recordings and *in vitro* electroretinogram recordings). We show example data demonstrating recording stability in long-term experiments, and provide an overview of the outcome which can be expected from such measurements. In addition, we discuss possible technical issues and provide troubleshooting suggestions.

Material

Perforated MEAs (60pMEA200/30iR by Multi Channel Systems MCS GmbH)

The 60pMEA200/30iR is a pMEA with 60 Titanium nitride electrodes. The electrodes are arranged in an 8×8 layout with 200 µm electrode distance and 30 µm electrode diameter. Electrodes are embedded in a perforated polyimide foil which allows perfusion and application of negative pressure to the retina (Fig. 1, further details can be found in the pMEA data sheet [14]). pMEAs are transparent and can therefore be used in upright and inverted setups. In this article we describe our experiments performed with a 60-electrode pMEA with glass ring and the MEA1060 amplifier. However, recordings with other pMEA systems should require only slight adaptations.

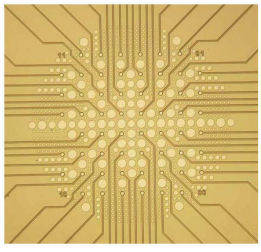

Figure 1. Layout of the 60-electrode pMEA. The electrodes are arranged in an 8×8 array with 200 µm electrode distance. Perforations of various size are visible in-between electrodes (source: 60pMEA200/30iR data sheet by Multi Channel Systems).
doi:10.1371/journal.pone.0106148.g001

Tissue

In previous studies we have used pMEAs in many experiments with retinas of several species. In the section "anticipated results" we discuss the quality of data to expect from retinas of various mouse strains, domestic pig retinas (sacrificed during independent studies at the Department of Experimental Surgery, Tübingen), Göttingen minipig retinas (Department of Urology) and human retinas (donated by patients of the University Eye Hospital in Tübingen). All recordings have been performed in the context of scientific studies in our laboratory. All studies were performed in accordance with German and European regulations. Use of human retinal tissue was approved by the Ethics Commission of the University Clinic Tübingen, approval number 531/2011. Written informed consent of the donors was obtained; the consent procedure was part of the Ethics Commission approval. Animal experiments were approved by the Regierungspräsidium Tübingen.

Setup components

The setup for pMEA recordings consists of two perfusion loops: An upper loop to supply the tissue with fresh solution (labeled "upper perfusion" and "suction" in Fig. 2), and a lower loop to adjust the proper negative pressure ("lower perfusion" and "vacuum system"). Here, we provide an overview of this dual perfusion system and a detailed list of the components we used to build our setup (excluding light stimulation and data acquisition). Details on how to use the system are described below in the section "experimental procedure". Except for the constant vacuum pump (D3), the amplifier baseplate that allows vacuum application, and some small components such as tubing, no additional material is needed compared to conventional MEA recordings. All numbers refer to Figure 2.

Upper perfusion. The upper perfusion system supplies the retina with fresh solution during the recordings. It can either be gravity driven (like in the scheme in Fig. 2, in which case the tubing can initially be filled with the help of a syringe, A1, v4), or it can be driven with a peristaltic pump. The solution is guided into the MEA chamber through a cannula or a stiff tube. A simple flow regulator (A2) can be used to adjust the speed of the solution flow in the gravity driven configuration. The components used for upper perfusion are listed below.

- Bottle with physiological solution
- 10–20 ml syringe (A1)
- Simple flow regulator (A2, e.g. Infudrop, Fresenius Kabi AG, Bad Homburg, Germany)
- Valve (v4)
- Cannula or similar
- Tubing (inner diameter)
  - 2×~1.6 mm to connect v4–A2 and A2–MEA
  - 2×~1.6 mm (or thicker) to connect v4–solution and v4–A1
  - Thinner tubes to connect to cannula (depending on cannula)
- Connectors for attaching the tubing to the other components

Suction. To prevent the MEA chamber from overflowing, a suction pump (B1) should be connected via a cannula to the MEA

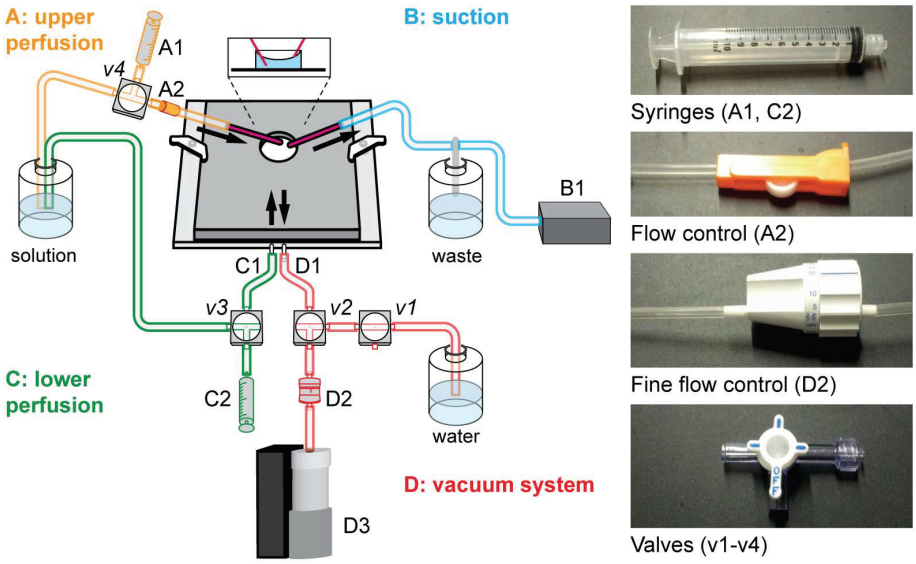

Figure 2. Setup for pMEA recordings. Our MEA setup consists of two perfusion loops. Solution is supplied to the MEA chamber from the top through the upper perfusion (A) and excessive solution is removed by the suction (B). The necessary negative pressure is supplied by the additional perfusion, consisting of the lower perfusion (C) and a vacuum (D). Details are given in the following text and figures.
doi:10.1371/journal.pone.0106148.g002

chamber. The solution can either be collected in an extra bottle and discarded after the experiment or, if the upper perfusion is performed with a peristaltic pump, it can be recycled and pumped back into the main solution bottle. The components for suction are listed below.

- Vacuum pump (B1)
- Bottle with gas washing bottle head
- Cannula or similar
- Tubing and connectors, appropriate to fit attachments for waste bottle and pump

Lower perfusion. The lower perfusion system is only used before the experiment and can be driven by gravity flow. Its purpose is to fill the MEA chamber with solution without introducing air bubbles into the vacuum system. The lower perfusion is connected to the shorter cannula of the pMEA amplifier baseplate (C1). To get the gravity-driven flow going, the tubing of the lower perfusion system can be filled with the help of a syringe (C2, v3). The components for lower perfusion are listed below.

- 10–20 ml syringe (C2, with screw connection for valve)
- Valve (v3)
- Tubing (inner diameter)
  - 1×0.8 mm to connect v3–C1
  - 1×~1.6 mm to connect v3–solution
- Connectors at v3

Vacuum system. The vacuum system provides negative pressure to pull the retina towards the electrodes. This negative pressure needs, first, to be constant to avoid fluctuations, and second, to be high enough to ensure good tissue-electrode contact, but low enough to not tear the tissue. Constant negative pressure is provided by a Constant Vacuum Pump (CVP, D3, Multi Channel Systems) and is further reduced by an additional fine flow control (D2) between the CVP (D3) and the MEA baseplate. The vacuum system is connected to the right (longer) cannula of the MEA baseplate (D1). The most important step for ensuring reliable negative pressure is the removal of air bubbles: any air bubble in the vacuum system will degrade the stable negative pressure. The additional valves (v1, v2) and the water bottle are needed for filling of the vacuum system and for removing air bubbles (see below). The components for the vacuum system are listed below.

- Constant vacuum pump (CVP, D3, Multi Channel Systems MCS GmbH, Reutlingen, Germany)
- Fine flow control (D2, Dosi-flow 10, P. J. Dahlhausen & Co. GmbH, Köln, Germany)
- Valves (v1, v2)
  Valve v1 can either be a 2-way valve, or a 3-way valve (like the other valves) with one connector closed with a plug
- Tubing (inner diameter)
  - 1×0.8 mm to connect v2–D1
  - 3×~1.6 mm to connect v2–D2, v2–v1, and v1–water bottle
- Connectors
- 1×18 ga blunt needle for 0.8 mm tubing at v2
- 1×plug for v1 if a 3-way valve is used
- Bottle with water

MEA Equipment. 60-electrode perforated MEA with glass ring (Multi Channel Systems MCS GmbH, Reutlingen, Germany).

- MEA1060 system (Multi Channel Systems MCS GmbH, Reutlingen, Germany)

Specific equipment for in vitro electroretinogram (in vitro ERG) recordings. Visual stimulation only possible from below

Step 1a) i

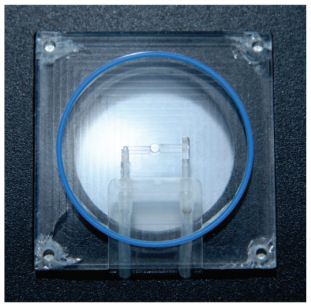

Step 1a) ii

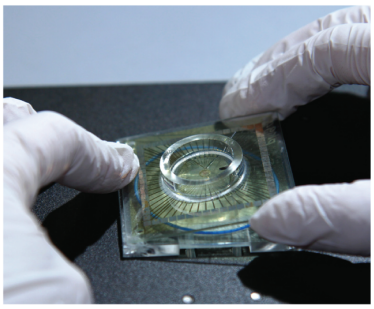

Step 1b) i-ii

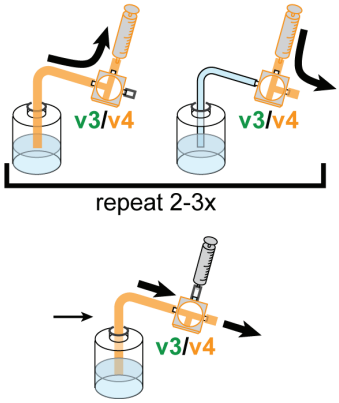

Step 1b) iii-v

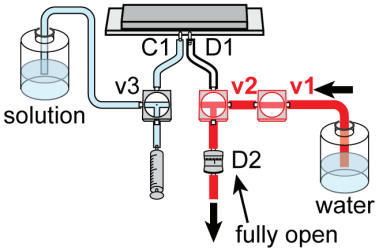

Step 1b) vi

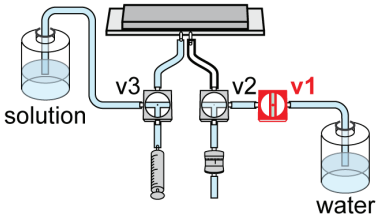

Step 1c) i

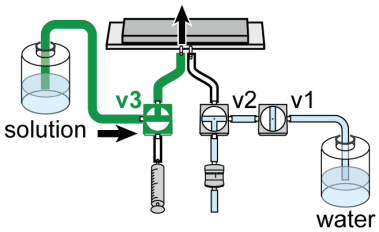

Step 1c) ii

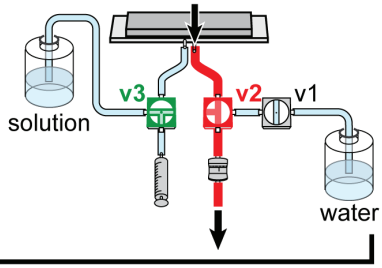

Step 1c) iii

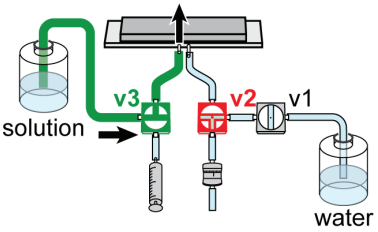

Step 1c) iv

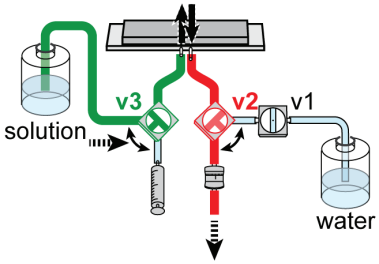

Step 1c) v

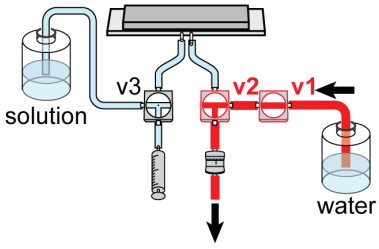

Step 1c) vi

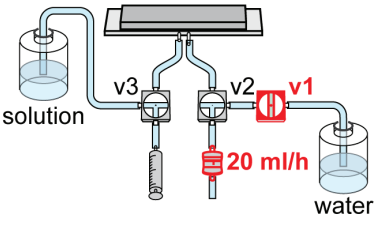

Figure 3. Experimental procedure Step 1: Filling of MEA chamber. Step 1a) Placing the MEA chamber on the baseplate. **Step 1b)** Preparation of perfusion and vacuum. **Step 1c)** Filling the MEA. Detailed description is given in the text.
doi:10.1371/journal.pone.0106148.g003

- Ag/AgCl pellet reference electrode (Science Products E-201ML)
- Insulated connector (e.g. wire ferrule with shrink-on tube) and optical shield (shrink-on tube) for reference electrode
- Holder for reference electrode
- Pharmacology: 50 µM L-AP4 (Sigma A7929 or Abcam ab120002), 10 µM NBQX (disodium salt, Tocris 1044), 10 µM RS-CPP (Tocris 0173) to block synaptic transmission to bipolar cells, 100 µM $BaCl_2$ (Sigma 342920) to block glial currents [15]

Other. Nitrocellulose filter papers (e.g. 13 mm diameter, 0.45 µm pore size, cat. no. HAWP01300, Merck Millipore, Billerica, USA).

Experimental Procedure

Step by step instructions

All specifications (e.g. flow control settings) are given for the equipment listed above and might have to be adjusted for different equipment. Although the procedure is explained for the 60-electrodes pMEA by Multi Channel Systems in combination with a MEA1060 amplifier, most steps could be transferred to experiments with other perforated MEA systems. For *in vitro* ERG recordings, most steps remain the same. Necessary adaptations and additional steps can be found in the section "Special considerations for *in vitro* electroretinogram recordings".

Setting up for pMEA recordings (including retina preparation and hardware preparation) takes approximately 40–60 minutes depending on the complexity of the setup and the visual stimulation. Except for the steps involving the vacuum system and preparation of the filter paper, all steps are very similar to conventional MEA recordings. Further, no coating of the MEA with substances such as poly L-Lysin (used to fix the retina on non-perforated MEAs) is necessary for pMEA recordings. Overall, pMEA recordings require about 10 minutes more preparation time than conventional MEAs.

IMPORTANT: Whenever negative pressure is applied to the MEA chamber, make sure that this is either for only a very short time or that you are perfusing with fresh solution in parallel. Due to the shape of the MEA chamber and the surface tension of the solution, the solution level in the middle of the chamber – directly above the perforated membrane – is significantly lower than at the edges of the chamber (see inset in Fig. 2). Therefore, the MEA chamber always needs to be almost full; otherwise air will enter the vacuum system which can harm the retina and impede the constant negative pressure necessary for stable recordings.

Step 1: Filling of MEA chamber. Illustrated in Figure 3. In this step, the MEA amplifier is prepared, the pMEA is filled with solution, and the vacuum is established. Two aspects are crucial in this step: first, that the MEA baseplate is tightly sealed, and second, that all air bubbles are removed from the perfusion-vacuum system.

a) Place pMEA on MEA baseplate

i. Place a rubber ring in the notch of the MEA baseplate.

IMPORTANT: Make sure that the ring is placed firmly in the notch

ii. Carefully place a clean and dry pMEA onto the ring. To do so, first place one edge of the MEA against the elevated edge of the MEA holder and then lower the MEA down onto the holder.

NOTE: By default, electrode number 15 is the reference electrode. Depending on the MEA amplifier this can be more or less easily changed. If you want to use the standard settings, make sure that the big reference electrode of the MEA is connected to recording pin 15 of the amplifier. This is achieved by placing the MEA with its reference electrode pointing to the right.

iii. Carefully touch the MEA chamber and try to move it: it should not move if it is placed correctly, otherwise it might wobble on the rubber ring.

iv. Close the amplifier.

b) Prepare perfusion and vacuum tubing

i. Upper perfusion: Wash and fill the tubing with physiological solution by the use of the syringe. Start gravity flow and then close the valve (v4). Do not yet connect it to the MEA chamber.

ii. Lower perfusion: Wash and fill the tubing of the lower perfusion in the same way. Close the valve

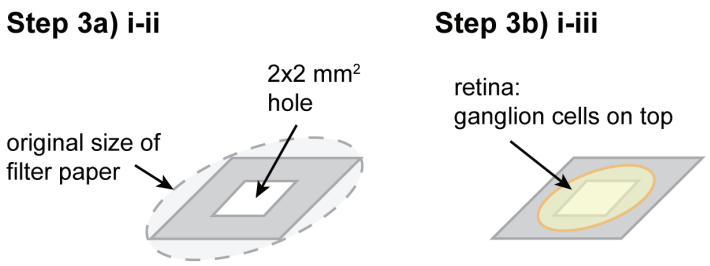

Figure 4. Experimental procedure Step 3: Fixation on filter paper. Step 3a) Preparation of filter paper. **Step 3b)** Fixation of retina on filter paper. Details are given in the text.
doi:10.1371/journal.pone.0106148.g004

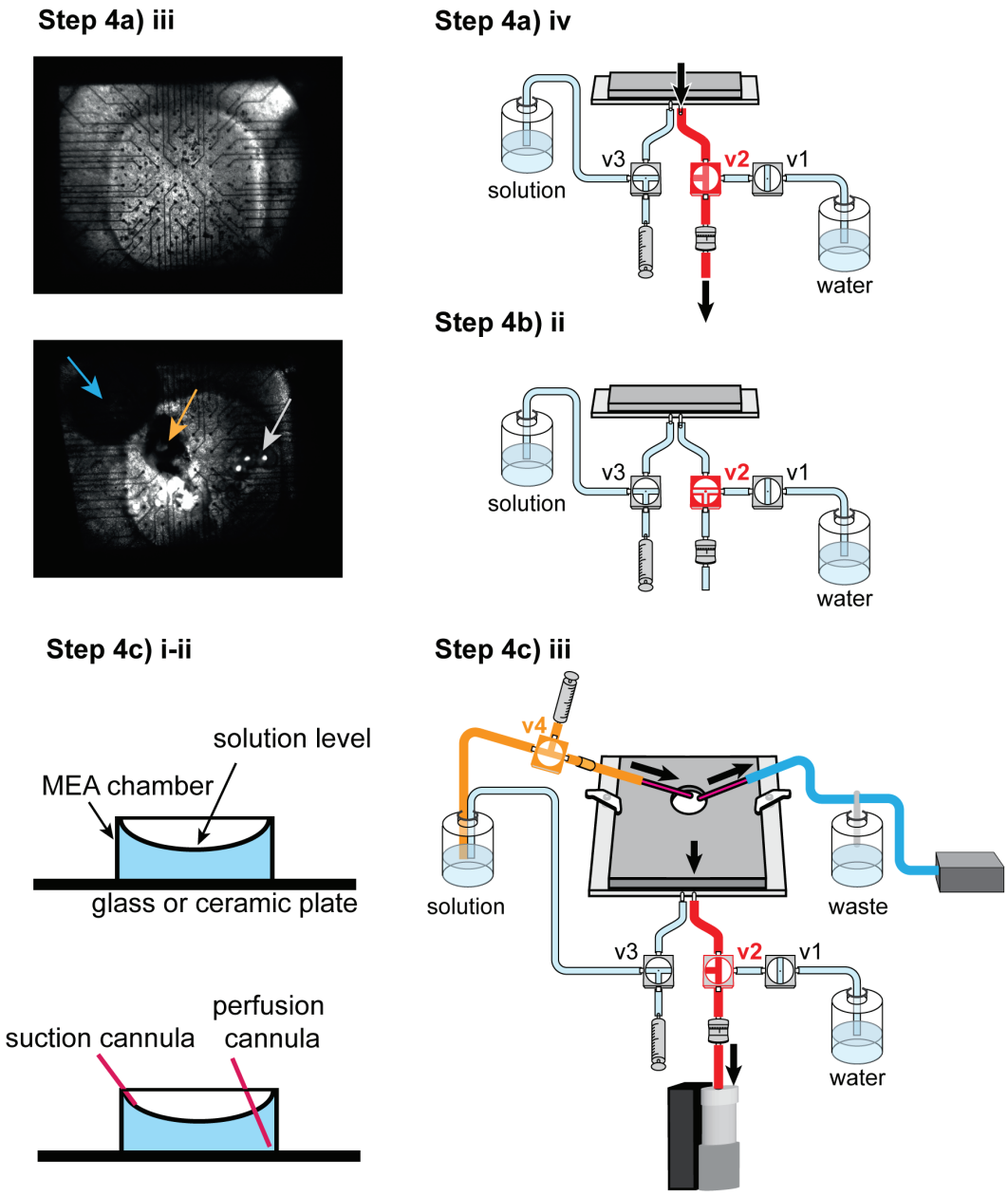

Figure 5. Experimental procedure Step 4: Transfer of retina to MEA chamber and setup. Step 4a) Placing the retina on the electrodes. **Step 4a) iii:** Top: Good MEA preparation. All electrodes are clearly visible; the retina looks homogeneous, flat, and without tears or holes. The retina and filter paper are nicely centered over the middle of the electrode array. Bottom: Bad MEA preparation with air bubble (blue arrow) and holes due to excessive negative pressure (gray arrow). Further, the filter paper is shifted towards the upper left corner. Orange arrow: optic nerve head. **Step 4b)** Transfer of MEA amplifier to setup. **Step 4c)** Installation of upper perfusion loop. Details are given in the text.
doi:10.1371/journal.pone.0106148.g005

(v3) so that no solution flows into the MEA chamber.

iii. Connect the lower perfusion to the left (shorter) cannula of the MEA baseplate and the vacuum tube to the right (longer) cannula.

iv. Set the valves so that the connection of the vacuum system to the MEA is closed (v2) but the connection to the water bottle is open (v1). Open the fine flow control (D2) to maximal flow.

v. Place the free end of the tubing into a bottle with water and switch on the constant vacuum pump

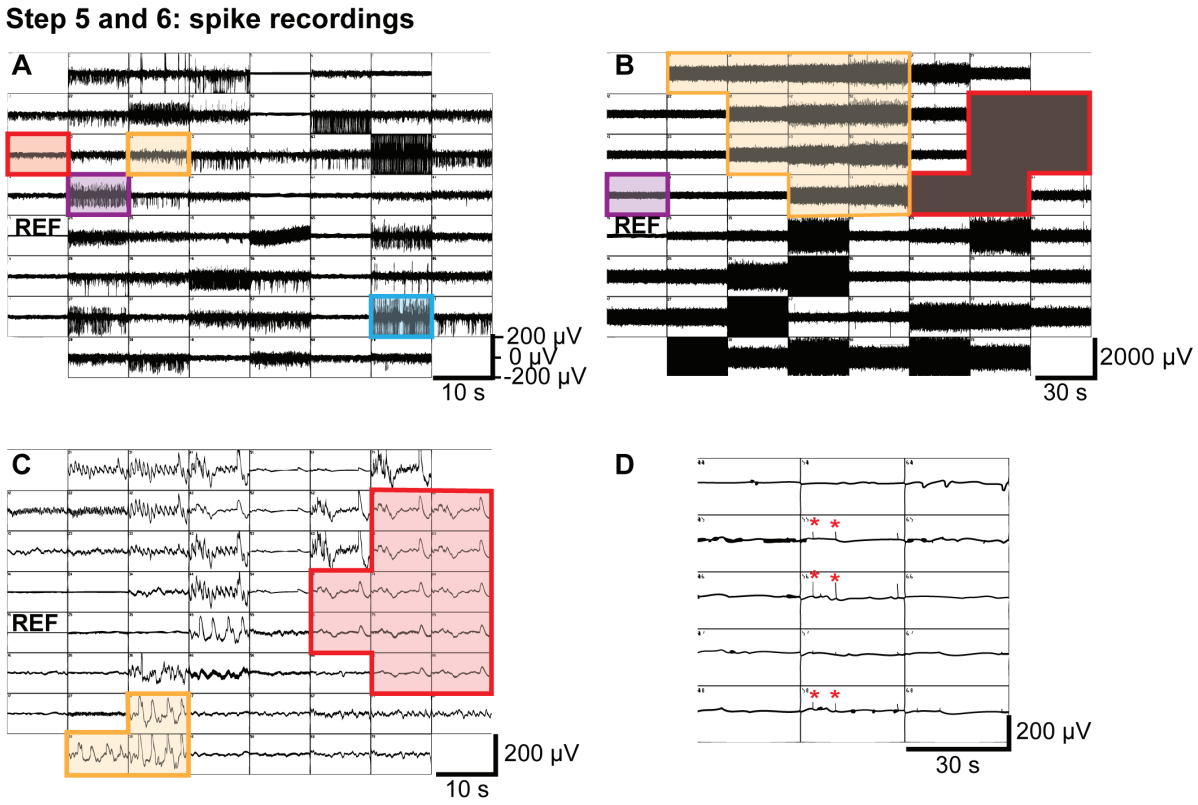

Figure 6. Experimental procedure Steps 5 and 6: Recording data (Spike recordings). A) Snapshot of a 500 Hz high-pass filtered MC_Rack display. Spiking activity with good signal-to-noise is visible on many electrodes. **B)** Snapshot of MC_Rack display after overflow. Noise with amplitudes of 200 to over 1000 µV due to wet electronics is visible on most electrodes. **C)** Snapshot of MC_Rack display several hours after strong overflow. Slow noise on many electrodes is visible either if the electronics is not fully dry yet or when the electronics has been irreversibly harmed. **D)** Snapshot with slow fluctuations and spike-like noise peaks (red asterisks). See text (Step 5 and 6, troubleshooting) for details.
doi:10.1371/journal.pone.0106148.g006

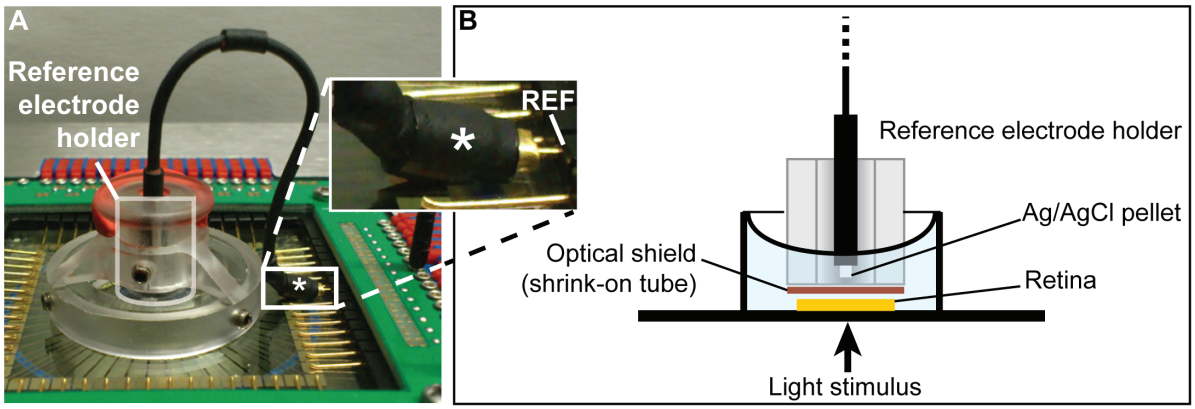

Figure 7. Additional steps for *in vitro* ERG recordings. A) Additions to Step 1: The AgCl reference is positioned over the MEA by a reference electrode holder and is attached to pin 15 (REF) by a wire ferrule insulated by shrink-on tubing (asterisk). **B) Additions to Step 5:** Schematic of the reference electrode and its holder as shown in A. Note the optical shield needed to avoid photoelectric artifacts resulting from light hitting the reference electrode.
doi:10.1371/journal.pone.0106148.g007

(set to ~80–100 mbar). Remove major air bubbles by flicking at connections that might trap air.

vi. When the tubing is filled with water, close the valve towards the water bottle (v1) so that all liquid flow is stopped.

c) Fill the MEA

In this step, the MEA and the cannulas of the MEA baseplate are washed, air bubbles are removed, and the MEA chamber is filled.

i. Fill the MEA by opening the valve of the lower perfusion (gravity flow, v3).

IMPORTANT: Solution should enter the MEA chamber within approximately 1–2 seconds; otherwise the system is most probably not tightly sealed. If it does fill slowly, stop gravity flow immediately, and open the amplifier to prevent the electrode contacts (top plate) from getting wet. See also troubleshooting section 1.

ii. When the MEA chamber is almost full, close the valve of the perfusion (v3). Then open the valve of the vacuum system towards the MEA (v2) and thereby suck out the solution from the MEA chamber. Repeat filling and emptying 2–3 times to wash the MEA chamber.

iii. Fill the MEA chamber again.

iv. Repeatedly open and close the lower perfusion and the vacuum system (alternating) to remove air bubbles from the MEA chamber as well as from the cannulas and the tube connected to the vacuum cannula. Make sure that the MEA chamber does not run empty during this procedure (this will introduce new bubbles) and that it is filled almost completely after having removed all air bubbles. Close the valves to the baseplate (v2, v3).

v. Remove again air bubbles from the tubing by washing through with water (open v1) and "flicking off" air bubbles.

IMPORTANT: Make sure that ALL air bubbles are removed from MEA baseplate cannulas, the MEA chamber, and the vacuum system.

vi. Close all valves and set the fine flow control to approximately 20 ml/h.

NOTE: The setting of the fine flow control determines the negative pressure that will eventually be applied to the retina. The retina will tear and be sucked through the perforation if that pressure is too high.

Step 2: Retina preparation. Prepare the retina as usually for physiology experiments. Pay special attention to removing the vitreous thoroughly in order to get good electrode contact. Further, do not introduce any holes or tears into the retina during preparation, especially when removing the optic nerve. Also do not cut the retina since any incisions or holes in the tissue might cause turbulences in the liquid flow through the perforation or might counteract the establishment of the necessary negative pressure.

Step 3: Fixation on filter paper. Illustrated in Figure 4. The filter paper is needed to flatten the retina without cutting the tissue.

NOTE: Using a filter paper is essential for small retinas with a strong curvature, such as mouse retina. In the case of big retinas (e.g. rabbit, pig, cow, human), a filter paper is often not necessary. Here, the retina is cut into small pieces, which have almost no curvature and which can be placed directly on the electrodes by the use of brushes. Sometimes, even large retinas can roll up after having been cut into small pieces. In this case, a filter paper can be used to flatten the retina.

a) Prepare filter paper

i. Use a piece of a razor blade to cut a ~2×2 mm hole into a filter paper.

ii. Cut the edges of the filter paper.

b) Place retina on filter paper

i. Center the retina with photoreceptors down over the hole in the filter paper.

ii. Carefully press the edges of the retina onto the filter paper with forceps. Start in one corner, and then fix the opposite corner while carefully flattening the retina. You may hold down on the already fixed part with one pair of forceps while fixing the opposite side with a second pair.

iii. Fix the rest of the retina while carefully flattening it.

Step 4: Transfer of retina to MEA chamber and setup. Illustrated in Figure 5.

a) Transfer retina to MEA chamber

i. Transfer the filter paper with the attached retina to the MEA chamber. This is best done with a spoon filled with solution so that the retina is always immersed in solution.

ii. The filter paper should be oriented such that the ganglion cells are facing the electrodes. Usually, this means that the filter paper has to be turned upside down.

iii. Center the retina over the electrodes. You can orient yourself using the layout of the wires connected to the electrodes.

IMPORTANT: Do not use forceps since you might destroy the electrodes or the perforated foil, instead use soft brushes to move the filter paper.

iv. Once the retina is centered, open the valve to the vacuum pump (v2). This will create negative pressure, pull the retina towards the electrodes, and hold it in place.

IMPORTANT: While applying negative pressure, the MEA chamber will slowly run dry. The next step has thus to be performed relatively swiftly.

b) Transfer MEA assembly to setup

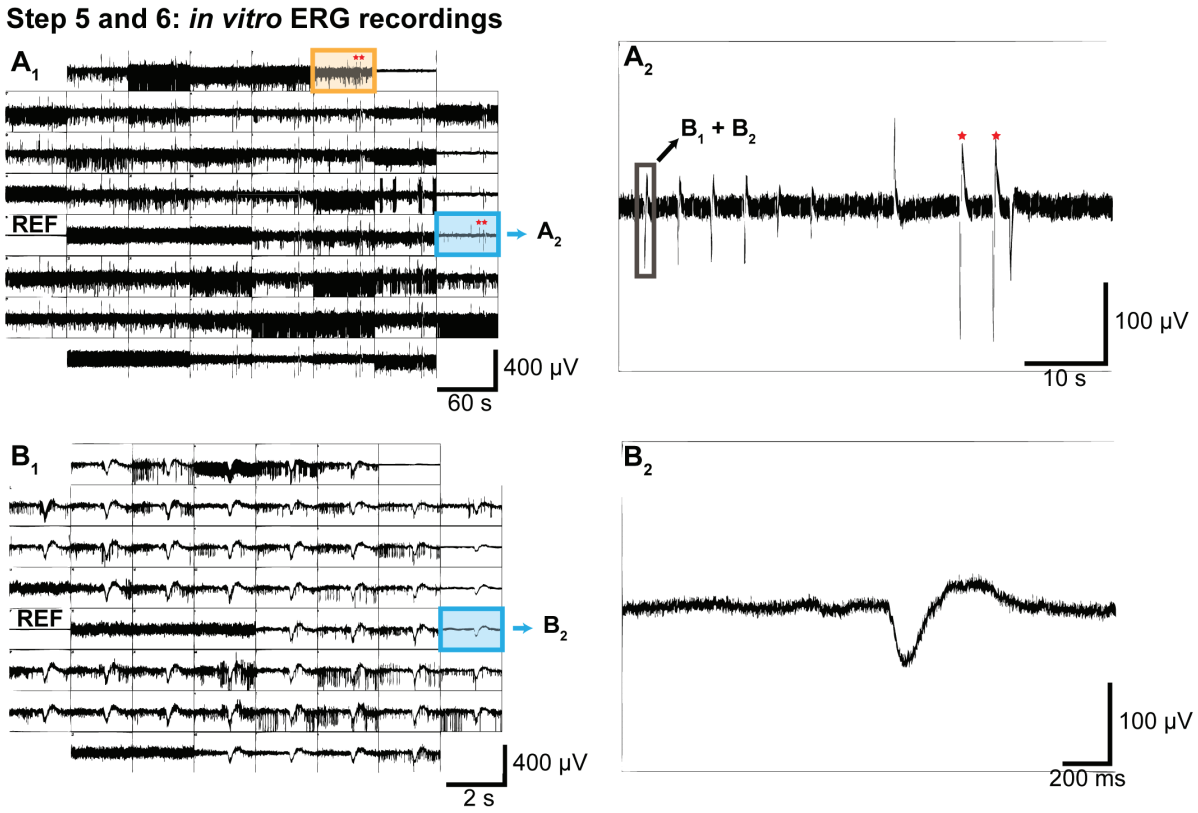

Figure 8. Experimental procedure Steps 5 and 6: Recording data (*in vitro* ERG recordings). A_1) Snapshot of the Longterm Data Display (raw data) from MC_Rack. Note that on most electrodes the ganglion cell spikes mask the *in vitro* ERG responses (e.g. the electrode marked in orange). Only the highest contrast flash elicits a response that is visible on most electrodes (red asterisks), while on some electrodes without ganglion cell spikes the *in vitro* ERG responses are clearly visible (electrode marked in blue). Reference electrode 15 (REF) is on the left. **A_2)** Zoomed view of the electrode marked in blue from panel A_1 showing the responses to flash stimuli of different contrast (highest two contrasts marked with red asterisks). The low-pass filtered data around the time highlighted by the box is shown in B_1+B_2. **B_1)** Data Display with 200 Hz low-pass filter applied. There is a clear response on almost all electrodes. Not all spikes get filtered out by the low-pass filter. Note the different time scale than in A_1. **B_2)** Zoomed view of the electrode marked in blue from panel B_1 that shows a very clear low frequency *in vitro* ERG response without contamination by ganglion cell spikes.
doi:10.1371/journal.pone.0106148.g008

i. If you performed the earlier steps outside of your recording setup, now move the MEA amplifier quickly into the setup and place it in the light path for visual stimulation.

ii. Once the MEA is in place, close the valve to the vacuum pump (v2). The retina is now sticking to the perforated membrane and will not easily move. Nevertheless, you should avoid moving the MEA amplifier while no negative pressure is applied. The vacuum can stay switched off (i.e. valve v2 can stay closed) for the next steps to prevent the MEA chamber from running dry.

c) Installation of upper perfusion loop

i. Add the top perfusion cannula into the MEA chamber. Make sure it is on the bottom and at the edge of the chamber. Placing it on the bottom of the chamber prevents dripping of solution into the bath, which would cause turbulence and noise in the recordings. Placing it into the edge of the chamber helps to prevent touching and damaging the retina.

ii. Add the suction cannula so that its opening is at the desired solution level (as high as possible without risking overflow).

iii. Switch on the top perfusion (v4) and the suction, and open the valve to the vacuum pump (v2).

NOTE: The lower perfusion is not used during the experiment. Flow through the perforation would cause turbulences and hence noise.
IMPORTANT: The flow speed of the upper perfusion has to be at least as fast as the suction speed of the (lower) vacuum pump, otherwise the MEA chamber will run dry. However, it is advisable to have the upper perfusion at a higher speed. The solution level in the MEA chamber will then rise up to the level at which solution is sucked away by the upper suction. Therefore, the cannula of the upper suction has to be placed low enough

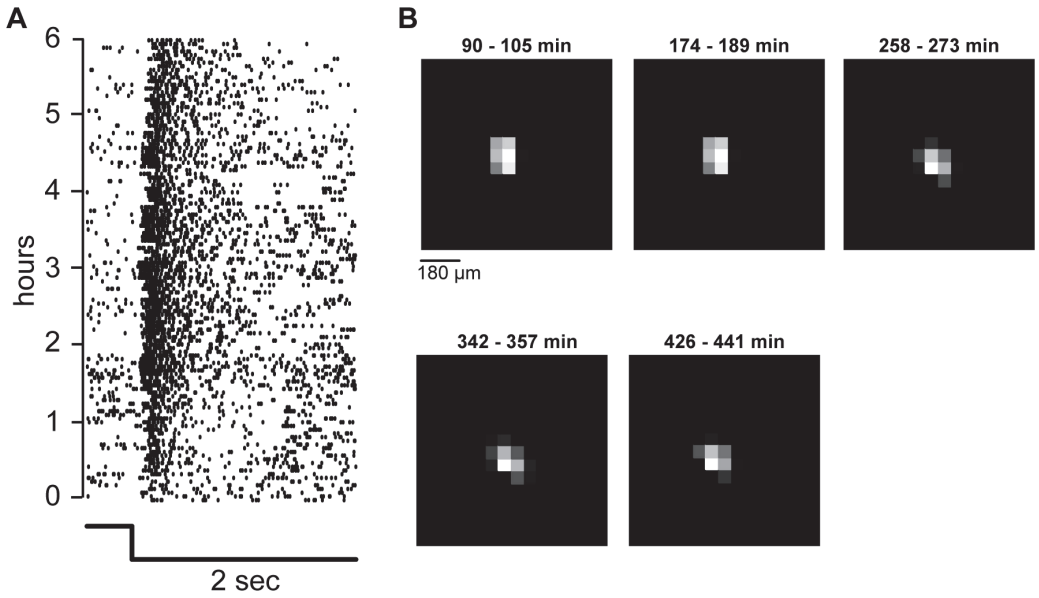

Figure 9. Recording stability. A) Responses of one ganglion cell to a step in contrast over 6 hours. A two second light decrement step has been shown >120 times over a period of 6 hours. Each dot in the raster plot represents one spike produced by the ganglion cell. The ganglion cell stably responded to the stimulus during the whole recording time. Changes in latency and number of spikes are due to different mean brightness levels used during the experiment. **B)** Receptive field of one ganglion cell calculated from checkerboard stimuli. 15×15 checkers out of 40×40 shown here. The stimulus has been repeated approximately every 90 minutes. Time above each receptive field map: presentation time of the checkerboard stimulus (0 min = beginning of experiment). The receptive field location and shape was stable during the whole 8 hours, indicating that the retina did not move significantly.
doi:10.1371/journal.pone.0106148.g009

to prevent overflow on one hand, and high enough to ensure sufficient liquid level.

Step 5: Check electrode contact. Illustrated in Figure 5 and 6. To check the contact of the retina with the electrodes, one can use visual inspection and check the signal-to-noise ratio.

a) Visual inspection

If the retina can be imaged in your setup (e.g., with an infrared camera system), visual inspection of the retina can be used to judge preparation and contact of retina with electrodes (photographs in Fig. 5). Contact with electrodes is usually good if the retina looks flat and if most or all electrodes can be seen through the retina. However, in the region of the optic nerve, the retina is often not totally flat. Now also the visual stimulus can be focused on the photoreceptors and centered on the middle of the electrode field.

b) Setting up MC_Rack software

Consult manuals provided by Multi Channel Systems for installation and setup of MC_Rack for recording of ganglion cell activity. In general, it is advisable to have a Longterm Data Display showing unfiltered activity for each electrode. In addition, it is useful to have a Data Display showing high-pass filtered data, i.e. spiking activity. To implement this, add a filter before the display with a 500 Hz high-pass Butterworth 2nd order filter. See also step 6 (spike recordings) and "Special considerations for *in vitro* electroretinogram recordings".

c) Signal-to-noise ratio

In addition to the *number* of electrodes with activity, the *amplitude* of this activity is crucial for the success of subsequent spike sorting. If the retina is flattened well, all electrodes should show activity (exceptions: those lying directly under the optic nerve, and the ground electrode). When inspecting the high-pass filtered data, the noise level should not exceed 20 µV and spiking activity should have an amplitude of 100–250 µV (signal-to-noise ratio of at least 5; see Fig. 6A). As a rule of thumb, the signal is strong if spiking activity is well visible or even filling the display window when the display y-axis is set to 200 µV; the spikes should be sortable for amplitudes of at least 100 µV. Raw data with smaller activity will most probably not be sortable.

NOTE: Spontaneous activity of ganglion cells can be very sparse in the beginning of the experiment. The retina should always be allowed to settle and adapt to the new environment (negative pressure, change in temperature, …) for at least 20 minutes before recording data. Usually, spontaneous activity appears during this time if it has not been present from the beginning. If there are very few spikes, the retina can be probed with some light stimuli and the elicited spikes can be used to check signal-to-noise ratios. If activity is still sparse and/or signal-to-noise ratio is low, increase the negative pressure slightly by changing the flow control to 30–50 ml/h. Also consult the troubleshooting section for possible counter-measures.

Step 6: Recording data. Illustrated in Figure 6. Spike recordings: In most cases, one uses MEAs to record spiking activity from ganglion cells. As mentioned above, when using the MC_Rack software, it is useful to show the data in two displays while recording: (1) Longterm Display with unfiltered data. Set the display y-axis to 500 µV for good overview. (2) Data Display with high-pass filtered data for better visualization of spiking activity. Add a 2nd order Butterworth 500 Hz high-pass filter before a Data Display and set the y-axis to 100 or 200 µV. Figure 6A shows such

filtered electrodes with the y-axis set to 200 μV. In optimal recordings, all electrodes would have activity with amplitudes such as the electrode marked in "blue". A signal-to-noise ratio and activity level like on the "purple" electrode is also sufficient for good spike sorting. Whether the spikes on the "orange" electrode are sortable will depend on how distinguishable the waveforms of various cells and of the noise are in each particular case. On the "red" electrode, the signal-to-noise ratio is clearly too small. The reference electrode 15 is on the left.

NOTE: Usually, the MEA is placed in the setup such that the vacuum and perfusion cannulas are at the "front" (i.e., facing the researcher). Note that in this configuration the physical reference electrode 15 is on the right side of the MEA chamber and electrodes 15–18, 25–28, 35–38 etc. will be in the upper half of the MEA (60-electrode pMEA, 8×8 layout). The orientation of electrodes in the MC_Rack displays is mirrored compared to that: the reference electrode 15 is on the left, electrodes 11–14, 21–24 etc. are displayed in the top half. Consequently, when showing a stimulus which moves from the top left to the bottom right corner of the MEA chamber, the retinal activity will move from the bottom right to the top left corner of the MC_Rack display.

Step 7: Removing the retina. The retina is a relatively thin tissue. It can thus rarely be removed entirely from the pMEA after the recording. In general, removing the retina works best when the vacuum system is off, the lower perfusion is switched on and the flow is slightly increased via the syringe. Use a very fine brush to help removing the retina from the recording chamber. Subsequent analysis of the tissue (e.g. histological stainings) is only possible if the negative pressure is kept as low as possible during the experiment and if the retina is removed very carefully from the perforated foil. This is easier for thicker (healthy) and bigger (species-dependent) retinas; however, we also performed experiments with very thin and vulnerable degenerated retinas (rd1 mouse model with quickly degenerating rods and cones). Even these retinas could be removed and stained after the recordings when only little negative pressure had been applied during the experiment (data not shown).

Special considerations for *in vitro* electroretinogram (ERG) recordings

Electroretinography (ERG) is the most common electrophysiological technique for recording retinal activity in both human patients and living animals. ERG signals reflect mainly the activity of cells oriented vertically in the retina, namely photoreceptors, bipolar cells and Mueller glia. The pMEA system can be configured to record an *in vitro* electroretinogram. For this, an additional reference electrode is added to achieve a recording configuration in which the retina is "sandwiched" between recording electrode(s) and reference electrode to record transretinal potential changes. Follow all procedures as outlined above for spike recordings and add the following steps:

Step 1a) iii. Place pMEA on MEA baseplate. Illustrated in Figure 7. An external reference electrode has to be attached to recording pin 15 of the amplifier before the next step. A wire ferrule soldered to an Ag/AgCl reference can be used to connect to pin 15. Shrink-on tube around the wire ferrule insulates from the MEA chamber's internal reference contact.

Step 5a) Visual inspection. After the stimulus is centered, the external reference electrode has to be put into the MEA chamber. Placing the reference electrode before this step would obscure the camera's view and make stimulus centering impossible (in configurations like in an upright microscope). It might be necessary to once again remove the upper perfusion/suction to place the reference electrode and reposition it after the external reference is in place. The Ag/AgCl pellet of the reference has to be positioned 2 to 3 mm above the center of the MEA electrode field and optically shielded from direct stimulus illumination to prevent photoelectric artifacts in the reference electrode. The upper suction has to be adjusted such that the solution level is high enough to completely immerse the Ag/AgCl pellet of the reference in the solution. Perforations in the optical shield that allow solution to pass but do not compromise the optical shielding, can help to achieve this. The suction has to be carefully adjusted so the solution level does not fluctuate; otherwise there will be periodic low frequency noise that can spoil the *in vitro* ERG data (see troubleshooting section).

Step 6) Recording data. Illustrated in Figure 8. For *in vitro* ERG recordings, the Data Displays in MC Rack are set up in a similar way as described above, except that the filter setting for the second Data Display is set to low-pass filter. This eliminates some of the ganglion cell spiking responses for clearer visualization of the slow *in vitro* ERG responses. Add a 2nd order Butterworth 300 Hz low-pass filter before the Data Display and set the y-axis to 100 or 200 μV.

In our experiments, synaptic transmission to bipolar cells and glial currents were pharmacologically blocked to isolate the field potentials generated by photoreceptor activity. Figure 8 shows example responses to several flashes with different contrasts (panels A) and a close-up view of a single flash response (panels B) from a good *in vitro* ERG recording.

Troubleshooting

Due to the two perfusion loops, solution leakage or overflow is encountered more often than with standard MEAs. Thus, most issues encountered during pMEA recordings will be linked to electronics which got in contact with solution, and will be recognizable in the noise level of the electrodes. In this troubleshooting section we discuss the 10 most frequent problems. The titles indicate the main aspect which will be noticed during MEA recordings. Each issue is then followed by a description of its possible causes, the detailed symptoms which can be observed, and the required actions.

1. MEA chamber fills very slowly during Step 1c) i. Possible cause (1): Leakage due to insufficient seal between MEA chamber and the baseplate (Step 1a) i). The solution from the lower perfusion can fill the space between the MEA chamber and the MEA baseplate, rather than being pushed quickly through the perforation.

Detailed symptoms (1): A long delay is observed between opening the lower perfusion and filling of MEA chamber.

Required actions (1): Immediately stop lower perfusion! Open the MEA amplifier immediately in order to prevent the solution from reaching the recording pins of the amplifier. MEA baseplate and the rubber ring should be dried completely and the MEA chamber should be placed again such that it does not move. Minor leakages are hard to detect while filling the MEA chamber and will reach the recording pins only later during the recording. These slow leakages are, however, very rare.

Possible cause (2): Mishandling of the MEA chamber (e.g. applying a relatively large force) can weaken the seal between MEA ring (forming the wall of the chamber) and MEA glass plate. This can introduce local gaps in the glue between wall and floor of the MEA chamber from where the solution can leak.

Detailed symptoms (2): A high latency is observed between opening the lower perfusion and filling of MEA chamber. Solution usually leaks from a specific region where the seal is weak.

Required actions (2): Immediately stop lower perfusion! Open the MEA amplifier immediately to avoid solution reaching

the recording pins. Experiment cannot be continued with this MEA chamber which should be sent to Multi Channel Systems for maintenance.

NOTE: Often the leak is not detected while filling the MEA but is reflected later in the signal as noise on a group of electrodes.

2. Noise observed on (almost) all electrodes. Possible cause: Overflow or leakage due to badly adjusted upper perfusion, negative pressure and suction. In this case the MEA chamber can either run dry, thereby damaging the tissue and introducing turbulences, or it can overflow and solution can reach the recording pins.

Detailed symptoms: Overflow or leakage lead to high amplitudes of noise in most of the recording electrodes, specifically the recording pins that are in contact with the solution. Figure 6B shows such a case. As visible in these traces, some electrodes are affected so strong (marked in red) that the noise is filling the whole display even when setting the y-axis to 1000 μV. But even on the electrode marked in purple the noise level is much higher than usual with amplitudes of around±200 μV. Often, distinct groups of electrodes have similar noise patterns (here one group in red and one in orange). This can be caused by "local" leakage/ overflow when only some of the pins have become wet. Alternatively, even when all pins are wet, the solution might seep into the electronic housing with different speeds and might thus affect the electronics of different channels with different delay.

Required actions: In the case of overflow, the recording should be stopped and the MEA amplifier should be removed immediately. If overflow was detected as soon as it started, the recording pins should be dried and carefully cleaned with a wet cotton swab (deionized water and/or alcohol). A tissue paper can be used to suck out solution from the small openings where the recording pins are connected to the MEA amplifier. If the overflow was detected at a later stage, a relatively large amount of solution could have entered the MEA amplifier. The whole amplifier should be placed in deionized water for several hours to wash out the salts, after which it requires 1–2 days to dry. The amplifier should then be tested using the model probe supplied with the amplifier. If the signal from the amplifier appears noise free (less than 20 μV amplitude) and does not show any slow fluctuations, it should be tested with a MEA chamber (filled with PBS or other physiological solution). If the electronics are not completely dry, localized slow noise waves, again affecting subgroups of electrodes (Fig. 6C: one group in red, one in orange), can be detected. However, if this noise persists after 2–3 days, most probably not all salts were washed out which possibly harmed the electronics. In such case, the MEA amplifier needs to be submitted to Multi Channel Systems for maintenance.

3. Stable high frequency noise on one or several electrodes. Possible cause: One or several electrodes are deteriorated either due to frequent and/or long-term use. Alternatively, they can also be harmed by use of forceps during placing or removing the retina.

Detailed symptoms: In contrast to noise caused by overflow, deteriorated electrodes often show very stable high frequency noise. Even if only one electrode is affected, the noise might spread to neighboring electrodes.

Required action: Refer to manuals provided by Multi Channel Systems for hardware or software based grounding of the affected electrodes.

4. Fluctuations/noise on a group of electrodes. Possible cause (1): Air bubbles under the retina, either above or below the perforated foil, can lead to significant noise levels. These bubbles usually arise either when air is trapped in the perfusion tubing or when the solution level in the MEA chamber becomes too low.

Detailed symptoms (1): Due to the continuous negative pressure, such air bubbles – once they are trapped in the MEA chamber – move around, change in size, and might disappear and reform constantly. They can easily be recognized when imaging the retina in the MEA chamber (Fig. 5, Step 4a) iii). These bubbles can often induce big voltage fluctuations on several electrodes, can cause large noise amplitudes or inhibit contact between solution/ tissue and electrodes (electrode traces are flat, as if connected without solution and retina).

Required Action (1): If air bubbles are caused by too little solution in the MEA chamber, the chamber should be filled immediately by increasing the flow speed of the upper perfusion and/or moving the suction cannula further up. If the bubbles do not disappear, the following two counter-measures can be applied:

i. *Increasing the negative pressure (short term)*

Increasing the negative pressure might "suck out" the air bubbles through the perforation. Make sure that your perfusion is fast enough so that the solution level does not drop again. Watch the retina closely to not increase the negative pressure too much, which might tear or destroy the retina. Try switching back to lower negative pressure once the air bubbles are removed.

ii. *Opening the lower perfusion*

Opening the lower perfusion can push out air bubbles from the space between retina and electrodes into the MEA chamber. This is often more effective when no negative pressure is applied; however, care should be taken not to wash away the retina.

Parallel application or quickly alternating the above mentioned measures can sometimes facilitate removal of the bubbles. It is advisable to image the retina and to observe noise levels and activity on the electrodes during this process.

NOTE: Air bubbles often cannot be removed and the experiment has to be stopped. The described measures are only advisable before recording data since the turbulences caused by the air bubbles as well as by the counter-measures will move the retina and might change the footprint of the recorded cells on the MEA electrodes.

Possible cause (2): Starting overflow or leakage due to incoherent upper perfusion, negative pressure and suction.

Detailed symptoms (2): As the overflow/leakage starts, only a group of electrodes is affected. In contrast to deteriorated electrodes, the noise is often a mixture of low and high frequencies and might show large fluctuations.

Required actions (2): Immediately stop the experiment and open the MEA amplifier. Check troubleshooting point 2 for further procedures.

5. High baseline noise on all electrodes. Possible cause: Poor grounding of the upper perfusion or suction system.

Detailed symptoms: Noise levels above 20 μV on all electrodes. Usually without big fluctuations.

Required actions: Refer to manuals provided by Multi Channel Systems for improving grounding.

6. Synchronous spike-like activity on all or a group of electrodes. Possible cause: Poor grounding of the upper perfusion can lead to spike-like activity (see Fig. 6D).

Detailed symptoms: Synchronous, regular, and sparse high frequency noise is observed on a group or all electrodes e.g. due to regular dripping of solution from the perfusion system.

Required actions: Check manuals provided by Multi Channel Systems for improving grounding.

7. Low signal-to-noise ratio. Possible cause: Poor retina preparation and placement or insufficient negative pressure can often lead to low signal-to-noise ratio.

Detailed symptoms: Spiking activity is visible, but very small.

Required actions: Once the retina is placed in the MEA chamber, contact can only be improved by increasing negative pressure. The flow control should not be set to values higher than 40–60 ml/h (depending on the species and retina condition). However, short term application of higher pressure (up to 100 ml/h flow) might increase signal-to-noise ratio. The negative pressure should not be changed during the recordings since it can move the retina and change the footprint of the recorded ganglion cells.

NOTE: During retina preparation, the vitreous should be completely removed from the retina and the retina should be properly flattened and carefully fixed on the filter paper.

8. Retina is suddenly out of focus (when imaging from top). Possible cause: The solution level is rising due to too fast upper perfusion or impaired suction.

Detailed symptoms: In the beginning of the experiment, while letting the retina settle down, the retina appears suddenly out of focus when imaged from top (sudden blurring of the camera image).

Required actions: Immediate adjustment of upper perfusion, suction, and/or negative pressure prevents overflow in this case. Noise levels have to be observed carefully to ensure that the solution does not reach the recording pins.

NOTE: The described procedures refer to very sudden blurring in the first 10–20 minutes after switching on the perfusion system. After many hours of recording, the solution level might have changed slightly so that the retina appears out of focus. In this case, usually no counter-measure is required.

9. Low frequency noise on some or all electrodes 1–2 days after overflow. Possible cause: Following an overflow, the electronics in the amplifier needs 1–2 days to dry completely. Low frequency noise indicates that either the electronics is not yet completely dry or that it has been harmed from salts.

Detailed symptoms: Slow noise waves, often affecting subgroups, are visible on most or all electrodes (Fig. 6C: one group in red, one in orange).

Required actions: The amplifier should be left to dry for an additional day. However, the noise can still persist after 2–3 days if not all salts were washed out which possibly harmed the recording pins or the electronics. In such case, the MEA amplifier needs to be submitted to Multi Channel Systems for maintenance.

10. Noise during ERG recordings. Possible cause: The external reference electrode is very sensitive to fluid level changes in the MEA chamber. Periodic fluctuations of the fluid level can be caused by use of a peristaltic pump for perfusion or, more importantly, by intermittent interruptions in the suction stream. This is usually caused by periods of rapid suction of solution until the fluid level drops below the suction cannula opening, followed by no solution being sucked out until the fluid level gets high again.

Detailed symptoms: Simultaneous high amplitude signals on most electrodes that often appear in regular intervals of up to tens of seconds. The noise signals can resemble ERG responses or look like spikes but can also have less stereotypical shape. Sometimes the noise signals look similar to sinusoidal 50 Hz noise.

Required actions: Adjust the depth and angle of the suction cannula. Ideally, an uninterrupted suction stream should be achieved that sets the fluid level in the MEA chamber such that the external reference electrode is fully immersed in solution at all times. This might require several adjusting steps and longer waiting times until the solution level stabilizes, and changes to the suction cannula might be necessary.

Anticipated results

pMEAs provide good signal-to-noise ratios

The vacuum applied through the perforation of pMEAs greatly enhances the contact between the tissue and the electrodes. In our experience, on good recording electrodes, we can detect and properly spike-sort one to three cells per electrode. On some electrodes, no spikes might be visible because blood vessels or the optic nerve lie on these electrodes. Our pMEAs have 59 recording electrodes. After multiple experiments, some electrodes might deteriorate and might not be usable anymore due to increased electrical noise. Good signal-to-noise ratios are crucial for most spike sorting algorithms since they usually depend on amplitude and principal component analysis of the recorded spikes. To get an estimate of the number of recorded cells that one might expect in such experiments, we counted the number of extractable cells in 153 recordings from mouse retina (without pre-selecting "good" and "bad" experiments), and found on average 38 ± 18 cells (median $\pm$ standard deviation) with 6 sorted cells in the worst and 110 cells in the best case. Pig (domestic and minipig) and human retina recordings often had even better signal-to-noise ratios and therefore lead to more sortable cells. In pig retina, we found on average 48 ± 31 cells (range: 13–109, $n = 20$ retinal pieces), and in human retina 51 ± 32 cells (range: 6–154, $n = 35$ retinal pieces).

pMEAs allow stable long-term recordings

Nutrient and oxygen supply is crucial for the survival of ganglion cells. If ganglion cells do not receive enough oxygen and nutrients, their responsiveness might change and/or decrease over time which leads to instability of light responses in long-term recordings. During conventional MEA experiments, the supply to the ganglion cell might be insufficient. It has been shown by Egert et al. that with pMEAs, the oxygenation of the bottom layer cells is greatly enhanced, and it can be assumed that the same is true for nutrient supply to these cells [8]. We additionally show the viability of the ganglion cells by example data from a long-term recording. We showed various light stimuli to a mouse retina on a pMEA during 6 hours and recorded ganglion cell responses. A very simple stimulus – namely a full-field step in contrast – was part of the stimulus set and has been presented over 120 times during these 6 hours. Fig. 9A shows the responses of one ganglion cell to all these repetitions. As visible in the raster plot (every dot represents one spike), the cell responded to every repetition of the stimulus, also after 6 hours of continuous recording. The differences in response latencies are due to switches in absolute brightness which have been part of the stimulus protocol.

pMEAs prevent movement of retina

The third advantage of applying negative pressure to the retina is that movement of the tissue is prevented. We recorded ganglion cell responses to binary checkerboard stimuli to calculate receptive fields and to visualize tissue movement. The checkerboard stimulus consisted of 40×40 checkers with 60 µm edge length. Fig. 9B shows the spatial receptive field of a single ganglion cell, repeatedly calculated from 15 min of checkerboard stimulus, presented every 90 minutes during this 8 hour recording. Location and shape of the calculated receptive fields are very stable. Note that slight changes in shape are also due to different absolute brightness levels used at each presentation (from scotopic to photopic).

Conclusions

In this article we provide a step-by-step procedure for retina recordings with perforated MEAs. Although the preparation and adjustment of the additionally required perfusion and vacuum system might seem complicated at a first glance, the additional time required for perforated compared to conventional MEA recordings amounts to only around 10 minutes. Further, little additional material is needed when switching from standard to perforated MEA recordings. Finally, pMEAs provide better oxygenation of ganglion cells which allows for long-term recordings, and the applied negative pressure facilitates flattening and placement of small retinas with strong curvature. Especially when isolating single cell responses from MEA recordings, the user will appreciate the resulting high signal-to-noise ratio in pMEA recordings.

Acknowledgments

We thank the University Eye Hospital Tübingen, Germany for support and organization of human retina donations; the Department of Experimental Surgery, Tübingen, Germany (Dr. Martin Schenk) for providing us with domestic pig eyes, and the Department of Urology, Tübingen, Germany (Dr. Martin Vaegler) for Göttingen minipig eyes. Further, we thank Prof. Vladimir Kefalov (Washington University, St. Louis, MI, USA) for his advice while establishing in-vitro ERG recordings.

Author Contributions

Conceived and designed the experiments: KR AT HS TAM. Performed the experiments: KR AT HS MM. Analyzed the data: KR AT HS MM BB TAM. Contributed reagents/materials/analysis tools: KR AT HS MM BB TAM. Contributed to the writing of the manuscript: KR AT HS SI MM BB TAM.

References

1. Meister M, Pine J, Baylor DA (1994) Multi-neuronal signals from the retina: acquisition and analysis. Journal of neuroscience methods 51: 95–106.
2. Zeck GM, Masland RH (2007) Spike train signatures of retinal ganglion cell types. The European journal of neuroscience 26: 367–380.
3. Frey U, Egert U, Heer F, Hafizovic S, Hierlemann A (2009) Microelectronic system for high-resolution mapping of extracellular electric fields applied to brain slices. Biosensors & bioelectronics 24: 2191–2198.
4. Chichilnisky EJ, Kalmar RS (2002) Functional asymmetries in ON and OFF ganglion cells of primate retina. The Journal of neuroscience: the official journal of the Society for Neuroscience 22: 2737–2747.
5. Segev R, Goodhouse J, Puchalla J, Berry MJ 2nd (2004) Recording spikes from a large fraction of the ganglion cells in a retinal patch. Nature neuroscience 7: 1154–1161.
6. Masland RH (2001) The fundamental plan of the retina. Nature neuroscience 4: 877–886.
7. Feitl M, Stett A, Nisch W, Boven KH, Möller A (2006) On Micro-Electrode Array Revival: Its Development, Sophistication of Recording, and Stimulation. In: Taketani M, Baudry M, editors. Advances in Network Electrophysiology: Using Multi-Electrode Arrays.
8. Egert U, Okujeni S, Nisch W, Boven KH, Rudorf R, et al. (2005) Perforated Microelectrode Arrays Optimize Oxygen Availability and Signal-to-Noise Ratio in Brain Slice Recordings. Mikrosystemtechnologie Kongress. Freiburg.
9. Gonzalez-Sulser A, Wang J, Motamedi GK, Avoli M, Vicini S, et al. (2011) The 4-aminopyridine in vitro epilepsy model analyzed with a perforated multi-electrode array. Neuropharmacology 60: 1142–1153.
10. Gonzalez-Sulser A, Wang J, Queenan BN, Avoli M, Vicini S, et al. (2012) Hippocampal neuron firing and local field potentials in the in vitro 4-aminopyridine epilepsy model. J Neurophysiol 108: 2568–2580.
11. Grosser S, Queenan BN, Lalchandani RR, Vicini S (2014) Hilar somatostatin interneurons contribute to synchronized GABA activity in an in vitro epilepsy model. PLoS One 9: e86250.
12. Motamedi GK, Gonzalez-Sulser A, Dzakpasu R, Vicini S (2012) Cellular mechanisms of desynchronizing effects of hypothermia in an in vitro epilepsy model. Neurotherapeutics 9: 199–209.
13. Schmidt SL, Chew EY, Bennett DV, Hammad MA, Frohlich F (2013) Differential effects of cholinergic and noradrenergic neuromodulation on spontaneous cortical network dynamics. Neuropharmacology 72: 259–273.
14. Multi Channel Systems MCS GmbH (2013) 60pMEA200/30iR-Ti.
15. Bolnick DA, Walter AE, Sillman AJ (1979) Barium suppresses slow PIII in perfused bullfrog retina. Vision Res 19: 1117–1119.

Publication 3 – Light adaptation changes retinal output

Alexandra Tikidji-Hamburyan*, Katja Reinhard*, Hartwig Seitter, Anahit Hovhannisyan, Christopher A Procyk, Annette E Allen, Martin Schenk, Robert J Lucas, Thomas A Münch. *Retinal output changes qualitatively with every change in ambient illuminance.* Nature Neuroscience 2015 Jan; 18(1):66-74. *equal contributions

Framework:

This is an original research paper. It shows for the first time concisely that ambient luminance can change retinal output in the majority of retinal ganglion cells. It combines findings on different levels within the early visual system, the retina and the Lateral geniculate nucleus (LGN). This is a collaborative publication together with the lab of Robert Lucas, University of Manchester (in vivo recordings) and Martin Schenk, University of Tübingen (pig retina recordings).

My contributions:

Many of the micro-electrode array recordings including data processing were done by me (represented in e.g. Fig 8, Fig S2, Fig S3, Fig S4). I helped develop the disk stimulation paradigm (Fig 8). In the patch-clamp experiments, most of the ganglion cells were recorded by me (Fig 6). I did all of the immunohistochemistry and microscopy on the recorded ganglion cells, while TAM did the stratification analysis and analysis of the spiking responses.

Other contributions:

ATH made the initial discovery of the phenomenon and described it in her doctoral thesis. She performed experiments (Fig 2-4) and was involved in analysis of the other MEA experiments. KR planned and performed many of the MEA recordings (Fig 5, Fig 8, Fig S2, Fig S3, Fig S4, Fig S5). She did most of the data analysis, together with ATH and TAM and also helped with analyzing the in vivo data. AH made some of the MEA recordings. In vivo experiments were designed by CAP, AEA and RJL, performed by CAP and AEA and analyzed by CAP, AEA and KR. MS provided access to pig eyes. The manuscript was written by KR, TAM and ATH with help from CAP, AEA and RJL and me.

ARTICLES

nature neuroscience

Retinal output changes qualitatively with every change in ambient illuminance

Alexandra Tikidji-Hamburyan[1,4,5], Katja Reinhard[1,5], Hartwig Seitter[1], Anahit Hovhannisyan[1], Christopher A Procyk[2], Annette E Allen[2], Martin Schenk[3], Robert J Lucas[2] & Thomas A Münch[1]

The collective activity pattern of retinal ganglion cells, the retinal code, underlies higher visual processing. How does the ambient illuminance of the visual scene influence this retinal output? We recorded from isolated mouse and pig retina and from mouse dorsal lateral geniculate nucleus *in vivo* at up to seven ambient light levels covering the scotopic to photopic regimes. Across each luminance transition, most ganglion cells exhibited qualitative response changes, whereas they maintained stable responses within each luminance. We commonly observed the appearance and disappearance of ON responses in OFF cells and vice versa. Such qualitative response changes occurred for a variety of stimuli, including full-field and localized contrast steps and naturalistic movies. Our results suggest that the retinal code is not fixed but varies with every change of ambient luminance. This finding raises questions about signal processing within the retina and has implications for visual processing in higher brain areas.

The mammalian visual system functions over a wide range of light intensities, spanning roughly a dozen orders of brightness magnitude. Specialized photoreceptors, the rods and cones, are active at low and high light intensities, respectively. At low light intensities, only rods are active (scotopic vision). With increasing luminance, cones become active (mesopic vision), while at high luminance, rods saturate but cones remain active (photopic vision). In the outer retina, signals from the photoreceptors are both combined within and distributed across more than ten different bipolar cell types. In the inner retina, the bipolar cell terminals interact with amacrine cell interneurons to bring about sophisticated responses in the output neurons of the retina, the ganglion cells. The diversity of ganglion cells is characterized by physiological parameters[1], as well as by functional specifications such as directional selectivity, approach sensitivity, object motion sensitivity and many more[2]. On a simpler level, all ganglion cells can be classified by their response polarity to step-like changes in brightness: ON cells increase spiking activity to light increments, OFF cells to light decrements, and ON-OFF cells to both. This property is often called "polarity" and is one of the most basic features for further classification of ganglion cells in the vertebrate retina.

It is not well understood how the properties of ganglion cell responses (that is, the retinal output) vary with changes in ambient luminance. On one hand, it is conceivable that adaptation in retinal circuitry counteracts the changes in ambient luminance to maintain a stable representation of the incoming visual scene. On the other hand, several reports suggest that the retinal output changes with changing ambient luminance. Some of these changes are linked to the switch from scotopic to mesopic vision; that is, from purely rod-mediated to mixed rod- and cone-mediated signaling. Examples include color vision[3], changing responses due to surround activation[4–6], changes in temporal and spatial frequency processing[7,8], 2-amino-4-phosphorobutanoic acid (APB)- and strychnine-resistant OFF responses appearing in response to dim high-contrast stimuli[9], or luminance-dependent inhibitory modulation of rod signals[10]. In addition, the coexistence of several parallel rod pathways[11] might allow different retinal processing within the scotopic range as well: for example, the primary rod pathway shifts from encoding of single photons to encoding of contrast modulations[12]. Furthermore, light adaptation switching from circuit-based to photoreceptor-based mechanisms has been found within both scotopic[13] and photopic regimes[14]. Finally, melanopsin-driven changes in retinal responses have been described within the photopic range[15]. Most of these reports concentrate on individual building blocks of the retinal circuit, and each describes luminance-dependent changes over a limited range of light intensities. What is missing is a systematic description of the retinal output and its modulation across a wide range of light intensities, from scotopic to photopic light levels.

We asked whether luminance-dependent changes of the responses of ganglion cells are a widespread phenomenon or whether they are restricted to few cell types or specific luminance transitions. Using multielectrode array (MEA) recordings from isolated mouse retina, we systematically surveyed ganglion cell responses across many orders of ambient luminance, in discrete steps separated by 1 log unit. We found that the output of the retina was qualitatively different at each tested light level. For example, we found OFF cells gaining or losing ON responses, and vice versa. Such response changes occurred

[1]Retinal Circuits and Optogenetics, Centre for Integrative Neuroscience and Bernstein Center for Computational Neuroscience, University of Tübingen, Tübingen, Germany. [2]Faculty of Life Science, University of Manchester, Manchester, UK. [3]Department for General, Visceral and Transplant Surgery, Institute for Experimental Surgery, University Hospital Tübingen, Tübingen, Germany. [4]Present address: Department of Neurosurgery and Hansen Experimental Physics Laboratory, Stanford University, Stanford, California, USA. [5]These authors contributed equally to this work. Correspondence should be addressed to T.A.M. (thomas.muench@cin.uni-tuebingen.de).

Received 25 August; accepted 28 October; published online 8 December 2014; doi:10.1038/nn.3891

to both simple stimuli and complex natural movies. Sometimes, but not always, these changes depended on modifications of the center-surround receptive field structure or on GABA-mediated inhibition. Consequently, diverse mechanisms seem to underlie the response changes in different ganglion cell types. In addition, we show that such alterations of the retinal output are not restricted to the isolated mouse retina but can also be observed *in vivo*, where the changing output of the retina is reflected by changing activity of dorsal lateral geniculate nucleus (dLGN) neurons, and in the retina of another species, the pig. It thus appears that luminance-dependent changes of retinal output are a phenomenon that is preserved across species and that higher visual centers are exposed to these changes.

RESULTS

Experimental procedure

We presented our visual stimuli, grayscale images, to isolated mouse retinas using a digital projector (**Supplementary Fig. 1**). The ambient light level was set by placing neutral density (ND) filters into the light-path, such that the intensity of the stimulus could be attenuated without changing the computer-controlled images presented by the projector. Consequently, the contrast of the stimuli remained constant during the experiment (**Fig. 1a**), independent of the ambient light level. The actual physical intensity of the stimuli associated with each ND-filter is shown in **Figure 1b**. We estimate (see Online Methods) that ND8 and ND7 correspond to scotopic conditions, ND6 weakly activates cones, ND5 is fully mesopic, and ND4 is photopic. Unless otherwise noted, we started our experiments from low intensity (ND8) and increased it in the course of the experiment (that is, from ND8 to ND4 in 1-log-unit steps). The retina was kept at each ambient luminance for 20 to 70 min, and we showed the same set of stimuli at each light level.

With this experimental procedure, we recorded from ganglion cells using MEAs and compared their responses across different ambient light levels, initially using spatially homogeneous contrast steps ('full-field steps') of positive and negative contrast ('white step' and 'black step', ± 66% Weber contrast; **Fig. 1a**). We will refer to increases of a cell's spike rate to light increments (both after the white step onset and black step termination) as ON responses and to increases of a cell's spike rate to light decrements (both after the black step onset and white step termination) as OFF responses.

Luminance-dependent changes of retinal output

To our surprise, most ganglion cells changed their response type (ON, OFF or ON-OFF) at different ambient luminance. The example cell in **Figure 2a** had OFF responses to all light decrements, but its ON responses were not consistent across light levels. First, they were absent at ND8 but present at ND7 to ND4. Second, when present, they occurred with either short or long latency ('early' or 'delayed',

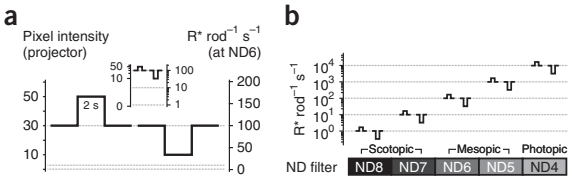

Figure 1 Overview of experimental procedure. (**a**) Light stimuli were grayscale images on a gray background. The full-field step stimulus had a Weber contrast of ± 66%. Inset, stimulus depicted at logarithmic scale. (**b**) Absolute intensity of stimuli, converted to R* rod^{-1} s^{-1}, as a function of the ambient luminance set by neutral density (ND) filters.

respectively), measured as time to peak of the firing rate. Third, at any given light level, the ON responses to the two stimuli (white and black steps) were either the same—that is they were absent (ND8) or had the same latency (ND4)—or they had different latencies (ND7, ND6 and ND5). We will refer to the latter as 'asymmetry' of the response at a given luminance. In summary, the OFF responses of this cell at the different light levels (ND8 to ND4) differed from each other only quantitatively (amplitude, duration and moderate latency changes), whereas the ON responses were affected qualitatively.

We take a 'qualitative change' of a response across light levels to mean not only its presence versus absence, but also alternations between early and delayed responses. Indeed, early and delayed responses, as seen in **Figure 2a**, seem to be two distinct response categories, and not merely separate realizations of a continuous latency distribution. The distributions of the response latencies (**Fig. 2b**), measured separately in ON cells and OFF cells and separately for ON and OFF responses, was unimodal for the preferred contrast—that is, for ON responses in ON cells and for OFF responses in OFF cells—with a median time to peak between 130 and 140 ms. In contrast, the distributions of latencies for responses to the anti-preferred contrast had an additional mode peaking between 600 and 800 ms, in both ON cells and OFF cells. In other words, delayed ON responses occurred only in OFF cells, whereas delayed OFF responses occurred only in ON cells. The bimodality of the distribution indicated two categories of responses and let us treat early and delayed responses as qualitatively different. In our analysis below, we concentrate only on the qualitative response changes. Quantitative aspects were not considered.

The response patterns of ganglion cells usually remained stable while probed at the same luminance level, tested up to 70 min (luminance levels with unreliable responses were excluded from the analysis; see Online Methods). When the response pattern of a cell changed at luminance transitions, the new pattern was observed from the very first stimulus presentation. The earliest time point we tested was 10 s after the luminance transition because a luminance increase by 1 log unit itself evoked a strong response in all cells.

The cell in **Figure 2a** could be classified as OFF at some light levels and as ON-OFF at other light levels on the basis of its full-field step responses. Since such luminance-dependent response changes were common in many ganglion cells, we used an ON/OFF classification based on properties of the cells' linear filters. We calculated the linear filters from responses to Gaussian white noise full-field flicker (see Online Methods). Cells with a downward deflected linear filter were marked as OFF and cells with an upward deflected filter as ON. In contrast to full-field step responses, almost all cells had consistent linear filter polarities over all luminance levels. The cell in **Figure 2a** fell into the OFF category at each light level, despite its changing ON responses. Note that with such a classification scheme, ON-OFF cells will not be categorized as such, but would fall into either the ON or OFF category, depending on which input was predominant; similarly, cells with an exceptionally strong surround might be mistaken for a cell of opposite polarity. Furthermore, if ON and OFF inputs were very well balanced, the cell would have a noisy linear filter. However, such cases were rare, and we excluded from the analysis all cells with noisy or changing linear filters across light levels (34 out of 517 recorded units were excluded).

We obtained 219 OFF and 264 ON cells (as based on their linear filter properties) from 15 wild-type retinas. The validity of this ON/OFF classification approach was supported by the observations that >97.5% of ganglion cells from the ON group consistently responded to light increments (that is, their preferred stimulus) at all light levels and >97.4% of cells from the OFF group consistently

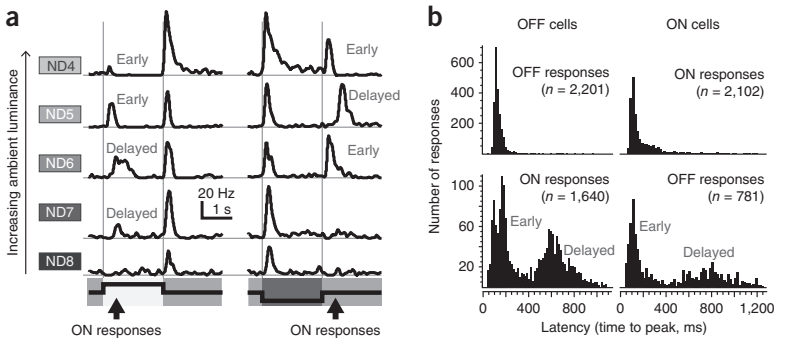

Figure 2 Early and delayed anti-preferred responses. (**a**) Responses (firing rate) of a single OFF ganglion cell to white and black full-field contrast steps (average firing rate to 45 repetitions at each of five different light levels, ND8 to ND4). (**b**) Histogram of response latencies (time to peak) in OFF cells (left column) and ON cells (right column), measured from responses of all units at all light levels, to both black and white full-field steps.

responded to light decrements. It follows that luminance-dependent changes mostly occurred in response to the anti-preferred contrast. In the following analysis, we concentrated on the responses to anti-preferred contrast steps (**Fig. 3**), and we describe the ON responses in OFF cells first.

ON responses in OFF ganglion cells

Across all light levels tested, only 9% of our OFF cells never had an ON response. The number of cells displaying early or delayed ON responses changed at different ambient light levels (**Fig. 3a**). Almost 100% of OFF cells had no ON responses at ND8, whereas at ND5, this number fell below 20%. Notably, the early and delayed responses could also occur together (most often at ND5). They were still easily separable in most cases because of the considerable difference in their latencies (for examples, see **Fig. 4** and **Supplementary Fig. 2**).

At every transition of ambient luminance, the ON responses of a considerable fraction of OFF cells changed (**Fig. 3b**), ranging from 38% at the ND8–ND7 transition (within the scotopic regime) to 83% at the ND6–ND5 and ND5–ND4 transitions. Overall, 89% of the OFF cells changed their responses at least once between ND8 and ND4. The response changes were diverse. At any given light level, some cells would lose a certain response type, others would gain it, and some cells would not change. Furthermore, the responses to white steps and black steps changed asymmetrically (**Fig. 3a**). For example, at ND6 there was a predominance of delayed responses to the white step and early responses to the black step, whereas at ND5 the ratio was opposite.

In summary, the presence of ON responses and their variability across light levels were two prominent features in OFF cells: we found that early and delayed ON responses in OFF cells could appear or disappear with changing ambient light levels, that they could occur independently or together during a response and that they could differ for white and black contrast steps. These findings suggest that these early and delayed ON responses in OFF cells may have independent origins and be heterogeneously affected in different OFF cell types by the immediate stimulus history (that is, white or black step) and by ambient luminance.

OFF responses in ON ganglion cells

Occurrences of OFF responses in ON cells (**Fig. 3c**,**d** for summary, **Fig. 4a**,**b** for examples) were less common than occurrences of ON responses in OFF cells. In fact, most ON cells were strongly suppressed by light decrements, such that their spiking activity fell below their spontaneous firing rates, often to zero. Black steps often suppressed spiking for the entire stimulus duration (2 s); white step termination, for about 500 ms (**Fig. 4a**). Strong pre- or postsynaptic inhibition may have counteracted excitation and decreased the occurrence of the OFF responses. Indeed, there were almost no OFF responses to black steps (**Fig. 3c**), with the exception of the photopic ND4 light level, at which 11% of ON cells had early OFF responses. Delayed OFF responses were observed quite frequently after white step termination, especially in scotopic and mesopic light levels (ND7 to ND5).

In our experiments, the luminance-dependent qualitative change of response patterns was such a surprising and yet prominent feature of most ganglion cells that this raises concerns about how trustable and stable these observations are. We tested the following: (1) How strongly are the different response types bound to a particular ambient luminance? (2) Do these response changes occur in morphologically identified ON and OFF cells? (3) Is this finding restricted to *in vitro*

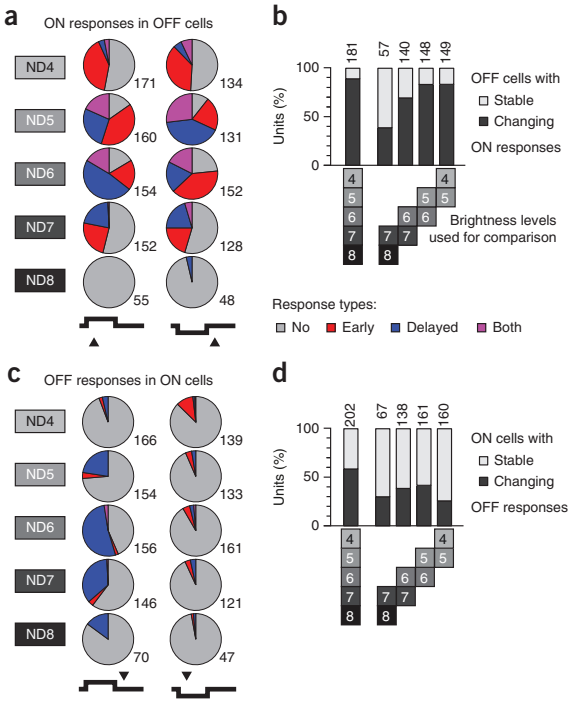

Figure 3 Summary of luminance-dependent response types. (**a**) Fraction of OFF cells displaying no, early and delayed ON responses at each luminance level to white and black full-field step stimuli. (**b**) Fraction of units with stable and changing responses. Cells were defined as stable if they had the same response type (no, early, delayed or both) at all compared light levels, both to the black step and to the white step. All other cells were defined as changing. (**c**,**d**) Same statistics as in **a** and **b** for OFF responses in ON cells. Numbers indicate units included in the analysis, selected on the basis of their reliable responses at these light levels (see Online Methods).

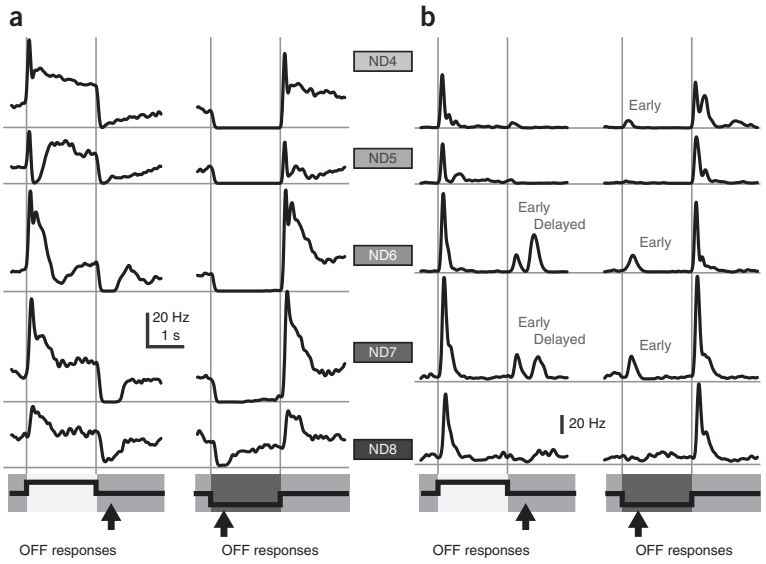

Figure 4 Responses (firing rate) of two ON ganglion cells. Stimulus was a 2-s white or black full-field step, presented at different ambient light levels. (**a**) Many ON ganglion cells were strongly suppressed by OFF stimuli. (**b**) ON ganglion cell with asymmetric and changing OFF responses.

conditions, or may it also be observed *in vivo*? (4) How much of the responses variability is due to the unnatural stimulus properties of full-field contrast steps? Furthermore, we investigated the contribution of center-surround receptive field interactions, GABAergic inhibition and rod-cone interactions to the mechanism of qualitative luminance-dependent response changes.

Response patterns are bound to individual light levels

As described above, the response patterns of ganglion cells were stable at each individual light level but could change after a luminance increase. We next tested whether ganglion cell responses would revert when the luminance returns to the previous level (**Fig. 5a**). Indeed, in the ND8 to ND5 luminance ranges, all recorded cells that changed their responses at a luminance transition (n = 16 from 2 retinas) immediately reverted to the previous pattern after an intermittent exposure to either lower or higher luminance levels (**Fig. 5b**,**c**). However, once exposed to ND4 (photopic level), cells did not immediately return to the response they had at ND5 earlier. This may be due to stronger bleaching caused by this light level (~10^4 R* rod^{-1} s^{-1}) or to some light adaptation triggered by this light level that reverses only slowly. In further experiments discussed below (**Supplementary Fig. 2**), 2 of the 15 cells studied did not revert to their previous response pattern at the ND7 light level after they had a different pattern during an interleaved exposure to ND6, while 13 of 15 cells did revert to their previous response pattern. Taken together, these results suggest that specific response patterns of ganglion cells are strongly associated with distinct luminance levels rather than with the history of luminance or with a luminance-independent drift.

Confirmation using single-cell recordings

Most cells in our data set had ON-OFF responses at least at one light level. Our cell type classification based on linear filter polarity cannot identify 'classical' ON-OFF cells (that is, cells stratifying in both ON and OFF sublaminae of the inner plexiform layer and having short-latency responses to both light increments and decrements) and distinguish them from 'real' ON cells or OFF cells (that is, cells with dendrites stratifying exclusively in the ON or OFF sublamina). To confirm that the latter can indeed have responses to anti-preferred contrast steps at some light level(s), we recorded action potentials from individual ganglion cells using patch electrodes. Most cells were filled with neurobiotin and imaged with confocal microscopy to assess whether they had typical ON or OFF morphology (**Fig. 6a–c**).

We recorded from three PV-5 ganglion cells, the well-studied[16,17] mouse homolog of the transient OFF-alpha cell (monostratified in the OFF sublamina of the inner plexiform layer; n = 2 of 3 cells confirmed with the neurobiotin marker). All three cells had delayed ON responses up to ND5 that disappeared at the photopic light level ND4. For one cell, we repeatedly switched between ND4 and ND5, and the responses reliably reverted (**Fig. 6d**). Consistent with the related MEA experiments (**Fig. 5**), switching from ND4 back to ND5 did not lead to an immediate reappearance of the delayed ON responses; here they reemerged about 1 min after the luminance switch. Four out of 5 more cells of unknown types, stratifying exclusively in the OFF (n = 3) or ON (n = 2) sublamina (**Fig. 6e**), had luminance-dependent response changes, confirming our findings based on MEA recordings.

Luminance-dependent response changes *in vivo*

One caveat of the results described so far is that they have been recorded from the isolated retina, and that these experiments can last several hours. Do luminance-dependent response changes also happen *in vivo*? To test this, we recorded from the dLGN of anesthetized mice (**Fig. 7a**) and projected step stimuli into their eyes that were comparable in absolute intensity and contrast to the stimuli we used for the *in vitro* recordings (**Fig. 7b**). Consistent with our findings in the *in vitro* retina preparation, in the dLGN 18 out of 28 units (n = 5 mice) changed their responses qualitatively with changing ambient luminance (**Fig. 7c**). We could also test higher light levels (ND3 and ND2) *in vivo* than *in vitro* (see also Discussion). More than one-third of the recorded neurons changed their responses within the photopic regime as well (ND4–ND3 and ND3–ND2), including the example shown in **Figure 7d**. These observations suggest that luminance-dependent qualitative changes of retinal ganglion cell responses also occur *in vivo* and that these changes are reflected in the thalamus. This confirms scattered reports of this phenomenon in the literature[3].

Luminance-dependent changes to naturalistic movies

Full-field contrast steps are easy to analyze and interpret. However, they are not a natural stimulus for the retina and visual system in general. The retina might employ specific mechanisms to stabilize the output to a more natural stimulus when it is presented under varying luminance conditions. We tested this by stimulating the retina with a naturalistic movie repeatedly shown at different light levels.

Ganglion cells (n = 172 units from 8 retinas) responded to the natural movie with interleaved sequences of spike bursts ('events') and silence, as described previously[18]. Such bursting events presumably correspond to features in the movie that are relevant to this ganglion

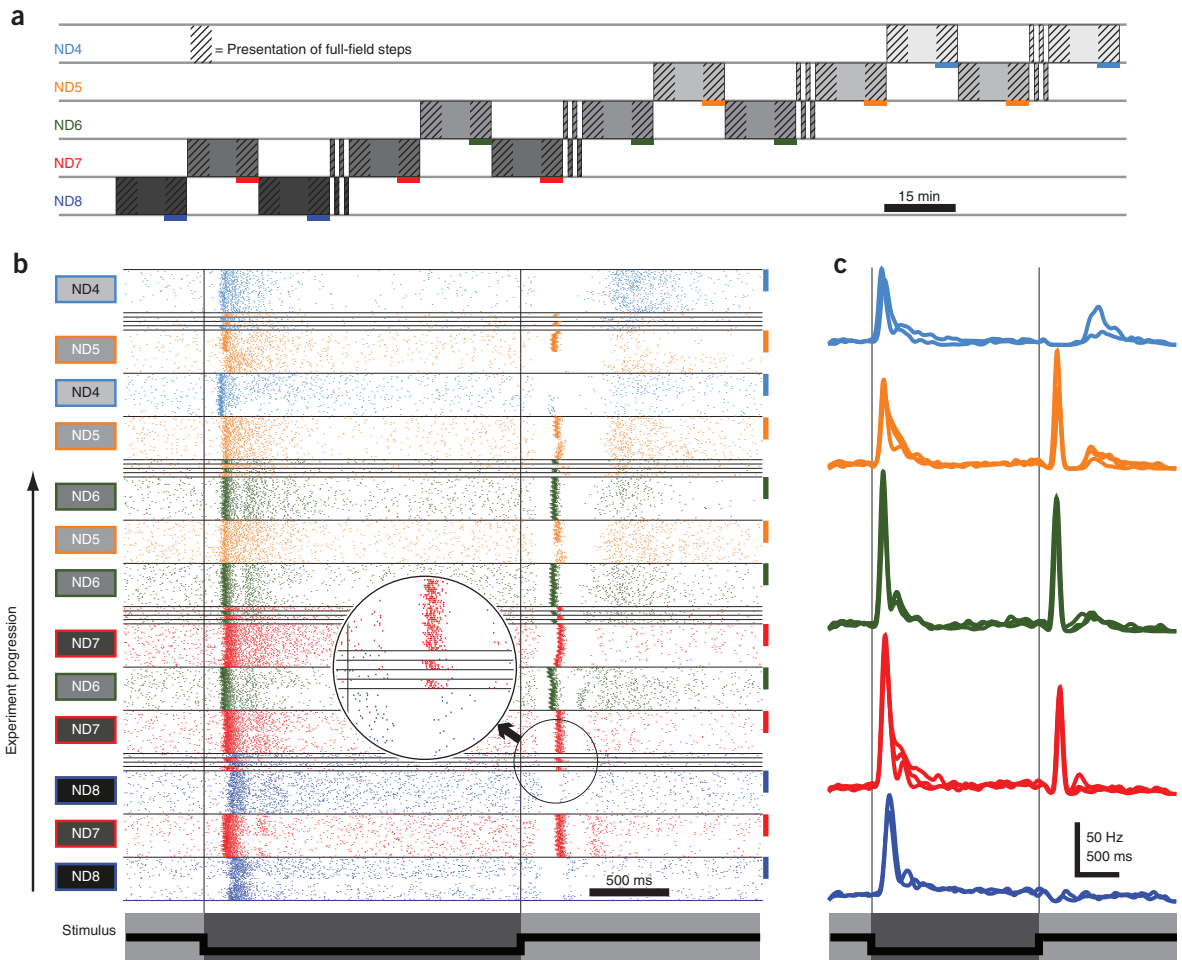

Figure 5 Stability of responses at individual light levels. (**a**) Experimental protocol. Colored bars label the last 5 min at each light level. (**b**) Raster plot of the responses of a single unit to all 730 presentations of the black full-field step (50 repetitions during each 15-min sequence, 5 repetitions during each 1-min sequence). Even quick luminance changes are immediately reflected in a different response pattern (see magnification). Colored bars mark the same experimental sections as in **a**. (**c**) Average spike rates of the responses marked by colored bars in **a** and **b**.

cell. If a cell had a robust bursting event at some light levels but not at others, we classified this as a qualitative response change (see Online Methods for details).

We observed such qualitative changes in 57% of the units (n = 98 of 172). For each of these units, some features (scenes of the movie) evoked a response at all light levels tested, and other features evoked a response only at certain light levels (**Supplementary Fig. 3a**,**b**). Some units (n = 55) were also tested with our full-field step stimulus. Response changes to the movie stimulus and to the full-field step stimulus could occur independently from each other (**Supplementary Fig. 3c**). This suggests that ambient luminance can alter different receptive field properties of ganglion cells, some of which are triggered by a homogeneous full-field step and some by a stimulus with more complex temporal and spatial properties.

Cells' peripheries involved in only some response changes

Most ganglion cells' receptive fields consist of a spatially distinct center and periphery. Stimulation of the center and periphery can evoke responses of opposite polarities in some ganglion cells[19]. Furthermore, it is known that the receptive field structure of some cells changes during light adaptation[5]. Thus, the changing response patterns that we observed in our experiments might have been caused by luminance-dependent changes in the balance of the receptive field center and periphery. To test this, we stimulated the retina with disks of 150 µm diameter with identical contrast properties to the full-field steps (n = 107 units in 4 retinas).

We observed the same variety of response types to the localized disk stimulus as for the full-field stimulation. 80% of the units changed the response type to the disk stimulus at least at one luminance transition, while 20% had stable responses at all light levels (**Fig. 8a**). At any individual luminance transition, between 44% and 61% of the units changed their responses. We also mapped the receptive fields of all units using a binary noise checkerboard flicker stimulus and measured how much of the disk stimulus lay within the receptive field center (**Fig. 8b**). For more than half the units, both with changing or stable responses, 80% or more of the disk stimulus was contained

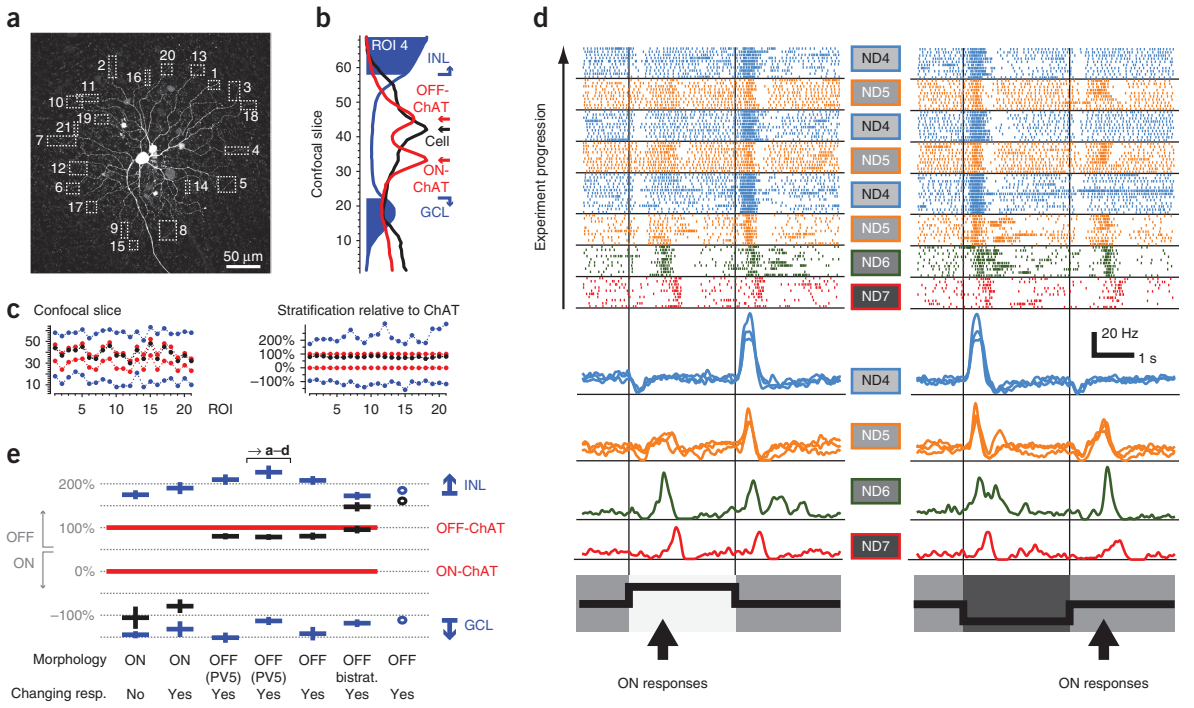

Figure 6 Responses recorded from individual ganglion cells. (**a**–**d**) Results from one PV5 ganglion cell. (**a**) Maximum-intensity projection of a confocal microscopy stack, showing the neurobiotin-filled PV5 ganglion cell and the regions of interests (ROIs) used for analyzing stratification level. (**b**) Fluorescence intensity profile along the *z* axis of ROI 4. Blue, DAPI nuclear label; red, choline acetyltransferase (ChAT) label; black, neurobiotin label. Stratification levels of cell and ChAT bands represent peaks of their intensity profiles. Borders of inner nuclear layer (INL) and ganglion cell layer (GCL) are drawn where the intensity profile dropped below 67% of its peak. (**c**) Left, stratification measurements for each ROI, as in **b**. Right, conversion of stratification relative to ChAT bands. (**d**) This OFF-stratifying cell had pronounced delayed ON responses from ND7 to ND5. (**e**) Dendritic stratification level (black, mean ± s.e.m. relative to the ChAT bands, red) of individually recorded cells. Bistrat., bistratified. For rightmost cell, ChAT staining was not successful. Most cells had luminance-dependent response changes.

within the receptive field center, suggesting that the stimulus had little influence on the periphery. The cell shown in **Figure 8c**, for example, was an OFF ganglion cell that acquired a delayed ON response to the white disk at ND7 and also to the black disk at ND6. The disk stimulus was 100% contained within the receptive field center. In this case, stimulation of the receptive field center alone elicited luminance-dependent response changes. In this and similar cases, luminance-induced reorganization of the center-surround receptive field structure cannot account for changing response patterns.

Nevertheless, the receptive field periphery did influence the responses of many units: the responses to the local disk and full-field stimuli differed from each other at least at one light level in 67 of the 107 units. Distinct responses to localized and full-field stimulation could be observed at all light levels, from ND8 (scotopic) to ND4 (photopic), suggesting that at least some ganglion cells possess a receptive field surround in scotopic conditions.

Notably, we observed several units that stably maintained their response type to disks with changing luminance but that qualitatively changed their responses to full-field steps (**Fig. 8d**). In these units, it is likely that a reorganization of the overall receptive field structure (for example, of center-surround interactions) is responsible for the changes of the responses, and not a reorganization of the central receptive field alone. Taken together, our results suggest that most units can change their responses to local stimulation but that a dynamic reorganization of the overall receptive field structure can be responsible for some qualitative luminance-dependent response changes as well.

GABAergic inhibition involved in some response changes

GABA-mediated inhibition can mask responses of ganglion cells[20,21]; release from GABAergic inhibition at some light levels might therefore be a valid mechanism for luminance-dependent response changes. To test this, we compared the responses of ganglion cells to full-field contrast steps at ND7 and ND6 with and without blockade of ionotropic GABA receptors (5 µM SR-95531 and 100 µM picrotoxin; **Supplementary Fig. 2a**). From two retinas, we extracted 37 units with stable responses during the two repeats of ND7 in control conditions.

The drugs had diverse effects on the ganglion cell responses (**Supplementary Fig. 2b**–**e**): in some cells, GABA blockers prevented luminance-dependent response changes, whereas in other cells they enabled such changes. In yet other cells, responses were not influenced by GABA blockade. In summary, we found that the mechanism of GABAergic response regulation was highly diverse and that it influenced some but not all luminance-dependent qualitative response changes.

Response changes do not require rod-cone interactions

Many ganglion cells changed their response pattern at transitions within the scotopic regime (ND8–ND7). This suggests that rod-cone circuit interactions are not required for all response changes.

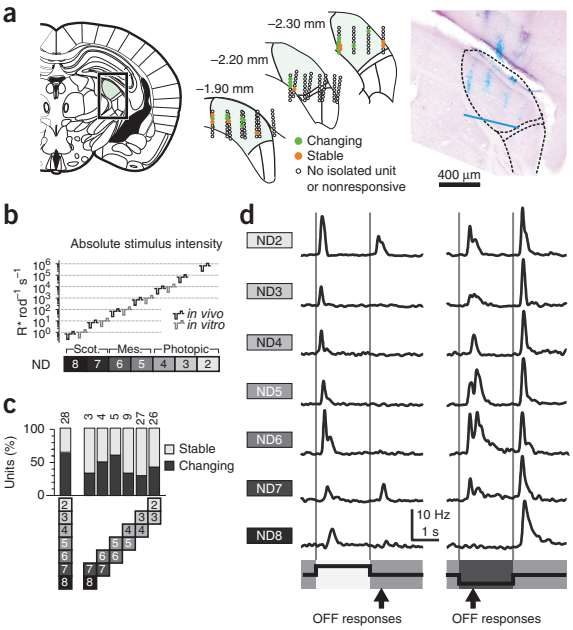

Figure 7 Luminance-dependent qualitative response changes in the dLGN. (**a**) Recording locations in the dLGN, outlined on the left. Middle, reconstructed positions (colored dots) of recording sites in three rostro-caudal positions relative to the bregma. Reconstruction was based on DiI labeling of electrode shanks (right); blue line, maximum depth of recording electrode. Brain schematics based on Paxinos and Franklin[50]. (**b**) Absolute stimulus intensities used for the *in vivo* experiments (black) in comparison to the intensities used during *in vitro* experiments (gray; see **Fig. 1b**). Note that the stimulus range is extended to higher intensities. Scot., scotopic; mes., mesopic. (**c**) Fraction of light-responsive units in the dLGN with changing or stable responses. Conventions as in **Figure 3b**. (**d**) A single ON unit from the dLGN that has both changing and asymmetric OFF responses at different ambient light levels.

To further explore how much of the response variability is brought about by the rod pathways, we used three different mouse models with nonfunctional cone photoreceptors ('rod-only retinas'): *Gnat2*^{cpfl3}, *Pde6c*^{cpfl1} (*Cpfl1*) and *Cnga3*$^{-/-}$ mice, which carry mutations in cone-specific members of the phototransduction cascade: a transducin, phosphodiesterase and cyclic nucleotide–gated channel, respectively.

In retinas from all three cone-deficient mouse lines, we found a similar prevalence of luminance-dependent response changes as in wild-type retinas (**Supplementary Fig. 4**). Together, these results confirm that not all luminance-dependent response changes rely on rod-cone interactions, as such changes can be observed in retinas with nonfunctional cones. Instead, some response changes might reflect more subtle changes in processing due to engaging different rod-mediated pathways[11] at low and high scotopic light levels.

Generalization to other species

To exclude the possibility that luminance-dependent response changes are a feature restricted to the mouse retina, we recorded from the isolated pig retina, using the same procedure as for the mouse retina. Luminance-dependent response changes were also commonly observed in pig ganglion cells (n = 98 cells, three retinal pieces from two different animals; **Supplementary Fig. 5**). While the pig and mouse data differed in some details (for example, hardly any delayed ON responses in pig OFF cells), the phenomenon of luminance-dependent qualitative response changes was observed in both species with comparable frequencies.

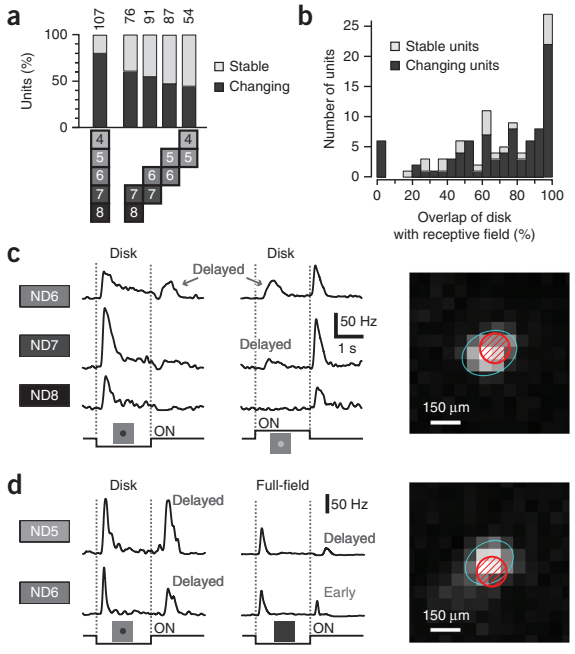

Figure 8 Luminance-dependent response changes to small localized disk stimuli. (**a**) Percentage of units with stable or changing responses across different luminance levels. Conventions as in **Figure 3b**, but combining both ON and OFF cells. (**b**) Histogram showing how much of the disk stimulus was contained within the receptive field center, as determined by a binary checkerboard flicker stimulus. (**c**) Example unit changing its responses to localized stimulation of the receptive field center. Right, overlap of the disk stimulus (red) with the receptive field (blue ellipse shows 2.5 σ of Gaussian fit). (**d**) Example unit that had stable responses to the disk stimulus but changing responses to the full-field step at the ND6–ND5 luminance transition.

DISCUSSION

We studied the responses of retinal ganglion cells to full-field contrast steps over 5 log units of background light intensities. We classified ganglion cells into ON and OFF groups based on their linear filter and found that most OFF ganglion cells and a large fraction of ON cells behave as ON-OFF at least at some luminance levels. In both groups, the responses to the anti-preferred stimulus contrast could have short latency (early responses) or long latency (delayed responses). Early and delayed responses, which may occur together in many cells (**Fig. 3a**,**c**), appeared to be distinct response categories (**Fig. 2b**) that can be regulated independently (**Supplementary Fig. 2**). Most intriguingly, over 80% of cells displayed different response types to the anti-preferred contrast at different background luminance (**Fig. 3b**,**d**). It is noteworthy that the linear filter polarity, obtained as spike-triggered average to full-field Gaussian white noise flicker, was stable at all light intensities despite changing responses to step stimuli.

Despite such a high degree of variability in the responses of ganglion cells, we found them to be reliably bound to the specific luminance: most cells would always respond in a similar way at a particular light

level, even if such trials were interleaved with exposure to higher or lower light levels (**Fig. 5**). Moreover, luminance-dependent qualitative changes of the responses were also demonstrated in recordings from dLGN neurons *in vivo* (**Fig. 7**) and to spatially heterogeneous stimuli, such as small disks (**Fig. 8**) and a naturalistic movie, which is a more ecologically relevant visual stimulus for the retina and the visual system in general. In several single-cell recordings from ganglion cells identified to be morphologically ON or OFF, we observed similar light-dependent response changes (**Fig. 6**), further corroborating the conclusions drawn from the MEA recordings. Finally, we found that luminance-dependent response changes were not restricted to the mouse retina but existed in pig retina as well (**Supplementary Fig. 5**).

In the isolated retina, stimulation at light levels higher than ND4 (corresponding to 10^4 R* rod^{-1} s^{-1}) led to subtle changes in response properties that are likely associated with excessive bleaching of photopigment (data not shown). While the retina continued to respond well to visual stimulation, the results obtained at those high intensities probably do not reflect normal retinal processing as it would happen in the intact eye (data not shown), and hence we excluded these higher light levels from our analysis. The recordings from the dLGN therefore not only confirm that luminance-dependent response variability occurs *in vivo*, but they also expand the range of light intensities at which that phenomenon was observed. Overall, we found luminance-dependent response changes over all intensity ranges and at each luminance transition we tested, from scotopic to photopic light levels.

The collective activity (firing pattern) of all retinal ganglion cells in response to a visual stimulus is sometimes referred to as the retinal code, which is, simply put, "what the eye tells the brain" about the stimulus[22]. Common research questions related to the retinal code often revolve around two topics: first, how does the retina encode the visual stimulus, and second, how might the visual brain decode the action potential pattern generated by the retinal ganglion cells? Our results have intriguing implications for both of these questions.

The first topic, encoding of visual stimuli, boils down to a mechanistic understanding of retinal circuits: how do cellular and circuit properties combine to produce certain ganglion cell responses? Decades of research have revealed fundamental aspects of this issue, ranging from the workings of the phototransduction cascade[23], to the identity of retinal cell types[24], to complex receptive and projective field organizations[2,25–27], to adaptation to first and higher order statistics of the visual stimulus[28–30]. Our results suggest that it may be worth revisiting many of these functional findings and comparing them in detail at different light levels.

Recent reports on the connectome of the inner retina can form a framework for understanding the mechanisms for the response variability we describe here. Three-dimensional electron microscopy reconstruction of the inner mouse[31] and rabbit[32] retina has shown that many bipolar cell types connect to many different ganglion cell types, including ON bipolar cells to OFF ganglion cells and vice versa. Such promiscuous connectivity was confirmed by physiological recordings in salamander retina[25]. Additionally, some ganglion cells receive excitatory drive during anti-preferred contrast steps through gap-junction coupling with amacrine cells[20]. These diverse connectivity patterns, in combination with amacrine cell–mediated feedback inhibition to veto synaptic release from bipolar cell terminals[21,25,33], provide all necessary building blocks for turning on or off certain inputs to ganglion cells under different (luminance) conditions. However, we have shown that the particular mechanism underlying luminance-dependent response variability may differ in different ganglion cell types. For example, two ganglion cells might change their responses during the same luminance transition for different reasons: while one cell gains a surround, the other cell remodels its central receptive field (**Fig. 8**). While one cell's response variability is regulated by GABAergic inhibition, the other cell changes its responses independently of GABA (**Supplementary Fig. 2**). Furthermore, we found many cells to change their responses at several luminance transitions, so that even a single ganglion cell might employ diverse mechanisms at different luminance transitions. This variety of observed effects suggests that the detailed mechanisms underlying luminance-dependent response changes likely need to be investigated on the level of individual ganglion cells and their circuits.

Related to the topic of encoding is the problem of functional classification of ganglion cell types. This question has been approached by describing ganglion cell responses with several parameters, such as polarity, latency, transiency, direction selectivity and so forth, usually in response to simple stimuli such as full-field flashes and moving bars[34–36]. However, as we show here, response properties of ganglion cells depend on the ambient luminance, including properties that serve as parameters used for cell classification. For example, a cell identified as an OFF cell at one luminance might behave as an ON-OFF cell at another luminance, even within the same coarse brightness range (scotopic, mesopic and photopic). Thus, two cells of the same cell type might be artificially separated into different groups if measurements were done under different luminance conditions. Consequently, using controlled and comparable luminance conditions, as well as similar stimuli, is crucial not only for proper comparison of response patterns between research groups, but also between several experiments within a single study. In the future, it will be important to rigorously test whether all ganglion cells of the same (morphological) type change their responses coherently during luminance transitions.

The recent advances in retinal prosthetic technology, including electrical retinal implants[37–39] and optogenetic approaches[40–43], have raised the bar on the stated goals in vision restoration: the goal is no longer to simply confer light perception on the blind patient, but to try to fully restore normal function. Ideally, an implant would encode the light stimulus such that the induced retinal output would be as natural as possible. Our work suggests that the 'natural' retinal output is a moving target. This may, in fact, be advantageous for prosthetics that lack cellular specificity, such as electrical retinal implants. They have always suffered from the problem of not being able to specifically stimulate ON or OFF cells (but see ref. 44). According to our results, ON responses are a common feature in OFF cells. Nonspecific electrical stimulation at light onset might therefore not confuse the brain as much as has been feared. Whether or not this really is the case, however, depends on how the retinal output is decoded.

The second topic, decoding of the retinal output, views the retina as a black box and asks questions about how the output of the retina is treated by receiving neurons. Is the exact spike timing important[45,46], or is the firing rate the relevant unit[47,48]? How is the correlation structure of multineuron firing patterns taken into account[49]? When we started this research project, we expected to see only a moderate influence of illuminance on the retinal output, maybe with more pronounced effects at certain brightness thresholds (namely, cone activation threshold and rod saturation threshold). Overall, however, we assumed that adaptation in the retina largely would compensate for illuminance differences, so that the retinal black box delivers a rather stable input to the visual brain. Since this does not seem to be the case, there is a whole new dimension that is added to the already existing questions on decoding. How does the brain deal with the changes of the retinal output? Are they successfully filtered out and discarded, or do they indeed carry important information, maybe even used to identify viewing conditions?

The data we present are probably insufficient to even start tackling these questions. Furthermore, in the current work we have only focused on qualitative response changes. In addition, there are widespread quantitative changes in response to both preferred and anti-preferred contrast steps (for example, response amplitude, transiency), as can be seen in many of the example responses depicted in our figures. Various aspects of quantitative luminance-induced changes have also been described by others[5,7]. In the future, it will be desirable to monitor the luminance-dependent changes of the retinal output on a better spatial scale. In particular, it will be important to test whether the information transmitted to the brain by a population of ganglion cells is, in aggregate, luminance independent despite the luminance-dependent changes of single cells. It is also possible that the phenomenon of changing output described in this paper allows the retina to encode the visual stimulus more efficiently in the ever-changing and dynamic luminance conditions of natural viewing[15].

METHODS

Methods and any associated references are available in the online version of the paper.

Note: Any Supplementary Information and Source Data files are available in the online version of the paper.

ACKNOWLEDGMENTS

We thank J. Wynne for technical assistance and M. Biel (LMU München) for supplying *Cnga3*$^{-/-}$ mice. This research was supported by funds of the Deutsche Forschungsgemeinschaft (DFG) to the Werner Reichardt Centre for Integrative Neuroscience (DFG EXC 307), by the Bundesministerium für Bildung and Forschung (BMBF) to the Bernstein Center for Computational Neuroscience (FKZ 01GQ1002), by funds of the Biotechnology and Biological Sciences Research Council (BBSRC BB/1007296/1) and the European Commission (ERC Advanced Grant MeloVision) to R.J.L., a Christiane-Nüsslein-Volhard Stipend to A.T.-H., and a Pro-Retina Stipend to K.R.

AUTHOR CONTRIBUTIONS

A.T.-H., K.R. and T.A.M. designed the study. MEA recordings and spike sorting were performed by A.T.-H., K.R., H.S. and A.H., and analyzed by A.T.-H., K.R. and T.A.M. Patch-clamp experiments and immunohistochemistry were conducted and analyzed by H.S. and T.A.M. *In vivo* experiments were designed by C.A.P., A.E.A. and R.J.L., performed by C.A.P. and A.E.A., and analyzed by C.A.P., A.E.A. and K.R. Pig eyes were provided by M.S. The manuscript was prepared by A.T.-H., K.R. and T.A.M. with the help of H.S., C.A.P., A.E.A. and R.J.L.

COMPETING FINANCIAL INTERESTS

The authors declare no competing financial interests.

1. O'Brien, B.J., Isayama, T., Richardson, R. & Berson, D.M. Intrinsic physiological properties of cat retinal ganglion cells. *J. Physiol.* (*Lond.*) **538**, 787–802 (2002).
2. Gollisch, T. & Meister, M. Eye smarter than scientists believed: neural computations in circuits of the retina. *Neuron* **65**, 150–164 (2010).
3. Reitner, A., Sharpe, L.T. & Zrenner, E. Is colour vision possible with only rods and blue-sensitive cones? *Nature* **352**, 798–800 (1991).
4. Enroth-Cugell, C. & Lennie, P. The control of retinal ganglion cell discharge by receptive field surrounds. *J. Physiol.* (*Lond.*) **247**, 551–578 (1975).
5. Farrow, K. *et al.* Ambient illumination toggles a neuronal circuit switch in the retina and visual perception at cone threshold. *Neuron* **78**, 325–338 (2013).
6. Sagdullaev, B.T. & McCall, M.A. Stimulus size and intensity alter fundamental receptive-field properties of mouse retinal ganglion cells in vivo. *Vis. Neurosci.* **22**, 649–659 (2005).
7. Grimes, W.N., Schwartz, G.W. & Rieke, F. The synaptic and circuit mechanisms underlying a change in spatial encoding in the retina. *Neuron* **82**, 460–473 (2014).
8. Umino, Y., Solessio, E. & Barlow, R.B. Speed, spatial, and temporal tuning of rod and cone vision in mouse. *J. Neurosci.* **28**, 189–198 (2008).
9. Protti, D.A., Flores-Herr, N., Li, W., Massey, S.C. & Wassle, H. Light signaling in scotopic conditions in the rabbit, mouse and rat retina: a physiological and anatomical study. *J. Neurophysiol.* **93**, 3479–3488 (2005).
10. Eggers, E.D., Mazade, R.E. & Klein, J.S. Inhibition to retinal rod bipolar cells is regulated by light levels. *J. Neurophysiol.* **110**, 153–161 (2013).
11. Bloomfield, S.A. & Dacheux, R.F. Rod vision: pathways and processing in the mammalian retina. *Prog. Retin. Eye Res.* **20**, 351–384 (2001).
12. Ke, J.B. *et al.* Adaptation to background light enables contrast coding at rod bipolar cell synapses. *Neuron* **81**, 388–401 (2014).
13. Dunn, F.A., Doan, T., Sampath, A.P. & Rieke, F. Controlling the gain of rod-mediated signals in the mammalian retina. *J. Neurosci.* **26**, 3959–3970 (2006).
14. Dunn, F.A., Lankheet, M.J. & Rieke, F. Light adaptation in cone vision involves switching between receptor and post-receptor sites. *Nature* **449**, 603–606 (2007).
15. Allen, A.E. *et al.* Melanopsin-driven light adaptation in mouse vision. *Curr. Biol.* published online, doi:10.1016/j.cub.2014.09.015 (7 October 2014).
16. Manookin, M.B., Beaudoin, D.L., Ernst, Z.R., Flagel, L.J. & Demb, J.B. Disinhibition combines with excitation to extend the operating range of the OFF visual pathway in daylight. *J. Neurosci.* **28**, 4136–4150 (2008).
17. Münch, T.A. *et al.* Approach sensitivity in the retina processed by a multifunctional neural circuit. *Nat. Neurosci.* **12**, 1308–1316 (2009).
18. Pitkow, X. & Meister, M. Decorrelation and efficient coding by retinal ganglion cells. *Nat. Neurosci.* **15**, 628–635 (2012).
19. Kuffler, S.W. Discharge patterns and functional organization of mammalian retina. *J. Neurophysiol.* **16**, 37–68 (1953).
20. Farajian, R., Pan, F., Akopian, A., Volgyi, B. & Bloomfield, S.A. Masked excitatory crosstalk between the ON and OFF visual pathways in the mammalian retina. *J. Physiol.* (*Lond.*) **589**, 4473–4489 (2011).
21. Roska, B. & Werblin, F. Vertical interactions across ten parallel, stacked representations in the mammalian retina. *Nature* **410**, 583–587 (2001).
22. Meister, M. & Berry, M.J. II. The neural code of the retina. *Neuron* **22**, 435–450 (1999).
23. Lamb, T.D. & Pugh, E.N. Jr. Phototransduction, dark adaptation, and rhodopsin regeneration: the Proctor lecture. *Invest. Ophthalmol. Vis. Sci.* **47**, 5137–5152 (2006).
24. Werblin, F.S. & Dowling, J.E. Organization of the retina of the mudpuppy, *Necturus maculosus*. II. Intracellular recording. *J. Neurophysiol.* **32**, 339–355 (1969).
25. Asari, H. & Meister, M. The projective field of retinal bipolar cells and its modulation by visual context. *Neuron* **81**, 641–652 (2014).
26. Lukasiewicz, P.D. Synaptic mechanisms that shape visual signaling at the inner retina. *Prog. Brain Res.* **147**, 205–218 (2005).
27. Thoreson, W.B. & Mangel, S.C. Lateral interactions in the outer retina. *Prog. Retin. Eye Res.* **31**, 407–441 (2012).
28. Baccus, S.A. & Meister, M. Fast and slow contrast adaptation in retinal circuitry. *Neuron* **36**, 909–919 (2002).
29. Smirnakis, S.M., Berry, M.J., Warland, D.K., Bialek, W. & Meister, M. Adaptation of retinal processing to image contrast and spatial scale. *Nature* **386**, 69–73 (1997).
30. Tkačik, G., Ghosh, A., Schneidman, E. & Segev, R. Adaptation to changes in higher-order stimulus statistics in the salamander retina. *PLoS ONE* **9**, e85841 (2014).
31. Helmstaedter, M. *et al.* Connectomic reconstruction of the inner plexiform layer in the mouse retina. *Nature* **500**, 168–174 (2013).
32. Lauritzen, J.S. *et al.* ON cone bipolar cell axonal synapses in the OFF inner plexiform layer of the rabbit retina. *J. Comp. Neurol.* **521**, 977–1000 (2013).
33. Geffen, M.N., de Vries, S.E. & Meister, M. Retinal ganglion cells can rapidly change polarity from Off to On. *PLoS Biol.* **5**, e65 (2007).
34. Farrow, K. & Masland, R.H. Physiological clustering of visual channels in the mouse retina. *J. Neurophysiol.* **105**, 1516–1530 (2011).
35. Rockhill, R.L., Daly, F.J., MacNeil, M.A., Brown, S.P. & Masland, R.H. The diversity of ganglion cells in a mammalian retina. *J. Neurosci.* **22**, 3831–3843 (2002).
36. Zeck, G.M. & Masland, R.H. Spike train signatures of retinal ganglion cell types. *Eur. J. Neurosci.* **26**, 367–380 (2007).
37. Dorn, J.D. *et al.* The detection of motion by blind subjects with the Epiretinal 60-Electrode (Argus II) retinal prosthesis. *JAMA Ophthalmol.* **131**, 183–189 (2013).
38. Wang, L. *et al.* Photovoltaic retinal prosthesis: implant fabrication and performance. *J. Neural Eng.* **9**, 046014 (2012).
39. Zrenner, E. *et al.* Subretinal electronic chips allow blind patients to read letters and combine them to words. *Proc. Biol. Sci.* **278**, 1489–1497 (2011).
40. Bi, A. *et al.* Ectopic expression of a microbial-type rhodopsin restores visual responses in mice with photoreceptor degeneration. *Neuron* **50**, 23–33 (2006).
41. Busskamp, V., Picaud, S., Sahel, J.A. & Roska, B. Optogenetic therapy for retinitis pigmentosa. *Gene Ther.* **19**, 169–175 (2012).
42. Lagali, P.S. *et al.* Light-activated channels targeted to ON bipolar cells restore visual function in retinal degeneration. *Nat. Neurosci.* **11**, 667–675 (2008).
43. Nirenberg, S. & Pandarinath, C. Retinal prosthetic strategy with the capacity to restore normal vision. *Proc. Natl. Acad. Sci. USA* **109**, 15012–15017 (2012).
44. Cai, C., Twyford, P. & Fried, S. The response of retinal neurons to high-frequency stimulation. *J. Neural Eng.* **10**, 036009 (2013).
45. Jacobs, A.L. *et al.* Ruling out and ruling in neural codes. *Proc. Natl. Acad. Sci. USA* **106**, 5936–5941 (2009).
46. Rathbun, D.L., Alitto, H.J., Weyand, T.G. & Usrey, W.M. Interspike interval analysis of retinal ganglion cell receptive fields. *J. Neurophysiol.* **98**, 911–919 (2007).
47. Berry, M.J., Warland, D.K. & Meister, M. The structure and precision of retinal spike trains. *Proc. Natl. Acad. Sci. USA* **94**, 5411–5416 (1997).
48. Funke, K. & Worgotter, F. On the significance of temporally structured activity in the dorsal lateral geniculate nucleus (LGN). *Prog. Neurobiol.* **53**, 67–119 (1997).
49. Schnitzer, M.J. & Meister, M. Multineuronal firing patterns in the signal from eye to brain. *Neuron* **37**, 499–511 (2003).
50. Paxinos, G. & Franklin, K. *The Mouse Brain in Stereotaxic Coordinates* (Academic Press, 2001).

ONLINE METHODS

Animals. As wild-type animals, we used PV-Cre × Thy-S-Y mice[17] (B6;129P2-*Pvalb*$^{tm1(cre)Arbr}$/J × C57BL/6-tg(ThystopYFPJS) and C57Bl/6J mice. For cone-deficient mice, we used *Cnga3*$^{-/-}$ (ref. 51, kindly provided by M. Biel, LMU München), *Cpfl1* (B6.CXB1-*Pde6c*^{cpfl1}, Jackson strain 3678), kindly provided by B. Chang (The Jackson Laboratory, Bar Harbor, ME), and *Gnat2*^{cpfl3} mice (B6.Cg-*Gnat2*^{cpfl3}/Boc, Jackson strain 6795). Wild-type animals were 5 weeks to 6 months old at the time of the experiments, *Cnga3*$^{-/-}$ animals 4.5–6 weeks old, *Cpfl1* animals 11–13 weeks old and *Gnat2*^{cpfl3} animals 12 months old. We used both male and female mice for all experiments. Mice were kept in groups of one to five animals. Animal use was in accordance with German, UK and European regulations and approved by the Regierungspräsidium Tübingen (*in vitro* experiments).

Pig retinas were obtained from two female domestic pigs sacrificed during independent scientific studies at the Department of Experimental Surgery, University of Tübingen. Pigs were sedated and anesthetized by injection of atropine, azaperone, benzodiazepine (midazolam), and ketamine, and sacrificed with embutramide (T61). Before administration of embutramide, heparin was injected. During sedation and anesthesia, the pigs were dark-adapted for 15–20 min. After death, the eyes were enucleated immediately under dim red light conditions, the cornea, lens and vitreous removed, and the eyecup kept in CO_2-independent culture medium (Gibco) and protected from light. After transportation to the laboratory, pieces ~4 × 4 mm^2 were cut from the mid-peripheral retina. Recordings were performed identically to those in experiments with mouse retina.

***In vitro* MEA recordings.** Mice were kept on a 12/12 h light/dark cycle, dark-adapted for 4–16 h before the experiment, and sacrificed under dim red light by cervical dislocation. The eyecups were removed, put in Ringer solution (in mM: 110 NaCl, 2.5 KCl, 1 $CaCl_2$, 1.6 $MgCl_2$, 10 D-glucose and 22 $NaHCO_3$) bubbled with 5% CO_2/95% O_2. The retina was isolated and attached to a nitrocellulose filter (Millipore) with a central 2 × 2 mm hole, with the optic nerve head centered. Experiments were performed at different circadian times with no noticeable effects on the outcome.

All recordings were performed with a perforated 60-electrode MEA (60pMEA200/30iR-Ti-gr, Multichannel Systems, Reutlingen) with square grid arrangement and 200 µm electrode distance. The mounted retina was placed ganglion cell–side down in the recording chamber, and good electrode contact was achieved by negative pressure through the perforated MEA. The tissue was superfused with Ringer solution at 34 °C. Data were recorded at 25 kHz with a USB-MEA-system (USB-MEA1060, Multichannel Systems) or a MC-Card based MEA-system (MEA1060, Multichannel Systems). The detailed experimental procedure has been published before[51].

Pharmacology. To block ionotropic GABA receptors, 5 µM SR-95531 (gabazine, an antagonist of $GABA_A$ receptors; Sigma) and 100 µM picrotoxin (an antagonist of $GABA_A$ and $GABA_C$ receptors; Sigma) were added to the Ringer solution. SR-95531 was dissolved in water at a concentration of 5 mM; picrotoxin was dissolved in DMSO at a concentration of 100 mM. Wash-in was performed during 10 min at a speed of approximately 1 ml/min.

Single-cell recordings, immunostaining and confocal microscopy. Retina preparation was carried out in Ringer solution, as described for MEA recordings. The isolated retina mounted on the nitrocellulose filter was attached in the recording chamber by vacuum grease. The same setup as for the MEA recordings, including visual stimulation hardware and software, was used. Patch electrodes pulled from borosilicate glass capillaries (Science Products, GB150F-8P) were filled with an internal solution (in mM: 115 potassium gluconate, 2 KCl, 0.5 $CaCl_2$, 1 $MgCl_2$, 1.5 EGTA, 10 HEPES, 4 ATP-Na_2, 0.5 GTP-Na_3, 7.75 neurobiotin chloride, <1 Alexa 568) and had resistances between 4 and 8 MΩ. Recordings were made from ganglion cells of PV-Cre × Thy-S-Y mice in loose cell-attached mode or whole-cell mode using current clamp (0 pA). Ganglion cells were targeted by two-photon imaging (920–950 nm) or chosen randomly. At the end of the recording, cells were filled with neurobiotin-containing internal solution and retinas were immersion-fixed in 4% PFA for 10 min at room temperature, washed in PBS, cryoprotected in 30% sucrose, frozen (at −150 °C) and thawed three times and washed again in PBS. After blocking 1 h in 10% normal donkey serum (NDS), 1% bovine serum albumin (BSA), 0.5% Triton X-100, 0.02% sodium azide in PBS, retinas were incubated 4–6 d with primary antibody goat anti-ChAT (Millipore, AB144P, 1:200)[52], diluted in 3% NDS, 1% BSA, 0.5% Triton X-100, 0.02% sodium azide in PBS. Retinas were washed in PBS and incubated overnight with secondary antibody donkey anti-goat Cy5 (Jackson ImmunoResearch, 705-175-147, 1:200)[53] and streptavidin-Cy3 (Jackson ImmunoResearch, 016-160-084, 1:200–1:400) or donkey anti-goat Alexa 555 (Invitrogen, A-21432, 1:200)[54] and streptavidin Cy5 (Rockland, S000-06, 1:200), diluted in 0.5% Triton X-100 in PBS. Retinas were washed in PBS, incubated with DAPI (2.5 µg/ml in PBS) for 20 min, washed again and mounted in Vectashield (Vector Laboratories). All steps were carried out at room temperature. Confocal image stacks of the filled ganglion cells were taken on a Zeiss LSM710, using a 40X NA1.3 oil immersion objective. *xy* image and *z*-stack size were chosen such that they covered the complete ganglion cell, including its entire dendritic arbor, and encompassed the full thickness of the inner plexiform layer. Dendritic stratification depths relative to ChAT bands and DAPI-stained nuclei of inner nuclear layer and ganglion cell layer were determined on several dendritic locations of each cell using a custom-written Mathematica script.

Light stimuli during *in vitro* experiments. *Intensities.* Light stimulation was performed with a digital light processing (DLP) projector (PG-F212X-L, Sharp) and focused onto the photoreceptors through the condenser of the microscope (**Supplementary Fig. 1**). The light path contained a shutter and two motorized filter wheels with a set of neutral density (ND) filters (Thorlabs NE10B-A to NE50B-A), having optical densities from 1 ('ND1') to 5 ('ND5'). To achieve light attenuation stronger than 5 log units, we serially combined an ND5 filter in one filter wheel with another ND filter in the second filter wheel. We refer to the filter settings as ND4 (brightest setting used, 10^4-fold light attenuation) to ND8 (darkest setting used, 10^8-fold light attenuation). While changing the ND filters during the experiment, we closed the shutter to prevent intermittent exposure to bright light. We usually started the experiments at ND8, and step by step increased the ambient stimulation luminance by changing the ND filters by 1 unit. Unless otherwise noted, we presented the same set of visual stimuli at each ND level during an experiment.

The stimulus projector output spanned 3 log units of light intensities (that is, a 1,000-fold difference between black (0) and white (255) pixels). We linearized the projector output, and limited our visual stimuli to the range of 0 to 60, with the background set to 30 (**Fig. 1a**). As a consequence, the brightest pixels at any given ND-filter setting were fivefold dimmer than the background illumination at the next brighter ND-setting (**Fig. 1b**).

Light intensity measurements. We measured the spectral intensity profile (in µW cm^{-2} nm^{-1}) of our light stimuli with a calibrated USB2000+ spectrophotometer (Ocean Optics). We transformed the stimulus intensity into equivalents of photoisomerizations per rod and per second, assuming dark-adapted rods[42]. Briefly, the spectrum was converted to photons cm^{-2} s^{-1} nm^{-1}, convolved with the normalized spectrum of rod sensitivity[5], and multiplied with the effective collection area of rods (0.5 µm^2)[55]. The results for a stimulus intensity of 30 ranged from 1 R* s^{-1} per rod (ND8) to 10^4 R* s^{-1} per rod (ND4) (**Fig. 1b**). These calculations, as well as recordings from mice lacking functional rods and functional cones (data not shown), suggest that ND8 and ND7 correspond to scotopic conditions, ND6 weakly activates cones, ND5 is fully mesopic and ND4 is photopic. Note that our characterization of ND7 as scotopic may partly be owed to our use of low-contrast stimuli. We cannot exclude the possibility that stimuli with stronger contrast might activate cones even at ND7 (see, for example, refs. 5,56).

Light stimuli. All stimuli were grayscale images with pixel values between 0 (black) and 60 (white). The background was kept at 30 (gray), and the stimuli were balanced to keep the mean intensity over time at 30.

Our stimulus set for MEA recordings contained the following: (1) Full-field steps (**Fig. 1a,b**). ON step: stepping to an intensity of 50 for 2 s from the background of 30 (66% Weber contrast); OFF step: stepping to 10 for 2s (−66%). (2) Full-field Gaussian flicker, 30 s or 1 min. Screen brightness was updated every frame (60 Hz) or every other frame (30 Hz) and was drawn from a Gaussian distribution with mean 30 and s.d. 9. This stimulus was used to calculate the linear filters of ganglion cells[57]. (3) Disk stimulus. Disks (diameter, 150 µm on the retina) were presented on a gray (30) background for 2s and had the same contrast as the full-field step stimulus (10 for black disks, 50 for white disks). They were centered over the recording electrodes. The sequence of disk locations was chosen such that the next disk was always at least 600 µm away from the previous disk, and at least 7 white and 7 black disks were presented at each location at

each ND level. (4) Binary checkerboard flicker, 15 min. The screen was divided into a 40 × 40 checkerboard pattern; each checker covered 60 × 60 μm^2 on the retina. The intensity of each checker was updated independently from the other checkers and randomly switched between 10 and 50. This stimulus was used to calculate the spatial receptive field of ganglion cells. (5) Natural movie, 22 s. It consisted of sequences taken from the music video "Rip It Up" by Bill Haley (https://www.youtube.com/watch?v=HdlfZ4213zM). The contrast of the movie was compressed so that it spanned brightness values between 0 and 60.

We used different combinations or subsets of these stimuli in different experiments, repeated several times at each ND filter. The complete experimental stimulus set lasted at least 20 min at each ND. See results for details.

Our stimulus set for single cell recordings contained the following: (1) Full-field steps (see above). (2) Full-field Gaussian flicker (see above). (3) Disk stimulus (see above). Disks were centered over the patched cell's soma. (4) Annulus stimulus. Full-field contrast step (see above) with an inner hole (diameter, 500 μm on the retina) staying at gray (30) background, centered on the patched cell's soma. The same set of stimuli was presented at each ND from ND8 to ND4, taking a total of 35 min. Only one cell was recorded from each retina.

Data analysis. *Spike sorting.* Data were high-pass filtered (500 Hz, tenth-order Butterworth filter), and spike waveforms and spike times were extracted from the raw data using Matlab (The MathWorks Inc., MA, USA). Spike sorting (assignment of spikes to individual units, presumably ganglion cells) was performed semimanually with custom written software (Matlab). The quality of each unit was individually and manually assessed by inter-spike interval and spike shape variation. Data analysis was based on the spiking responses of individual units.

Calculation of cell polarities and receptive fields. We calculated linear filters in response to full-field Gaussian flicker and to binary checkerboard flicker by summing the 500-ms stimulus history before each spike. Linear filters calculated in response to the full-field flicker were used to determine cell polarity. Latency and amplitude of the first peak of the filter were determined. If the peak was positively deflected, the cell was categorized as an ON cell. If negatively deflected, the cell was categorized as an OFF cell. Linear filters calculated in response to the binary checkerboard flicker were used to determine the spatial receptive field. For each checker, we determined the s.d. along the 500-ms temporal kernel. From the resulting 40 × 40 matrix entries, we calculated the mean and s.d., set all checkers lying below mean + 4 s.d. to zero, fit a two-dimensional Gaussian, and took the 2.5-σ ellipse as a representation for the receptive field (**Fig. 8c**,**d**).

Firing rate calculation. We estimated the instantaneous firing rate by convolving the spike train (time series of 0's and 1's) with a Gaussian with σ = 40 ms and amplitude = 0.25 σ^{-1} $e^{1/2}$ (≈10 Hz for σ = 40 ms), unless otherwise noted.

Algorithm to detect and classify early and delayed responses. For the step-stimuli (full-field and disks), we applied an algorithm to automatically detect ON responses in OFF cells or OFF responses in ON cells and to classify them as early or delayed (see Results for definitions). Responses were rejected as unreliable for specific light levels if less than 50% of them were strongly correlated with each other ("strong correlation" was defined here as pairwise Pearson correlation coefficient of at least 0.4; 0.2 for experiments where automated classification was only taken as a suggestion and manually corrected). Then we applied an automatic algorithm to detect and classify early and delayed responses at each reliable light level. Briefly, we compared the maximal firing rates during spontaneous activity on the one hand and the relevant time windows for early (50–350 ms after the stimulus) and delayed (350–1,000 ms) responses on the other hand. If the peak firing rate in the response windows was higher than during spontaneous activity and also more correlated from trial to trial, we categorized the response as present, regardless of its absolute amplitude (that is, binary classification 'absent/present'). Additional checks were implemented to distinguish these responses from 'tails' of sustained responses to the preferred contrast and to distinguish a delayed response from a slowly declining early response (in both cases, we checked for 'valleys', or firing rate decreases, before the response peak). Mostly, the specific parameters used by the algorithm were based on heuristics and we made extensive checks to confirm that the automatic classification was valid. The responses to the small disk and in *Gnat2* retinas had smaller signal-to noise ratio; for those responses we treated the result of the automated algorithm only as a suggestion and confirmed each individual response by hand. Responses during GABA blocker application had different shapes in some cells (sharp peaks, thus slightly different latency distribution). Responses obtained during these experiments were checked manually and corrected where necessary. Responses of the LGN neurons were classified by hand.

We next compared the responses across light levels. Overall, a cell was classified as stable if, at all light levels being compared, it always had the same response type to the black step (that is, no response, early response, delayed response, or both early and delayed response) and always the same response type to the white step. Otherwise the unit was classified as changing. If a cell had unreliable responses at some light level (see above), this light level was not considered for the analysis. For example, if a cell had unreliable responses at ND6, we did not compare this cell's responses for the ND7/6 or the ND6/5 transition, but we still compared its responses between all other light levels, for example, between ND7 and ND5. This is the reason for the different numbers of cells for each luminance transition in the plots showing the fraction of changing and stable units (for example, **Fig. 3b**,**d**). As a consequence, a cell may be classified as stable even if it had unreliable responses at one or more light levels. The fraction of changing cells can therefore be viewed as a conservative estimate.

Analysis of movie responses. Responses to the movie typically consisted of interleaved sequences of spike bursts ('events') and silence. To test whether the response to the movie would change across light levels, we analyzed whether a cell would have an event during some light level(s), but not other(s). This analysis proceeded in several steps: (1) Alignment. We calculated the average spike rate for each light level (see above) with a σ of 10 ms, and calculated the pairwise cross-correlation to estimate the relative temporal shift of the spike trains (spiking always gets faster at higher intensities). We then aligned the spike trains across light levels. (2) Event detection. (a) From the aligned spikes, we calculated the average firing rate across the whole experiment with a σ of 30 ms. Events were preliminarily defined as periods where the spike rate exceeded the mean firing rate of the 2 s before movie onset + 3 STD. (b) If spike bursts occur close to each other, they are fused into 1 event because the calculated firing rate does not drop below the threshold between the bursts. We therefore identified local minima in the spike rate and split events at those minima. (c) Of the resulting events we discarded those that were shorter than 20 ms and those that had a peak firing rate smaller than 5% of the second-largest event. (3) Response strength. We counted the spikes in each event at each light level, and converted that count into an average spike rate (number of spikes/s per movie presentation). We refer to this as the activity of the cell during an event and at each light level. (4) Light levels with very low activity. Events are inherently defined by high activity. To look for qualitative response changes across light levels, we therefore identified light levels during which there was low activity during an event. We applied 2 criteria to identify such 'silent' light levels: (a) Comparison across light levels within an event: the activity during a silent light level had to be lower than 10% of the maximal activity during this event. (b) Comparison across events within a light level: The activity during a silent event had to be less than 10% of the mean activity across all events at that light level. For analysis we counted only such events as silent that fulfilled both criteria (dark gray in **Supplementary Fig. 3**).

Statistical analysis. No statistical methods were used to predetermine sample sizes, but our sample sizes are similar to those generally employed in the field. No statistical tests were required for analysis of the data presented.

***In vivo* recordings.** Five adult female C57 wild-type mice (6–8 weeks, housed in a 12-h light-dark cycle with 6 animals per cage) were used for experiments between 8 a.m. and 6 p.m. Mice were anaesthetized by i.p. injection of 30% (w/v) urethane (1.5 g/kg; Sigma, UK) and placed in a stereotaxic apparatus (SR-15 M; Narishige International Ltd., UK). Additional top up doses of anesthetic (0.2 g/kg) were applied as required and body temperature maintained at 37 °C with a homoeothermic blanket (Harvard Apparatus, Kent, UK).

An incision to expose the skull surface was made and a small hole (~1 mm diameter) drilled 2.5 mm posterior and 2.3 mm lateral to the bregma, targeting the dorsal LGN. The pupil, contralateral to the craniotomy, was dilated with topical 1% (w/v) atropine sulfate (Sigma) and the cornea kept moist with mineral oil. A recording probe (A4X8-5 mm-50-200-413; Neuronexus, MI, USA) consisting of four shanks (spaced 200 μm apart), each with eight recordings sites (spaced 50 μm apart) was then positioned centrally on the exposed surface in the coronal plane, and lowered to a depth of 2.5–3.3 mm using a fluid-filled micromanipulator (MO-10; Narishige).

Once the recording probe was in position and light responses confirmed, mice were dark adapted for 1 h, which also allowed neuronal activity to stabilize after

probe insertion. Neural signals were acquired using a Recorder64 system (Plexon, TX, USA). Signals were amplified ×3,000, high-pass filtered at 300 Hz and digitized at 40 kHz. Multiunit activity (spikes with amplitudes >50 μV) were saved as time-stamped waveforms and analyzed offline (see below).

Light stimuli (λ_{max}, 460 nm; half peak width, ± 10 nm) were generated by a custom-built LED-based light source (Cairn Research Ltd.), passed through a filter wheel with various ND filters and focused onto a 5-mm-diameter piece of opal diffusing glass (Edmund Optics Inc., York, UK) positioned 3 mm from the eye contralateral to the recording probe. LED intensity and filter wheel position were controlled by a PC running LabView 8.6 (National instruments). At each intensity, starting from the lowest (6.1×10^{-1} R* rod^{-1} s^{-1}), a 2-s light increment from background (+66% contrast) was followed by a 5-s inter-stimulus interval of background light, after which a 2-s light decrement (−66% contrast) was presented. This was repeated 120 times at each background level before being increased by a factor of ten, spanning a 6-log-unit range in total. Mice were otherwise kept in complete darkness.

At the end of the experiment mice were transcardially perfused with 0.1 M PBS followed by 4% PFA. The brain was removed, postfixed overnight, cryoprotected with 30% sucrose and sectioned at 50 μm on a freezing sledge microtome. Sections were mounted with DPX (Sigma), coverslipped and electrode placement in the dLGN confirmed by visualization of a fluorescence dye (Cell Tracker CM-DiI; Invitrogen Ltd. Paisley, UK) applied to the probe before recording.

Multichannel, multiunit recordings were analyzed in Offline Sorter (Plexon). Following removal of cross-channel artifacts, principal component–based sorting was used to discriminate single units, identifiable as a distinct cluster of spikes in principal component space with a clear refractory period in their inter-spike interval distribution. Following spike sorting, data were exported to Neuroexplorer (Nex technologies, MA, USA) and Matlab R2013a for construction of peristimulus histograms and further analysis. Light-responsive units were identified as those for which the peristimulus average showed a clear peak (or trough) that exceeded the 99% confidence limits estimated from a Poisson distribution derived from the prestimulus spike counts.

Corneal irradiance was measured using a calibrated spectroradiometer (Bentham Instruments, Reading, UK; Ocean Optics, FL, USA). Retinal irradiance was calculated by multiplying these values by pupil area/retinal area, based on calculations by Lyubarsky *et al.*[58], where a pupil size of 3.2 mm^2 and retinal area of 17.8 mm^2 were used to generate a correction factor of 0.18. Effective photon flux was calculated by multiplying retinal irradiance by spectral transmission through the mouse lens[59]. Photoisomerizations were calculated as described for MEA recordings. All procedures conformed to requirements of the UK Animals (Scientific Procedures) Act, 1986.

A **Supplementary Methods** checklist is available.

51. Reinhard, K. *et al.* Step-by-step instructions for retina recordings with perforated multi electrode arrays. *PLoS ONE* **9**, e106148 (2014).
52. Yonehara, K. *et al.* Spatially asymmetric reorganization of inhibition establishes a motion-sensitive circuit. *Nature* **469**, 407–410 (2011).
53. Gavrikov, K.E., Nilson, J.E., Dmitriev, A.V., Zucker, C.L. & Mangel, S.C. Dendritic compartmentalization of chloride cotransporters underlies directional responses of starburst amacrine cells in retina. *Proc. Natl. Acad. Sci. USA* **103**, 18793–18798 (2006).
54. Hoover, J.L., Bond, C.E., Hoover, D.B. & Defoe, D.M. Effect of neurturin deficiency on cholinergic and catecholaminergic innervation of the murine eye. *Exp. Eye Res.* **122**, 32–39 (2014).
55. Nikonov, S.S., Kholodenko, R., Lem, J. & Pugh, E.N. Jr. Physiological features of the S- and M-cone photoreceptors of wild-type mice from single-cell recordings. *J. Gen. Physiol.* **127**, 359–374 (2006).
56. Szikra, T. *et al.* Rods in daylight act as relay cells for cone-driven horizontal cell–mediated surround inhibition. *Nat. Neurosci.* doi:10.1038/nn.3852 (26 October 2014).
57. Chichilnisky, E.J. A simple white noise analysis of neuronal light responses. *Network* **12**, 199–213 (2001).
58. Lyubarsky, A.L., Daniele, L.L. & Pugh, E.N. Jr. From candelas to photoisomerizations in the mouse eye by rhodopsin bleaching in situ and the light-rearing dependence of the major components of the mouse ERG. *Vision Res.* **44**, 3235–3251 (2004).
59. Jacobs, G.H. & Williams, G.A. Contributions of the mouse UV photopigment to the ERG and to vision. *Doc. Ophthalmol.* **115**, 137–144 (2007).

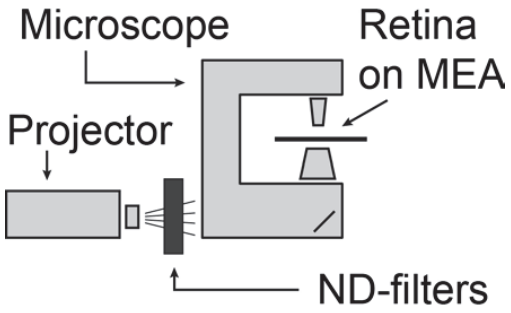

Supplementary Figure 1
Experimental setup for multi-electrode array recordings.

The retina was placed on a multi-electrode array and visual stimulation was achieved with a projector through the condenser of the microscope. Neutral density (ND) filters were used to decrease the mean luminance of the visual stimulation in 1-log-unit steps.

Nature Neuroscience: doi:10.1038/nn.3891

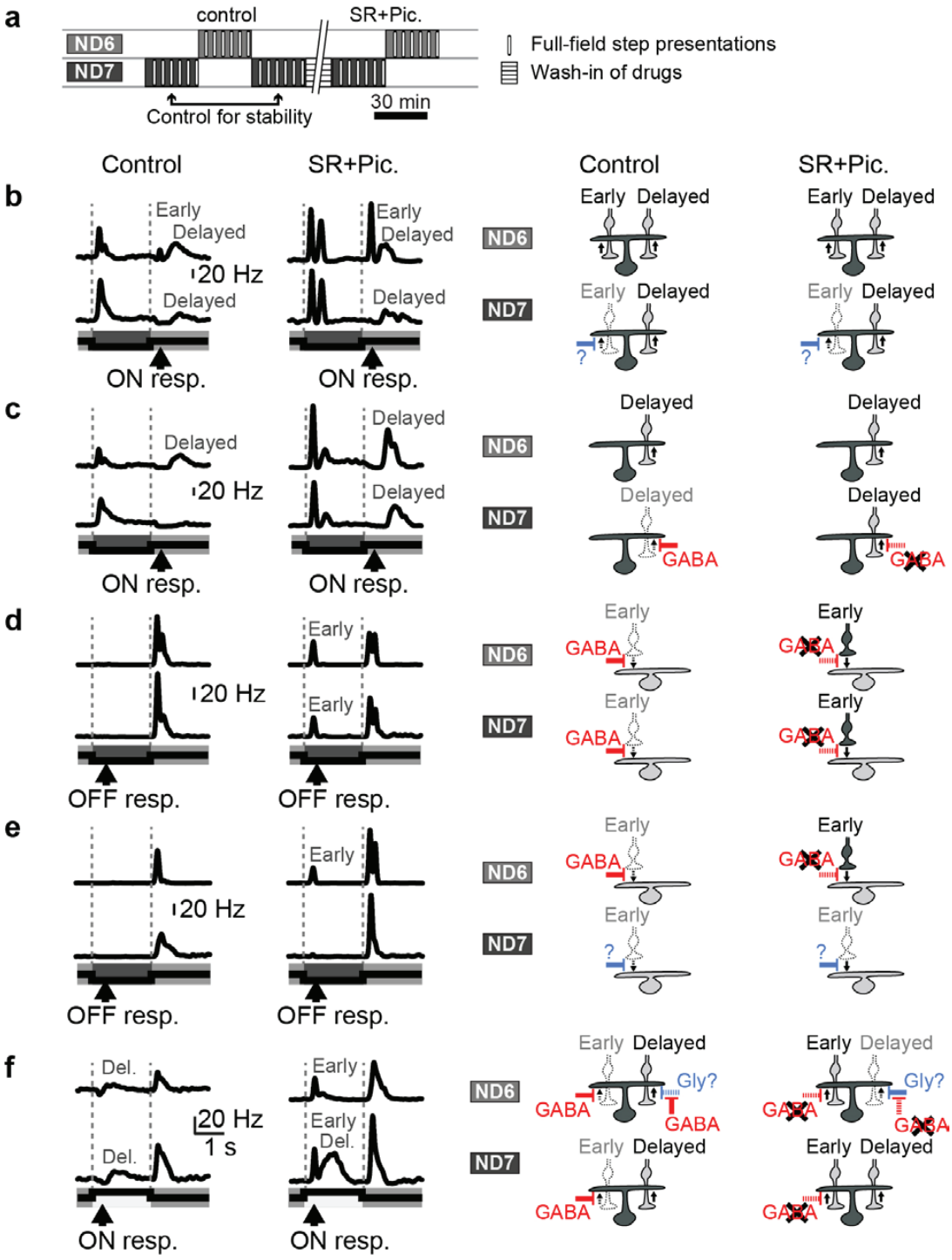

Nature Neuroscience: doi:10.1038/nn.3891

Supplementary Figure 2
Luminance-dependent response changes with and without GABA blockers.

(**a**) Stimulus protocol. SR: SR-95531 (gabazine), Pic.: picrotoxin. (**b–e**) Examples of luminance- and GABA-blocker-dependent response patterns in three OFF cells (**b**,**d**,**f**) and two ON cell (**c**,**e**). Left: Spike rates at ND7 and ND6 luminance levels with and without GABA blockers. Right: One possible circuit scheme each which is consistent with the observed responses. The five examples represent the following categories of observations: (**b**) *Luminance-dependent response changes not influenced by GABA* (observed in n = 3 units; the example shows appearing early ON response at ND6 under both control and drug condition). Such cells changed their response properties identically under control and drug conditions between ND7 and ND6. Thus, these luminance-dependent response changes were independent of GABAergic regulation. (**c**) *Luminance-dependent GABAergic masking of responses* (n=3; example cell has a delayed ON response masked at ND7). In such cells, light responses differed at ND7 and ND6 under control conditions, but not in the presence of GABA blockers. This suggests that GABAergic inhibition masked a response at one light level. (**d**) *Luminance-independent GABAergic masking of responses* (n=12; example: unmasked early response at ND7 and ND6). Such cells did not show any luminance-dependent changes, neither in control nor with GABA blockers, but their responses were different between control and drug conditions within each light level. This suggests that GABAergic inhibition regulated responses at both luminance levels. Potentially, these masked responses might be revealed at other brightness levels. Note that the same phenomenon applies to the early ON responses in **f**. (**e**) *GABA-dependent stabilization of responses* (n=13; the example illustrates this effect for early OFF responses). Such cells with stable responses under control conditions had changing responses under drug conditions. Thus, those changing response themselves were GABA-independent, while at the same time GABA stabilized the responses during the luminance-switch under control conditions. Note that the same phenomenon applies to the delayed ON responses in **f**. (**f**) *GABA-dependent disinhibition* (n=6, the example shows disappearance of delayed ON response with GABA blockers at ND6). While in all examples above GABA blockers revealed additional responses, in few cells responses disappeared in GABA blockers (n=2 at ND7, n=5 at ND6, of which 1 unit was affected at both NDs). This suggests luminance-dependent disinhibitory GABAergic mechanisms.

The phenomena described by these examples occurred in both ON and OFF cells. In some cells, we observed one phenomenon to the white step, and another phenomenon to the black step, highlighting the response asymmetry already observed in control conditions (**Fig. 3**). In summary, we found that the mechanism of GABAergic response regulation is highly diverse, and that it underlies some but not all luminance-dependent qualitative response changes.

Nature Neuroscience: doi:10.1038/nn.3891

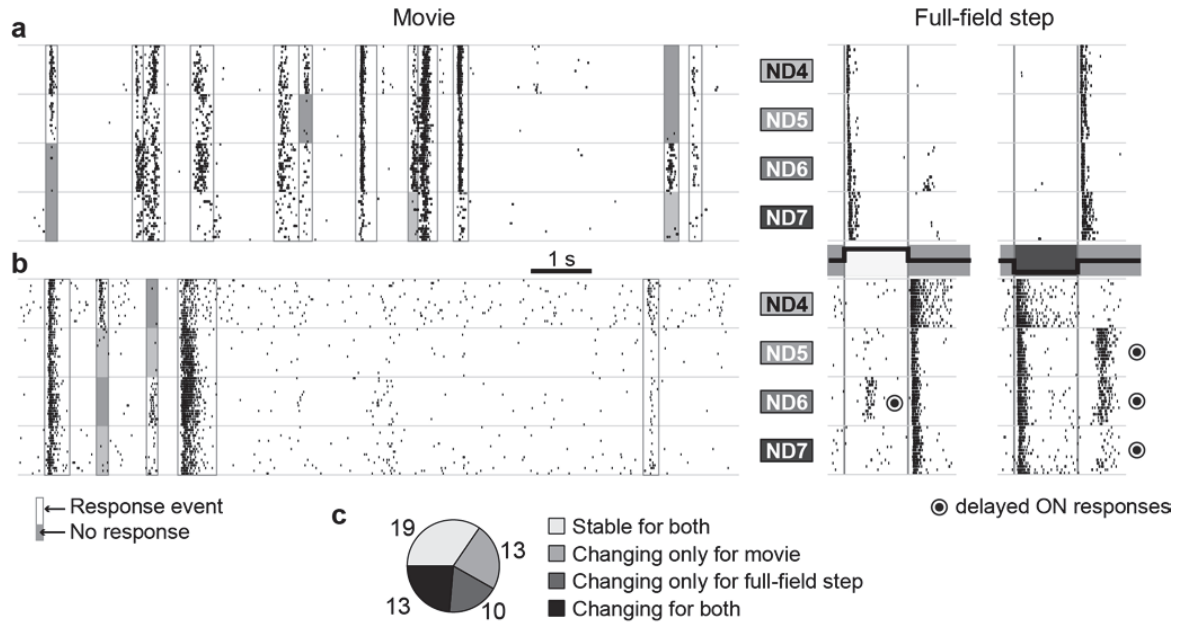

Supplementary Figure 3
Luminance-dependent changes in ganglion cell responses to a naturalistic movie.

Raster plots: responses of individual ganglion cells to the movie stimulus (left) and to the full-field step stimulus (right). Shaded regions indicate events where the neuron was silent, even though it responded at other light levels. (**a**) ON ganglion cell with stable responses to the full-field step, but qualitative changes in its movie response. (**b**) OFF ganglion cell with changing responses to both movie and full-field step stimulus. (**c**) Response changes to full-field steps do not always occur together with response changes to movies, and vice versa. Numbers indicate the number of units in each group.

Nature Neuroscience: doi:10.1038/nn.3891

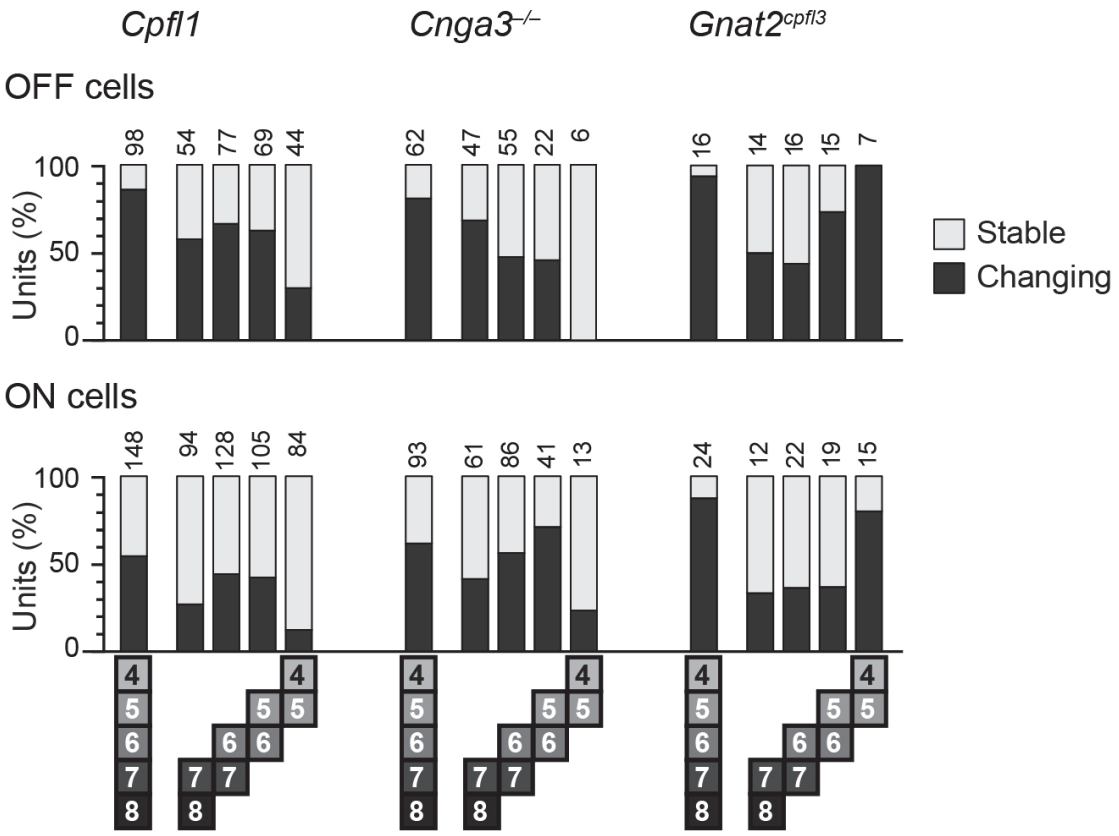

Supplementary Figure 4
Luminance-dependent qualitative response changes in different mouse lines lacking functional cones.

Cpfl1: 98 OFF cells and 148 ON cells from 6 retinas. *Cnga3*$^{-/-}$: 62 OFF cells and 93 ON cells from 6 retinas. *Gnat2*^{cpfl3}: 16 OFF cells and 24 ON cells from 5 retinas. Conventions as in **Fig. 3b**.

Nature Neuroscience: doi:10.1038/nn.3891

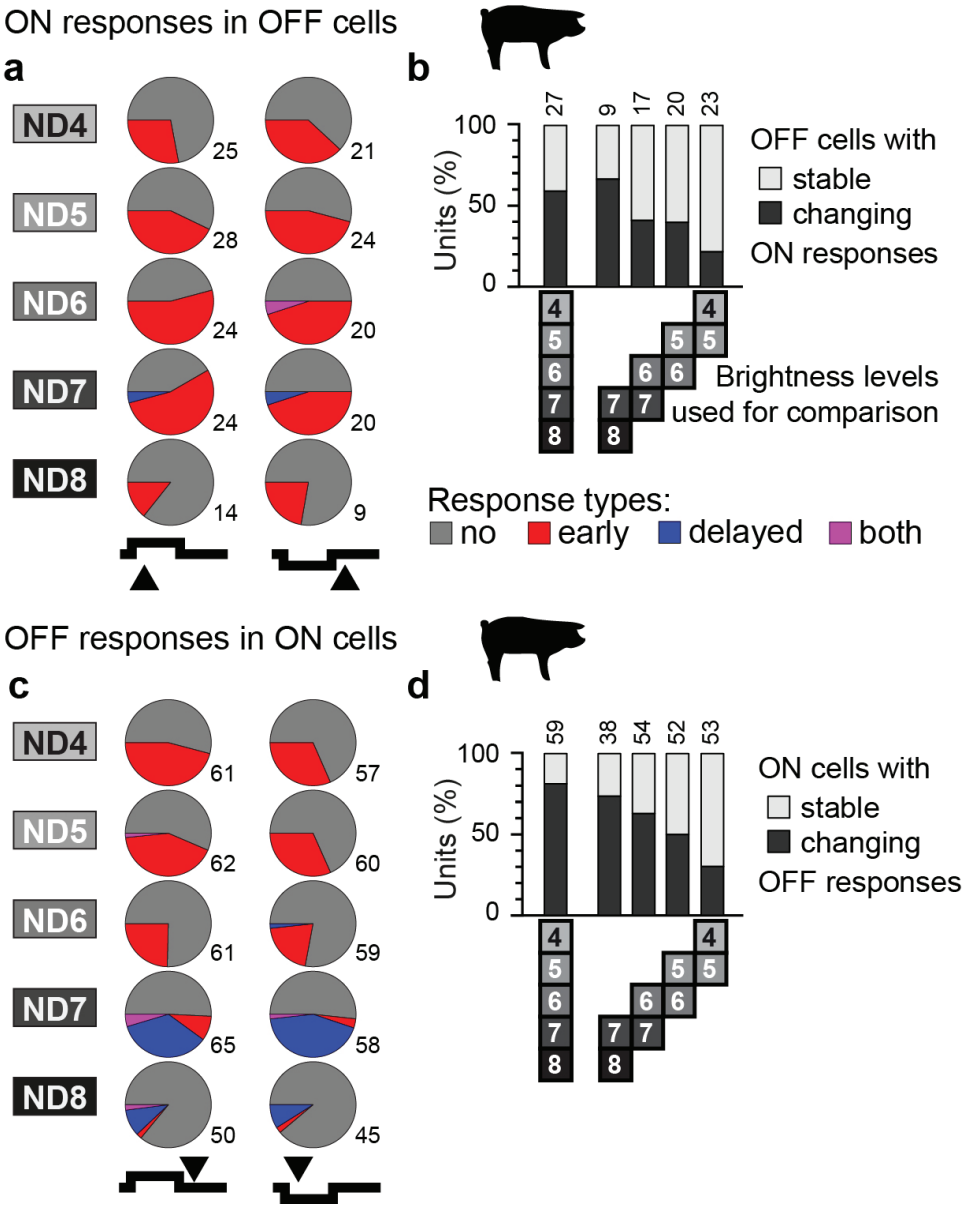

Supplementary Figure 5
Summary of luminance-dependent response types in pig retina.

Data is based on recordings from 27 ON cells and 59 OFF cells from 3 retinal pieces from 2 animals. Conventions as in **Fig. 3**.

Publication 4 – Rod-driven reponses in daylight conditions

Alexandra Tikidji-Hamburyan*, Katja Reinhard*, Riccardo Storchi*, Hartwig Seitter, Katherine E. Davis, Johannes Dietter, Robert Bedford, Marius Ueffing, Petri Ala-Laurila, Robert J Lucas, Thomas A Münch. Rods escape saturation to drive visual responses in daylight conditions. (under revision) *equal contributions

Framework:

This is an original research paper. It shows the contribution of rod photoreceptors to photopic light responses and highlights for the first time that the hitherto presumed rod saturation at higher light levels in fact is reverted back to a dynamically modulated state more effectively with increasing luminance. It combines findings on different levels within the early visual system as well as a model for the underlying mechanism. This is a collaborative publication together with the labs of Robert Lucas, University of Manchester (in vivo recordings), Marius Ueffing, University of Tübingen and Petri Ala-Laurila, University of Helsinki (computational modeling).

Own contributions:

Many of the micro-electrode array recordings of all three mouse models including data processing were done by me (represented e.g. in Fig 1, Fig 2, Fig S2). I developed the in vitro electroretinography paradigm, designed the stimulus and experimental protocols and did most of the experiments. Processing of the in vitro electroretinographic data and first line evaluation and analysis was done by me. I participated in writing of the manuscript.

Other contributions:

ATH made the initial discovery of the phenomenon and described it in her doctoral thesis. KR planned the MEA recordings and performed many of them. She analyzed the MEA as well as the in vivo recordings of cone-deficient animals and also did some electroretinography experiments. RS performed and analyzed the in vivo experiments with wild type-like animals. KED performed and processed the in vivo experiments with cone-deficient animals. RB helped with in vivo experiments. JD, MU and TAM did the modeling with help of PAL. RJL and TAM helped with design and analysis of in vivo and in vitro experiments. KR, ATH, TAM and RJL wrote the manuscript.

Rods Escape Saturation to Drive Visual Responses in Daylight Conditions

Short title: Rods Drive Light Responses in Daylight Conditions

Alexandra Tikidji-Hamburyan[1,2,*], Katja Reinhard[1,2,*], Riccardo Storchi[3,*], Hartwig Seitter[1,2], Katherine E. Davis[3], Johannes Dietter[4], Robert Bedford[3], Marius Ueffing[4], Petri Ala-Laurila[5,6], Robert J. Lucas[3,#], Thomas A. Münch[1,4,#]

*equal contribution

[#] Correspondence:

RJS: robert.lucas@manchester.ac.uk

TAM: thomas.muench@cin.uni-tuebingen.de

Author affiliations

[1] Retinal Circuits and Optogenetics, Centre for Integrative Neuroscience and Bernstein Center for Computational Neuroscience, University of Tübingen, Tübingen, Germany

[2] International Max Planck Research School, University of Tübingen, Tübingen, Germany

[3] Faculty of Life Science, University of Manchester, Manchester, UK

[4] Institute for Ophthalmic Research, University of Tübingen, Tübingen, Germany

[5] Department of Biosciences, University of Helsinki, Helsinki, Finland

[6] Department of Neuroscience and Biomedical Engineering (NBE), Aalto University School of Science and Technology, Espoo, Finland

Current address:

ATH: Department of Neurosurgery and Hansen Experimental Physics Laboratory, Stanford University, Stanford, California, USA

KR: Visual Circuits Laboratory, Neuro-Electronics Research Flanders, IMEC and KU Leuven, Leuven, Belgium

HS: Institute of Pharmacy, Department of Pharmacology and Toxicology, University of Innsbruck, Innsbruck, Austria

Abbreviations

MEA	–	multi-electrode array
ND	–	neutral density
R*	–	rod isomerizations

Abstract

The division of labor between rod and cone photoreceptors allows the retina to reliably signal across many orders of light intensity. While the sensitive rods support vision under dim illumination, the extent of their saturation at high irradiances remains controversial. Using electrophysiological recordings from the retina and dorsal lateral geniculate nucleus of cone-deficient and visually intact mice, we show that rods can contribute to vision at any physiological light level. Upon stepping to high irradiances their contrast sensitivity is initially strongly reduced. However, over time rods recover and respond to moderate contrast. Surprisingly, rods regain responsiveness faster at higher light levels. This is mechanistically consistent with a model incorporating changes in phototransduction gain and bleaching adaptation. Overall, our data reveal that rods can respond across all irradiances to contrasts typically found in natural scenes, and that, paradoxically, raising irradiance across the photopic range increases the likelihood of eliciting such responses.

Introduction

Our visual system can function over a wide range of light intensities spanning about a dozen orders of magnitude [1,2]. This remarkable dynamic range requires a precise set of neural mechanisms that allow visual processing under dim and bright light conditions. The main mechanism underlying this ability is the use of two different photoreceptor classes, namely the rods and the cones. Rods are specialized for high-fidelity signaling at low light levels, whereas cones mediate fast signaling at higher light levels. Based on the division of labor between rods and cones, light intensities are called scotopic (only rods are active, starlight vision), mesopic (both rods and cones are active), and photopic (rods are saturated, and only cones are active, daylight vision). This division of light intensities has become a dogma in vision.

The distinction between mesopic and photopic conditions is, by definition, determined by the background irradiance at which rods saturate. The saturation point of rods has proved difficult to estimate and depends on the experimental approach, such as the properties of the background [3] and the stimulus [4]. Reported background intensities for rod saturation span 10^2-10^5 rod

isomerizations (R*) [3,5-7]. Overall, most textbooks [8-10] and studies, including recent ones [11-13], assume that increasing light intensity provides the best opportunity for minimizing retinal responses that are actively driven by rods.

At the same time, some studies suggest that this picture might be wrong or at least incomplete. Demontis et al recorded from guinea pig rods and found that while they are initially saturated by the background illumination of 10^3 R*, in a few seconds they partially recover responses to a bright flash, reaching 20% of the dark-adapted amplitude [14]. Furthermore, Yin et al argued that rods contribute to spatial vision at similar light levels ($1.38 \cdot 10^5$ R*) by measuring the light responses of horizontal cells and brisk transient ganglion cells in the guinea pig retina [15]. Finally, Naarendorp et al demonstrated in behavioral experiments that mouse rods may detect light flashes at a background light of 10^5 R* [16].

There is thus inconsistency in the literature regarding the degree to which bright backgrounds suppress rod responses. To some extent, these discrepancies could reflect methodological differences, e.g. species studied, endpoint measured, or experimental conditions [17-19]. However, there is currently neither an accepted mechanistic explanation for rod activity at high irradiance, nor a conceptual framework for predicting the extent of rod contributions at high irradiance, beyond the widely held assumption that once above the mid mesopic range increasing intensity provides the best opportunity for minimizing rod responses.

We set out to systematically explore the limits of rod vision by recording electrophysiological responses to light pulses presented over a wide range of background light intensities (up to 8 log units) in mice with non-functional cones. At each light level, we repeatedly measured light responses in the retina over 30 minutes to capture possible light adaptation effects. We find that rod responses to modest contrast stimuli are strongly reduced upon increasing the light level above a certain threshold ('photopic' threshold), but that following a suitable period they become detectable under all light intensities tested, both *in-vitro* and *in-vivo*. Most surprisingly, we find that, once within the photopic range, increasing the light intensities can even accelerate the recovery of rod responses - an observation that, to our knowledge, has never been reported. In-vivo recordings

from mice with intact cone function suggest that active rod contributions indeed affect visual responses at high light levels. Building upon a previously published computational model [20], we identified changes in phototransduction gain and bleaching adaptation as potential mechanisms for rod responses at high light levels. In summary, our data indicate that rods can contribute to visual responses at all physiological light intensities; and that contrary to conventional wisdom, raising the background light intensity within the 'photopic' range may even make this rod contribution more robust.

Results

Ganglion cells respond to contrast steps at all light levels in cone-deficient retinas

Using multi-electrode arrays (MEAs), we recorded spiking activity of ganglion cells from isolated cone-deficient (*Cnga3*$^{-/-}$) retinas to determine the irradiance at which rod responses to moderate contrast stimuli would disappear (n=10 retinas). During each experiment, we increased the ambient light level at 10-fold increments every 30 min, from $2{\cdot}10^{8}$ rod-effective photons cm^{-2} s^{-1} (1 R*rod^{-1} s^{-1}, neutral density filter 8; ND8) to $2{\cdot}10^{15}$ rod-effective photons cm^{-2} s^{-1} (10^{7} R*rod^{-1} s^{-1}, ND1, Fig 1A-C). The responses of a representative single ganglion cell to full-field steps of positive contrast (+0.25 Michelson, +0.66 Weber, see Methods for definition of contrast) or negative contrast (–0.49 Michelson, –0.66 Weber) are shown in Fig 1D and E, respectively. We presented blocks of 5 repeats of this stimulus every 5 minutes (spike raster shown on the left, average spike rate shown on the right). After switching from ND5 to ND4 (from $2{\cdot}10^{11}$ to $2{\cdot}10^{12}$ rod-effective photons cm^{-2} s^{-1}), the cell shown in Fig 1D,E did not respond to the stimulus during the first presentation, consistent with the view that rods had become saturated. This corresponds to a background at which other authors have described rod saturation (10^{4} R*rod^{-1} s^{-1} [3,5,6]) and we therefore refer to ND4 and brighter as the 'photopic' light range from here on. However, responses returned after continued exposure to this background. Surprisingly, rather than showing further evidence of saturation, responses of this cell actually became more apparent with subsequent

112 increases in irradiance (even up to ND1, 1000-fold above the background at which responses had
113 first disappeared).

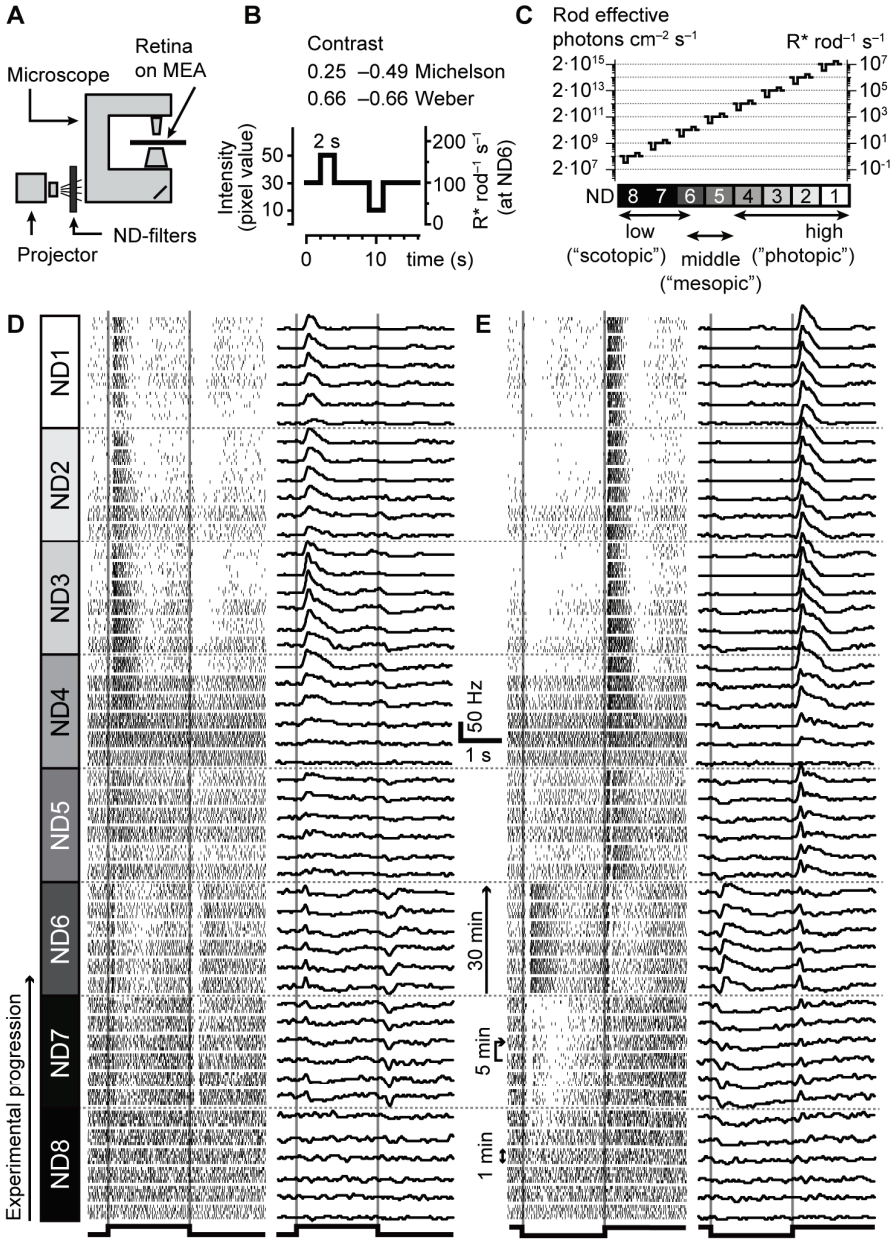

Fig 1. Example responses of a single Cnga3$^{-/-}$ ganglion cell across brightness levels.
A *Different light levels were achieved experimentally by inserting neutral density (ND) filters in the stimulation light path.*
B *Full-field contrast step stimulus, consisting of positive and negative contrast steps.*
C *Absolute intensities of the stimulus shown in* ***B*** *at different experimental light levels.*
D, E *Raster plots (left) and firing rates (right) for a single ganglion cell in response to the full-field positive (****D****) and negative (****E****) contrast steps. Blocks of 5 consecutive repetitions (left) are averaged in one trace on the right. This cell showed responses at all light levels (very weakly responding at ND8), with a short suppression of responses in the beginning of ND4. Note that in this ganglion cell, the rod-mediated responses are even stronger at high (ND4 to ND1) than at lower (ND8 to ND5) light levels.*

126 This behavior was also apparent across the population of retinal ganglion cells (Fig 2). The fraction
127 of ganglion cells showing a clear response to positive or negative contrast steps was high through
128 the lower irradiances and fell dramatically upon initial switch to ND4 ($2 \cdot 10^{12}$ rod-effective photons
129 cm^{-2} s^{-1}, 10^4 R*rod^{-1} s^{-1}), only to recover over time (Fig 2A). Responses collapsed again after
130 switching to ND3 ($2 \cdot 10^{13}$ rod-effective photons cm^{-2} s^{-1}, 10^5 R*rod^{-1} s^{-1}), but once again recovered,
131 and were then retained even at extremely high irradiances (ND2 and ND1, Fig 2A). An analysis of
132 mean response amplitude (averaging the amplitudes of only those units responding in any given
133 epoch, Fig 2B) painted a similar picture, with only transient loss of response strength upon
134 switching to ND4 and ND3, but otherwise clear responses at all irradiances. Indeed, some units,
135 like the one shown in Fig 1, had their biggest responses at the brightest backgrounds.

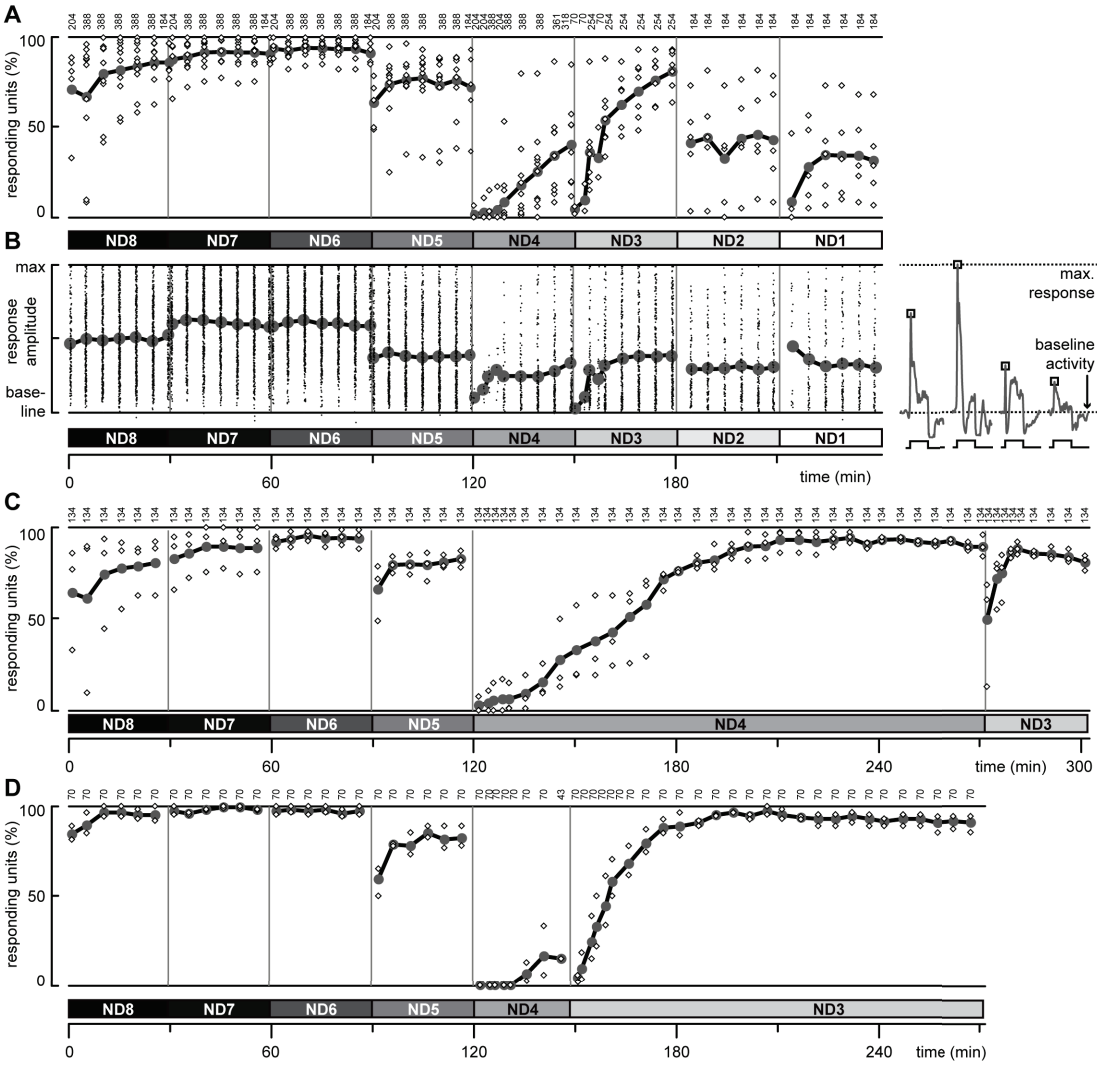

Fig 2. Responsiveness of ganglion cells in isolated Cnga3$^{-/-}$ retina

A *Percentage of responsive ganglion cells in each retina (small white diamonds) and across all experiments (large gray disks and thick line) that responded to a full-field positive or negative contrast step. The numbers on top indicate the total number of ganglion cells recorded at each time point of the experimental paradigm.*

B *Response amplitude (normalized peak spike rate) of all individual units that responded (small dots) and their mean response amplitude (large gray dots and thick line). Right panel: Schematic of how response amplitude was determined. Each ganglion cell was followed throughout the experiment, and response strength was taken as the relative peak spike rate (indicated by squares) between the baseline activity of the cell and the cell's maximal response. For simplicity, schematic shows only the positive contrast step.*

C *Percentage of responsive ganglion cells in a subset of experiments (n=3 retinas) in which we stayed at ND4 for 2.5 hours. Data from these retinas (up to 150 min) are also part of **A** and **B**.*

D *Percentage of responsive ganglion cells in a subset of experiments (n=2 retinas) in which we stayed at ND3 for 2 hours. Data from these retinas (up to 180 min) are also part of **A** and **B**.*

The results shown in Fig 2A indicated that the major difference between the two photopic light levels ND4 and ND3 might be the rate at which responses recovered following the irradiance increment. To explore this in more detail, we held a subset of retinas at these backgrounds for 2.5 hours. In both cases, the fraction of responding units fell close to zero immediately after the step to ND4 (Fig 2C) or ND3 (Fig 2D), but reached nearly 100% by the end of the recording. There was, however, a big difference in the rate of recovery, which occurred much faster at the brighter background (ND3, taking about 10 min for half of the ganglion cells to recover their responses) than at the dimmer background (ND4, taking between 30 and 60 min). Put another way, switching to the brighter background led to a faster recovery of responses than simply holding at ND4. We observed similar behavior as in Fig 2A and B in two other cone-deficient mouse lines (*Pde6c*$^{cpfl1/cpfl1}$ and *Gnat2*$^{cpfl3/cpfl3}$, see S2 Fig).

These in vitro ganglion cell recordings from cone-deficient mice thus reveal that: 1.) rods can drive responses to moderate contrast stimuli across all irradiances tested; and 2.) once within the 'photopic' range, increasing irradiance can make rod-driven responses more robust.

ERG recordings confirm rod responses at high light levels in cone-deficient retinas

We next set out to confirm these findings using a more direct recording of rod activity. To this end, we applied pharmacological agents (see Methods) to inhibit second-order responses in retinal explants of *Cnga3*$^{-/-}$ mice and recorded the isolated photoreceptor response using electroretinography (*in-vitro* ERG, Fig 3). The stimulus shown in Fig 3A, consisting of a variety of 50-ms light flashes of moderate to high contrasts, was shown 16 times at each light level (30 min) from ND8 to ND2. We quantified the strength of the elicited ERG signal as the mean amplitude of the negative voltage deflection during 300 ms directly after the flash onset, while the 300 ms voltage signal preceding the flash was used as a baseline to test for significance of the flash-elicited responses (Wilcoxon rank sum test, resulting p-Values are color-coded in Fig 3B).

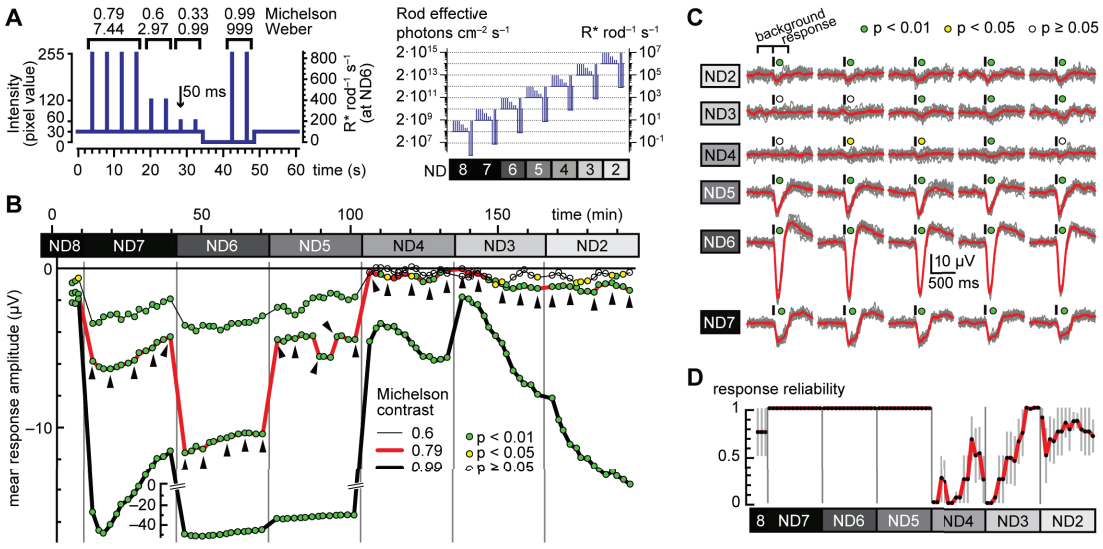

Fig 3. In-vitro ERG recordings from isolated Cnga3$^{-/-}$ retina

A *Stimulus used for in-vitro ERG recordings consisted of 50-ms flashes ranging from 0.33 to 0.99 Michelson contrast. Right: absolute stimulus intensities with different ND filters.*

B, C *Data from one representative retina.* ***B*** *Running average of the mean negative voltage deflections in the 300 ms after flash onset (response minus background). Each data point shows mean from 3 consecutive stimuli (i.e. from 12 individual flashes for 0.79 Michelson contrast, and 6 flashes for the other contrasts; data for the lowest contrast is omitted for clarity). Neighboring data points are shifted by 1 stimulus. The color-coded disks indicate the level of significance of the response relative to the background activity (Wilcoxon rank sum test). The raw traces underlying the data points indicated by the triangles are shown in* ***C*** *(gray: individual responses; red: average of 12 responses; black bars above traces: timing of flash).*

D *Response reliability of ERG responses (see Methods and Suppl. Fig S1B) to the flashes of 0.79 Michelson contrast (mean ± s.e.m. of n=4 retinas) calculated from the p-Values in* ***B****. Even though ERG responses are small at high light levels, they can be reliably detected. Response reliability for flashes of other contrasts are shown in S3 Fig.*

192 In using this method we were unable to record responses to the lower contrasts (0.33 and 0.6
193 Michelson contrast) at higher irradiance (ND4 to ND2; Fig 3B and S3 Fig). This observation, taken
194 by itself, would support the concept of rod saturation. However, in other respects, the ERG
195 responses replicated our findings from ganglion cell recordings: ERG responses to the
196 intermediate contrast (Michelson contrast 0.79, red curve in Fig 3B, individual flash responses in
197 Fig 3C), were transiently lost upon switching to ND4 ($2 \cdot 10^{12}$ rod-effective photons cm^{-2} s^{-1}, 10^4
198 R^*rod^{-1} s^{-1}), but reemerged over time. The same occurred after switching to brighter light levels
199 with responses first disappearing, but then reappearing with a time course that was faster for
200 higher light levels. The time course of reemerging responses at the intermediate contrast of 0.79
201 was consistent across all tested retinas (n=4, mean ± s.e.m., Fig 3D). In this way, the rod-derived
202 ERGs showed a similar pattern of loss and subsequent recovery at high irradiances to the retinal
203 ganglion cells above (Fig 2). We confirmed these findings with qualitatively identical and
204 quantitatively similar results in two other cone-deficient mouse lines ($Pde6c^{cpfl1/cpfl1}$ and
205 $Gnat2^{cpfl3/cpfl3}$, S3 Fig).

206 Two wider implications emerge from these experiments. First, our data support the view of
207 saturation as a loss of contrast sensitivity [16,21], as photopic responses were visible to the
208 highest contrast (0.99 Michelson contrast) throughout, to medium contrast (0.79) only after
209 recovery from transient saturation, and never to the lowest contrasts (0.6 and 0.33). This implies
210 that stimulus contrast is a critical aspect of experimental design in revealing rod responses under
211 photopic conditions. Second, in our ganglion cell recordings (Fig 2), photopic rod-driven responses
212 were apparent with a stimulus contrast of only 0.25, while the ERG recordings required 0.79
213 Michelson contrast (Fig 3). This discrepancy highlights that different experimental approaches can
214 yield different estimates of rod sensitivity under photopic backgrounds. Together, these recordings
215 show that contrast sensitivity of rods is substantially reduced upon stepping to high irradiances, but
216 that this recovers over time and that this recovery occurs faster at higher irradiances.

217

218

Rods drive light responses at high irradiances *in-vivo* in the *Cnga3*$^{-/-}$ thalamus

Having described rod responses in explanted retinas under even the brightest backgrounds, we next asked whether rod mediated light responses would also be apparent in an intact preparation. To this end, we recorded multiunit activity from the dorsal lateral geniculate nucleus (dLGN) of anesthetized *Cnga3*$^{-/-}$ mice (Fig 4, recording positions shown in Fig 4D) in response to 50-ms flashes of positive contrast (0.75 Michelson Contrast). For these experiments we changed the sequence of irradiance presentations so that recordings at higher (photopic) irradiances (ND4, ND3, and ND2) were interspersed with a moderate background (mesopic, ND5, predicted to support strong rod responses), in order to confirm that the preparations retained good visual responses throughout the recording session.

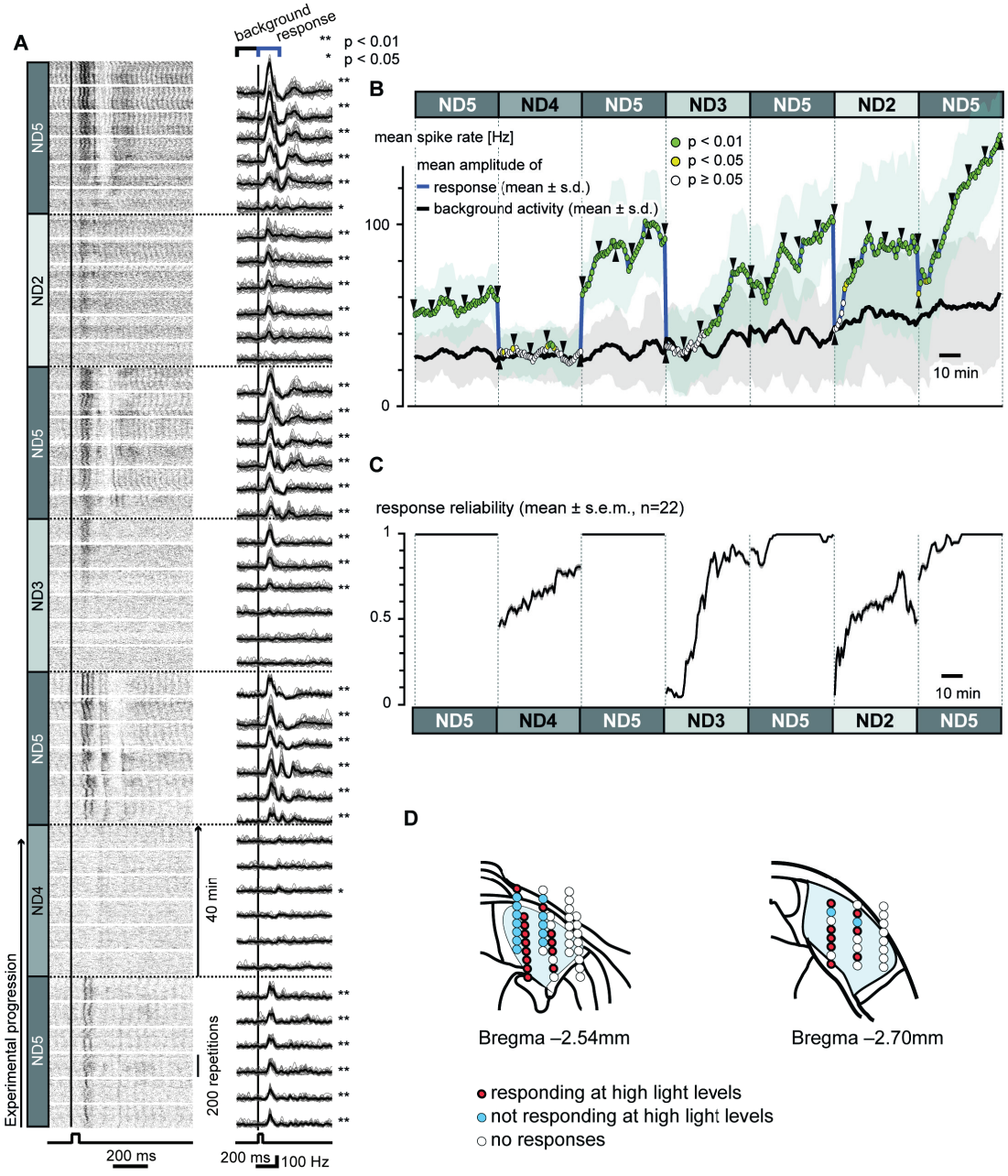

229

230 ***Fig 4. Rod responses in in-vivo dLGN recordings in Cnga3$^{-/-}$.***
231 ***A*** *Example response of one multiunit to a 50 ms flash at different light levels. Responses to each*
232 *of the 8400 single repetitions are shown in the raster plot (left). For analysis, 10 consecutive*
233 *repetitions were averaged (1 "group", gray lines on the right). In black, the averages over 20 such*
234 *groups (200 flashes) are shown.*
235 ***B*** *Response amplitude (blue curve) and background activity (black curve) of the multiunit shown in*
236 ***A*** *(moving average over runs of 20 groups (=200 flashes), shifted by 1 group. Arrowheads mark*
237 *values corresponding to the raw traces shown in the right column in A). Responses significantly*
238 *above background are color-coded in green (p<0.01) and yellow (p<0.05, rank sum test). This*

example multiunit stops responding after switching to ND4. However, at ND3 and ND2 the responses reappear after several minutes.
***C** Population data for those multiunits responding at high light levels (n=22/36, mean ± s.e.m.), depicting the reliability of their responses (see Metods and S1 Fig). Responses at high light levels recovered with an intensity-dependent time course.*
***D** Electrode positions during LGN recordings. Electrodes on which responses recovered at high light levels are color-coded in red, electrodes with responses only at moderate light levels are colored in blue.*

Firing patterns of a representative multiunit recording are shown in Fig 4A. As predicted, strong and stable flash responses were recorded at ND5 ($4.52 \cdot 10^{11}$ rod-effective photons cm^{-2} s^{-1}). In this example, responses became hard to discern at ND4 ($4.52 \cdot 10^{12}$ rod-effective photons cm^{-2} s^{-1}), while at the higher irradiances, responses transiently disappeared immediately following the irradiance step, but returned during extended exposure to that background. Similar to the *in-vitro* recordings, the rate of response recovery was positively correlated with irradiance. These general patterns were borne out by a more systematic analysis of these data (Fig 4B), in which response amplitude (difference in spike rate in 200-ms windows before and after the flash) and reliability (p-Value for Rank Sum Test comparing these values) were plotted as a function of time.

Across the population of multi-unit traces there was more diversity in response characteristics. Of those that responded well at ND5, a minority (n=14/36) failed to show consistent responses at the highest irradiances ND3 and ND2 ($p>0.05$ for Rank Sum Test for at least half of trials at these irradiances). The majority (n=22/36), however, recovered sensitivity over time after an initial drop of responsiveness immediately after switching to these bright backgrounds (Fig 4C). Once again, the rate of recovery was reliably fastest at the brightest background (ND2). Behavior at the intermediate irradiance (ND4) was variable, with some multiunit traces matching the very poor responses shown for the single example in Fig 4A, B, while others responded reliably (Fig 4C).

These experiments suggest that rods can drive visual responses at high light levels also *in-vivo*. The observed time course of response reemergence at high light levels (faster for brighter background) was consistent with the observations *in-vitro*.

Rods shape thalamic responses at high light levels in the presence of cones

The experiments with cone-deficient mice revealed that rods can function across all physiological background light intensities in this species. A reasonable question is whether this allows rods to contribute to visual responses in animals with an intact visual system (i.e., when cones are also functional), or whether the amplitude of rod signals at bright backgrounds is so weak that they are "drowned out" by cone activity. To answer this, we sought a method of identifying any putative rod contribution to the overall visual response in cone-sufficient mice. Our approach was to take advantage of a transgenic mouse line (*Opn1mw*^{R}) in which the mouse M-opsin coding sequence is replaced by the human long-wavelength sensitive ('L' or 'Red') opsin sequence [22,23] in this animal, the wavelength sensitivity of rods and cones is very different, allowing us to ask if rods impact the spectral sensitivity of visual responses under bright backgrounds. To avoid the possibility of recording melanopsin-driven responses we crossed these *Opn1mw*^{R} animals with a melanopsin knockout (*Opn4*$^{-/-}$) line for use in our experiments.

Anaesthetised *Opn1mw*^{R}*:Opn4*$^{-/-}$ animals were adapted to a violet light (λ_{max}=400nm) to which rods, and cones containing L-opsin and S-opsin are approximately equally sensitive (Fig 5A, B). Responses to blue (λ_{max}=430), cyan (λ_{max}=480) or red (λ_{max}=630) flashes, presented in pseudorandom order at 15 different intensities superimposed upon the background (Fig 5B), were recorded in the contralateral dLGN (recording positions shown in Fig 5F). Given the divergence in spectral sensitivity between rods and both S-opsin and L-opsin there is a big difference in the effective contrast of these flashes for rods and cones across the wavelengths. In particular, while flashes at all three wavelengths present significant contrast for L-opsin, rods should be much more responsive to the blue and cyan stimuli, while S-opsin contrast is much lower at all wavelengths (Fig 5B). Under true photopic conditions, i.e. with rods truly saturated, we would expect equivalent responses to flashes at all wavelengths when expressed in L-cone contrast, while rod intrusion at mesopic irradiances should produce differential responses to blue and cyan versus red flashes.

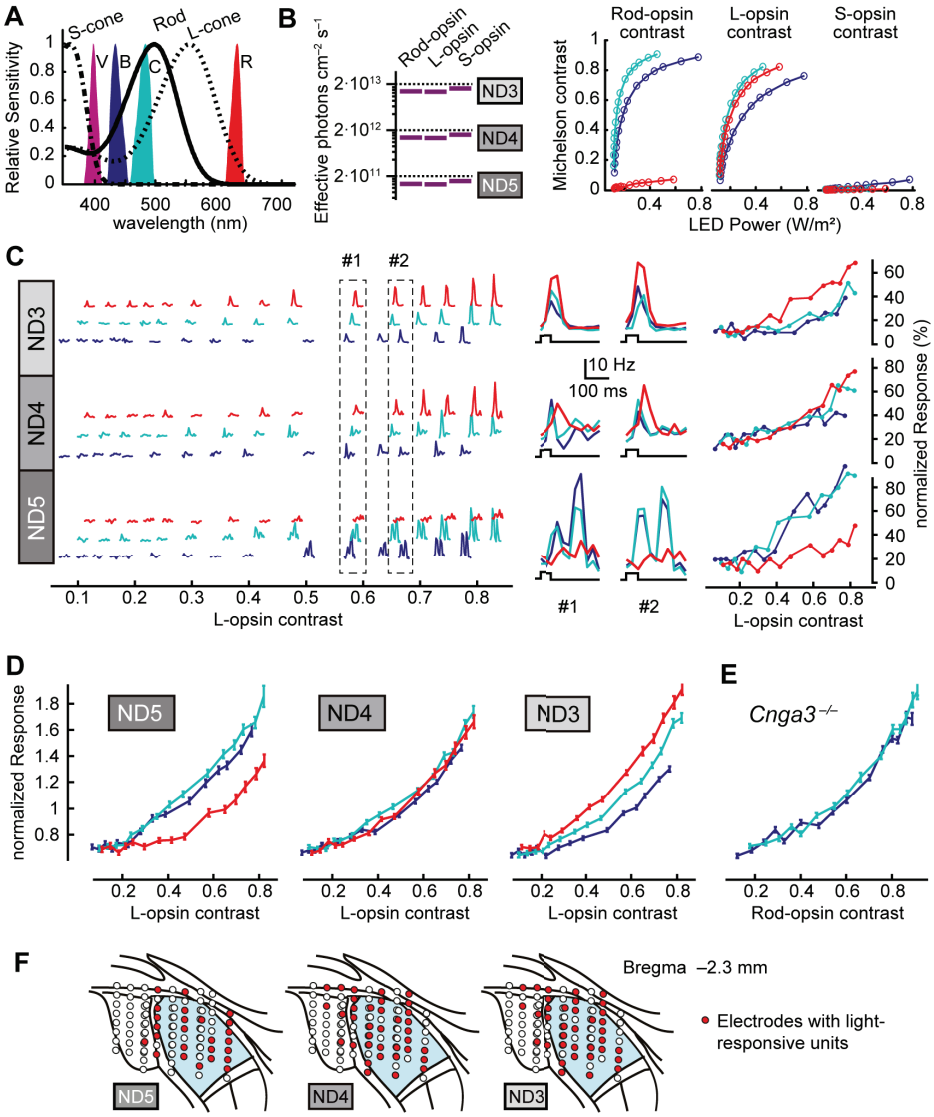

294

295 ***Fig 5. Rod responses in in-vivo LGN recordings in mice with rods and cones.***
296 *Across all panels, cyan symbols/lines represent data from cyan flashes, blue symbols/lines data*
297 *from blue flashes and red symbols/lines data from red flashes.*
298 ***A** Spectral power of flash stimuli in relation to rod and cone spectral sensitivity. S-opsin, rods and*
299 *L-opsin are roughly equally sensitive to the violet (V) background, but differ markedly in their*
300 *sensitivity to blue (B), cyan (C) red (R) flash stimuli.*
301 ***B** Estimated absolute intensity of the violet background (retinal irradiance, left) and Michelson*
302 *contrast of blue, cyan, and red flash stimuli for rod, L-opsin, and S-opsin (right). All flash colors are*
303 *of similar contrast for L-opsin, while rods are only activated by blue and cyan stimuli, and all stimuli*
304 *present very low contrast to S-opsin.*
305 ***C** Responses of an example unit at medium (ND5), high (ND4) and very high (ND3) irradiances.*
306 *Left panel shows mean PSTH for stimuli of all presented contrasts; middle panel an expanded*
307 *comparison of responses to blue, cyan and red stimuli of roughly equivalent L-opsin contrast; and*
308 *right panel shows the relationship between normalized mean response amplitude (see methods)*
309 *and L-opsin contrast across all flashes.*

D *Mean ± s.e.m. of normalized response amplitude (normalized by the mean response across contrasts and colors, see methods) to blue, cyan and red flashes as a function of L-opsin contrast for all light-responsive units at ND5 (n=131 units from n=6 out of 7 mice); ND4 (n=201 units from n=7 mice) and ND3 (n=213 units from n=7 mice). Responses at the three wavelengths could be adequately fit with a single function at ND4 (consistent with the view that they are driven by L-opsin), but not at either ND5 or ND3 (statistical analysis of curve fits for each wavelength are summarized in S5 Table).*
E *Mean ± s.e.m. of normalized response amplitude (see methods) for cyan and blue flashes presented to Cnga3$^{-/-}$ mice at ND6 plotted as a function of estimated rod contrast (n=229 responsive units from 3 mice; in mice 1 and 2 we collected data from two different electrode placements, in mouse 3 from three placements). The responses at the two colours were indistinguishable confirming the suitability of our methods for estimating photoreceptor spectral sensitivity in vivo (BC: R^2_{BC} = 0.448, $R^2_{BC,null}$ = 0.448, $\Delta R^2_{BC} \approx 0$).*
F: *Histological confirmation for electrode placements in n = 3 Opnmw^R:Opn4$^{-/-}$ animals.*

When these flashes were presented at ND5 (1.38 10^{11} rod-effective photons cm^{-2} s^{-1}, at which rod responses were always strong in our recordings with cone-deficient mice, Fig 4), we found clear evidence of rod intrusion in the composite flash responses. Thus, when flash intensities were expressed in L-opsin contrast, responses were consistently larger for blue and cyan flashes than for red flashes, as shown in Fig 5C for a single unit and in Fig 5D for the population of recorded units (see S5 Table A for statistical analysis). Stepping up to ND4, this difference disappeared, with response amplitude at all wavelengths being adequately predicted by L-opsin contrast. Responses at ND4 could thus be interpreted as being truly photopic. In common with the other data presented here, however, a further increase in irradiance produced an increase in rod intrusion. At ND3, flash response amplitude could no longer be predicted by L-opsin contrast. In this case, blue and cyan responses were consistently smaller than those elicited by red flashes of similar cone contrast. These data indicate an inhibitory influence of rods on the cone flash response at this high photopic level (such inhibitory rod-cone interactions have precedent in the psychophysics literature [24]. To confirm that the effect at ND3 was not attributable to some methodological error, we first tested how robust it was to errors in our estimate of *in-vivo* L-opsin spectral sensitivity. We varied the two parameters that could strongly influence this estimate (pigment optical density and pre-receptoral spectral filtering; see Methods), but found that the reduced responsiveness at blue and cyan was retained (S5 Table B). We next confirmed that responses to blue and cyan flashes in *Cnga3$^{-/-}$* mice were equivalent to each other when expressed as a function of our estimated rod contrast (Fig 5E),

suggesting that the difference to blue and cyan flashes at ND3 in *Opn1mw*^{R}*:Opn4*$^{-/-}$ mice could be attributable to a difference in relative excitation of rods and L-opsin (L-opsin to Rod-opsin ratio of excitation at brightest flash: 0.48 for blue and 0.44 for cyan). In summary, while our data are consistent with flash responses being wholly cone generated at ND4, they reveal a significant rod contribution at the brighter background (ND3).

Computational model: Phototransduction gain and bleaching adaptation as possible mechanisms

What physiological processes could explain the pattern of rod responses under bright backgrounds that we observed? As a framework for thinking about this problem, we explored the most detailed available computational model of rod phototransduction [20]. This model of Invergo et al simulates the phototransduction cascade with a system of ordinary differential equations (ODE) to describe the reaction network of the involved molecular species. We used the model to predict photocurrents induced by a sinusoidally modulated stimulus (0.25 Hz) of either high contrast (0.98 Michelson contrast, full amplitude: 2 log units) or moderate contrast (0.7 Michelson contrast, full amplitude: 0.75 log units, black traces in Fig 6) against a range of irradiances mimicking our experiments: every 30 min the background increased by 1 log unit, spanning low (ND8) to high (ND1) intensities (Fig 6).

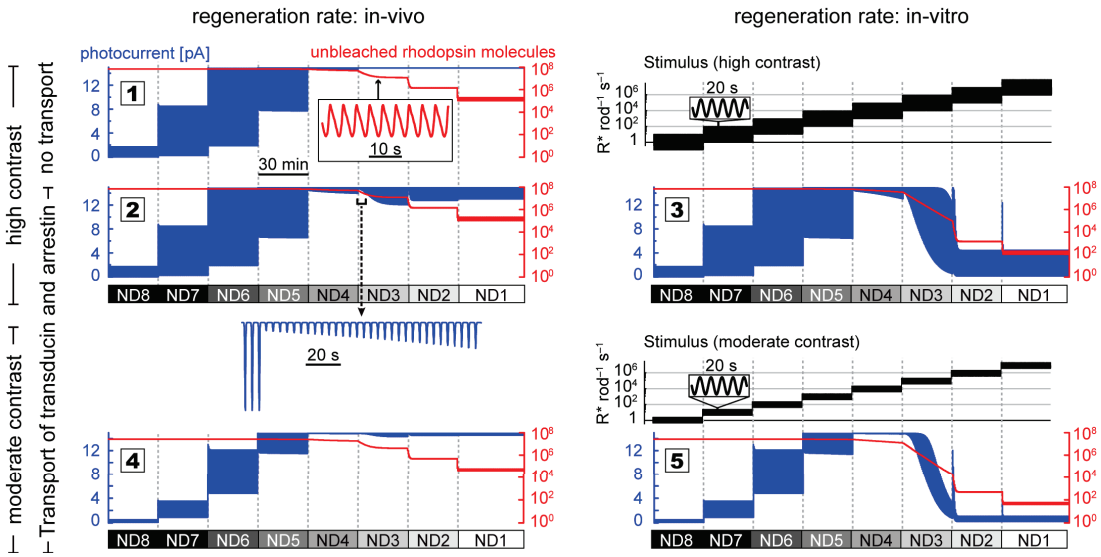

Fig 6. Computational model of rod behavior at different light levels for various parameter combinations.
The model was fed with a sinusoidal stimulus of high (upper panels) or moderate contrast (lower panels, stimulus shown in black). Mean brightness levels were changed every 30 minutes by 1 log unit as in our experiments. In-vivo and in-vitro experimental conditions (columns) were mimicked by adjusting the rhodopsin regeneration rate (parameter k_{recyc}). Without transducin and arrestin translocation (panel 1), even the high-contrast stimulus did not elicit photocurrents (blue curves) at high light levels (ND4 and brighter). With transport, high-contrast responses were apparent (panel 2). Low-contrast responses (panel 4) elicited weak modulation with similar amplitude as at ND8. Reducing the rhodopsin regeneration rate to mimick in-vitro experimental conditions (panels 3 and 5) promoted photocurrents at high light levels. Rhodopsin bleaching (red curves) supports response re-emergence. For panels 4 and 5, rhodopsin content was set to $2.6 \cdot 10^7$ molecules (other panels: $7 \cdot 10^7$).

The original model of Invergo et al, without any modifications, did not replicate our experimental findings, but instead predicted rod saturation at high light levels (Fig 6, panel 1; blue curves in Fig 6 show the photocurrents predicted by the model). However, the model also predicted that the concentration of unbleached rhodopsin (red curves in Fig 6) would keep being modulated at all irradiances through isomerization events triggered by the sinusoidal stimulus (see inset in panel 1). This indicates that a reduced gain of the phototransduction cascade might prevent saturation and allow rods to respond to this stimulus.

One feature of photoreceptor physiology that the original model does not include is the irradiance-dependent translocation of arrestin and transducin between inner and outer segments [25,26]. At higher light levels, arrestin moves into the outer segment, increasing its effective concentration; while transducin leaves the outer segment, reducing its concentration. Both translocations have the net effect of reducing the gain of the phototransduction cascade, thereby contributing a mechanism of light adaptation. We modified the model to include these events in a very simplified manner, namely as an instantaneous increase/decrease of their concentrations upon light-level transitions (S4 Fig B). This modification resulted in modulated photocurrents to the high contrast stimulus at all light levels (Fig 6, panel 2, blue curve). Moreover, the model replicated our observations that responses are initially weak after the light level increase, but gain strength with a time course that is faster at higher light levels (see also magnified view below panel 2). Note that this time course of the photocurrents needs to be shaped by other adaptive mechanisms beyond the translocation of transducin and arrestin, as the translocations were implemented as instantaneous changes. We

found that the faster response re-emergence at higher irradiances coincided with the increased rate of rhodopsin bleaching (red curve in panel 2). Rhodopsin bleaching reduces the rate of isomerization events and might thus be one of the mechanisms allowing for rod responses at high light levels, similar to the suggested role of bleaching adaptation in cones [27].

We indeed found that the model behavior at high light levels (but not at low and moderate irradiances) was quite sensitive to parameter variations that influenced the rhodopsin concentration. The first model parameter we turned to was the rhodopsin regeneration rate (k_{recyc}). This parameter is highly relevant in the context of comparing our *in-vitro* and *in-vivo* experiments. We estimate that the regeneration rate is about 1000-fold lower in explanted retina because of the lack of pigment epithelium. The model predicts rod response reemergence at high irradiances in both *in-vitro* and *in-vivo* cases (panels 2 and 3 in Fig 6); however, while photocurrents *in-vivo* remained closer to saturated values (panel 2), they were more robust in isolated retina (panel 3). Indeed, the predicted properties of photoresponses *in-vitro* at bright backgrounds approached those under “scotopic” conditions. This predicts that increased bleaching promotes escape from saturation, which may also explain our paradoxical experimental findings that rod responses reemerged more quickly and were more robust at the highest irradiances.

In fact, any variation of model parameters that resulted in a lower rhodopsin concentration promoted high-irradiance rod responses. S4 Fig A gives an overview of the model behavior for all parameter combinations we tested. Only moderate reductions of either k_{recyc} (panel b in S4 Fig A) or of the total number of rhodopsin molecules (R_{total}, panel g in S4 Fig A) were necessary to rescue the responses to moderate-contrast stimuli, which were saturated with the original values for these model parameters (Fig 6, panel 4). Reducing both parameters (k_{recyc}, R_{total}) in concert required even smaller adjustments that are well within physiologically reasonable values (S4 Fig C). Taken together, we found that the model could reproduce all key features of our experimental data: the transient saturation when stepping to high backgrounds, the gradual recovery of responses at all backgrounds, both in-vivo and in-vitro, and the irradiance-dependence of the rate of recovery. This could be achieved by physiologically plausible variations of the model parameters compared to the

423 model devised by Invergo et al [20] (arrestin/transducin translocation and realistic changes in k_{recyc}
424 and R_{total}).

425

426 **Discussion**

427 Our experiments were initially motivated by a desire to take advantage of transgenic cone-deficient
428 mice to describe the transition to rod saturation as irradiance increases. Although the concept of
429 rod saturation in bright backgrounds is widely accepted [5,12] and can be readily found in standard
430 neuroscience textbooks [8-10], the conditions under which rods saturate are poorly resolved in the
431 literature. On the one hand, there is a large body of literature postulating rod saturation at high
432 backgrounds [11,13,28]. This dates back at least to the classical study of Aguilar and Stiles [21]
433 who found rod saturation psychophysically with the two-color incremental threshold test - findings
434 which are reflected in the daily experience of achromatopsia patients (rod monochromats). These
435 individuals are blinded in a bright environment because they lack functional cones [29]. The
436 phenomenon of rod saturation has also been successfully used as a research tool. For example,
437 Santos-Feirrera et al showed the feasibility of cell replacement in the adult retina with the help of
438 *Pde6c*$^{cpfl1/cpfl1}$ mice (a cone-deficient mouse line which we also used in our study, S2 Fig and S3
439 Fig): in their study, *Pde6c*$^{cpfl1/cpfl1}$ retinas treated by transplanting cone-like cells maintained
440 photopic responsiveness, while untreated or sham treated *Pde6c*$^{cpfl1/cpfl1}$ retinas lost ganglion cell
441 responses upon stepping to photopic backgrounds [30]. At the same time, there are studies that
442 suggest that rods may support vision at all light levels [4,15,16,31].

443 By continuously probing rod responses under exposure to a range of background light, our data
444 has provided a new conceptual framework within which to resolve these inconsistencies and
445 predict rod activity at high irradiance. We found that upon stepping to irradiances within the
446 'photopic' range (> $2 \cdot 10^{12}$ rod-effective photons cm^{-2} s^{-1}; 10^4 R*rod^{-1} s^{-1}; ND4), rod responses to
447 moderate contrast were commonly lost, indicative of saturation. However, this effect was transient,
448 with responses re-emerging under continuous exposure to any background. Furthermore, the rate
449 of re-emergence was positively correlated with irradiance, whether we progressively increased

irradiance (Fig 2) or jumped to different light levels within the photopic range (Fig 4). As a consequence, saturation lasted longest at the dimmest 'photopic' irradiance and was progressively transient at higher irradiance. This lead to the most surprising observation that rod saturation was less commonly observed at the brighter backgrounds.

The transient nature of rod saturation, and the unexpected relationship between irradiance and the rate of response recovery, may thus be one reason that different studies reach different conclusions regarding rod saturation. On the one hand, we do see evidence of rod saturation under irradiances typically considered 'photopic'. At the right irradiance, this saturation can last a long time. On the other hand, our data confirm that rods can escape saturation to drive responses to moderate contrast stimuli under all background light intensities. This is consistent with the view that no physiologically relevant irradiance can be assumed to saturate rods. As a result, published studies could come to quite different conclusions regarding the extent of rod saturation under 'photopic' conditions depending on the exact light levels used and the duration of exposure to photopic illuminance. Moreover, because the rate of rod recovery is positively correlated with irradiance, attempts to maximally saturate rods by using increasingly brighter backgrounds are predicted to have exactly the opposite effect. These insights are helpful both in interpreting published work and designing future experiments.

A second reason why rod responses at photopic light levels may have been missed is their lower amplitude [32,33] in addition to their reduced contrast sensitivity. Rod responses could thus be invisible when using low contrasts and/or measurement systems with inherently low signal-to-noise ratio (Fig 3). Furthermore, the small rod signal may be hard to detect in visual pathways with low spatiotemporal pooling. This could explain the wide spread of relative response amplitudes in individual ganglion cells we find (Fig 2D); why rod responses at high backgrounds were not apparent in all visually responsive dLGN neurons; and a previous report [34] that cone-deficient mice lose the optokinetic reflex at backgrounds (10 $R^*rod^{-1}\ s^{-1}$) well below established rod saturation thresholds.

476 The process of exploring the computational model and its parameters highlighted a couple of
477 features of the rod response at high irradiance that are worthy of comment. Firstly, the gradual
478 recovery of rod responses during extended exposure to bright backgrounds could have at least two
479 plausible origins. The most parsimonious is that it simply reflects the kinetics of bleaching
480 adaptation. In our model, bleaching could successfully recreate both the reappearance of rod
481 signals over time and the observation that this occurs more rapidly at higher irradiance. However,
482 time-dependent changes in transducin and arrestin location likely also contributed to the time
483 course of response reemergence. Secondly, because the amplitude of rod responses depended
484 strongly upon k_{recyc} (rhodopsin regeneration rate), it is very likely that rod activity at high light levels
485 will recover more quickly and be stronger in isolated retina in which native pigment regeneration
486 mechanisms are impaired - a conclusion that may first seem counterintuitive. It follows that one
487 cannot ensure suppression of rod responses experimentally by simply increasing the background
488 irradiance; the opposite is true: such an approach is likely to even enhance rod responses, as
489 reemergence of rod responses (mediated by bleaching, exchange of enzymes between inner and
490 outer segment, and potentially additional adaptive processes) may require dozens of minutes at
491 the dimmest high (photopic) light levels, but can be accelerated to a short time at brighter light
492 levels.

493 Aside from this, our modeling suggests that the presence of rod responses at high light levels
494 could be very sensitive to naturally occurring variations in the gain of the phototransduction
495 cascade, in addition to variations of the total rhodopsin concentration (R_{total}) and the regeneration
496 rate of rhodopsin (k_{recyc}). It is thus conceivable that slight variations in the properties of the rod
497 phototransduction cascade and its regulation (e.g. differences in molecular concentrations, in
498 kinetic properties, in translocation processes, in the volume of the outer segment) would result in a
499 different preponderance of rods to support vision at high light levels. Such differences might exist
500 between species, between individuals of the same species, between different rods in the same
501 retina, or even within the same rod during the circadian cycle. The experience of human rod
502 monochromats (achromatopsia patients) supports the idea of such diversity. While these patients
503 are commonly photophobic and blinded in a bright environment [29], for some individuals this is not

504 the case [35] – their rod system does apparently not saturate. Deeper insight into the underlying
505 mechanisms of this non-saturating phenotype in some individuals might even reveal new
506 opportunities to treat rod monochromats by appropriately reducing the gain of the rod cascade.
507 While such a reduced gain would be counterproductive for low-light vision, our daily lives, with
508 electrical lighting all around us, happen mostly beyond the scotopic range, so that such treatment
509 could indeed have a net positive benefit for the patients.
510

511 ## Methods

512 ### 1. Animals

513 There are several transgenic mouse lines in which cone responses are abolished due to mutations
514 disrupting the cone phototransduction cascade. In *Cnga3*$^{-/-}$ mice [36], kindly provided by M. Biel
515 for in-vitro experiments, the cone-specific alpha-subunit of the cyclic nucleotide gated channel is
516 mutated, preventing voltage changes in cones upon light activation. *Cnga3*$^{-/-}$ mice were 4.5 to 6
517 weeks old for ganglion cell recordings, 8 weeks for ERG recordings, and approximately 6 to 8
518 weeks for in-vivo experiments. In *Pde6c*$^{cpfl1/cpfl1}$ mice (Jackson strain #3678), kindly provided by Bo
519 Chang (The Jackson Laboratory, Bar Harbor, ME), the cone-specific phosphodiesterase is non-
520 functional. *Pde6c*$^{cpfl1/cpfl1}$ mice were 11 to 13 weeks old. In *Gnat2*$^{cpfl3/cpfl3}$ mice (Jackson strain
521 #6795), the cone-specific transducin is non-functional. *Gnat2*$^{cpfl3/cpfl3}$ mice were 5 to 13 months old.
522 All in-vitro experiments were performed with explanted retinas, with retinal pigment epithelium
523 removed. “Red opsin” mice (Opn1mwR; Opn4$^{-/-}$) of approximately 6 to 18 weeks were used for in-
524 vivo experiments and bred in-house at the University of Manchester, UK. Animal use was in
525 accordance with German, UK and European regulations and approved by the
526 Regierungspräsidium Tübingen (in vitro experiments) and the local Manchester Animal Welfare
527 and Ethical Review Board (AWERB; Manchester, UK; in-vivo experiments).

528 ### 2. In vitro MEA recordings

529 MEA setup

530 Mice were kept on a 12/12 hour light/dark cycle, dark-adapted for 4-16h before the experiment,

and sacrificed under dim red light by cervical dislocation, with or without preceding exposure to CO_2. Experiments were performed during daylight circadian times (experiment start in the morning or early afternoon). The eye cups were removed, put in Ringer solution (in mM: 110 NaCl, 2.5 KCl, 1 $CaCl_2$, 1.6 $MgCl_2$, 10 D-Glucose, and 22 $NaHCO_3$) bubbled with 5% CO_2 / 95% O_2. The retina was isolated and attached to a nitrocellulose filter (Millipore) with a central 2x2 mm hole, with the optic nerve head centred.

All recordings were performed with a perforated 60-electrode MEA (60pMEA200/30iR-Ti-gr, Multichannel Systems, Reutlingen). The electrodes are arranged on a square grid with a 200 µm distance between neighboring electrodes. Experiments were performed as described previously [37]. Briefly, the mounted retina was placed ganglion cell-side down in the recording chamber, and good electrode contact was achieved by negative pressure through the perforated MEA. The tissue was superfused with Ringer solution at 34 °C. Data was recorded at 25 kHz with a USB-MEA-system (USB-MEA1060, Multichannel Systems, Reutlingen) or an MC-Card based MEA-system (MEA1060, Multichannel Systems).

Ganglion cell spike recordings

Data was high-pass filtered (500Hz, 10th-order butterworth filter), and spike waveforms and spike times were extracted from the raw data using Matlab (MathWorks). Spike sorting and thereby assignment of spikes to individual units (presumably ganglion cells) was performed semi-manually with custom written software (Matlab). Quality of each unit was individually/manually assessed by interspike interval and spike shape variation. Data analysis was based on the spiking responses of individual units. We estimated the instantaneous firing rate of ganglion cells by convolving the spike train (i.e. time series of 0's and 1's) with a Gaussian with sigma of 40 ms.

In-vitro ERG recordings

In vitro ERG recordings were performed as described previously utilizing the same 60-electrode MEA system as described above [37]. An Ag/AgCl pellet reference electrode (Science Products E-201ML) was connected instead of the internal reference electrode of the MEA chamber. The AgCl reference was positioned 2 to 3 mm above the center of the MEA electrode field and was optically shielded from direct visual stimulation. Synaptic transmission from photoreceptors to bipolar cells

559 was blocked with 50 µM L-AP4 (Sigma A7929 or Abcam ab120002), 10 µM NBQX (disodium salt,
560 Tocris 1044) and 10 µM RS-CPP (Tocris 0173). Glial currents (slow PIII component) were inhibited
561 with 100 µM $BaCl_2$ (Sigma 342920) [38]. Data was low-pass filtered (300Hz, 4^{th}-order butterworth
562 filter) and downsampled to 1 kHz. Noisy electrodes were discarded and all remaining electrodes
563 were averaged for the analysis of in-vitro ERG responses.

564 **3. Light stimulation and analysis: in vitro experiments**

565 Experimental control of light intensities

566 The retina was stimulated with full-field gray scale visual stimuli with a computer-controlled digital
567 light processing (DLP) projector (PG-F212X-L, Sharp or K11, Acer) and focused onto the
568 photoreceptors through the condenser of the microscope (Fig 1A). The stimulus projector produced
569 output spanning 3 log units of light intensities (i.e. 1000-fold difference between black ('0') and
570 white ('255') pixels). We linearized the gamma function of the projector output. The light path
571 contained a shutter and two motorized filter wheels with a set of neutral density (ND) filters
572 (Thorlabs NE10B-A to NE50B-A), having optical densities from 1 ("ND1", 10^1-fold light attenuation)
573 to 5 ("ND5", 10^5-fold light attenuation). To achieve light attenuation stronger than 5 log units, we
574 serially combined an ND5-filter in one filter wheel with another ND-filter in the second filter wheel,
575 to achieve optical densities from 6 to 10. We refer to the filter settings as ND1 (brightest setting
576 used) to ND8 (darkest setting used). While changing the ND filters, we closed the shutter to
577 prevent intermittent exposure to bright light. We usually started the experiments at ND8 (i.e.
578 combination of ND5 and ND3 filter), and step by step increased the ambient stimulation luminance
579 by changing the ND filters by 1 unit. Unless otherwise noted, we presented the same set of visual
580 stimuli at each ND-level during an experiment.

581 Light Intensity Measurements

582 We measured the spectral intensity profile (in µW cm^{-2} nm^{-1}) of our light stimuli with a calibrated
583 USB2000+ spectrophotometer (Ocean Optics). We then transformed the stimulus intensity into
584 rod-effective photon flux cm^{-2} s^{-1} by converting the spectrum to photons cm^{-2} s^{-1} nm^{-1}, and
585 integrating it with the normalized spectrum of rod sensitivity [24]. In addition, for comparison we
586 report stimulus intensity in equivalents of photoisomerizations per rod and second, assuming dark-

adapted rods, by multiplying the photon flux with the effective collection area of rods (0.5 µm² [28]). The results for a stimulus intensity of '30' range from $2 \cdot 10^7$ photons cm^{-2} s^{-1} (1 R* s^{-1} rod^{-1}, ND8) to $2 \cdot 10^{15}$ photons cm^{-2} s^{-1} (10^7 R* s^{-1} rod^{-1}, ND1), see Fig 1B, C. Note that the intensity values given as "R* s^{-1} rod^{-1}" serves for only comparison. It truly reflects photoisomerizations only at low intensities; at high backgrounds, bleaching adaptation leads to a much lower effective rate of isomerizations.

Specific stimuli and response analysis: Contrast

We report stimulus contrast in "Michelson contrast" and, for comparison, also in "Weber contrast". For a flash stimulus of intensity I, presented on a background of intensity I_{back}, the definitions are as follows:

Michelson contrast = $(I - I_{back}) / (I + I_{back})$

Weber contrast = $(I - I_{back}) / I_{back}$

For the sinusoidal stimulus used in the model we report the Michelson contrast based on the minimum and maximum deflections of the sinusoid: Michelson contrast = $(I_{max} - I_{min}) / (I_{max} + I_{min})$

Specific stimuli and response analysis: Ganglion cell spiking responses

Stimulus. Ganglion cell spiking responses were probed with full-field contrast steps (step duration: 2s) on a gray ('30' RGB pixel intensity) background (positive contrast: '30' → '50', Michelson: +0.25, Weber: +0.66; negative contrast: '30' → '10', Michelson: –0.49, Weber: –0.66, see Fig 1B). Five positive and five negative steps were interleaved and presented as one block, and the firing rate to these 5 repetitions was averaged and taken as "one response". The firing rate curves on the right in Fig 1D and E represent these "responses" which were used for further analysis; the rasters on the left show the underlying 5 individual responses.

Responsiveness. Whether or not a ganglion cell responded to a block (5 repetitions) of contrast steps was determined manually. For each unit and each stimulus block we manually inspected spike raster plots and firing rates. If a cell responded clearly and consistently to at least 3 out of 5 repetitions within one stimulus block, it was considered as "responding" and was tagged with "1". Since the purpose of this analysis was to see if rods can drive light responses in ganglion cells,

614 also purely “negative responses” (stimulus-evoked spike suppression) was counted as a response.
615 Stimuli for which a cell responded to only 1 or 2 repetitions or for which the response was weak
616 and/or sluggish were tagged with “0.5”. If a cell did not respond during a stimulus block, it was
617 tagged with “0”. The average value of these assignments across all units was used as the value for
618 “responsiveness” in Fig 2A, C and D.

619 *Amplitude*. The amplitude of the response (used in Fig 2B) was determined automatically as
620 follows: first, the baseline firing rate was subtracted from the response (baseline firing rate was
621 defined as the mean firing rate during 1300 ms before contrast step onset); second, we took the
622 absolute value of the response (such that also negative deflections in the firing rate would be
623 recognized as a response of the cell to stimulation); third, looking at all four brightness transitions
624 (onsets and offsets of the positive and negative contrast steps) we took the maximal response
625 value within 50 to 400 ms after the contrast step. This gave one “amplitude” value for each
626 ganglion cell and for each stimulus block. For further analysis, we only considered amplitude
627 values during stimulus blocks to which the cell actually responded (responsiveness tags “0.5” or
628 “1”, see above). These amplitudes were normalized for each ganglion cell separately to its
629 maximal response across the experiment.

630 *Averaging across experiments*. In most experiments, full-field contrast steps were presented at the
631 same time points after light-level transitions, with the earliest presentation about 4 min after the
632 ND-filter switch and then regularly every 5 min (Protocol 1 in S1 Fig; other stimuli, not discussed
633 here, were presented in between. Note that the other stimuli were also presented on a background
634 of ‘30’ and their maximal intensity did not exceed ‘60’, ensuring no excessive contribution to light
635 adaptation compared to the full-field contrast step stimuli.) In the experiments depicted in Fig 2B
636 and C, we changed the order of stimuli and presented full-field contrast steps more closely after
637 the light level switch (Protocol 2 in S1 Fig). In those experiments, we probed the ND4 and ND3
638 light levels at even tighter intervals (Protocol 3) to follow the dynamic changes of ganglion cell
639 responses with higher temporal precision. S1 Fig shows how the data points in Fig 2 were
640 averaged across experiments in which different stimulus protocols were used.

641 Specific stimuli and response analysis: In-vitro ERG recordings

642 *Stimulus*. For in-vitro ERG recordings we used a series of 50 ms-flashes of different positive
643 contrasts (Fig 3A). One stimulus set consisted of 4 flashes with Michelson contrast +0.79 (Weber:
644 +7.44, '30' → '255'), and 2 flashes each of Michelson contrast +0.6 (Weber: +2.97, '30' → '120'),
645 +0.33 (Weber: +0.99, '30' → '60'), and +0.99 (Weber: +999, '0' → '255'). In order to achieve the
646 high contrast (+0.99) it was necessary to intermittently reduce the gray background from '30' to '0'.
647 16 such stimulus sets were shown among other stimuli at each light level (30 min) from ND8 to
648 ND2. The other stimuli, not discussed here, were limited to a brightness range between '0' and
649 '60', presented on a background of '30'.

650 *Analysis*. We quantified the strength of the recorded ERG signal by measuring the mean amplitude
651 of the negative voltage deflection during 300 ms directly after the onset of a 50-ms flash. The 300
652 ms voltage signal preceding the flash was used as a baseline to test for significance of the flash-
653 elicited responses (Wilcoxon rank sum test). Significance testing was performed by using flashes
654 of 3 consecutive stimulus sets, i.e. n=12 flashes for contrast +0.79 and n=6 flashes for the other
655 contrasts. Fig 3B shows the moving average for this analysis (averaging 3 stimulus sets per data
656 point, shifting by 1 stimulus set for the next data point; no averaging was done across light level
657 transitions).

658 *Response reliability*. ERG responses at high light levels were usually very small, but nevertheless
659 often clearly distinct from the voltage fluctuations of the background activity. As a measure of the
660 reliability of such small signals, we devised a "response reliability index", which we calculated from
661 the statistical measure of the presence of a response (namely p-value resulting from the Wilcoxon
662 rank sum test, see above) according to the relationship depicted S1 Fig B.

663 **4. In vivo dLGN recordings**

664 In vivo setup

665 Mice were anaesthetised using a single dose of urethane (30% w/v in dH2O, 1.6mg/kg, i.p) and
666 placed in a stereotaxic frame (SR 5-M; Narishige, Japan) on a temperature-regulating 37°C heat
667 mat (Harvard Apparatus, UK). A craniotomy was drilled above the coordinates for the dLGN (B–

2.2mm to 2.6mm, ML 1.5-3mm) relative to the mouse stereotaxic atlas [39]. A 32 contact recording electrode (A4x8-5mm-50-200-177/413-A32; Neuronexus, USA) was lowered into the dLGN and extracellular spiking activity collected through a Recorder64 system (Plexon, USA). Light stimuli were delivered to the eye contralateral to the recorded brain hemisphere. Upon completion, animals were sacrificed by cervical dislocation and the brain fixed in 4% paraformaldehyde. Electrode placement (the electrode was dipped in fluorescent dye; CM-DiI, Life Technologies, UK) was verified in post-hoc histology.

Light stimuli

For *in-vivo* experiments, we delivered multi-spectral stimuli using a Spectra X light engine (Lumencor, USA). Stimuli were created by stepping four LEDs in combination from a low background to a high level (Blue, Cyan, Green and Yellow λ_{max} = 430nm, 480nm, 511nm and 575nm respectively). Light stimuli were presented through a light guide to the atropine-dilated eye as diffuse illumination of a Lambertian disc (10 mm in diameter, placed <5mm from corneal surface). A circular ND wedge (100FS04DV.4, Newport) in the light path between the exit point of the light engine and the end of the optical fiber, allowed light intensity to be modulated over a 4 log unit range. Spectral power densities for each LED were measured using a calibrated spectroradiometer (Bentham Instruments Ltd., UK). These were converted to retinal irradiance in rod-effective photon cm^{-2} s^{-1} to match the light levels used in *in-vitro* experiments by converting the corneal irradiance and correcting for the pre-receptoral filtering of the lens. For the light levels used *in-vivo*, we use as a short-hand the “ND5” to “ND2” nomenclature, as these are the closest corresponding intensities in the *in-vitro* experiments. Background intensity was $4.52*10^{14}$ rod-effective photon cm^{-2} s^{-1} at the brightest light level (“ND2”). 1200 flashes (duration: 50 ms) were shown at 1 Hz at each light level (+0.75 Michelson contrast for rods). These flashes were interleaved with a lower contrast (+0.5, data not shown here), thus protocol took 40 min per light level.

Data analysis *Cnga3*$^{-/-}$ mice

We measured 40 light responsive multi-units from 3 mice. 4 multi-units were excluded because they stopped responding completely after the first light level switch. In one mouse, recordings

could only be performed up to ND2, but not for the last ND5 repetition. Firing rate has been calculated by convolving the spike train (i.e. time series of 0's and 1's) with a Gaussian with sigma of 5 ms. Then, responses to 10 flashes were averaged (= 1 group). For each group, we calculated the mean background firing rate for the 190 ms directly before stimulus onset. The background firing rates from 20 groups was then averaged and taken as the mean background firing rate for these 20 groups. The mean response rate 50 to 250 ms after the flash stimulus was considered as response. We applied a Wilcoxon rank sum test (1-sided) to test for significant differences between the 20 background and the 20 response values, i.e. we tested for significant light responses. These significance tests were performed on a running average with shifts of 2 groups for each data point. No averaging was performed across ND-borders. This resulted in approximately 350 p-values per recorded multiunit over the whole series of light levels. The measured p-values were then transformed into a response reliability as shown in S1 Fig B.

Detecting rod contributions to the visual response of *Opnmw^{R};Opn4$^{-/-}$* mice.

Stimulus. We presented a series of blue, cyan and red flashes (50 ms duration) at 2Hz frequency on a light adapting violet background (λ_{max} = 400nm, Fig5A). We used the same light engine and ND wedge described in section “Light Stimuli”. Flashes followed a pseudorandom order for colors (λ_{max} = 430nm, 480nm and 630nm respectively for Blue, Cyan and Red LEDs) and intensities (15 different levels per color) to prevent contrast adaptation in the response.

Stimulus intensity and contrast. Our estimate of S-, L-cone and rod Normalized Sensitivity for calculating flash contrasts was based upon Govardovskii nomograms [7], using λ_{max} = 365nm for S-cones, λ_{max} = 556nm for L-cones [23] and λ_{max} = 498nm for rods [16], adjusted for photopigment optical density (POD) [40] and lens absorption, using a function adapted from [41]:

$$\text{Normalized Sensitivity} = 10^{-\mu(\lambda)D} * \text{Sensitivity} / \max(\text{Sensitivity})$$

with $\text{Sensitivity} = (1 - 10^{-POD*S(\lambda)})$, $S(\lambda)$ is the pigment nomogram, D is the lens thickness (D = 2.07mm) [41], and $\mu(\lambda)$ is the attenuation coefficient calculated as

$\mu(\lambda) = c * (\lambda^{d} - \lambda_0^{d})$ for $\lambda < \lambda_0^{d}$; $\mu(\lambda) = 1$ otherwise;

722 The values for c and λ_0 (= wavelength of maximal lens transmission) were obtained by fitting
723 tabulated data (c = 5.33*10^4; d = -2.27; λ_0 = 700nm) [42].

724 The absolute stimulus intensity of the violet background (effective photons cm^{-2} s^{-1} flux for the
725 brightest background, ND3: rod-opsin 1.3758 10^{13}, L-opsin: 1.3473 10^{13}, S-opsin: 1.5833 10^{13}) and
726 contrast of the flashes (assuming POD=0.1 for cones, POD=0.01 for rods, and c = 5.33*10^4) are
727 depicted in Fig 5B.

728 *Analysis*. 45 PSTHs were estimated (15 intensities * 3 colours) for each light responsive unit and a
729 PSTH matrix with mean firing rate responses (<fr>) was generated. In order to remove the high
730 frequency noise due to the finite number of trials we computed the eigenvalue decomposition of
731 the PSTH covariance matrix ($PSTH^T$*PSTH). Then we selected the smallest subset of eigenvectors
732 whose associated eigenvalues accounted for >90% power of the PSTH covariance matrix. Finally
733 we used the selected eigenvectors and their projections to reconstruct a "de-noised" version of the
734 original PSTH matrix. The 45 responses were then calculated as the Euclidean norms of the "de-
735 noised" PSTHs as follows:

736 Response = sqrt(Σ$<fr>^2$)

737 with the summation taken across 20 time bins (time bin duration 15ms) in the first 300ms after the
738 flash onset. We initially evaluated the possibility to measure flash responses as
739 increments/decrements in firing rate in respect to the baseline. However we chose to use the
740 Euclidean norm because we observed that a significant fraction of units exhibited multiphasic
741 responses where those increments and decrements in firing rate tended to cancel each other out.

742 *Statistical analysis of colored flash responses*. The procedure for statistical analysis and their
743 results are described in S5 Table.

744 **5. Computational model**

745 We have employed the model of Invergo and co-workers [20] to simulate the phototransduction
746 cascade within the rod outer segment. This model is an adaptation to mouse rods of previous
747 models intended to simulate the phototransduction cascade in amphibians [43,44]. The current
748 model of Invergo et al describes the phototransduction cascade on the system-level, i.e., based on

749 a reaction network for the molecular species, a system of ordinary differential equations (ODE) is
750 derived by simplifying assumptions like mass action kinetics. The numerical solution of this ODE-
751 system yields the time dependence of each of the involved molecular species and as the main
752 outcome the photo-response to a prescribed stimulus. We have implemented the model in the
753 simulation software COPASI [45]. Compared to the original parameters of Invergo et al, we have
754 made the following adjustments: In all simulations, we have adjusted the total number of rhodopsin
755 molecules (R_{total}). We used a maximum number of 7x10^7 [46] instead of 10^8, and reduced that
756 number in some simulations to investigate the dependency of rod responses on that parameter
757 (rows in S4 Fig). We have varied the parameter for the rhodopsin regeneration rate (k_{recyc}) to mimic
758 the different experimental conditions (*in-vitro*, *in-vivo*) and to investigate the dependency of rod
759 responses on that parameter.

760 The original parameters of this model had been fit to biochemical and physiological data based on
761 very different stimuli than the stimulus used in our study, namely to very brief and moderate-
762 intensity flash stimuli on a dark-adapted rod (lasting tens of milliseconds of at most 2000 R* rod^{-1}
763 $flash^{-1}$). Given the long duration and high intensity range of our stimulus, we took into account that
764 arrestin and transducin are transported between the outer and inner segments [25] and refs
765 therein, resulting in a near-exchange of these molecular species between inner and outer segment.
766 Under intense illumination, arrestin is transported from the inner segment to the outer segment,
767 while transducin moves in the opposite direction. We have implemented this transport as a
768 simplified step-wise change of concentration upon light-level transitions (S4 Fig B). None of our
769 parameter-adjustments changed the model behavior to the original stimuli used for parameter-
770 fitting by Invergo et al (2014) (not shown).

771

772 **Acknowledgements**

773 We thank Martin Biel for supplying the *Cnga3*$^{-/-}$ mouse line for the in-vitro experiments.

774

775

References

1. Land MF, Nilsson D-E (2002) Animal Eyes: Oxford University Press.
2. Rodieck RW (1998) The First Steps in Seeing: Sinauer Assn.
3. Adelson EH (1982) Saturation and adaptation in the rod system. Vision Res 22: 1299-1312.
4. Blakemore CB, Rushton WA (1965) Dark adaptation and increment threshold in a rod monochromat. J Physiol 181: 612-628.
5. Green DG (1971) Light adaptation in the rat retina: evidence for two receptor mechanisms. Science 174: 598-600.
6. Nakatani K, Tamura T, Yau KW (1991) Light adaptation in retinal rods of the rabbit and two other nonprimate mammals. J Gen Physiol 97: 413-435.
7. Govardovskii VI, Calvert PD, Arshavsky VY (2000) Photoreceptor light adaptation. Untangling desensitization and sensitization. J Gen Physiol 116: 791-794.
8. Purves D, Augustine GJ, Fitzpatrick D, Hall WC, Lamantia AC, et al. (2008) Chapter 11 Vision: The Eye. Neuroscience. 4 ed: Sunderland (MA): Sinauer Associates.
9. Bear MF, Connors BW, Paradiso MA (2006) Chapter 9 The Eye. Neuroscience: Exploring the Brain: Lippincott Williams and Wilkins.
10. Squire L, Berg D, Bloom F, Du Lac S, Ghosh A, et al. (2008) Chapter 27 Vision. Fundamental Neuroscience. 3 ed: Academic Press.
11. Farrow K, Teixeira M, Szikra T, Viney TJ, Balint K, et al. (2013) Ambient illumination toggles a neuronal circuit switch in the retina and visual perception at cone threshold. Neuron 78: 325-338 doi: 10.1016/j.neuron.2013.02.014.
12. Kefalov VJ (2012) Rod and cone visual pigments and phototransduction through pharmacological, genetic, and physiological approaches. J Biol Chem 287: 1635-1641.
13. Szikra T, Trenholm S, Drinnenberg A, Juttner J, Raics Z, et al. (2014) Rods in daylight act as relay cells for cone-driven horizontal cell-mediated surround inhibition. Nat Neurosci: doi: 10.1038/nn.3852.
14. Demontis GC, Bisti S, Cervetto L (1993) Light sensitivity, adaptation and saturation in mammalian rods. Prog Brain Res 95: 15-24.
15. Yin L, Smith RG, Sterling P, Brainard DH (2006) Chromatic properties of horizontal and ganglion cell responses follow a dual gradient in cone opsin expression. J Neurosci 26: 12351-12361 doi: 10.1523/JNEUROSCI.1071-06.2006.
16. Naarendorp F, Esdaille TM, Banden SM, Andrews-Labenski J, Gross OP, et al. (2010) Dark light, rod saturation, and the absolute and incremental sensitivity of mouse cone vision. J Neurosci 30: 12495-12507 doi: 10.1523/JNEUROSCI.2186-10.2010.
17. Azevedo AW, Rieke F (2011) Experimental protocols alter phototransduction: the implications for retinal processing at visual threshold. J Neurosci 31: 3670-3682.
18. Nikonov S, Engheta N, Pugh EN, Jr. (1998) Kinetics of recovery of the dark-adapted salamander rod photoresponse. J Gen Physiol 111: 7-37.
19. Nymark S, Heikkinen H, Haldin C, Donner K, Koskelainen A (2005) Light responses and light adaptation in rat retinal rods at different temperatures. J Physiol 567: 923-938 doi: 10.1113/jphysiol.2005.090662.
20. Invergo BM, Dell'Orco D, Montanucci L, Koch KW, Bertranpetit J (2014) A comprehensive model of the phototransduction cascade in mouse rod cells. Mol Biosyst 10: 1481-1489 doi: 10.1039/c3mb70584f.
21. Aguilar M, Stiles WS (1954) Saturation of the rod mechanism of the retina at high levels of illumination. Optica Acta 1: 59 –65.
22. Allen AE, Storchi R, Martial FP, Petersen RS, Montemurro MA, et al. (2014) Melanopsin-driven light adaptation in mouse vision. Curr Biol 24: 2481-2490 doi: 10.1016/j.cub.2014.09.015.
23. Smallwood PM, Olveczky BP, Williams GL, Jacobs GH, Reese BE, et al. (2003) Genetically engineered mice with an additional class of cone photoreceptors: implications for the evolution of color vision. Proc Natl Acad Sci U S A 100: 11706-11711 doi: 10.1073/pnas.1934712100.
24. Zele AJ, Maynard ML, Joyce DS, Cao D (2014) Effect of rod-cone interactions on mesopic visual performance mediated by chromatic and luminance pathways. J Opt Soc Am A Opt Image Sci Vis 31: A7-A14 doi: 10.1364/JOSAA.31.0000A7.

831 25. Calvert PD, Strissel KJ, Schiesser WE, Pugh EN, Jr., Arshavsky VY (2006) Light-driven
832 translocation of signaling proteins in vertebrate photoreceptors. Trends Cell Biol 16: 560-
833 568 doi: 10.1016/j.tcb.2006.09.001.
834 26. Slepak VZ, Hurley JB (2008) Mechanism of light-induced translocation of arrestin and
835 transducin in photoreceptors: interaction-restricted diffusion. IUBMB Life 60: 2-9 doi:
836 10.1002/iub.7.
837 27. Burkhardt DA (1994) Light adaptation and photopigment bleaching in cone photoreceptors in
838 situ in the retina of the turtle. J Neurosci 14: 1091-1105.
839 28. Vlasits AL, Bos R, Morrie RD, Fortuny C, Flannery JG, et al. (2014) Visual stimulation switches
840 the polarity of excitatory input to starburst amacrine cells. Neuron 83: 1172-1184 doi:
841 10.1016/j.neuron.2014.07.037.
842 29. Aboshiha J, Dubis AM, Carroll J, Hardcastle AJ, Michaelides M (2015) The cone dysfunction
843 syndromes. Br J Ophthalmol: doi: 10.1136/bjophthalmol-2014-306505.
844 30. Santos-Ferreira T, Postel K, Stutzki H, Kurth T, Zeck G, et al. (2015) Daylight vision repair by
845 cell transplantation. Stem Cells 33: 79-90 doi: 10.1002/stem.1824.
846 31. Altimus CM, Guler AD, Alam NM, Arman AC, Prusky GT, et al. (2010) Rod photoreceptors
847 drive circadian photoentrainment across a wide range of light intensities. Nat Neurosci 13:
848 1107-1112 doi: 10.1038/nn.2617.
849 32. Wang JS, Estevez ME, Cornwall MC, Kefalov VJ (2009) Intra-retinal visual cycle required for
850 rapid and complete cone dark adaptation. Nat Neurosci 12: 295-302 doi: 10.1038/nn.2258.
851 33. Wang JS, Kefalov VJ (2009) An alternative pathway mediates the mouse and human cone
852 visual cycle. Curr Biol 19: 1665-1669 doi: 10.1016/j.cub.2009.07.054.
853 34. Umino Y, Solessio E, Barlow RB (2008) Speed, spatial, and temporal tuning of rod and cone
854 vision in mouse. J Neurosci 28: 189-198 doi: 10.1523/JNEUROSCI.3551-07.2008.
855 35. Jacobson SG, Cideciyan AV, Peshenko IV, Sumaroka A, Olshevskaya EV, et al. (2013)
856 Determining consequences of retinal membrane guanylyl cyclase (RetGC1) deficiency in
857 human Leber congenital amaurosis en route to therapy: residual cone-photoreceptor vision
858 correlates with biochemical properties of the mutants. Hum Mol Genet 22: 168-183 doi:
859 10.1093/hmg/dds421.
860 36. Biel M, Seeliger M, Pfeifer A, Kohler K, Gerstner A, et al. (1999) Selective loss of cone function
861 in mice lacking the cyclic nucleotide-gated channel CNG3. Proceedings of the National
862 Academy of Sciences of the United States of America 96: 7553-7557.
863 37. Reinhard K, Tikidji-Hamburyan A, Seitter H, Idrees S, Mutter M, et al. (2014) Step-by-step
864 instructions for retina recordings with perforated multi electrode arrays. PLoS One 9:
865 e106148 doi: 10.1371/journal.pone.0106148.
866 38. Kofuji K, Nakamura M, Isobe T, Murata Y, Kawashima S (2008) Stabilization of alpha-lipoic
867 acid by complex formation with chitosan. Food Chem 109: 167-171 doi:
868 10.1016/j.foodchem.2007.11.078.
869 39. Paxinos G FK (2001) The Mouse Brain in Stereotaxic Coordinates: Academic Press.
870 40. Thomas PBM, Formankiewicz MA, Mollon JD (2011) The effect of photopigment optical density
871 on the color vision of the anomalous trichromat. Vision Research 51: 2224-2233 doi: DOI
872 10.1016/j.visres.2011.08.016.
873 41. Lei B, Yao G (2006) Spectral attenuation of the mouse, rat, pig and human lenses from
874 wavelengths 360 nm to 1020 nm. Exp Eye Res 83: 610-614 doi:
875 10.1016/j.exer.2006.02.013.
876 42. Jacobs GH, Williams GA (2007) Contributions of the mouse UV photopigment to the ERG and
877 to vision. Doc Ophthalmol 115: 137-144 doi: 10.1007/s10633-007-9055-z.
878 43. Dell'Orco D, Schmidt H, Mariani S, Fanelli F (2009) Network-level analysis of light adaptation in
879 rod cells under normal and altered conditions. Mol Biosyst 5: 1232-1246 doi:
880 10.1039/b908123b.
881 44. Invergo BM, Montanucci L, Koch KW, Bertranpetit J, Dell'orco D (2013) Exploring the rate-
882 limiting steps in visual phototransduction recovery by bottom-up kinetic modeling. Cell
883 Commun Signal 11: 36 doi: 10.1186/1478-811X-11-36.
884 45. Hoops S, Sahle S, Gauges R, Lee C, Pahle J, et al. (2006) COPASI--a COmplex PAthway
885 SImulator. Bioinformatics 22: 3067-3074 doi: 10.1093/bioinformatics/btl485.
886 46. Lyubarsky AL, Daniele LL, Pugh EN, Jr. (2004) From candelas to photoisomerizations in the
887 mouse eye by rhodopsin bleaching in situ and the light-rearing dependence of the major

components of the mouse ERG. Vision Res 44: 3235-3251 doi: 10.1016/j.visres.2004.09.019.
47. Nakagawa S, Cuthill IC (2007) Effect size, confidence interval and statistical significance: a practical guide for biologists. Biol Rev Camb Philos Soc 82: 591-605 doi: 10.1111/j.1469-185X.2007.00027.x.
48. Montgomery D. C. RGC (2010) Applied Statistics and Probability for Engineers: Wiley.

Supplementary Figures and Tables

S1 Fig. Supplementary information about methods.

S2 Fig. Responsiveness of ganglion cells in isolated *Pde6c*$^{cpfl1/cpfl1}$ and *Gnat2*$^{cpfl3/cpfl3}$ retina.

S3 Fig. In-vitro ERG recordings from isolated *Cnga3*$^{-/-}$, *Pde6c*$^{cpfl1/cpfl1}$, and *Gnat2*$^{cpfl3/cpfl3}$ retina.

S4 Fig. Model responses across the tested parameter space

S5 Table. Statistical analysis of responses to blue, cyan and red flashes in the dLGN of *Opn1mw*^{R}*:Opn4*$^{-/-}$ mice.

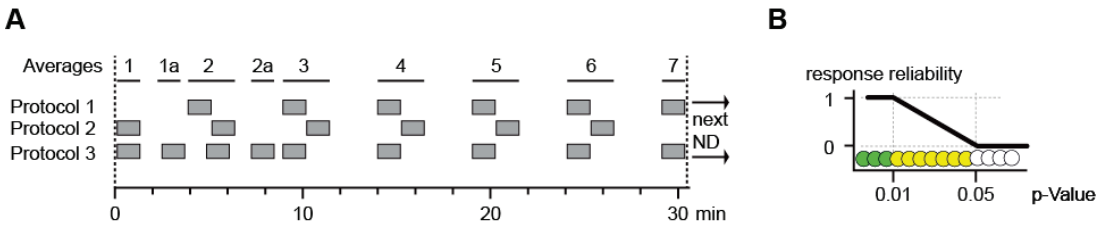

S1 Fig. Supplementary information about methods.

A Full-field contrast steps (see Fig. 1B) were always presented in blocks of 5 repetitions, lasting approximately 1 min (gray rectangles). In different experiments we presented these blocks at different times after transitioning to a new light level. In most experiments we used Protocol 1, in which the first presentation started at time 4 min. In some experiments we used Protocol 2 instead. We averaged across these different experiments as indicated on top, yielding 7 data points at each light level (see Fig. 2). At the ND4 and ND3 light levels, we used Protocol 3 instead of Protocol 2, yielding the additional data points 1a and 2a.

B Calculation of response reliability (see Figs. 3, 4 and Suppl. Fig. S3) was based on the significance (p-Value) of an observed response. Responses which hardly differed from background activity ($p>0.05$) were considered unreliable (reliability = 0). Correspondingly, highly significant responses ($p<0.01$) were considered very reliable (reliability = 1). p-values between 0.05 and 0.01 were converted linearly to reliability-values between 0 and 1.

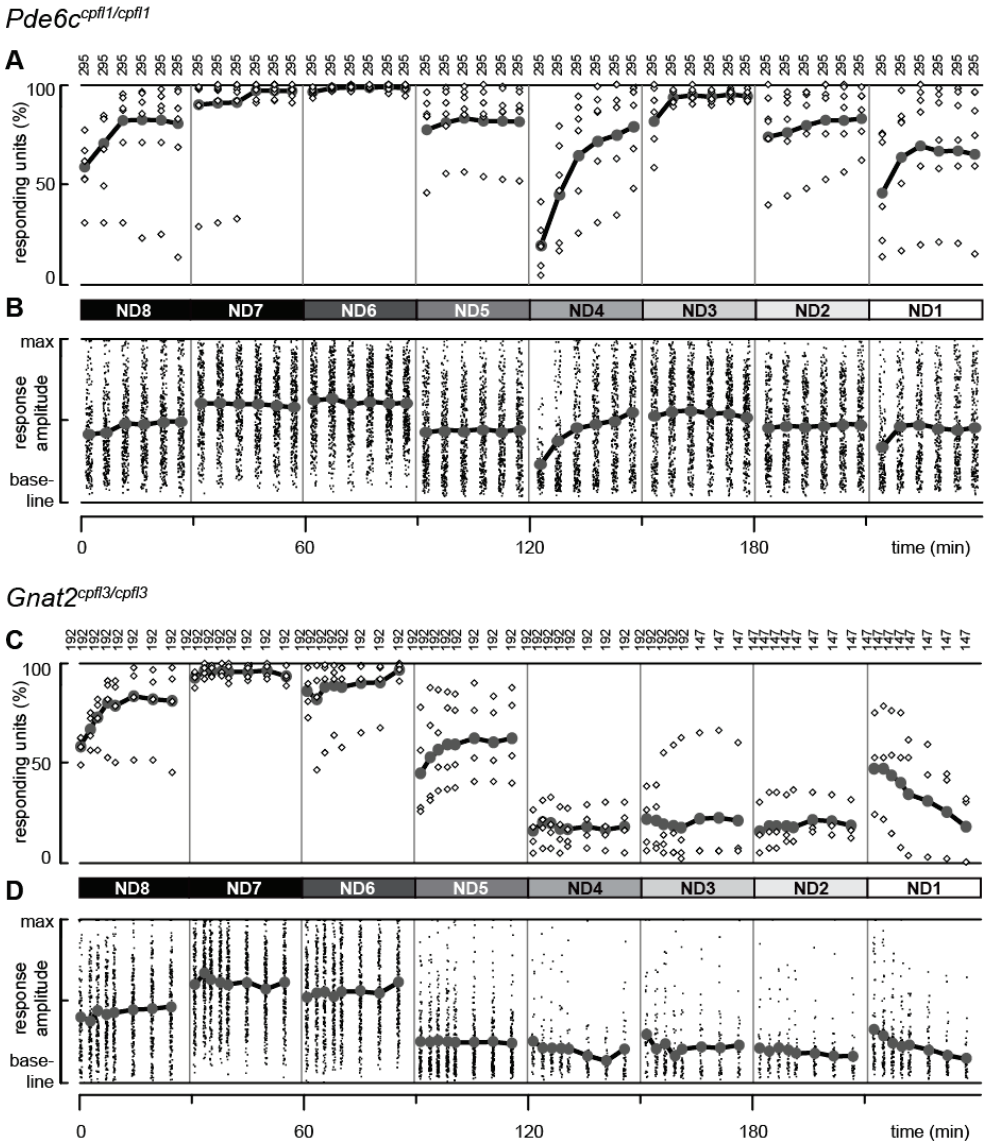

S2 Fig. Responsiveness of ganglion cells in isolated *Pde6c*$^{cpfl1/cpfl1}$ and *Gnat2*$^{cpfl3/cpfl3}$ retina.
A + B Percentages (A) and relative amplitudes (B) of responding units in *Pde6c*$^{cpfl1/cpfl1}$ retinas (n=5). The percentage of responding units dropped in the beginning of high light levels, but recovered with a similar time course as found in *Cnga3*$^{-/-}$ retinas (Fig. RGC A). On a population level, the relative amplitude was stable across light levels, except for a small drop in the beginning of ND4 comparable to our findings in *Cnga3*$^{-/-}$ (Fig. RGC D).
C + D Percentages (C) and relative amplitudes (D) of responding units in *Gnat2*$^{cpfl3/cpfl3}$ retinas (n=4). Consistent with our findings in *Pde6c*$^{cpfl1/cpfl1}$ and *Cnga3*$^{-/-}$ retinas, rods drove visual responses at any light level also in *Gnat2*$^{cpfl3/cpfl3}$ retinas.

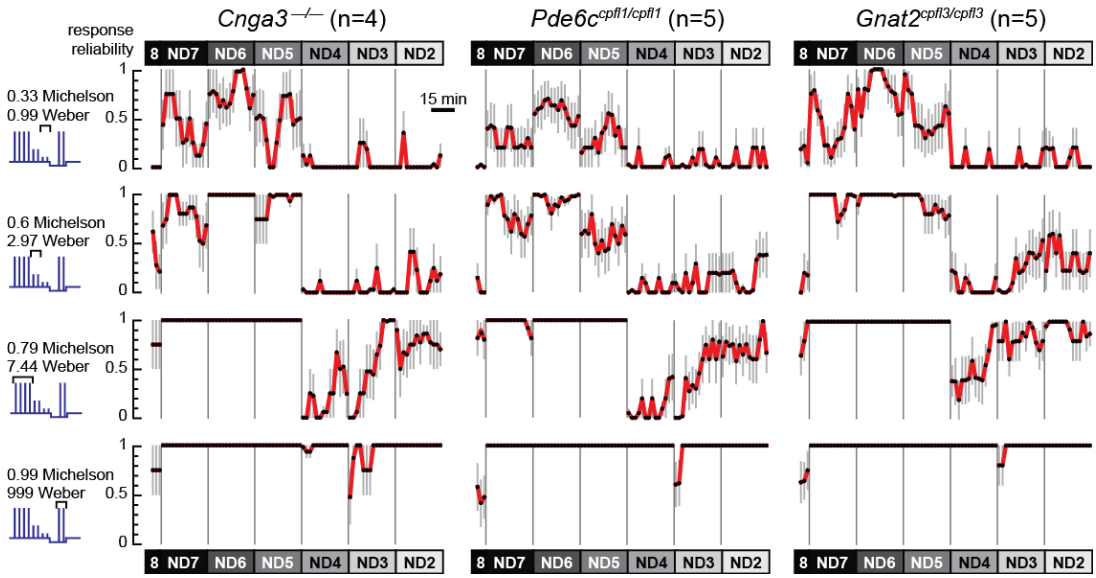

S3 Fig. In-vitro ERG recordings from isolated *Cnga3*$^{-/-}$, *Pde6c*$^{cpfl1/cpfl1}$, and *Gnat2*$^{cpfl3/cpfl3}$ retina. Response reliability of ERG responses (mean ± s.e.m.) for *Cnga3*$^{-/-}$ (n=4 retinas), *Pde6c*$^{cpfl1/cpfl1}$ (n=5), and *Gnat2*$^{cpfl3/cpfl3}$ (n=5) retinas to flashes of 0.33, 0.6, 0.79, and 0.99 Michelson contrast. Response reliability was calculated from the p-Values resulting from comparing background and response activity (as described in Supl. Fig. S1B and Methods). Similar contrast dependence of ERG responses was found for all three mouse strains. At high light levels (ND4 to ND2), responses could be detected reliably for stimuli with Michelson contrast of 0.79 and higher (for *Gnat2*$^{cpfl3/cpfl3}$ already for stimuli with contrast 0.6). For smaller contrast, only responses to low and medium light levels (ND8 to ND5) were reliably detectable. The time-dependent re-emergence of rod-driven light responses found for stimuli of contrast 0.79 in *Cnga3*$^{-/-}$ retinas was also present in the two other mouse strains.

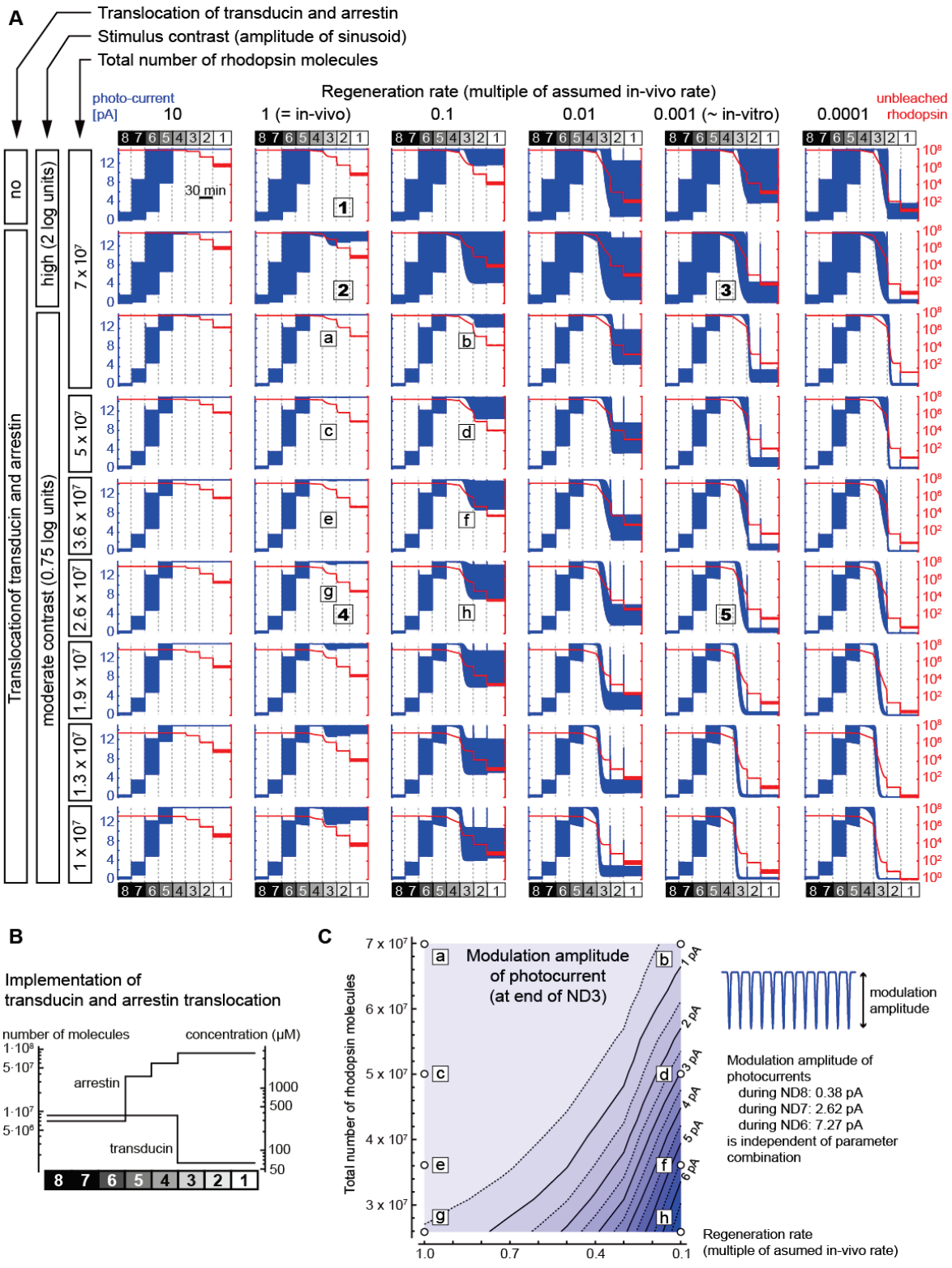
A
Translocation of transducin and arrestin
Stimulus contrast (amplitude of sinusoid)
Total number of rhodopsin molecules
photo-current [pA]
Regeneration rate (multiple of assumed in-vivo rate)
10
1 (= in-vivo)
0.1
0.01
0.001 (~ in-vitro)
0.0001
unbleached rhodopsin
30 min
no
high (2 log units)
moderate contrast (0.75 log units)
Translocationof transducin and arrestin
7 x 10⁷
5 x 10⁷
3.6 x 10⁷
2.6 x 10⁷
1.9 x 10⁷
1.3 x 10⁷
1 x 10⁷
B
Implementation of transducin and arrestin translocation
number of molecules
concentration (µM)
arrestin
transducin
C
Modulation amplitude of photocurrent (at end of ND3)
Total number of rhodopsin molecules
Regeneration rate (multiple of asumed in-vivo rate)
modulation amplitude
Modulation amplitude of photocurrents
during ND8: 0.38 pA
during ND7: 2.62 pA
during ND6: 7.27 pA
is independent of parameter combination

939

940

S4 Fig. Model responses across the tested parameter space

A Model behavior for various rhodopsin concentrations (R_{total}, rows) and regeneration rates (k_{recyc}, columns). We simulated the photocurrent (blue) and the number of unbleached rhodopsin molecules (red) in response to a sinusoidal stimulus for rhodopsin concentrations varying between 7 x 10^7 (published upper bound (Lyubarsky et al. 2004), first three rows) down to 1 x 10^7 molecules (last row), and for multiples of the assumed *in-vivo* regeneration rate of rhodopsin varying between 0.0001 and 10 times the *in-vivo* value (columns).

[Note about the parameter k_{recyc}: We assume here that the value for k_{recyc} used in the original model (Invergo et al. 2014) (k_{recyc} = 0.007) corresponds to the *in-vivo* regeneration rate of rhodopsin. However, estimates for the "true" regeneration rate vary. In fact, for estimating rod responses at low and medium light levels, knowing the "true" value of k_{recyc} is of little importance. Across the full range of parameter variations presented here, responses at low light levels are hardly affected. For example, the stimuli used by Invergo et al for fitting the parameters of their original model produce the same output for all parameter combinations shown here.]

For low regeneration rates (0.0001 to 0.1 times in-vivo rates, last 4 columns), responses always reemerged at high light levels (ND4 and higher), independent of the other parameter values of the model. For the assumed *in-vivo* regeneration rate (column 2), responses reemerged only when transport of transducin and arrestin was implemented (rows 2 to 9), and only for high-contrast stimuli (panel 2), or for lower rhodopsin concentrations (starting with panel "e" downward). Panels 1 through 5 are also depicted in Fig. 6; panels "a" through "h" span the parameter range scrutinized more closely in **C**.

For the low-contrast stimuli (rows 3 to 9), the model showed similar behavior from ND8 to ND5 for all 42 parameter combinations shown. In other words, for low and medium light levels, the qualitative model behavior is robust even against these large variations of parameter values. Another consistent observation for all parameter combinations was that for this stimulus of moderate contrast (0.7 Michelson contrast) photocurrents initially vanished after switching to ND4 - the rod becomes saturated. However, the further qualitative development at ND4 and higher light levels depended strongly on the choice of parameters, especially on the choice of the regeneration rate k_{recyc}. Here, the assumed *in-vivo* regeneration rate of rhodopsin (second column) proved to be a turning point of the model behavior. For larger values of k_{recyc} (left-most column), rods always remained saturated. For smaller values of k_{recyc} (columns 3 to 6, including the estimated *in-vitro* regeneration rate, column 5), photocurrents always re-emerged independently of the absolute rhodopsin concentration. For the value of k_{recyc} used in the Invergo-model (the assumed *in-vivo* value), however, re-emergence of rod responses depended on the absolute rhodopsin concentration. Low rhodopsin concentration promoted responses at high light levels (lowest five rows, starting with panel "e"), while high rhodopsin concentration led to stable saturation (panels "a" and "c").

B Implementation of arrestin and transducin translocation in the computational model. Concentrations in the outer segment were adjusted in an instantaneous, step-like fashion upon light-level transitions.

C Detailed characterization of the modulation amplitude of the photocurrent, measured at the end of ND3, for variations of the parameters R_{total} and k_{recyc}. Parameter combinations corresponding to panels "a" through "h" in **A** are indicated. Note that the left-most contour line in the plot (corresponding to 0.5 pA) represents stronger modulation than the modulation observed under scotopic (ND8) conditions (0.38 pA).

S5 Table. Statistical analysis of responses to blue, cyan and red flashes in the dLGN of *Opn1mw^{R}:Opn4$^{-/-}$* mice.

A: POD_{Lopsin} = 0.1; c = $5.33*10^4$

	R^2_{BCR}	R^2_{null}	ΔR^2
ND5	47.5%	40.2%	7.3%
ND4	48.7%	48.3%	0.4%
ND3	57.3%	52.5%	4.8%

B: varying POD and c

ND5	R^2_{BCR}	R^2_{null}	ΔR^2
0.75*c	47.5%	40.6%	6.9%
1.25*c	47.4%	39.9%	7.6%
POD_{Lcone}=0.01	47.5%	40.4%	7.1%
POD_{Lcone}=1	47.5%	38.6%	8.9%

ND4	R^2_{BCR}	R^2_{null}	ΔR^2
0.75*c	48.7%	48.3%	0.4%
1.25*c	48.7%	48.3%	0.4%
POD_{Lcone}=0.01	48.7%	48.4%	0.3%
POD_{Lcone}=1	48.7%	47.4%	1.3%

ND3	R^2_{BCR}	R^2_{null}	ΔR^2
0.75*c	57.3%	52.0%	5.3%
1.25*c	57.3%	52.9%	4.4%
POD_{Lcone}=0.01	57.3%	52.5%	4.8%
POD_{Lcone}=1	57.3%	51.8%	5.5%

In order to analyze population responses, we first normalized single unit responses by their mean value across flashes and colours. This normalization was important to reduce the additional source of variability represented by the large differences in firing rates (both spontaneous and evoked) across units. Then, at each light level, we pooled normalized responses across units and flash intensities into three groups based in flash color (B: Blue, C: Cyan and R: Red). We observed that, separately, each group's response to flashes (as a function of L-opsin contrast) could be well fitted by using a quadratic polynomial model (i.e. two covariates and a constant term). We then asked whether responses to flashes of the three wavelengths, when expressed in L-opsin contrast, could be adequately described by a single function. Because of the large sample size (each group was constituted by more than 1000 responses) comparisons based on

unstandardized p-values made little sense as even the slightest difference would result in highly significant comparisons (see e.g. Nakagawa & Cuthill (Nakagawa and Cuthill 2007) for a review). Instead we focused on the explained variance that provided a meaningful measure of the effect size. Our null hypothesis was that L-opsin contrast could account for all the explainable variance. Therefore, if L-opsin contrast was the only drive for the observed responses, we would expect that, by pooling data from all three wavelengths, the explained variance would not be smaller than the one obtained by using a more complicated model that took into account the difference in flash colours (i.e. six covariates and a constant term). In order to compare the explained variance under the null and alternative hypothesis we used the R^2-adjusted as in (Montgomery D. C. 2010) so that the variance explained by null "pooled" model would be indicated as R^2_{null} and the variance explained by the alternative model would be indicated as R^2_{BCR}. The size of the effect was also evaluated as $\Delta R^2 = R^2_{BCR} - R^2_{null}$.

A Results of this analysis when cone contrast was calculated using our default estimates of pigment optical density (POD) and lens correction (parameter c, see methods). We observe that the Null hypothesis can explain the variance adequately only at ND4 ($\Delta R^2 < 1\%$), but not at ND5 or ND3.

B Impact of varying c and POD on these fits: results are stable in spite of large variations in these parameters and, again, the null hypothesis adequately describes our observations only at ND4.

IV. Acknowledgements

Mein besonderer Dank gebührt meinem Doktorvater Thomas Münch, der immer ein offenes Ohr hatte und der mir sehr viel Freiheit gab mein Projekt durchzuführen, neue Techniken zu lernen, internationale Meetings zu besuchen und der mit seiner fröhlichen Art die familiäre Atmosphäre mit geschaffen hat, an die ich mich immer gerne zurückerinnern werde.

Ich bedanke mich sehr herzlich bei meinen Advisory Board Members Jutta Engel und Bernd Wissinger für den tollen Support und das Interesse und Engagement, das stets zu spüren war.

Weiterhin möchte ich mich bei Sebastian Ströh, Karin Dedek und Arndt Meyer bedanken, die mich in Oldenburg beherbergt und mir mit Geduld und außergewöhnlichem Einsatz das patchen isolierter Horizontalzellen beigebracht haben und bei Antonella Pirone, die mir erstmal die Grundzüge der Molekularbiologie näherbringen musste.

Thanks for the coffee caravans to the kitchen, lunch breaks, movie nights, barbeques, cake-sharings and polish swearings. The best lab mates I could have wished for: Katja, Natalia, Saad (aka BATMAN), Anahit, Boris (and Sven and Co), Marion, Alex, Elli and Nadine. You are family.

To all the other PhD students and Postdocs of the CIN that I had the great pleasure to get to know and whom I cannot mention all: You are all amazing people and I hope we will meet again!

Meine persönliche Dankbarkeit schulde ich meinen Großeltern, Heinz und Anneliese Häring, die kurz vor Beendigung meiner Dissertation aus dem Leben geschieden sind und mit denen ich den Abschluss nicht mehr teilen kann.